

**IMPROVEMENT IN THE PROPERTIES OF
THERMALLY SPRAYED HYDROXYAPATITE
COATING REINFORCED WITH CARBON
NANOTUBE FOR ORTHOPAEDIC
APPLICATIONS**

Thesis

Submitted in partial fulfillment of the requirement for the degree of

DOCTOR OF PHILOSOPHY

By

**DEEP SHANKAR
(REG. NO. 187128ME019)**



**DEPARTMENT OF MECHANICAL ENGINEERING
NATIONAL INSTITUTE OF TECHNOLOGY KARNATAKA
SURATHKAL, MANGALORE – 575025**

August, 2024

**IMPROVEMENT IN THE PROPERTIES OF
THERMALLY SPRAYED HYDROXYAPATITE
COATING REINFORCED WITH CARBON
NANOTUBE FOR ORTHOPAEDIC
APPLICATIONS**

Thesis

Submitted in partial fulfillment of the requirements for the degree of

DOCTOR OF PHILOSOPHY

By

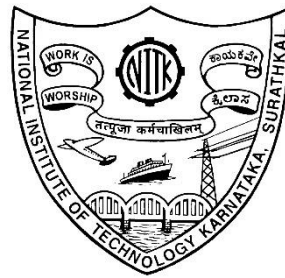
DEEP SHANKAR

(Reg. No. 187128ME019)

Under the guidance of

Dr. SUDHAKAR C. JAMBAGI

Associate Professor



**DEPARTMENT OF MECHANICAL ENGINEERING
NATIONAL INSTITUTE OF TECHNOLOGY KARNATAKA
SURATHKAL, MANGALORE – 575025**

August, 2024

DECLARATION

I hereby declare that the Research Thesis entitled "**Improvement in the properties of thermally sprayed hydroxyapatite coating reinforced with alumina and carbon nanotube for orthopedic applications,**" which is being submitted to the National Institute of Technology Karnataka, Surathkal, in partial fulfilment of the requirements for the award of the **Degree of Doctor of Philosophy in Mechanical Engineering** is a *bonafide report of the research work carried out by me*. The material contained in this *Research Thesis* has not been submitted to any University or Institution for the award of any degree.

Register Number: **187128ME019**

Name of the Research Scholar: **DEEP SHANKAR**

Signature of the Research Scholar: 

Department of Mechanical Engineering

Place: NITK, Surathkal

Date: 12-08-2024

CERTIFICATE

This is to certify that the Research Thesis entitled "**Improvement in the properties of thermally sprayed hydroxyapatite coating reinforced with alumina and carbon nanotube for orthopedic applications,**" submitted by **DEEP SHANKAR** (Register Number: **187128/187ME019**) as the record of the research work carried out by him, is accepted as the *Research Thesis* submission in partial fulfilment of the requirements for the award of the degree of **Doctor of Philosophy**.

S. C. Jambagi
13/8/2024

Research Guide

Dr. Sudhakar C. Jambagi

Associate Professor

Department of Mechanical Engineering

NITK, Surathkal


Chairman - DRPC

Department of Mechanical Engineering
National Institute of Technology Karnataka
Surathkal, Mangalore - 575025



ACKNOWLEDGMENTS

I am pleased to thank everyone who has assisted, motivated, and supported me throughout my Ph.D. journey at NITK Surathkal. First and foremost, I would like to express my heartfelt gratitude to my mentor, **Dr. Sudhakar C. Jambagi**, Associate Professor, Mechanical Engineering Department, National Institute of Technology Karnataka, Surathkal, Mangalore, for his support and advice that have motivated and guided me in the right path.

I am immensely grateful to our director, **Prof. B Ravi**, for instilling in students a desire to conduct research. I thank **Prof. S. M. Murigendrappa**, Professor, Head of the Department, and DRPC chairman, Department of Mechanical Engineering, National Institute of Technology Karnataka, Surathkal, Mangalore, for providing the necessary facilities. I would also like to thank RPAC members **Dr. Gnanasekaran N**, Associate Professor, Department of Mechanical Engineering, and **Dr. Rajasekaran Balasundaram**, Associate Professor, Department of Metallurgical and Materials Engineering, as well as DRPC secretary **Dr. Parthasarathy P**, Assistant Professor, Department of Mechanical Engineering, National Institute of Technology, Karnataka, Surathkal for their insightful comments and extending support in completing this work for their insightful comments and extending support in completing this work.

I profusely thank **Dr. Niranjan Gowda**, Director, Sanjay Gandhi Institute of Trauma and Orthopedics (SGITO), Bengaluru, **Dr. Laxmi K.S**, Head of the Department, Department of Pathology, **Dr. Jayanthi K.J**, Assistant Professor, Department of Pathology, **Dr. Pratibha S**, Head of the Department, Department of Microbiology, **Dr. Shanthi Jyothi**, Department of Immunohematology and Blood Transfusion, **Mr. Ashok N**, Lab Technician, Department of Pathology, SGITO, Bengaluru for their valuable support in the different stages of my research work.

I express my gratitude to CRF Chairman **Prof. Keyur Raval** and staff **Mr. Nishant**, **Mr. Pradeep**, **Mr. Kiran**, **Mrs. Thrithila**, **Mrs. Aniz**, **Mrs. Pratheeksha**, and Ms. Disha for providing access to various characterization facilities.

I want to thank the Department of Science and Technology (DST)-SERB for their

financial support.

Throughout my Ph.D. studies, I am indebted to **Dr. Vishwanath Bhajantri F, Nagarjuna, Jagadeeshanayaka N, Jayaganesh K, and Vikash Kumar Chaudhary**, my research group members of the Surface Engineering Laboratory, for their continuous support.

I want to express my deepest gratitude to my parents, **Anita Devi** and **Ashok Kumar Prasad**, and Grandmother **Saraswati Devi**, who always supported me in my endeavors. Their confidence in my ability to succeed was the impetus I needed to move forward and confront obstacles. I am grateful to my sister **Ruchi** and brothers **Hari Shankar** and **Amit Kumar** for their support. I want to thank my wife, **Manisha**, for her unconditional love, support, and motivation during this long and tedious journey.

Without friends, life would not have been as exciting and intriguing. I want to thank my dearest friends **Santosh Kumar, Aayush Kumar, Saket Kumar, Pramod**, and **Mohammad Alam**, who were always there for me during my Ph.D. work. I thank God for showering me with blessings and gifting me with such lovely family and friends.

DEEP SHANKAR

ABSTRACT

Aseptic loosening is responsible for ~21.9% of Total Knee Arthroplasty (TKA) failures in Germany, while non-hemocompatibility accounts for ~ 31% of medical device failures in the US, often resulting in expensive and painful revision surgery. Although hydroxyapatite (HA) has been used to provide a bioactive coating to titanium implants, its mechanical strength is limited and tends to phase changes at high temperatures, contributing to implant failure. This study firstly examines the physiochemical properties and blood compatibility of bioactive powders ((0.5–2 wt % carbon nanotube (CNT)/alumina)-20 wt %) produced through a heterocoagulation colloidal technique followed by ball milling HA. Heterocoagulated powder with 2wt% CNT (HAC2) showed a dispersion index of 1.20, indicating the uniform and homogenous dispersion of CNT in the matrix. The 1wt.% CNT (HAC1) composite demonstrated a surface charge ~5 times higher than HA at pH 7.4, with a value of -11 mV compared to -2 mV. This increase in electrostatic charge is desirable for achieving hemocompatibility, as evidenced by a range of blood compatibility assessments. The HAC1 powder exhibited hemolysis ranging from 2-7%, and the blood clot investigation indicated its nonthrombogenicity with no platelet activation, suggesting the excellent hemocompatibility for HAC1 powder than others, thereby attesting to the non-toxicity of CNTs when introduced to human blood. The next step is identifying the most suitable thermal spray process for spraying the powders. For this purpose, we aimed to investigate the relative efficacy of three thermal spray processes of different temperature ranges: Atmospheric plasma spray (APS) (high temperature), Flame spray (FS) (moderate temperature), and High-Velocity Oxy-Fuel spray (HVOF) (low temperature), and study their impact on HA coating's surface properties, affecting blood components and implant's strength. The crystallinity of the HA coating increased by 32 % with a decrease in the operating temperature (APS < FS < HVOF). HVOF coating exhibited a ~ 34 % and ~ 120 % improvement in adhesion strength and ~ 31 % and 59 % increment in hardness compared to APS and FS coating, respectively, attributed to its low porosity, low coating thickness (~55 μm), and high degree of crystallinity. The HVOF coating displayed good apatite growth, non-hemolytic, and nonthrombogenicity with no platelet activation owing to its low processing temperature, high degree of

crystallinity (89.7%), hydrophilicity, smooth ($\sim 4 \mu\text{m}$) and dense ($\sim 97\%$) microstructural properties. Finally, the powder with excellent hemocompatibility, i.e., HAC1 powder, was sprayed onto titanium implants with the HVOF spray (best thermal spray) and assessed for the implant's durability, longevity, and biocompatibility. HAC1 coating improved adhesion strength by $\sim 120\%$, hardness by $\sim 45\%$, wear resistance by $\sim 32\%$, and $\sim 17\%$ under simulated body fluid (SBF) and dry environments, respectively than HA coating, attributed to the retention and uniform distribution of CNT obtained by heterocoagulation and the use of low temperature. HAC1 coating showed 52% more apatite growth than HA after 30 days and displayed exceptional non-hemolytic behavior ($\sim 0.2\%$). Furthermore, the platelet adhered to the HAC1 coating was ~ 2.8 times lower than the negative control, attributed to its hydrophilicity ($\sim 88^\circ$), dense microstructure (97.2%), and surface charge (-11 mV), indicating its excellent hemocompatibility. Ultimately, an in-vivo study revealed encouraging results for HAC1 implants implanted in rabbits. The HAC1 implants showed an improvement of $\sim 11.4\%$ in the histological values, as seen from the microscopic images of the implantation sites. Thus, HVOF-HAC1 coating could be a promising material for orthopedic applications intended for human use due to its enhanced mechanical integrity, tribological resistance, and biocompatibility.

Keywords: *High-velocity oxy-fuel; Hydroxyapatite; Carbon nanotubes; Tribological behavior; Apatite growth; hemocompatibility; Thermal spray*

CONTENTS

DECLARATION

CERTIFICATE

ACKNOWLEDGEMENT

ABSTRACTi

CONTENTS.....iii

LIST OF FIGURESix

LIST OF TABLESxix

ABBREVIATIONSxxi

NOMENCLATURE.....xxiii

CHAPTER 1 INTRODUCTION..... 1

1.1 Preamble 1

1.2 Surface Modification 1

1.3 Biomaterials 4

1.4 Bioceramics..... 5

1.5 Hydroxyapatite (HA) properties 7

1.5.1 Thermal behavior of HA at different temperatures..... 8

1.5.2 Mechanical Properties..... 9

1.6 Metal Implants 10

1.7 Carbon Nano Tube (CNT) 13

1.7.1 Bioactivity and Toxicity of CNTs..... 15

1.8 Nature and Properties of Alumina 15

1.9 Deposition of HA coatings..... 17

1.10 Thermal spray 18

1.10.1 Atmospheric Plasma Spray (APS)..... 19

1.10.2 Flame spray (FS)..... 22

1.10.3	Cold spray	24
1.10.4	High-velocity oxy-fuel (HVOF) Spray	26
1.11	Overview of the thesis	32
1.12	Summary	33
CHAPTER 2 LITERATURE REVIEW		35
2.1	Preamble	35
2.2	Consumables used for thermally sprayed coatings in the medical industry 35	
2.2.1	HA coatings	35
2.2.2	HA reinforced alumina coatings	43
2.3	Carbon nanotubes in medical implants	45
2.4	Functionalization and dispersion of CNT	48
2.5	Mechanical properties of the coatings	53
2.6	Wear resistance of the coatings.....	61
2.7	Biocompatibility of the powders and the coatings.....	65
2.8	Basis of Objectives Formation.....	81
2.9	Objectives	84
2.10	Summary	85
CHAPTER 3 MATERIALS AND METHODS.....		87
3.1	Introduction.....	87
3.2	Powder preparation and their physiochemical characterization	87
3.2.1	Feedstocks used	87
3.2.2	Processing of CNT	88
3.2.3	Size and morphology of powders	89
3.2.4	Phase Identification and crystal size	89
3.2.5	Raman spectroscopy	90

3.2.6	Fourier transform infrared spectroscopy (FTIR)	90
3.2.7	Zeta potential/Surface charge	90
3.3	Hemocompatibility assessment of powders	90
3.3.1	Hemolysis study	91
3.3.2	Whole blood clot study	92
3.3.3	Platelet adhesion and activation study	94
3.3.4	Coagulation Assays.....	95
3.4	Coating deposition	97
3.5	General characteristics of the deposited coatings	99
3.6	Simulated Body Fluid (SBF) immersion test.....	101
3.7	Hemocompatibility assessment of the coatings	101
3.7.1	In-vitro hemolysis study	101
3.7.2	Whole Blood (WB) clot assay	102
3.7.3	Platelet adhesion and activation study	103
3.7.4	Coagulation assays- PT and aPTT	104
3.8	Antimicrobial Analysis	105
3.9	Tribological experiments	105
3.10	In-vivo study	107
3.11	Summary	108
CHAPTER 4 POWDER PREPARATION AND CHARACTERIZATION....		111
4.1	Introduction.....	111
4.2	Bio-ceramics composite preparatory method	111
4.3	Morphology.....	113
4.4	Phase identification and crystal size determination by XRD.....	115
4.5	Raman analysis	115
4.6	FTIR spectra analysis.....	118

4.7	Zeta potential/Surface charge of the powders.....	119
4.8	Hemocompatibility assessment of the powders	120
4.8.1	Hemolysis study.....	120
4.8.2	Whole blood clot study	123
4.8.3	Platelet adhesion and activation study	125
4.8.4	Coagulation assays: PT and aPTT	127
4.9	Summary	128
CHAPTER 5 HA COATINGS BY DIFFERENT THERMAL SPRAY		129
5.1	Introduction.....	129
5.2	Microstructural properties of the coatings	129
5.3	Phase identification and crystal size of the coatings.....	134
5.4	Raman Analysis of the feedstock and coatings.....	136
5.5	Contact Angle/Surface Wettability	137
5.6	Scratch Adhesion Strength and Hardness of the Coatings.....	140
5.7	In-vitro Simulated Body Fluid (SBF) Immersion Test.....	145
5.8	Hemocompatibility assessment of HA coatings	149
5.8.1	Hemolysis study.....	149
5.8.2	Whole Blood Clotting Time Assay.....	151
5.8.3	Platelet adhesion and activation assay	153
5.8.4	Coagulation assays.....	156
5.9	Qualitative Antimicrobial Assay.....	158
5.10	Summary	160
CHAPTER 6 TRIBOLOGICAL AND IN VIVO STUDY OF THE COATINGS		161
.....		
6.1	Preamble	161
6.2	Microstructure of feedstocks and coatings	161

6.3	X-ray analysis of coatings for phase distribution and quantification	165
6.4	Raman spectroscopy to determine the retention of the CNT in the matrix 166	
6.5	Scratch adhesion strength and hardness of the coatings	168
6.6	In-vitro bioactivity study.....	173
6.7	Blood-compatibility assessments.....	178
6.8	Tribology studies for HA and HAC1 coatings in dry and wet environments.....	179
6.8.1	Analysis of the worn surface morphology of wear tracks	179
6.8.2	Topographical evolution of the worn surface	181
6.8.3	Sliding friction and wear behavior in dry and wet conditions	182
6.8.4	EDS analysis of the worn track.....	183
6.8.5	Prediction of Wear Mechanisms Based on Wear Debris Size Distribution	187
6.8.6	Raman analysis of wear track	189
6.8.7	Topographical analysis of the worn ball	189
6.8.8	Effect of surface roughness (R_a) on wear	191
6.8.9	Effect of reinforcements on wear behavior.....	192
6.9	In-vivo assessment of implants in New Zealand white rabbits.....	193
6.10	Summary	197
CHAPTER 7 CONCLUSION.....		199
7.1	Preamble	199
7.2	Conclusion	199
7.3	Future scope, limitations, and challenges	205
REFERENCES.....		211
LIST OF PUBLICATIONS		231
BIO-DATA.....		233

LIST OF FIGURES

Figure 1.1 Different properties required for an ideal implant.....	11
Figure 1.2 Illustration exhibiting several applications of medical implants in the human body (Gautam et al. 2022).	13
Figure 1.3 Structure of SWCNTs and MWCNTs (Devi and Gill 2021).	14
Figure 1.4 Coating deposition technologies (Stokes 2003).	18
Figure 1.5 Schematic diagram of the plasma spray system (Budinski 1988).....	20
Figure 1.6 Schematic diagram of the flame spray system depicts various units of the setup (www.griekspoorthermalcoatings.com).	24
Figure 1.7 Schematic diagram of the cold spray process (Ogawa and Seo 2011).....	26
Figure 1.8 HVOF process schematic diagram (Chandra Yadaw et al. 2018).....	27
Figure 1.9 Different ways to assess the biocompatibility of biomaterials.	32
Figure 2.1 In-situ tensile elongation of single-walled carbon nanotubes (Huang et al. 2006).....	46
Figure 2.2 Schematic representation of zeta potential (Tengku Mohd et al. 2016).....	50
Figure 2.3 Heterocoagulation of Alumina and CNT particles with corresponding surfactant.	53
Figure 2.4 Micrographs showing the worn surface scar of (a) HA, (b) HA-4C, (c) HA-4C-5Ce, and (d) HA-4C-5Ce-5Ag (yellow and red arrows show cracks and delamination, respectively) (Pandey et al. 2018b).	63
Figure 2.5 Microscope images of Ti6Al4V control, HA/Ti6Al4V, and MgO/SiO ₂ HA/Ti6Al4V-sectioned implants stained by a modified Masson–Goldner trichrome stain. Larger gaps were observed between the Ti6Al4V implant surface with surrounding osseous tissue. The HA coating enhanced osseointegration between the implant surface and osseous tissue and was further enhanced by the MgO/SiO ₂ -HA coating. Osteoid formation is depicted in red/ orange, and mineralized bone in blue/green (Bose et al. 2020).	75

Figure 2.6 Morphology of platelets adhered on (a) collagen-coated glass, (b) silicone tube, (c) HAP, and (d) HAF samples (Ooi et al. 2019).	76
Figure 2.7 Hemolysis studies of GOs and oxidized NDs of different sizes with human RBCs. (a) Hemolysis percentages were measured at the 25–400 $\mu\text{g}/\text{mL}$ concentration range for GOs and 4 different ND samples (35, 100, 250, and 500 nm in diameter) incubated with RBCs at 25°C for 2 h. GOs served as the positive control. (b) Photographs of human RBCs treated with GOs and NDs of 4 different sizes at 25–400 $\mu\text{g}/\text{mL}$ concentrations range. The red color of the solution is due to the release of hemoglobin from the damaged RBCs, and the red pellets at the bottom of the Eppendorf tubes are intact RBCs precipitated by centrifugation. PBS and DDW were negative (–) and positive (+) controls, respectively. The experiments were repeated in triplicate (Li et al. 2013).	78
Figure 3.1 Photograph of functionalized MWCNT in acetone shows complete dispersion.....	89
Figure 3.2 The pictograph shows the procedure for conducting a hemolysis test for HA and its based composites (Shankar et al. 2024a).	92
Figure 3.3 Pictograph depicts the procedure for conducting a whole blood clot test (Shankar et al. 2024a).	93
Figure 3.4 The pictograph shows the procedure for generating PRP from whole blood, followed by the platelet adhesion test methodology (Shankar et al. 2024a).	95
Figure 3.5 The pictograph depicts the procedure for conducting a coagulation assay with PPP (a) PT test and (b) aPTT test (Shankar et al. 2024a).....	97
Figure 3.6 Schematic principles of operation of Vickers hardness machine (a) and Vickers hardness test (Kah et al. 2011).	101
Figure 3.7 (a) Schematic illustration to show wear test mechanism under SBF environment, and (b) Experimental set-ups for wear test under dry and physiological (SBF) conditions.	106
Figure 3.8 Different stages involved in the in vivo implantation of HA-based implants in New Zealand white rabbits.....	108

Figure 4.1 (a) Alumina suspended in DW with SDS surfactant at pH- 8, (b) FCNTs suspended in DW with CTAB surfactant at pH- 8, and (c) Heterocoagulated composite precipitated at the bottom of the container (Shankar et al. 2024a). .. 112

Figure 4.2 FESEM morphology for (a) HA, (b) Alumina, (c) TEM image for FCNT, (d) FESEM image for AC2 Composite, (e) Dot mapping for AC2, (f) Binary image for AC2 dot map shows the degree of dispersion of CNTs, (g and h) TEM image for HAC1 and HAC2, respectively showed different junctions formed by CNTs, and (i) schematic illustration to understand the electrostatic interaction between HA/Alumina/CNTs during powder preparation (Shankar et al. 2024a). 114

Figure 4.3 XRD spectra for (a) HA, (b) AC2, (c) HAC2, Raman spectra for (d) HA, (e) Alumina, (f) FMWCNT, and (g) HAC2 (Shankar et al. 2024a). 117

Figure 4.4 FTIR spectroscopy for HA and HAC2 powder (Shankar et al. 2024a).... 119

Figure 4.5 Variation of zeta potential with pH for (a) Alumina, Alumina with SDS, CNTs, CNTs with CTAB, and heterocoagulated sample (AC1 and AC2), and (b) HA and HAC composites (n=3) (Shankar et al. 2024a). 120

Figure 4.6 A bar graph shows the percentage hemolysis of different powders with varying concentrations for (a) HA, (b) HAC0.5, (c) HAC1, and (d) HAC2, colorimetric image to show RBC damage by (e) HA, (f) HAC0.5, (g) HAC1, and (h) HAC2. The white and light red colored tubes represent non-hemolytic, and the dark red colored solution depicts hemolytic behavior (Shankar et al. 2024a). 122

Figure 4.7 Absorbance vs. Time graph for whole blood clotting time measurement for the samples and the control, n=5, and (b) schematic diagram to illustrate clot formation when triggered by foreign material, and negative charge for HAC composites repels adjacent blood components, hinders clot formation (Shankar et al. 2024a). 124

Figure 4.8 (a) Percentage of platelet adhesion on HA-based composites, negative and positive control, n=5, (b) Schematic diagram that shows the change in platelet morphology when in contact with foreign materials, FESEM images of platelets

adhered on (c) Negative control, (d) HA, (e) HAC0.5, (f) HAC1, (g) HAC2, and (h) Positive control (Shankar et al. 2024a).....	126
Figure 4.9 Coagulation assays (a) PT and (b) aPPT coagulation time of PPP incubated with different concentrations of HA-based composites at 5, 20, and 80 mg (n = 5) (Shankar et al. 2024a).....	128
Figure 5.1 FESEM micrographs (a) HA powder, (b) nanoporous structure of individual HA particle. FESEM top surface morphology for (c) APS, (e) FS, and (g) HVOF-HA coatings. Cross-sectional microstructure of (d) APS, (f) FS, and (h) HVOF-HA coatings. The white arrow represents partially melting, the black arrow shows the unmelting, and the yellow arrow depicts the complete melting of HA. (i) The top surface microstructure showed a nanoporous structure of the HVOF coating, similar to HA feedstock. (j) Histogram shows particle size distribution for HA powder fitted with a log-normal distribution function (Solid black line) (Shankar et al. 2024b).....	132
Figure 5.2 3D surface profiles of surface roughness (Ra) for (a) APS, (b) FS, and (c) HVOF-HA coatings (Shankar et al. 2024b).	133
Figure 5.3 Top surface FESEM micrograph with corresponding EDS elemental mapping and EDS spectra shows Ca, P, and O as the coating elements for (a) APS-HA, (b) FS-HA, and (c) HVOF-HA coatings (Shankar et al. 2024b).	133
Figure 5.4 (a) XRD spectra of feedstock powder and all coated samples with corresponding ICDD file numbers for different phases of HA. (b) Raman spectral analysis shows different HA phases for feedstock and coatings. (c) The surface roughness (Ra) value for Ti and coated samples was obtained using a 3D profilometer (n = 5). (d) Contact angle and corresponding front-view photographs show hydrophilicity and hydrophobicity behavior for titanium and coatings (n = 5). The error bar represents the standard deviation (Shankar et al. 2024b).....	140
Figure 5.5 Optical micrographs of scratch tracks of as-deposited HA coating for APS (a) scratch track, (b) First cracking, (c) first delamination, (d) Total delamination, Flame spray (e) Scratch track, (f) First cracking, (g) First delamination, (h) Total delamination, HVOF spray (i) Scratch track, (j)First cracking, (k) First	

delamination, (l) Total delamination. (m) Bar graph shows the adhesion strength of the different HA coatings ($n = 3$; * p -values < 0.05). The error bar represents the standard deviation. Optical microscope image of the Vickers hardness indentation for (n) APS, (o) FS, and (p) HVOF-HA coating, where D1 and D2 are the horizontal and vertical diagonal lengths of the indentation (Shankar et al. 2024b)..... 144

Figure 5.6 3D optical profilometer images show the coated samples' scratch track, (a-c) APS, (d-f) FS, and (g-i) HVOF-HA coatings (Shankar et al. 2024b). 144

Figure 5.7 FESEM images show the change in apatite morphology on the surface of different HA coatings obtained after 15,30 and 60 days of immersion in SBF (a-d) APS, (e-h) FS, and (i-l) HVOF-HA coatings. (m) % weight gain by HA coatings as a function of the time immersed in SBF ($n = 3$). The error bar represents the standard deviation. (n) The XRD pattern shows the change in apatite growth observed over time in HA coatings (Shankar et al. 2024b)..... 148

Figure 5.8 (a) Bar graph shows the percentage hemolysis for titanium and HA coatings ($n = 5$; * p -values < 0.05). The error bar represents the standard deviation. All samples displayed less than 5% hemolysis, indicating their non-hemolytic behavior. (b) Colorimetric images showing RBC damage for positive control-DW, negative control-saline, and samples. The white-colored tube represents no rupture of RBCs, and the red-colored tube shows a complete rupture of RBCs. Microscopic stained images show the change in RBCs morphology for (c) APS, (d) FS, (e) HVOF coatings, and (f) Positive control (Shankar et al. 2024b)..... 151

Figure 5.9 (a) Bar graph shows the absorbance value of the whole blood clot study at different time points (15, 30, 45 minutes) for titanium and HA coatings ($n = 5$; * p -values < 0.05). The error bar represents the standard deviation, and the dotted line represents the absorbance of free hemoglobin in unclotted blood. A significant increase in free hemoglobin is present on all coated surfaces compared to the uncoated titanium at respective time intervals. Colorimetric images of the samples after (b) 15 minutes, (c) 30 minutes, and (d) 45 minutes. The dark red tube shows the release of free hemoglobin, indicating that the samples are non-

thrombogenic. On the other hand, the light red tube in color depicts the thrombogenicity of the samples (Shankar et al. 2024b). 153

Figure 5.10 (a) Bar graph represents the percentage of platelets adhered to titanium and coated samples ($n = 3$; *p-values < 0.05). The error bar represents the standard deviation. FESEM morphology of platelets adhered on the surfaces of (b) Negative control, (c) Titanium, (d) APS, (e) FS, and (f) HVOF-HA coatings. (g) Schematic illustration shows the role of implant surface properties (zeta potential, wettability) on platelet adhesion and the mechanism underlying different stages involved in the change in platelet morphology and clot formation (Shankar et al. 2024b)..... 155

Figure 5.11 (a) Bar graph shows the coagulation time for different samples and a control incubated with PPP for 1 hour ($n = 5$; *p-values < 0.05). The error bar represents the standard deviation. The error bar represents the standard deviation. (b) A schematic illustration depicts the mechanism underlying the role of implant surface properties (wettability, surface roughness) in clot formation (Shankar et al. 2024b)..... 157

Figure 5.12 Agar diffusion test for the titanium and HA coatings with (a) Gram-negative E. Coli and (b) Gram-positive S. aureus shows no inhibition zone formation around the discs. The dotted circle represents the formation of the no-inhibition zone around the discs, indicating the non-microbial property of HA (Shankar et al. 2024b)..... 160

Figure 6.1 FESEM micrograph (a) spherical morphology for HA powder, (b) Angular and blocky structure for alumina particle, (c) Kink and bulges represents functionalization of CNT, (d) Heterocoagulated alumina/CNT shows CNT gets adsorbed and completely engulfed alumina particles, (e and f) TEM images showed various junctions of CNT attached to HA/alumina particles due to electrostatic interaction between the ions, FESEM micrograph (g) Plain smooth titanium surface, (h and i) Low and high magnification images showed top surface microstructure for HA coating displayed smooth surface with unmelted and partially melted HA particles, (j) Back scattered micrograph for HA coating with corresponding EDS analysis and dot mapping, (k and l) Low magnification

images showed top surface microstructure for HAC1 coating, (m) High magnification image for HAC1 coating shows crack arresting, hook structure and homogenous dispersion and retention of CNT in HA matrix, and (n) Back scattered micrograph of HAC1 coating with corresponding EDS analysis and dot mapping, indicates no impurities were added during thermal spraying. 164

Figure 6.2 (a') X-ray diffraction spectra of the feedstocks and their corresponding coatings with the ICDD file numbers. The graph displays the retention of HA phases along with reinforcement elements (b') Raman spectra for feedstock powder and their HVOF-sprayed coating. The graph shows the retention of HA phases and D and G peaks for CNT in the coatings and the corresponding wear tracks..... 168

Figure 6.3 (a) Optical micrographs of scratch track for HA coating show different critical load of failures, (b-d) FESEM image of scratch track for HA coating shows critical loads and its failure mechanism, (e) EDS mapping shows the presence of Ti, Al, V along the scratch track for HA coating, indicates the penetration of indenter into the coating, (f) Optical micrographs of scratch track for HAC1 coating shows different critical load of failures, (g-i) FESEM image of scratch track for HAC1 coating shows different critical loads and bridging mechanism by CNT, (j) EDS mapping shows the presence C, Ca, P, Al, along the scratch track for HAC1 coating, indicates the toughening mechanism of CNT in the HA matrix, and Optical microscope image of the indentation for (k) HA (l) HAC1 coating shows horizontal (D_1) and vertical (D_2) diagonal lengths to determine Vickers hardness, $n=3$ 172

Figure 6.4 3D optical profilometer images show the HVOF-sprayed coated samples' scratch track, (a-b) HA, and (c-d) HAC1 coatings. L_{c1} denotes the critical load for cohesion failure, and L_{c2} denotes the critical load for adhesion failure..... 173

Figure 6.5 Percentage weight gain by HA coatings as a function of the time immersed in SBF ($n = 2$). The error bar represents the standard deviation. 175

Figure 6.6 Apatite formation at the 0th, 7th, 15th, and 30th day for pure HA (a-e), HAC1 coating (f-j). The FESEM images show the apatite layer precipitation on the HA

and HAC1 coatings, which testifies to the non-toxicity of CNT..... 177

Figure 6.7 In-vitro blood compatibility assessments (a) colorimetric images show the non-hemolytic behavior of HAC1 coating similar to the negative control, FESEM morphology of the platelets adhered on to (b) HAC1 coating surface, and (c) negative surface. The dotted yellow circle indicates round platelets adhered to coatings similar to the negative control, indicating no sign of platelet activation. 179

Figure 6.8 Wear profile for titanium alloy in the dry condition (a) FESEM images of wear track, (b) low magnification image shows scars on the wear track, (c) High magnification images show debris cracks and crater generated, (d-f) 3d profile images depicting the depth profile and the volume loss from the wear track, (g and h) wear debris size and its composition, (i) dot mapping with elemental analysis of wear track. Wear profile for HVOF-HA coating in dry condition (a) FESEM images of wear track, (b) low magnification image shows scars on the wear track, (c) High magnification images show debris cracks and crater generated, (d-f) 3d profile images depicting the depth profile and the volume loss of the wear track, (g and h) wear debris size and its composition, and (i) dot mapping with elemental analysis of wear track..... 185

Figure 6.9 Wear profile for HVOF-HAC1 coating in dry condition (a) FESEM images of wear track, (b) low magnification image shows scars on the wear track, (c) High magnification images show debris cracks and crater generated, (d-f) 3d profile images depicting the depth profile and the volume loss of the wear track, (g and h) wear debris size and its composition, (i) dot mapping with elemental analysis of wear track. Wear profile for HVOF-HAC1 coating with SBF as lubricant (a) FESEM images of wear track, (b) low magnification image shows scars on the wear track, (c) High magnification images show debris cracks and crater generated, (d-f) 3d profile images depicting the depth profile and the volume loss of the wear track, (g and h) wear debris size and its composition, (i) dot mapping with elemental analysis of wear track. 186

Figure 6.10 FESEM images show wear debris morphology generated from (a) Titanium substrate, (b) HA, (c and d) HAC1 coatings in dry and SBF

environments, respectively, and (e) Box plot shows the wear debris size distribution for the samples. 188

Figure 6.11 A bar graph shows (a) the Coefficient of friction generated during wear, (b) the Roughness of the samples before and after wear, (c) the width of the wear track generated after wear, (d) the Depth of the wear track, 3D profile images shows the wear of the counter-ball to determine the volume loss for (e-h) Titanium, (i-l) HA coating, (m-p) HAC1 coating, (q) Bar graph shows wear volume of the corresponding balls and r) Roughness of the counter-ball generated during wear. The error bar represents the standard deviation (n=3). 190

Figure 6.12 Histopathology images (a) HA coating, (b) HDPE (control), (c) HAC1 coating, and (d) HDPE (control) implanted in the femur bone of rabbits (n=10). The figure shows different inflammatory responses to the coatings. 197

LIST OF TABLES

Table 1.1 Classification of biomaterials (Heness and Ben-Nissan 2004).....	5
Table 1.2 Bone and HA composition comparison (Levingstone 2008).....	8
Table 1.3 Thermal decomposition of HA (Bulina et al. 2021).	9
Table 1.4 Mechanical strength comparison of HA and bone (Ben-Nissan et al. 2004).	10
Table 2.1 Physiochemical properties of the surfactants (Lin 2004).	51
Table 2.2 Comparison of atmospheric plasma-spray (APS), flame spray (FS), and high-velocity oxy-fuel (HVOF) techniques.....	84
Table 3.1 Deposition parameters for Atmospheric Plasma Spray (APS) (Hadipour et al. 2015; Method 2018), Flame Spray (FS) (Singh et al. 2014), and High-velocity oxy-fuel (HVOF) (Vilardell et al. 2020) - HA coatings.	99
Table 4.1 Powders Designation with its processing description.....	112
Table 5.1 Comparative analysis of HA coatings acquired through APS, FS, and HVOF thermal spray techniques based on their in vitro results (Shankar et al. 2024b).....	158
Table 6.1 Microstructural, mechanical, and bioactivity properties of as-deposited coatings.....	176
Table 6.2 Characterization from a ball-on-disc test of Titanium and HA-based HVOF- sprayed samples under dry and wet (SBF) environments.	193
Table 6.3 List of different types of implants embedded in the femoral bone of the rabbits.	196

ABBREVIATIONS

ACP	Amorphous Calcium Phosphate
APS	Atmospheric Plasma Spray
aPTT	Activated Partial Thrombin Time
ASPS	Atmospheric Suspension Plasma Spray
ASTM	American Society for Testing and Materials
BD	Bulk density
CNT	Carbon nanotube
CoF	Coefficient of Friction
DMEM	Dulbecco's Modified Eagle Medium
DW	Distilled Water
EDS	Energy dispersive spectroscopy
EPD	Electrophoretic Deposition
ePTFE	Polytetrafluoroethylene
FDA	Food and Drug Administration
FESEM	Field emission electron microscopy
FMWCNT	Functionalized Multi walled carbon nanotube
FS	Flame Spray
FTIR	Fourier transform infrared
HA	Hydroxyapatite
HRTEM	High resolution transmission electron microscopy
HVAF	High Velocity Air-Fuel
HVOF	High-Velocity Oxy-Fuel
HVSFS	High Velocity Suspension Flame Spray
ICDD	International Centre for Diffraction Data
ISO	International Organization for Standardization
MWCNT	Multi walled carbon nanotube
OA	Oxyapatite
OD	Optical Density
PBS	Phosphate-buffered saline
PC	Platelet Count

PCL	Polycaprolactone
PEEK	Polyetheretherketone
PFR	Powder Flow Rate
PLD	Pulsed Laser Deposition
PMMA	Polymethylmethacrylate
PPP	Platelet Poor Plasma
PRP	Platelet Rich Plasma
PSU	Polysulfone
PT	Prothrombin Time
RBC	Red Blood Cells
SBF	Simulated Body Fluid
SCFH	Standard cubic feet per hour
SDS	Sodium dodecyl sulfate
SLPM	Standard litre per minute
SOD	Stand-off Distance
SWCNT	Single walled carbon nanotube
CfSWCNT	Carboxyl functionalized single-walled carbon nanotubes
TCP	Tricalcium Phosphate
TTCP	Tetracalcium Phosphate
WB	Whole blood
XRD	X-ray diffraction
ZP	Zeta potential

NOMENCLATURE

%	Percentage
°	Degree
°C	Degree Celsius
μm	Micrometre
cm	Centimetre
g	Gram
h	Hour
m	Meter
min	Minute
mm	Millimetre
nm	Nanometre
V	Volt
wt%	Weight percentage
θ	Theta
λ	Wavelength
L _c	Critical load for occurring damage in scratch testing
θ _{CA}	Contact angle
R _a	Average roughness
W _R	Wear Rate
W _V	Wear Volume
¥	Calibration factor

CHAPTER 1 INTRODUCTION

1.1 Preamble

This chapter delves into categorizing biomaterials and the different methods to modify their surfaces to produce medical bioimplants. The objective is to give readers a fundamental comprehension of the physical, chemical, and mechanical characteristics of the biomaterials employed in orthopedics. Additionally, it includes a detailed discussion of the thermal spray techniques utilized for producing hydroxyapatite-based implants, followed by an introduction to the basic properties of carbon nanotubes and alumina and hemocompatibility of biomaterials. Lastly, the chapter concludes with an overview of the thesis.

1.2 Surface Modification

Surface engineering is applying a range of techniques to modify the surface properties of a material to improve its performance. According to the ASM Handbook (1994), surface engineering can be defined as "the alteration of the surface or near-surface layer of a material to provide one or more specific functional properties that differ from those of the bulk material."

Some of the common surface modification techniques include:

1. *Coatings*: Coatings are applied to the surface of a material to improve its properties, such as wear resistance, corrosion resistance, and biocompatibility. Common coating methods include electroplating, chemical vapor deposition, physical vapor deposition, and thermal spray techniques.
2. *Surface treatments*: Surface treatments include shot peening, sandblasting, and polishing, which alters the surface texture and increases its hardness, strength, and durability.
3. *Surface alloying*: Surface alloying is a process that involves diffusing one or more elements into the surface of a material to improve its properties. Common methods include ion implantation, laser surface alloying, and diffusion bonding.
4. *Surface patterning*: Surface patterning involves creating a specific pattern on the surface of a material to improve its properties, such as adhesion or friction. Common methods include micro- and nano-patterning using lithography or etching techniques.

The choice of surface modification technique depends on the specific application and the desired properties of the material. Different strategies can be employed to achieve the desired surface properties, such as improving adhesion, reducing friction, or enhancing biocompatibility. These strategies include changing the surface chemistry, modifying the surface topography, and introducing functional groups or biomolecules. Surface engineering is required in many engineering applications where the material's surface properties are crucial for its performance. One example is the aerospace industry, where components are exposed to harsh environmental conditions, including high temperatures, corrosive gases, and wear. The surface properties of materials used in aerospace applications, such as turbine blades, must be carefully engineered to ensure their longevity and reliability. Another example is in the electronics industry, where the surface properties of materials used in microelectronics, such as semiconductors and thin films, are critical for their performance. Surface engineering techniques such as surface passivation and surface doping can be used to improve the surface properties of these materials and enhance their electrical conductivity and performance. Surface engineering is also important in biomedical applications, where the interaction between the implant's surface and the surrounding tissue is crucial for its success. The surface properties of implants, such as their biocompatibility, bioactivity, and osseointegration, are critical factors that determine their performance. Surface engineering techniques such as coatings, surface treatments, and surface patterning can improve the surface properties of implants and enhance their integration with the surrounding tissue. Surface modification strategies for bioimplants involve altering the surface properties of biomaterials to improve their biocompatibility, bioactivity, and osseointegration. There are several techniques for surface modification, including physical, chemical, and biological methods. Physical methods include sandblasting, shot peening, and laser treatment, which alter the implant's surface roughness. Chemical methods, such as etching, anodizing, and sol-gel coating, modify the surface chemistry of the implant. Biological methods, such as plasma treatment and biomimetic coating, mimic the body's natural processes to improve the implant's integration with the surrounding tissue. These surface modification strategies can enhance the performance and longevity of bioimplants, reduce the risk of implant failure, and improve patient outcomes. In summary, surface

engineering is required in many engineering applications where the surface properties of materials are critical for their performance, and different surface modification techniques and strategies can be employed to achieve the desired properties for a specific application.

Metals are widely used in medical applications and comprise a significant percentage of clinically used materials. Load-bearing applications such as total joint replacements and hip prostheses require metals with properties such as strength, fracture toughness, and impact resistance. Metallic biomaterials have been used for medical treatments for about 20 years. Only three commonly used metals, namely stainless steel (316L), cobalt-based alloys, and titanium-based alloys (Jambagi and Malik 2021), are biocompatible and approved by the United States Food and Drug Administration (FDA) for use as biomedical implant materials. Titanium alloys are the material of choice for many critical applications due to their excellent corrosion resistance and high toughness-to-mass ratio. These alloys find applications in gas turbine engine components, oil refinery heat exchangers, chemical processing, desalination, valve and pump parts, and marine equipment. In addition, titanium alloys have been widely used in the medical industry as orthopedic implants. However, they have relatively poor surface properties against wear and corrosion (Nicholson 2020). After their application, implant integration with bone tissue generally takes several months, and there is growing interest in shortening the process toward osseointegration (Jagadeeshanayaka et al. 2022). Coating titanium implants with hydroxyapatite has been the research focus for the past three decades. Thermal sprayed hydroxyapatite (HA) coatings allow a natural fixation on metal implants for diverse applications, such as total hip and knee replacement, that improve the patient biomechanics, extend the implant lifetime, and increase the patient's life quality. Coatings must be biocompatible, and have resistance to high-temperature and mechanical forces. Commercial techniques such as Plasma spray (PS), Flame spray (FS), and High-velocity Oxy-Fuel (HVOF) are available to deposit the HA coating on metal-based biomaterials. Plasma spray, the only FDA-approved thermal spray technique used to produce HA-based implants, is a fast, effective, and low-cost coating method but requires investigation for further improvements in coating quality due to the

irregularities associated with the resulting coating (Jagadeeshanayaka et al. 2022). The mechanical and physiochemical properties of the coating at the coating-base material interface are crucial properties required by the coating as they directly or indirectly influence the biocompatibility of the implants. Therefore, studying the different properties of the coating-base material interface becomes essential. This research aims to manufacture components that meet the requirements to be used as bone substitutes to produce mechanically and biologically sound implants. This is a step further toward producing composite components for cortical bone substitution using a technique/process that has never been used.

1.3 Biomaterials

Biomaterials are designed to interact with biological systems in a therapeutic or diagnostic capacity. They can be natural or synthetic and are used in various biomedical applications, including implants, prosthetics, drug delivery systems, and tissue engineering.

There are four main types of biomaterials (Ong et al. 2015):

1. *Metals*: Metals are commonly used in medical implants due to their strength and durability. Examples include titanium, stainless steel, and cobalt-chromium alloys.
2. *Polymers*: Polymers are synthetic materials that can be engineered to have various properties, including flexibility, biodegradability, and biocompatibility. Examples include polyethylene, polyurethane, silicone, polyetheretherketone (PEEK), polysulfone (PSU), and polymethylmethacrylate (PMMA).
3. *Ceramics*: Ceramics are inorganic materials often used in orthopedic and dental implants due to their biocompatibility and ability to support bone growth. Examples include hydroxyapatite and alumina.
4. *Composites*: Composites are materials made up of two or more different materials that combine their individual properties to create a material with unique properties. Examples include carbon fiber-reinforced polymers and bioactive glass-ceramic composites.

Biomaterials can be classified into three main types based on their biological response: bioinert, bioactive, and bioresorbable (Table 1.1).

Bioinert biomaterials do not interact with the surrounding biological environment and are used primarily for structural purposes. They are typically made of titanium, stainless steel, and ceramics and are commonly used in orthopedic and dental implants.

Bioactive biomaterials are designed to interact with the biological environment and promote tissue growth and regeneration. They are typically made of hydroxyapatite, similar in composition to natural bone, and can integrate with the surrounding tissue to promote bone growth.

Bioresorbable biomaterials are designed to be gradually broken down and absorbed by the body over time. They are typically used for temporary implants, such as sutures and drug delivery systems, and are made of polylactic acid, polycaprolactone (PCL), and polyglycolic acid. Some bioceramics, such as tricalcium phosphates (TCP) and tetracalcium phosphates (TTCP), are also biodegradable. Each biomaterial type has its advantages and disadvantages, and the choice of material depends on the specific application and the desired biological response.

Table 1.1 Classification of biomaterials (Heness and Ben-Nissan 2004).

Biomaterial	Tissue response	Interaction	Examples
Bioinert	Minimal/no-response	Mechanical fixation	Al ₂ O ₃ , ZrO ₂ , TiO ₂ , Ti, PEEK, etc.
Bioactive	Positive response	Chemical bonding	HA, bioactive glasses, glass ceramics, etc.
Bioresorbable	Gradually dissolve	Replacement by tissue	TCP, PCL, etc.

1.4 Bioceramics

Ceramics are a broad category of materials known for their unique properties. They are typically made from inorganic compounds heated to high temperatures, resulting in a hard, brittle material resistant to heat, wear, and corrosion. Ceramics have many applications, including construction materials, electronics, and biomedical implants.

Bioceramics are a type of ceramic material that is specifically designed for use in biomedical applications. They are typically made from calcium phosphate, alumina, and zirconia and are used in various medical applications, including bone grafts, dental implants, and joint replacements. Bioceramics typically comprise calcium phosphate compounds, such as hydroxyapatite and tricalcium phosphate. Depending on the specific application, they can be designed to have varying porosity, stiffness, and mechanical strength levels. One of the most important properties of bioceramics is their biocompatibility, which means they do not cause an adverse reaction when they come into contact with living tissue. This is critical for their use in medical applications, as the body's immune system must not cause inflammation or rejection. Another important property of bioceramics is their ability to bond with living tissue. This process, known as osseointegration, allows the bioceramic material to integrate with the surrounding bone or tissue. This is critical for the success of biomedical implants, as it ensures that the implant remains securely in place and functions correctly. Bioceramics can be used in a variety of medical applications, including:

1. Bone grafts: Bioceramics can replace missing or damaged bone tissue. They can be shaped to fit the defect, and once implanted, they promote the growth of new bone tissue.
2. Dental implants: Bioceramics can make biocompatible dental implants fusing with the surrounding bone tissue.
3. Joint replacements: Bioceramics can be used in joint replacements to provide a durable, long-lasting, biocompatible material that can bond with the surrounding bone tissue.

Overall, bioceramics have revolutionized the field of biomedical engineering, providing a range of durable, biocompatible materials that can be used in various medical applications. In addition to their use in traditional orthopedic applications, bioceramics are also being explored for their potential use in tissue engineering and regenerative medicine. Bioceramic scaffolds can be designed to support the growth and differentiation of stem cells, which can then be used to regenerate damaged or diseased tissue. Recent research in bioceramics has focused on improving their mechanical properties, enhancing their bioactivity, and exploring new applications for these materials in orthopedics and beyond. For example, researchers have investigated using carbon nanotubes, alumina, zirconia, etc., to reinforce bioceramics, improve their

mechanical strength, and use surface modifications to enhance their bioactivity and promote osseointegration.

1.5 Hydroxyapatite (HA) properties

The scientific community has investigated calcium phosphates (CaPs) as potential biomedical materials for bone substitutes since the early 1900s. The first study on CaPs dates back to 1920, when they were used in rabbits to repair critical size bone defects as filler material (Albee 1920). Due to their osteogenic potential *in vitro* and *in vivo*, as well as physico-mechanical properties similar to human bone, CaPs are widely used in various fields of medicine, including skull and maxillofacial reconstruction, otolaryngology, spinal surgery, orthopedics, treatment of bone fractures and disorders, percutaneous implants, and dentistry/periodontal surgery (Jeong et al. 2019). In 2010, a study conducted in the USA revealed that around 1.3 billion dollars were invested solely in CaP-based bone substitutes (Dorozhkin 2015). The term "CaPs" refers to a group of minerals that contain calcium cations (Ca^{2+}) and metaphosphate (PO^{-3}), orthophosphate (PO_4^{3-}), or pyrophosphate ($\text{P}_2\text{O}_7^{4-}$) anions, as well as hydroxyl (OH^-) or hydrogen (H^+) ions. CaPs are the primary constituents of bone (~60 wt.%) and tooth enamel (~90 wt.%) (Fiume et al. 2021). For this reason, they are extensively studied for bone regeneration and repair.

Hydroxyapatite (HA) is a naturally occurring mineral and is the main inorganic component of bone and tooth enamel. It has a chemical formula of $\text{Ca}_{10}(\text{PO}_4)_6(\text{OH})_2$ and a 502.31 g/mol molecular weight. Its crystal structure is hexagonal, with a Ca/P ratio of 1.67, and has a density of 3.16 g/cm³ (Pandey et al. 2018a). HA is bioactive and biocompatible, which makes it an ideal material for orthopedic implants. Its chemical composition is similar to that of human bone, allowing excellent integration with the surrounding tissue. HA is also osteoconductive, which means it promotes bone growth and regeneration. Table 1.2 compares bone and HA chemical composition, indicating their similarity level.

Table 1.2 Bone and HA composition comparison (Levingstone 2008).

Constituents (wt %)	HA	Bone
Ca	39.6	24.5
P	18.5	11.5
Ca/P ratio	1.67	1.65
Na	Trace	0.7
K	Trace	0.03
Mg	Trace	0.55
CO ₃ ²⁻	-	5.8

1.5.1 Thermal behavior of HA at different temperatures

The thermal behavior of hydroxyapatite (HA) can vary at different temperatures. Understanding how HA reacts under different conditions is important to optimize its properties for various applications. Many studies have shown that HA can undergo phase transformations at high temperatures, leading to changes in its crystal structure and potentially affecting its mechanical properties (Gadow et al. 2010; Vilardell et al. 2020). Other research has focused on the thermal stability of HA coatings and their ability to withstand high temperatures without degrading. Overall, a better understanding of the thermal behavior of HA can lead to improved performance and durability in various biomedical and industrial applications. Most processing techniques like plasma spray, flame spray, Sol-gel method, and high-velocity oxy-fuel used to produce HA coatings or bulk materials involve elevated temperatures, which lead to HA decomposition (Jagadeeshanayaka et al. 2022). Thermal decomposition of HA occurs in several steps, as explained in Table 1.3.

Table 1.3 Thermal decomposition of HA (Bulina et al. 2021).

Temperature	Reaction
25-200°C	Evaporation of absorbed water
200-600°C	Evaporation of lattice water
600-800°C	HA decarbonation
800-900°C	HA de-hydroxylates to form oxyapatite (OA)
1120-1470°C	β -TCP, stable up to 1120° C, transforms to α -TCP
1550°C	Incongruent melting of HA
1630°C	TTCP melting temperature, Formation of CaO
1730°C	TCP melting temperature

1.5.2 Mechanical Properties

Hydroxyapatite (HA) is ideal for bone grafts and orthopedic coatings. The mechanical properties of hydroxyapatite are crucial for its performance in biomedical applications, particularly in load-bearing implants. Hydroxyapatite exhibits a Vickers hardness in the range of 3-7 GPa (Kumar and Agrawal 2023), which is influenced by the processing conditions and purity of the material. The hardness is a critical factor affecting HA coatings' wear resistance on implants. The compressive strength of HA can vary significantly depending on its porosity. Dense, sintered hydroxyapatite can have a compressive strength of about 900-1000 MPa, which decreases with increasing porosity. This property is essential for supporting physiological loads without fracturing. Hydroxyapatite has a relatively low tensile strength of about 50-100 MPa (Ong and Chan 2000). This limitation is often addressed by reinforcing HA with other materials, such as polymers or metals, to improve its performance in tensile loading conditions. The fracture toughness of hydroxyapatite is in the range of 1-2 MPa m^{1/2} (Jagadeeshanayaka et al. 2022). This relatively low value indicates that HA is quite brittle, which is a concern for its use in load-bearing applications. Table 1.4 compares the mechanical properties of different bone and HA scaffolds.

The mechanical properties of hydroxyapatite are a subject of ongoing research,

especially in the context of improving its performance in biomedical applications. The development of HA-based composites and advanced processing techniques continues to enhance its mechanical properties, making it more suitable for a broader range of applications in orthopedics and dentistry. The quality of HA's mechanical properties is influenced by several factors, including its chemical composition, crystallinity, and microstructure (Jagadeeshanayaka et al. 2023). By introducing reinforcing phases like carbon nanotubes, alumina, zirconia, titania, and graphene, among others, along with carefully controlling processing parameters, the mechanical properties of HA can be significantly improved. These reinforcements can enhance fracture toughness, flexural strength, hardness, and elastic modulus. Employing surface modification techniques like thermal spray can also enhance HA coatings' adhesion strength and wear resistance. Utilizing appropriate processing and modification techniques is crucial to optimize HA's mechanical properties for specific biomedical applications. Although HA is biocompatible and osteoconductive, it is unsuitable for load-bearing purposes. Therefore, it is typically used as a substrate coating material to improve its strength and fatigue resistance.

Table 1.4 Mechanical strength comparison of HA and bone (Ben-Nissan et al. 2004).

Properties	Cortical Bone	Cancellous Bone	HA Scaffolds
Compressive Strength (MPa)	8-164	23	350-450
Tensile Strength (MPa)	82-114	10-20	38-48
Young's Modulus (GPa)	3.8-11.7	0.2-0.5	7-13

1.6 Metal Implants

Bioimplants are medical devices or tissues that replace or support damaged or diseased body parts. Bioimplants can be made from various materials, including metals, ceramics, polymers, and composites. These materials are chosen based on their biocompatibility, good mechanical properties, corrosion resistance, and ability to promote tissue regeneration (Figure 1.1). Bioimplants are used in a variety of

biomedical applications, including orthopedics, cardiology, ophthalmology, and dentistry. Examples of bioimplants include artificial joints, stents, heart valves, corneal implants, and dental implants. The success of bioimplants depends on their ability to integrate with the surrounding tissue and perform their intended function without causing adverse reactions.

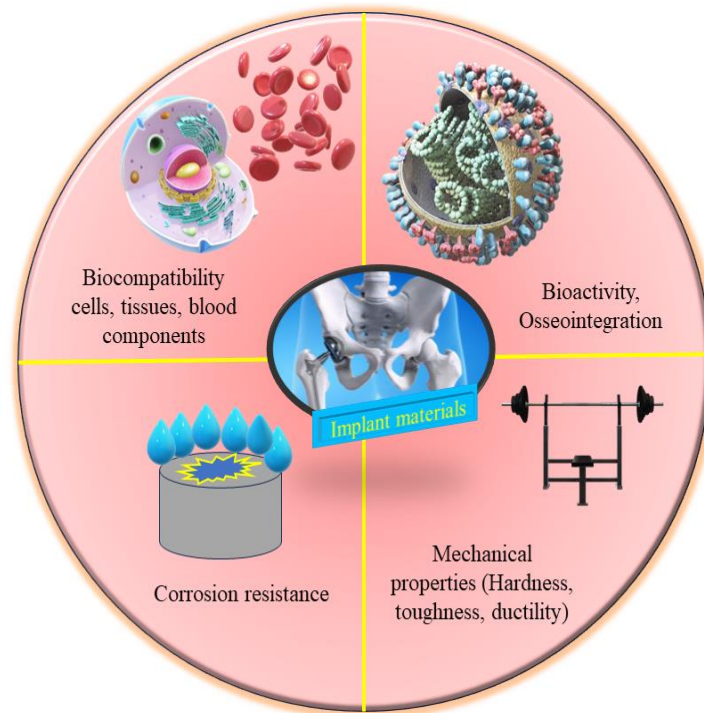


Figure 1.1 Different properties required for an ideal implant.

In the medical industry, various metals and alloys are produced. Still, only a select few can be used as implant materials for an extended period without causing adverse reactions within the body. These materials can be categorized into four groups based on their primary alloying element. These groups include cobalt-based alloys, stainless steel, titanium-based alloys (Jambagi and Malik 2021), and other miscellaneous alloys like NiTi and Mg-Ta. The United States Food and Drug Administration (FDA) has approved medical implants made from metallic materials in the first three groups commonly used in orthopedic medicine (Al-Shalawi et al. 2023). Although 316L stainless steel has moderate biocompatibility, it is less satisfactory than Co-Cr and titanium alloys due to its higher corrosion rates (Jambagi and Malik 2021). Titanium is an essential metal that can be significantly strengthened by alloying and deformation

processing. After processing, titanium alloys can be categorized into four groups based on their microstructure: Alpha alloys, near-alpha alloys, Alpha+Beta alloys, and Beta alloys. The modulus of elasticity of titanium and its alloys is roughly half that of stainless steels and cobalt–molybdenum alloys (Geetha et al. 2009). Titanium has superior specific strength (strength/density) compared to stainless steels and cobalt–chromium alloys. However, it has inferior tribological properties (Lahiri et al. 2011). In orthopedics, Grade 5 titanium is commonly used. Titanium alloys are gaining popularity as biomaterials because of their lower modulus, superior biocompatibility, and enhanced corrosion resistance compared to stainless steels and cobalt-based alloys. These characteristics led to commercial pure titanium (CP-Ti) and Ti–6Al–4V alloys, widely used in the aerospace and biomedical industries. Titanium metal is physiologically inert due to its nanometric surface amorphous oxide layer, making its use in implants highly successful. Titanium has a prolonged corrosion rate in biological media, making it biostable and not releasing ions under normal operating circumstances (Jambagi and Malik 2021). Commercially pure titanium integrates better into bone than titanium alloys because of this. However, under stress and wear circumstances, the corrosion kinetics of Ti can accelerate. The issue of protein adsorption by titanium has been widely researched, and it has been confirmed that titanium surfaces can support cell growth and differentiation. In vivo tests have shown that bone closely relates to titanium, but an amorphous biological layer separates both. There is no sign of chronic inflammation but a risk of developing foreign body giant cells (Facca et al. 2011). Therefore, surface modification of metal implants is needed to tackle these drawbacks. Figure 1.2 depicts the biomaterials used in the different parts of the human body.

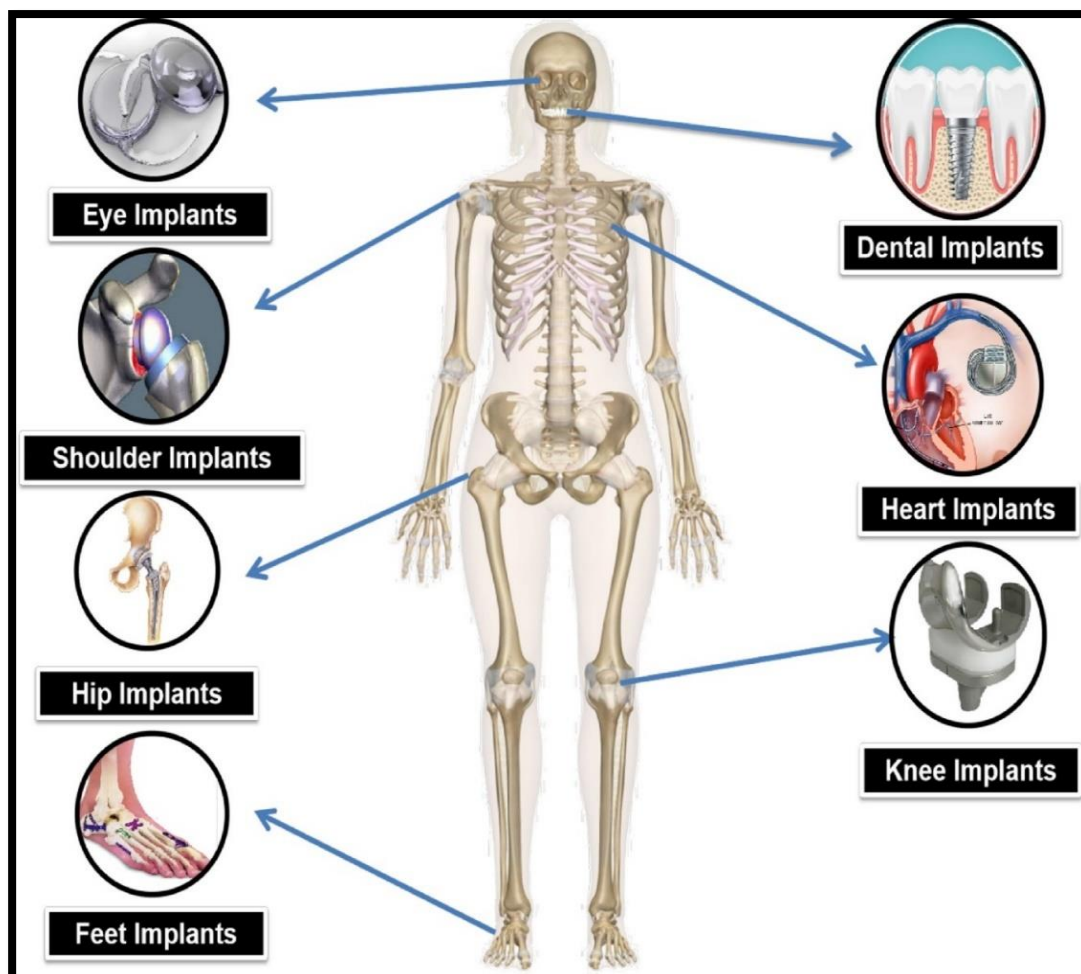


Figure 1.2 Illustration exhibiting several applications of medical implants in the human body (Gautam et al. 2022).

1.7 Carbon Nano Tube (CNT)

Carbon nanotube (CNT) belongs to the family of carbon allotropes, including diamond, graphite, graphene, fullerene, and amorphous carbon. It is particularly interesting due to its one-dimensional form with an aspect ratio greater than 1000 (Iijima 1991; Jambagi and Bandyopadhyay 2017; Tanaka et al. 1999). The bonding in carbon nanotubes is sp^2 , and each atom is connected to three neighbors, similar to graphite. Carbon nanotubes are essentially rolled-up graphene sheets, which are individual graphite layers. This type of structural bonding, stronger than the sp^3 bonds found in diamonds, gives the molecules their unique strength (Saifuddin et al. 2013). The properties of nanotubes depend on the atomic arrangement, diameter, length of the

tubes, and morphology or nanostructure. Single-walled carbon nanotubes (SWCNTs) are made up of a single sheet of graphene rolled seamlessly to form a cylinder with a diameter of about 1 nm and a length of up to centimeters (Figure 1.3 (a)). On the other hand, multi-walled carbon nanotubes (MWCNTs) comprise an array of cylinders formed concentrically and separated by 0.35 nm, similar to the basal plane separation in graphite (Figure 1.3 (b)). MWCNTs can have diameters ranging from 2 to 100 nm and lengths of tens of microns (De Volder et al. 2013). The challenge with SWCNTs is that they are much more difficult to synthesize and process in large quantities than MWCNTs. CNTs have many advantages over other materials in terms of mechanical, electrical, and thermal properties, although there is no consensus on their exact properties. According to Qian et al. (2002), theoretical and experimental results have revealed unusual mechanical properties with Young's modulus reaching as high as 1.2 TPa and tensile strength ranging from 50–200 GPa. CNTs are some of the toughest materials discovered, with a tensile strength that is one hundred times higher than steel's, although their density is almost seven times lower than steel's (Yu et al. 2000). Another notable property of CNTs is their resistance to erosion; they can withstand exposure to strong acids and alkalis without being structurally affected (Li et al. 2015).

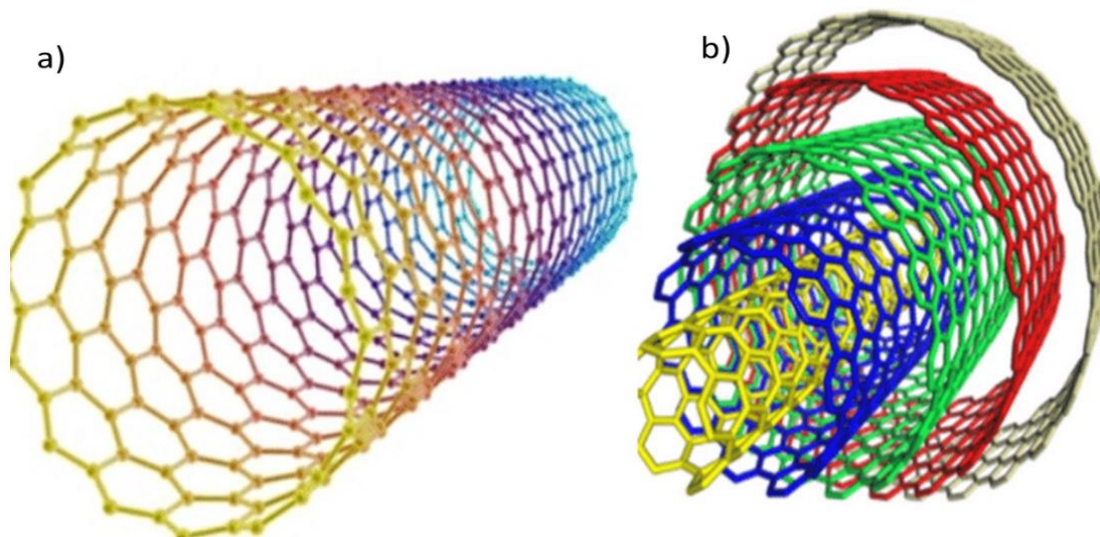


Figure 1.3 Structure of SWCNTs and MWCNTs (Devi and Gill 2021).

1.7.1 Bioactivity and Toxicity of CNTs

CNTs are a fascinating material that has attracted much interest recently due to its unique properties. Some studies have shown that CNTs can be bioactive and interact with biological systems, including cells and tissues. However, there are also concerns about the potential toxicity of CNTs (Vijayalakshmi et al. 2022), especially for human health and the environment. While some studies have found evidence of toxicity, others have reported no adverse effects (Facca et al. 2011). As such, more research is needed to fully understand the bioactivity and toxicity of CNTs and develop guidelines for their safe use. If CNTs are to be incorporated into composite materials for medical applications, evidence of their bioactivity and toxicity is essential. The biocompatibility of CNTs in orthopedic applications is also established by studies showing accelerated bone growth and increased proliferation and differentiation of osteoblast cells (Balani et al. 2007a). The recent report on the non-toxicity of MWCNT and functionalized CNT when used in low concentration further strengthens the drive for bio-related applications of CNTs (Vijayalakshmi et al. 2023). Though the biocompatibility of CNT is still not in universal agreement due to contradictory reports, the cytotoxic effect of CNT is mostly attributed to other factors, e.g., the presence of metallic catalyst particles, agglomeration, etc., and not due to CNT itself (Lahiri et al. 2012). Moreover, CNTs promote bone growth (Usui et al. 2008) and osteoblast proliferation, which fortifies its candidature as an orthopedic biomaterial. While reports of both aspects vary, the majority of studies thus far suggest that not only can CNTs serve a mechanical role, but they can also stimulate bone regeneration and are nontoxic in vivo when functionalized to be water-soluble.

1.8 Nature and Properties of Alumina

Oxides contain at least one oxygen atom bonded to another element. They are ubiquitous and are essential to many chemical and physical processes. There are many different oxides, including metal, non-metal, acidic, basic, and amphoteric. Some of the benefits of oxides include:

1. Corrosion resistance: Metal oxides are often used as coatings to protect metal surfaces from corrosion. The oxide layer is a barrier, preventing moisture and other

corrosive materials from reaching the underlying metal.

2. Catalysis: Metal oxides are also catalysts in many chemical reactions. They can speed up the reaction rate, increase the yield of products, and improve the selectivity of the reaction.

3. Electrical conductivity: Some oxides, such as titanium oxide and indium tin oxide, have semiconducting properties and are used in electronic devices such as solar cells and touchscreens.

4. Optical properties: Many oxides, such as zinc and titanium, have unique optical properties and are used in applications such as sunscreen, pigments, and optical coatings.

5. Thermal insulation: Some oxides, such as alumina and zirconia, have excellent thermal insulation properties and are used in high-temperature applications such as furnace linings and turbine blades.

Overall, oxides play a critical role in many industrial and technological applications, and their properties make them an attractive material choice for a wide range of applications.

Alumina, also known as aluminum oxide or Al_2O_3 , is an odorless and colorless oxide ceramic with a hexagonal crystal structure. It has a high hardness of 18-20 GPa (Aarik et al. 2022), making it highly refractory and suitable for use in various applications such as thermal liners, high-temperature insulating systems, ceramic boards, brackets, crucibles, and heaters. The majority of Al_2O_3 powder, a raw material, is produced by the Bayer process from bauxite. Alumina has a wide range of applications, particularly in biomedical engineering. High-purity Al_2O_3 , labeled as 99.99% integrity, is increasingly favorable for dental and orthopedic applications, such as femoral components in total hip replacements. Alumina is recognized for its exceptional material properties, such as high hardness, low friction, excellent wear resistance, and good corrosion protection. These features make it an optimal choice for articulating surfaces in orthopedic applications (Ferrage et al. 2017). Al_2O_3 -based bioceramics were introduced as alternative hip joint prostheses and dental implant components. However, the brittleness of Al_2O_3 limits its usage as it is easily prone to fracturing. Alumina properties have been extensively studied for biomedical

applications due to their significant potential in enhancing the biomaterials employed, such as bone screws, ossicular (middle ear) bone substitutes, alveolar ridge (jaw bone) and maxillofacial reconstruction materials, segmental bone replacements, and substitutes for corneal, among others (Miri et al. 2024).

1.9 Deposition of HA coatings

Different methods are utilized for creating HA coatings, including electrophoretic deposition (Kaya et al. 2008), pulsed laser deposition (Koch et al. 2007), electrodeposition (Guan et al. 2012), sol-gel technique (Kaur et al. 2019), and thermal spray (Clavijo-Mejía et al. 2020; Vu et al. 2019). Nevertheless, these conventional coating processes face limitations, and current research centers on developing more advanced techniques. Out of the various options, thermal spray techniques are favored, with Atmospheric Plasma Spraying (APS) being the sole FDA-approved approach for biomedical implant materials. Although we will touch briefly on APS, our primary focus will be on the emerging low-temperature operated thermal spray techniques that address APS's drawbacks when depositing bio-ceramic HA. A synopsis of different coating techniques used for producing HA coatings is explained in Figure 1.4.

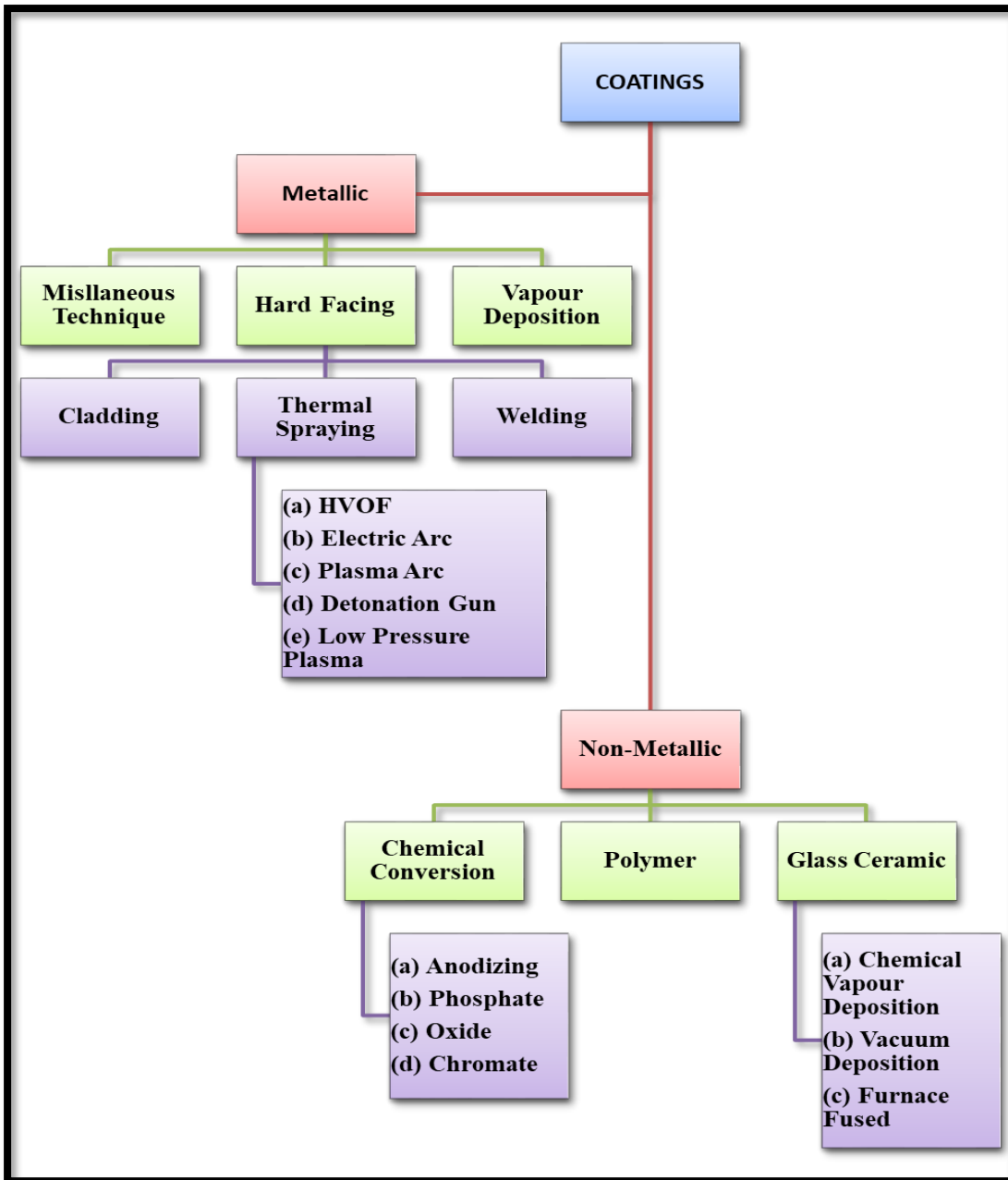


Figure 1.4 Coating deposition technologies (Stokes 2003).

1.10 Thermal spray

Thermal spraying is when a coating material is heated or melted to a high temperature and sprayed onto a surface to create a decorative or protective coating. This process utilizes a powder, rod, or wire that is heated using a plasma arc or a flame. The molten material is then sprayed onto the surface using a high-pressure air or gas stream, solidifying and forming a coating. Thermal spraying is widely used in various

industries, such as aerospace, automotive, and biomedical, to create coatings with specific properties like biocompatibility, corrosion resistance, and wear resistance. Depending on the method, a feedstock material (wire, powder, rod, or suspension) is heated to a semi-molten or molten state using chemical or electrical means. The softened particles are then propelled toward the substrate, deposited, cooled, and built into a coating. A thermally sprayed coating comprises numerous individual particles that are mechanically and chemically interlocked and adhere to the substrate through mechanical anchoring. The air gaps between particles create varying percentages of porosity in the coating, depending on the process used. Thermal spraying has several advantages as a coating technique. Firstly, it can deposit various materials onto different substrates, making it a versatile technique for coating several different types of surfaces. Secondly, depending on the application requirements, coatings can be created with a range of thicknesses, from a few microns to several millimeters. Thirdly, it is a relatively low-cost technique compared to other coating methods, making it an attractive option for industrial applications (Vuoristo 2014). Thermal spraying also offers good adhesion to the substrate, which helps ensure the durability of the coating. Finally, it can create coatings with specific properties, such as high wear resistance, corrosion resistance, or thermal insulation, making it an ideal technique for various applications. It is also environmentally friendly compared to other processes, such as plating. However, the thermal process has several drawbacks. The main limitation of the thermal spraying process is its line-of-sight limitation, which typically prevents plasma spraying from being used to coat holes or other topographical features on a workpiece. The process can also be time-consuming and costly, requiring specialized equipment and trained personnel to spray. Nowadays, several coating deposition techniques are available. However, thermal spraying is the most crucial part of this research; hence, the following section concentrates on this technique.

1.10.1 Atmospheric Plasma Spray (APS)

Atmospheric plasma spraying (APS) is a widely used thermal spray technique that utilizes a plasma jet to melt and accelerate particles onto a substrate. Figure 1.5 depicts a diagrammatic representation of the plasma spraying process. The plasma is generated by a high-voltage arc discharge between a cathode and an anode, which ionizes a gas

(usually argon or nitrogen) and creates a high-temperature plasma jet (6000-15000 °C) (Jagadeeshanayaka et al. 2022). An ionizing gas, such as argon, helium, hydrogen, or nitrogen, is fed into the arc, which becomes ionized and forms a plasma flame. In some cases, a mixture of gases is used. The gas becomes excited to high energy levels and forms a plasma. The plasma formed is unstable and recombined to form a gas again, releasing much thermal energy. The particles to be sprayed are fed into the plasma stream, where they are heated and accelerated to high velocities. Upon impact with the substrate, the particles form a coating. The APS process involves several steps. First, the substrate is cleaned and prepared to ensure good adhesion of the coating. Then, the powder feedstock is introduced into the plasma jet, where it is heated and melted. The plasma jet accelerates the molten particles toward the substrate, where they solidify and form a coating. The APS process has several advantages over other thermal spray techniques, such as high deposition rates, spraying a wide range of materials, and producing thick coatings. However, the process also has some limitations, such as poor control over the coating microstructure and the possibility of oxide formation in the coating. In summary, atmospheric plasma spraying is a versatile and widely used thermal spray technique that relies on a high-temperature plasma jet to melt and accelerate particles onto a substrate. The process can produce coatings with a wide range of properties and is commonly used in various industrial applications, including aerospace, automotive, and biomedical industries.

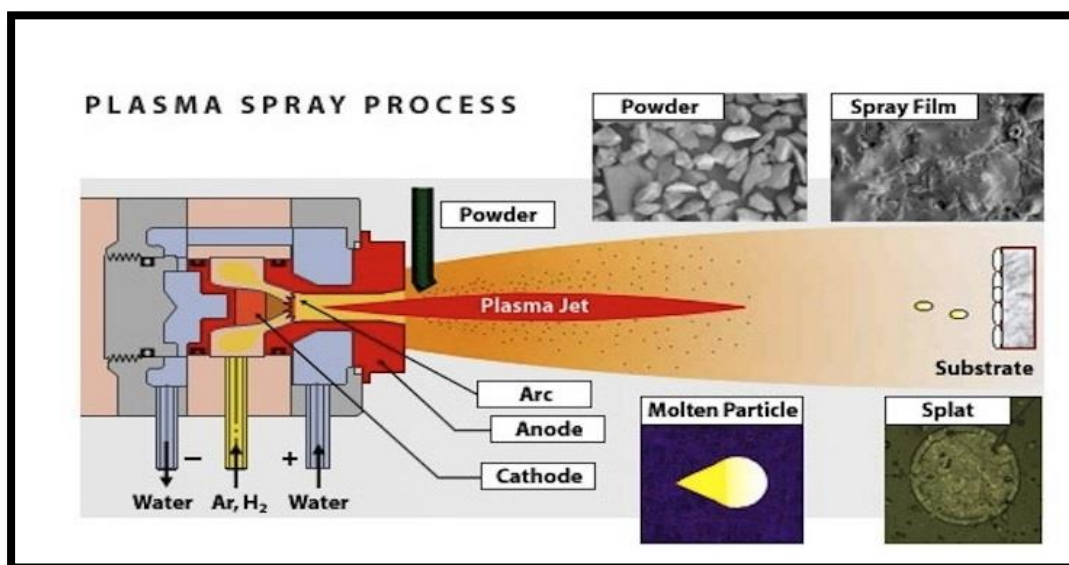


Figure 1.5 Schematic diagram of the plasma spray system (Budinski 1988).

The atmospheric plasma spray system typically consists of the following equipment units:

1. Plasma torch: The plasma torch generates a high-temperature plasma flame that melts and accelerates the powder particles toward the substrate.
2. Powder feeder: The powder feeder delivers the powder to the plasma flame and controls the powder feed and flow rates.
3. Gas delivery system: The gas delivery system provides the plasma-forming and secondary gas to the plasma torch.
4. Cooling water system: The cooling water system cools the plasma torch and the powder feeder.
5. Substrate holder: The substrate holder holds the substrate in place during the coating process.
6. Control system: The control system controls the plasma torch and powder feeder parameters, such as the plasma power, powder feed rate, and gas flow rate.

The process parameters in APS play a crucial role in determining the coating's quality, properties, and performance. Some of the critical process parameters in APS include:

1. Plasma gas flow rate: The flow rate of the plasma gas, typically argon, is a critical parameter that affects the energy and temperature of the plasma arc. Higher flow rates result in a more stable and hotter plasma arc, which can improve the coating quality and reduce defects.
2. Plasma power: The power of the plasma arc is another critical parameter that determines the energy and temperature of the plasma. Higher power can produce a more intense and hotter plasma, improving the coating adhesion and density.
3. Spray distance: The distance between the spray gun and the substrate, also known as the stand-off distance, is a vital process parameter that affects the coating morphology and thickness. Higher spray distances can result in more uniform and thinner coatings.
4. Powder feed rate: The rate at which the coating material is fed into the plasma spray gun is a critical parameter that affects the coating thickness, density, and morphology. Higher feed rates can result in thicker coatings but can also lead to defects such as splats

and pores.

5. Substrate temperature: The temperature of the substrate is a crucial parameter that affects the adhesion and bonding strength of the coating. Higher substrate temperatures can result in better adhesion and bonding strength but can also lead to thermal stresses and cracking.

Optimizing these process parameters can produce high-quality, uniform, and defect-free coatings with improved mechanical, thermal, and chemical properties. Therefore, it is essential to carefully monitor and control these parameters during the APS process to ensure consistent and reliable coating performance. The coating properties produced by the plasma spray process are affected by several factors, including the plasma gas composition, plasma spray parameters, and feedstock material properties. These factors can influence the coating's microstructure, porosity, chemical composition, and mechanical properties. For example, the plasma gas composition can affect the coating's chemical composition and microstructure by altering the temperature and velocity of the plasma jet. Similarly, the plasma spray parameters, such as the spray distance and particle velocity, can affect the coating's porosity and mechanical properties.

1.10.2 Flame spray (FS)

Flame spray (FS) is a thermal spray coating process that uses a fuel gas and oxygen to produce a flame that melts and propels molten particles onto a substrate. The process involves heating a wire or powder feedstock to its melting point and then spraying it onto the substrate. The feedstock is fed into the flame, where it melts and is propelled onto the substrate by a compressed air stream. The flame spray process deposits materials onto various substrates, including metals, ceramics, and polymers. The coatings produced by this process are typically dense, uniform, and have good adhesion to the substrate. The flame spray process principle uses a combustion flame to make the heat necessary to melt the feedstock. The combustion flame is produced by burning a fuel gas (such as acetylene or propane) with oxygen. Oxygen acetylene torches are the most common, using acetylene (C_2H_2) as the primary fuel in combination with oxygen to generate the highest combustion temperature of approximately 3160 °C (Vuoristo

2014). The heat generated by the combustion flame melts the feedstock and propels it onto the substrate. Overall, the flame spray process is versatile and cost-effective for depositing high-quality coatings onto various substrates. Figure 1.6 shows the basic setup for the process, which displays various units of the spray system. The gun consists of a fuel gas supply, an oxygen supply, and a nozzle. 2. Compressed air supply: The compressed air is used to atomize the coating material and carry it to the coated surface. 3. Powder feeder: The powder feeder feeds the coating material into the flame spray gun. 4. Control panel: The control panel is used to regulate the flow of fuel gas, oxygen, and compressed air to the flame spray gun. 5. Safety equipment: This includes safety glasses, gloves, and protective clothing to protect the operator from the hot flame and coating material. The spray system possesses several advantages and limitations, which are discussed below:

Advantages:

1. *Cost-effective*: Flame spraying is a low-cost process that requires minimal equipment and training. It is one of the most affordable thermal spray methods available.
2. *High deposition rate*: Flame spraying can achieve high deposition rates, making it an ideal choice for large-scale production.
3. *Versatile*: Flame spraying can apply various coatings, including metals, ceramics, and polymers.
4. *Portable*: Flame spraying equipment is lightweight and portable, making it ideal for on-site repairs and maintenance.
5. *Easily automated*: Flame spraying can be easily automated, which reduces labor costs and increases production efficiency.

Limitations:

1. *Limited coating thickness*: Flame spraying is unsuitable for creating thick coatings, as the process relies on the melting and atomization of materials.
2. *Limited material selection*: Some materials are unsuitable for flame spraying due to their high melting points or chemical properties.
3. *Poor surface finish*: The surface finish of flame-sprayed coatings is often rough and

uneven, which may require additional finishing operations.

4. *Limited control over coating properties:* Flame spraying lacks the precision and control of other thermal spray methods, which may result in variations in coating properties.

5. *Safety concerns:* Flame spraying involves flammable gases and high heat, posing safety risks if improperly handled.

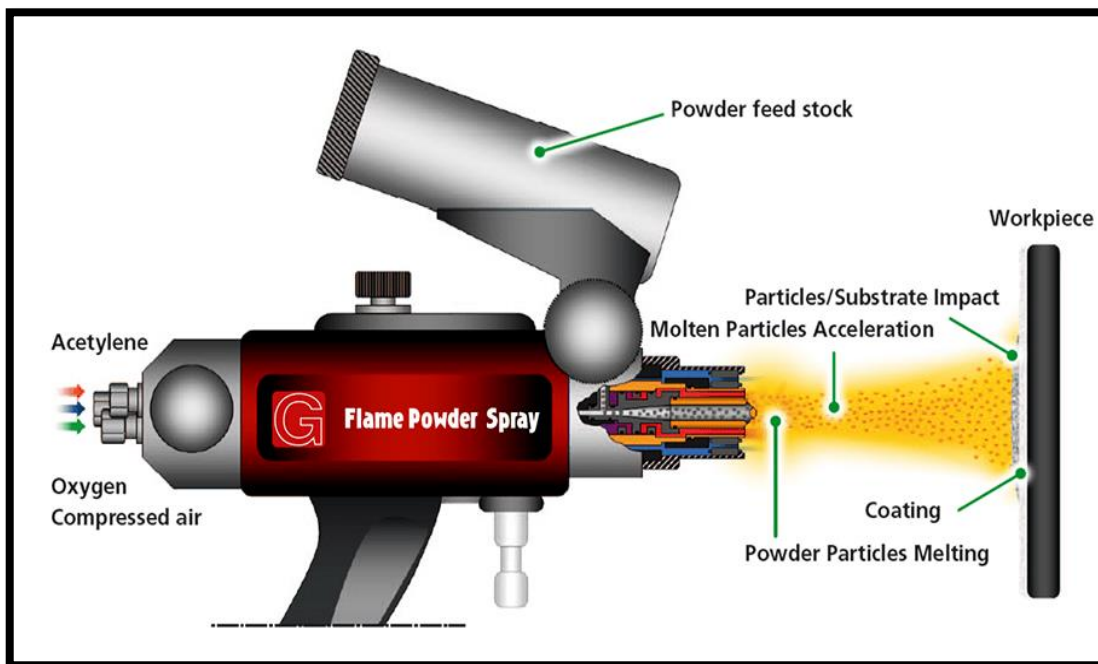


Figure 1.6 Schematic diagram of the flame spray system depicts various units of the setup (www.griekspoorthermalcoatings.com).

1.10.3 Cold spray

Cold spray is a coating deposition technique that involves accelerating micron-sized particles to supersonic velocities and impacting them onto a substrate. The cold spray process utilizes a high-pressure gas, such as helium, nitrogen, or air, to accelerate the powder particles to velocities ranging from 500 to 1200 m/s and can have low operating gas temperatures (~ 1100 °C) (Vilardell et al. 2020). The powder particles are heated only by the kinetic energy of the gas stream and not by an external heat source, which differentiates it from other thermal spray techniques. The impact of the particles on the substrate creates a strong bond and forms a dense coating. Figure 1.7 displays the basic setup for the cold spray process, which shows various units of the spray system.

The principle mechanism of cold spray involves three stages: particle acceleration, particle deposition, and coating formation. During the particle acceleration stage, the powder particles are entrained in the high-pressure gas stream and accelerated to supersonic velocities. The gas stream is generated by a converging-diverging de Laval nozzle, which compresses and accelerates the gas to supersonic velocities. The powder particles are injected into the gas stream at the nozzle's throat and entrained in the high-speed gas stream. During the particle deposition stage, the powder particles impact the substrate and deform plastically, forming a splat. The splat spreads laterally and radially, forming a disk-shaped deposit. The impact of the particles on the substrate generates high strain rates and strain gradients, which cause plastic deformation and work hardening of the particles, resulting in increased strength and hardness. During the coating formation stage, the deposited splats merge and bond, forming a dense and continuous coating. The bonding mechanism is primarily mechanical interlocking and solid-state diffusion. The high strain rates and strain gradients generated during particle deposition cause localized plastic deformation and work hardening of the substrate surface, resulting in surface roughening and increased surface area for bonding. The cold spray process is a highly efficient and versatile coating deposition technique that can deposit various materials, including metals, ceramics, polymers, and composites. The absence of an external heat source and low process temperatures make it suitable for depositing temperature-sensitive materials and reducing heat-affected zones and distortion. The coatings' high deposition rates and low porosity make them ideal for industrial applications, including aerospace, automotive, and biomedical.

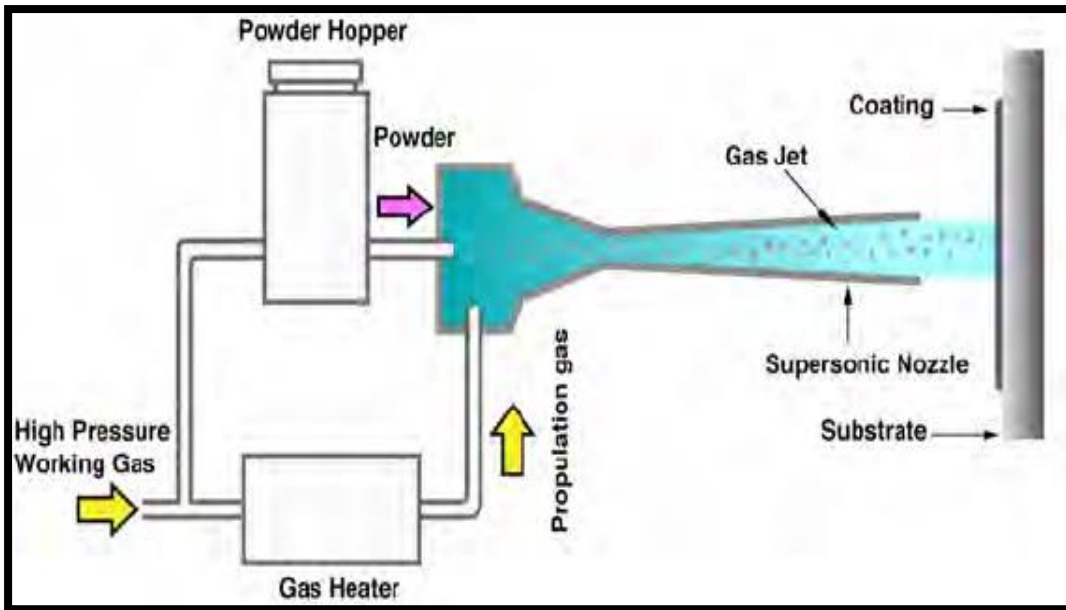


Figure 1.7 Schematic diagram of the cold spray process (Ogawa and Seo 2011).

1.10.4 High-velocity oxy-fuel (HVOF) Spray

High-velocity oxy-fuel (HVOF) is a thermal spray process that involves heating and accelerating gas and powdered coatings to create a high-speed ($400\text{-}1000\text{ ms}^{-1}$) (Jagadeeshanayaka et al. 2022), high-temperature jet ($1800\text{-}2300\text{ }^{\circ}\text{C}$) (Shankar et al. 2024b). The process involves using a gun that mixes and ignites oxygen and fuel gases, such as propane or natural gas, to create a high-velocity flame. The flame is then directed towards the powder feedstock, fed into the flame, and heated to a molten state. The molten particles are then propelled at high speeds and deposited onto the substrate, forming a dense, adherent coating. Figure 1.8 shows the basic setup for the process, which displays various units of the HVOF spray system. The HVOF process produces coatings with high bond strength, low porosity, and high hardness, making them suitable for various applications, including aerospace, automotive, and biomedical industries. The coatings produced by HVOF have excellent wear resistance, corrosion resistance, and thermal barrier properties, making them ideal for use in harsh environments. The HVOF process is also environmentally friendly, producing minimal waste and emissions compared to other coating processes.

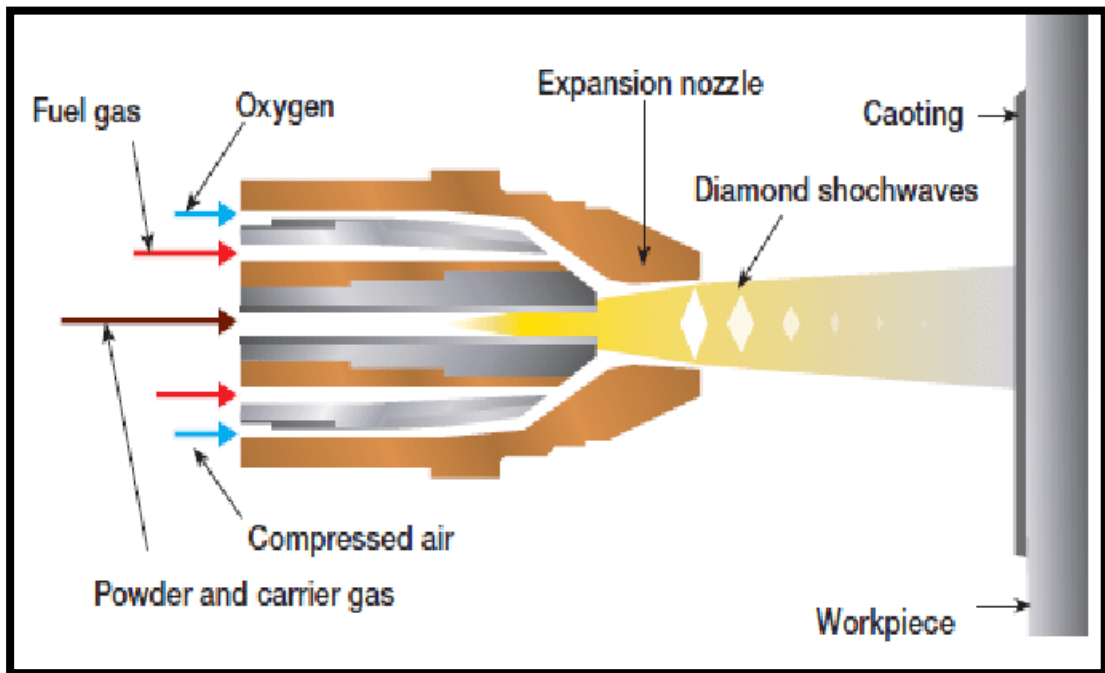


Figure 1.8 HVOF process schematic diagram (Chandra Yadaw et al. 2018).

Some of the commonly used equipment units for HVOF thermal spray include:

1. *HVOF spray gun*: This is the core component of the HVOF thermal spray system, which is used for spraying the coating material onto the substrate. The gun is designed to generate a high-velocity, high-temperature gas stream that accelerates the powder particles to supersonic speeds.
2. *Powder feeder*: The powder feeder feeds the coating material into the HVOF spray gun. The feeder controls the powder particles' flow rate and size distribution to ensure uniform coating thickness and quality.
3. *Gas supply system*: The gas supply system provides the high-pressure gas required for the HVOF spray gun. The gas can be oxygen or air, depending on the coating material.
4. *Control system*: The control system is used to monitor and control the various parameters of the HVOF thermal spray process, such as gas flow rate, powder feed rate, and gun temperature.
5. *Cooling system*: The cooling system is used to cool the HVOF spray gun and the substrate to prevent overheating and damage.

6. *Exhaust system*: The exhaust system removes the exhaust gases and the excess powder particles generated during the HVOF thermal spray process.

These equipment units are essential for the HVOF thermal spray process and play a vital role in ensuring the quality and performance of the coatings produced.

The high-velocity oxy-fuel (HVOF) spray coating process involves the deposition of coating material onto a substrate using a high-velocity stream of gas and powdered material. The process parameters that affect the coating quality include the spray gun design, gas flow rate, powder feed rate, spray distance, and substrate temperature. The spray gun design can affect the velocity and temperature of the gas stream and the powder feed rate. The gas flow rate can affect the velocity and temperature of the gas stream, while the powder feed rate can affect the deposition rate and the quality of the coating. The spray distance can affect the velocity and temperature of the gas stream, the deposition rate, and the quality of the coating. Finally, the substrate temperature can affect the coating's adhesion and microstructure. Optimization of these process parameters is necessary to achieve a high-quality HVOF spray coating.

- Additional benefits of HVOF processes are as follows (Stokes 2003).
 - i. Lower flame temperature compared with plasma spraying.
 - ii. A more favorable environment due to a less oxidizing atmosphere.
 - iii. Minimal reaction and phase transformations.
 - iv. High compressive residual stress is possible.
 - v. Strong adhesion to substrates.
 - vi. High cohesive strength.
 - vii. Lower capital cost and ease of use compared to other processes.
 - viii. More uniform and efficient particle heating due to high turbulence.
 - ix. Reduce mixing with ambient air once the jet and particle leave the gun.
 - x. Thicker coatings can be produced than those produced with plasma and arc spraying.
 - xi. Lower ultimate particle temperatures compared to other processes.
 - xii. Smooth as-sprayed surface finish.

The High Velocity Oxygen Fuel (HVOF) spray technique has a few limitations. One of the significant limitations is the cost of the equipment required for the process, which can be pretty expensive. Additionally, HVOF requires a large volume of gases, which can be costly to obtain and store. Another limitation of HVOF is the limited range of materials sprayed using this technique. Lastly, the high temperatures and pressures involved in HVOF spraying can cause thermal stresses and deformation in the substrate material, affecting the coating's quality and adhesion.

Further, the effect of powder size on different spray coating methods plays a crucial role in achieving uniform and stable coatings on bioimplants. The coating method and the coating process's characteristics directly impact the implants' quality, performance, and reliability. Here's a detailed look at how size effects influence various spray coating methods and their implications for bioimplants (Claase et al. 2014)ASS:

1. High-velocity oxygen Fuel (HVOF) Spraying

Powder Size Distribution: HVOF spraying is sensitive to the size distribution of the powder. Uniform powder size distribution is critical for achieving consistent coating thickness and quality. Powders that are too fine may lead to excessive fragmentation, while too coarse powders may result in an uneven surface.

Particle Velocity: The size of the powder particles affects their velocity and impact on the substrate. Larger particles may have higher momentum but can cause more significant surface roughness and potential cracking. Smaller particles may improve coating uniformity but require precise control of spray parameters to avoid insufficient adhesion.

Implications:

Uniform Coating: Properly sized powders help ensure a uniform coating with good adhesion and minimal porosity.

Stability: The coating's stability is influenced by the particle size and velocity, affecting the mechanical properties and durability of the bioimplant.

2. Plasma Spraying

Powder Size and Feed Rate: Plasma spraying allows for a wider range of powder sizes compared to HVOF. However, the powder feed rate and size distribution impact the coating's uniformity. Fine powders may be more prone to oxidation in the plasma, while larger powders might not fully melt, leading to uneven coatings.

Thermal Decomposition: Hydroxyapatite, for example, is sensitive to high temperatures. The size of the particles affects how well they can withstand the plasma environment without decomposing or altering their phase.

Implications:

Coating Quality: The size and feed rate of the powder must be optimized to achieve a uniform and adherent coating. Variations in powder size can lead to inconsistencies in coating thickness and properties.

Material Preservation: Controlling the size and feed characteristics for temperature-sensitive materials like HA helps preserve the material's properties and enhance coating stability.

3. Cold Spraying

Powder Size and Kinetic Energy: Cold spraying relies on the kinetic energy of particles rather than thermal energy. The size of the powder particles affects their ability to achieve the necessary velocity for effective coating. Larger particles may require higher velocities to bond well, while smaller particles might be more easily accelerated but could result in a denser coating.

Particle Size Distribution: A narrow particle size distribution is often preferred to ensure consistent deposition and uniform coating quality.

Implications:

Uniformity: Cold spraying can produce coatings with a relatively uniform microstructure, but the particle size and velocity must be controlled to ensure proper adhesion and coating density.

Material Integrity: Since cold spraying does not involve high temperatures, it is better suited for temperature-sensitive materials like hydroxyapatite, maintaining their

original properties.

4. Chemical Vapor Deposition (CVD) and Physical Vapor Deposition (PVD)

Deposition Rate and Thickness: Both CVD and PVD methods typically result in very fine and uniform coatings. The size effects here are more about the control of deposition rate and layer thickness rather than particle size.

Surface Uniformity: For CVD and PVD, uniform deposition is achieved by controlling parameters such as deposition time, temperature, and pressure, rather than directly managing particle size.

Implications:

Coating Uniformity: These methods are highly effective in achieving uniform coatings with controlled thickness. They are often used for thin films and coatings where precise control is required.

Adhesion and Stability: The coatings produced by CVD and PVD are generally stable and adhere well to substrates, though they may be less suited for very thick coatings.

Powder Size and Distribution: For methods like HVOF and plasma spraying, optimizing powder size and distribution is critical for achieving uniform and stable coatings. Ensure that the size distribution is narrow and appropriate for the process used.

Process Control: Consistent process parameters such as spray distance, temperature, and feed rates are essential for all spray coating methods to achieve uniformity and stability.

Material-Specific Considerations: For temperature-sensitive materials like hydroxyapatite, methods that minimize thermal exposure (e.g., cold spraying) may be preferred to preserve material properties.

In summary, the size effects of powders and process parameters are crucial in achieving uniform and stable coatings for bioimplants. Each coating method has its specific considerations, and optimizing these factors is key to producing high-quality and reliable implants.

1.11 Hemocompatibility of biomaterials

Hemo/blood compatibility is important when designing and selecting biomaterials for medical applications. Hemocompatible materials do not cause adverse reactions when in contact with human blood or blood components. The hemocompatibility of a biomaterial is dependent on its surface properties, such as surface chemistry, roughness, and charge. Surface modifications can be used to improve the hemocompatibility of biomaterials. Additionally, using hemocompatible coatings can enhance the biocompatibility of the biomaterial. It is crucial to ensure the hemocompatibility of biomaterials to prevent thrombosis, inflammation, and hemolysis. Further there are different ways/stages of determining the biocompatibility of biomaterials used in the medical industry, as seen in Figure 1.9.

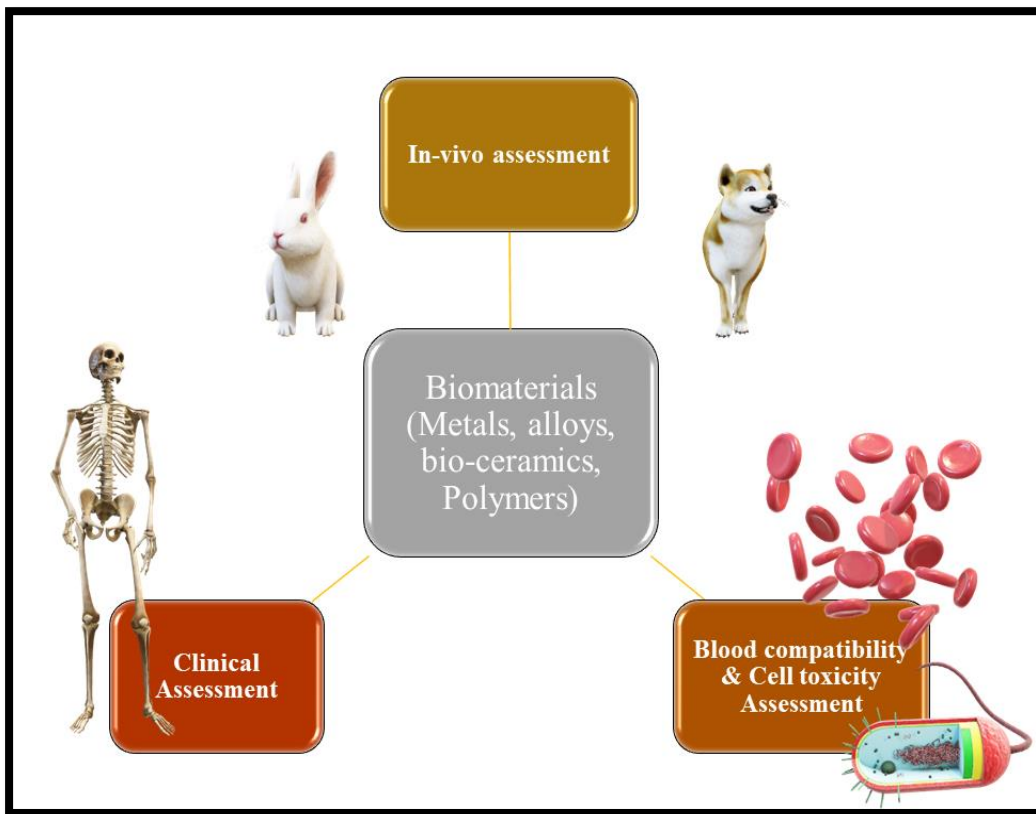


Figure 1.9 Different ways to assess the biocompatibility of biomaterials.

1.11 Overview of the thesis

Chapter 1 briefly describes the surface modification methods in general, different biomaterials used in the medical industry, various thermal spray coatings, a brief

discussion of alumina and toxicity of carbon nanotubes, and the hemocompatibility of biomaterials.

Chapter 2 presents a compressive literature review on thermally sprayed HA coatings with and without reinforcements. The research gaps identified from the literature helped frame the present work's objectives.

Chapter 3 focuses on this investigation's materials, methods, and equipment.

Chapter 4 describes the heterocoagulation of composite powders followed by ball milling with HA powder, characterized by different physiochemical properties that influence the hemocompatibility of HA-based composite powder. The degree of CNT dispersions, phases, and surface charge of all powders were evaluated. The better performance of the composite powder was used for coating purposes.

Chapter 5 begins with the microstructure of the HA coatings obtained through different thermal spray techniques. The HA coatings are characterized by their microstructure, phase quantification, and coating properties like microhardness, porosity, crystallinity, zeta potential, and contact angle, which were assessed and compared. The effect of different surfaces generated by thermal spray was then evaluated for biocompatibility, mainly using simulated body fluid tests and different hemocompatibility tests. The coating technique that outperformed others was used to spray the better biocompatible composite powder from the previous study.

Chapter 6 presents the durability and biocompatibility of the composite coating obtained through the best thermal spray techniques resulting from previous outcomes. The coatings were then studied for their suitability for clinical use by implanting the rods in rabbit bones.

Chapter 7 presents concluding observations on the current study's findings, discusses the scope for future investigation, and gives a brief idea of the limitations and challenges of the current study.

1.12 Summary

This chapter describes the fundamental concept of surface engineering and several surface modification techniques. The fundamental characteristics and properties of different biomaterials like HA, alumina, and titanium used in orthopedic applications are briefly described. The properties of carbon nanotubes and their toxicity are also emphasized. Thermal spray techniques' principal mechanisms, advantages, and drawbacks were discussed extensively. A brief understanding of the hemocompatibility of biomaterials is also discussed. Finally, an overview of the thesis' various chapters was prepared. This chapter aims to introduce the reader to the purpose of the basic understanding of materials and techniques used in the biomedical industry. The next chapter discusses a literature review of our research subjects and the formation of thesis objectives based on this literature review.

CHAPTER 2 LITERATURE REVIEW

2.1 Preamble

This chapter provides a thorough review of the literature pertinent to the study. It begins by examining the literature on current significance, specifically HA, and the impact of various reinforcements, such as alumina and carbon nanotubes, on their physiochemical, mechanical, and biological properties. The literature is subsequently categorized based on the different thermal spray coatings used to create HA-based implants in the biomedical industry. Lastly, a succinct literature review on the hemocompatibility of biomaterials is also discussed. This extensive literature review informs the objectives of the present study.

2.2 Consumables used for thermally sprayed coatings in the medical industry

Today, a large number of thermal spraying consumables are available commercially. Table 1.1 lists some major consumables used widely in the orthopedic industry. The selection of the consumable depends on the usage of the coated component. For example, alumina and HA are well-known materials for medical implants (Rattan et al. 2022), and zirconia is a standard thermal barrier coating (TBC) consumable (Singh et al. 2006). Recently, carbon nanotubes (Sahu et al. 2023) have gained importance in improving the tribological properties of the coated implants.

2.2.1 HA coatings

HA coating is prevalent in modifying surface properties of metallic materials to meet biological requirements and has a wide range of biomedical applications. Biomedical applications of HA include but are not limited to augmentation of the alveolar ridge; maxillofacial reconstruction; middle ear reconstruction; bioreactors; drug carriers; spinal surgery; enhancement of guided tissue regeneration; dental and orthopedic applications (Jagadeeshanayaka et al. 2022; Ong and Chan 2000). HA coatings are a significant market for hard tissue replacements or orthopedic applications, as they are a physical barrier between substrate and tissue and reduce metal ion release. HA coatings also promote a strong chemical and biological bond with surrounding bone tissue in orthopedic implants, leading to bone ingrowth between the implant and the

bone without causing any adverse effects on the body. Corrosion protection, prevention of slippage, facilitation of natural tissue function, minimization of implant failure, and enhancement of durability, survivability, and quality of life are other benefits of HA coatings (Dorozhkin 2023). Roy et al. (2011) observed osteoid formation at the HA coating and bone interface, which resulted from the differentiation of osteoblast from collagen and mesenchymal cells to form mineralized bone. However, only a few osteoids were observed over the uncoated implant with a clear interface gap. Heimann (2016) also presented similar observations, where the HA surface actively responded to the biological system and offered a firm biological bond between the implants and bone. However, the fractured bone and bare Ti-6Al-4V implant could not fill the bone gap even after 2 months.

The effect of different surface modification techniques on HA coating properties like microstructure, crystallinity, phase change, and mechanical properties obtained by various researchers is described below:

Hussain et al. (2023) investigated the impact of hydroxyapatite (HA) powders synthesized at different temperatures and deposited on titanium alloy using an atmospheric plasma spray process was investigated. The HA powders were synthesized from Indian clam seashells through the hydrothermal technique at temperatures ranging from 700 to 1000°C for two hours and then spray-dried to obtain agglomerated powders suitable for coating application. The study used standard methods to estimate the crystallite size, Ca/P ratio, and crystallinity of agglomerated HA powders and their respective coatings. The microstructure and phases of the feedstock and coating materials were examined using a FESEM and an XRD, respectively. The results showed that the crystallite size and crystallinity of spray-dried synthesized HA powders increased with synthesizing temperature from 700 to 900°C. All the feedstock HA powders were non-stoichiometric and Ca-rich in nature. All HA coatings had mostly stable HA phases and low TCP and CaO phases. A few metastable phases of HA were also formed in HA-900 and HA-1000 coatings. The crystallite size and crystallinity of HA coating increased with an increase in synthesis temperature from 700 to 900°C. With an increase in the synthesis temperature of HA from 700 to 1000°C, both surface roughness and porosity of the deposited coatings decreased. The degree of melting and

subsequent spreading of HA particles improved with increased synthesis temperature. The study found that the adhesion strength of the HA coating increased with an increase in the synthesis temperature from 700 to 900°C. The high degree of melting of HA-900 powders and the compatibility of HA-900 coating material with the Ti-alloy in terms of thermal properties helped to achieve the strongest coating adhesion with the substrate. With an increase in the synthesis temperature of HA from 700 to 900°C, the hardness of the coating increased significantly. However, the hardness of the HA-1000 coating decreased due to its relatively lower crystallinity. Under the ball-on-disc type wear tests, the HA coatings failed through both adhesive and brittle fracture failure mechanisms. The presence of unmelted cores led to a higher specific wear rate of HA-700 and HA-800 coatings. The HA-900 coating showed the maximum wear resistance property and was the hardest material.

Jagadeeshanayaka et al. (2023) examined the application of HA (CAPTAL-30) onto a Ti-6Al-4V substrate using high-velocity air fuel (HVOF) for orthopedic application. The researchers conducted various tests, including X-ray diffraction, Raman analysis, Fourier transform infrared spectroscopy, and $\sin^2\psi$ method, to assess the coating's characteristics, such as crystallinity index, phase analysis, residual stress, and tribological performance. The results showed that the coating maintained a crystallinity index of over 90%, with a crystallite size of 41.04 nm, a compressive residual stress of -229 ± 34.5 MPa, and a wear rate of 1.532×10^{-3} mm³/Nm. Furthermore, the study utilized computational fluid dynamics to analyze the in-flight particle characteristics of the HA particles (5 to 60 μm). The analysis revealed that 90% of the particles were deposited at velocities ranging from 700 to 1000 m/s and temperatures ranging from 900 to 1450 K, with a mean residence time of 2.1 ms. The study also found that particle oxidation during flight was minimized while particle impact deformation was maximized, resulting in severe plastic deformation and a crystalline, compressive residual stressed coating.

Ganvir et al. (2021) studied the influence of different HA feedstock characteristics on coating microstructure, phase content, and mechanical properties. Three different suspension-deposited HA coatings, namely suspension A (HA, 4-5 μm), suspension B (HA, 0.3-0.6 μm), and suspension C (HA+bioglass (20 wt%), 0.3-0.6 μm) were

investigated and compared with powder-deposited HA (Capital 30 SD, Plasma Biotol Ltd.) coating on a Ti6Al4V substrate. All four feedstocks were sprayed using an Axial III high-power plasma torch (Northwest Mettech Corp., Vancouver, Canada). Phase characterization has shown retention of hydroxyapatite phase and coating crystallinity in the deposited coatings. In contrast, the adhesion strength of the HA coating decreased from ~40 MPa to ~13 MPa when bioglass was added to the feedstock material. The highest crystallinity was obtained for the APS-HA powder (66 %) coating, followed by ASPS-A (43 %), ASPS-B (40 %), and ASPS-C (37 %). The coating hardness was highest for HA coating (334 ± 20) and lowest for suspension B and C coatings (87 ± 13 and 89 ± 20). The suspension's lower solid load content and lower mean solute particle size were beneficial in achieving porous, rougher, and well-adhering coatings.

Gkomoza et al. (2019) studied the surface, mechanical, and bioactivity properties of two HA powders coated with the APS technique onto 304 SS. The two types of HA powder used were commercial XPT-D-703 with spherical morphology (Sulzer Metco Company, $38.31 \mu\text{m}$) and nanostructured PYRO 4-HA powders ($<5 \mu\text{m}$), ball milled to nano size. The nano-sized particles agglomerated into final large particles ($57.08 \mu\text{m}$) with tear-like shaped morphology due to the sintering of grains. Four different coatings were produced by varying the process parameters of the APS technique, namely: Plasma energy (30-50 kW) and SOD (7-9 cm). The four coatings were coating 1 (XPT-D-703, P.E \uparrow , and SOD \downarrow), coating 2 (PYRO 4, P.E \uparrow , and SOD \downarrow), coating 3 (XPT-D-703, P.E \downarrow , and SOD \uparrow), and coating 4 (PYRO 4, P.E \downarrow , and SOD \uparrow). Surface roughness was measured using TR-200 portable surface roughness testers manufactured and developed by Time Group Inc. The thickness of the specimen was observed using Leica's image analysis (LAS image analysis). Two different techniques estimated the porosity of all the coatings: MIPAR Image Analysis, Optical Microscope (Leica DMILM), and Mercury (Hg) Porosimetry (Thermo Finnigan Pascal 440 Porosimeter). Morphological and microstructural analysis of the surfaces and the cross-sections of the coatings, respectively, was executed by using the Optical Microscope coupled with the LAS Image Analysis tool and Scanning Electron Microscope (SEM) (JEOL JSM-6390) equipped with an Energy dispersive (EDS) detector (EDS Oxford Instruments INCAx-sight Elemental Detector). X-ray diffraction, using Bruker D8 ADVANCE X-Ray

Diffractionmeter (Bruker Corporation, Massachusetts, USA) with a scanning range of 10-80, was employed for assessing the crystallinity and phase composition of the coatings. Wolpert and Wilson Vickers tester (Wolpert Wilson Instruments) with an imposed load of 300 gf was employed to determine the hardness of the coatings. Adhesion strength was tested using the Pull-Off Strength method via Elcometer 110 Pneumatic Adhesion Tester (Elcometer Instruments Ltd., Manchester, England) in accordance with the international standard ASTM 4541. An in-vitro bioactivity study was conducted by immersing the sample in a simulated body fluid (SBF) solution and observing it via an SEM apparatus and an optical microscope. The roughness (R_a , μm) value for the coating obtained from nanopowders (13.80 ± 1.25) was much higher compared to XPT-D-703 powders (9.72 ± 0.79). The Image Analysis of the coating showed average porosity percentages for Coatings 1 and 2 at 10% and 6.4%, respectively, for the type of specimen covered with XPT-D-703 powder and PYRO 4 powder. The porosity % for Coatings 3 and 4 was 20.3% and 34.8%, respectively, which was much higher due to lower energy and increased SOD, resulting in inadequate melting of the as-sprayed particles and the formation of pores throughout the coating material. The porosimeter software also calculated the average pore radius and total porosity percentage. Regarding Coatings 1 and 2, the estimated values were $1.084\mu\text{m}$ and 0.3856% and $0.178\mu\text{m}$ and 0.3824%, respectively. For Coating 3, the calculated values were $0.2923\mu\text{m}$ and 0.2447%, while for the PYRO 4 Coating 4, the corresponding calculated values were $0.2922\mu\text{m}$ and 0.6049%. The adhesion strength of the PYRO 4 coating (26.76 MPa) was as much as 0.85 times greater than the adhesion strength of the XPTD-703 coating (14.45 MPa). SEM images showed the formation of cracks on the coating-substrate interface of Coatings 1 and 2, indicating poor adhesion properties. Coating 3 and 4 showed enhanced adhesion due to mechanical interlocking, as any signs of cracks were absent. Microhardness values ranged between 231 and 278 HV 0.3 and were practically very close for all the coatings. Coating 4 was determined to be fairly crystalline compared to others, as the highest intensity peak on the relative spectra almost reaches 900 counts; this is near to HA powder counts, i.e., 940. Optical Microscope revealed a thin layer on top of the hydroxyapatite coatings on all four coatings. The overall coating thickness of the samples decreased, except for Coating 4, in which it increased. In addition, nanosized apatite particle agglomerations with a

diameter of $< 2 \mu\text{m}$ are formed on the surface of the coatings.

Mardali et al. (2019) investigated the relationship between the microstructure and phase composition of HA coating applied to an Mg-based alloy through HVOF, and the amount of hydrogen released during corrosion in an SBF solution was examined. HA powder was created using high-energy planetary milling with bovine bone and a ball-to-powder ratio of 10:1 for 8 hours. The phase composition of the coatings was determined using XRD, while FESEM was used to explore the coatings' powder particle morphology, surface topography, and cross-sections. An EDS analyzer also characterized the HA coatings' elemental distribution map. After undergoing immersion tests in an SBF solution for 30 hours, the coated samples were analyzed to investigate the hydrogen evolution reaction. The XRD results showed a high degree of crystallinity due to the nature of deposition via HVOF. The thickness of the sprayed layer ranged from 11.9 to 29 μm , and the surface morphology displayed flattened splats and partially or semi-melted particles. Anodized and anodized plus HA-coated samples exhibited uniform corrosion behavior for up to 10 hours, while the amount of released hydrogen from anodized samples was much higher than that for anodized and HA-coated samples. Thus, it was concluded that the secondary HA coating had a barrier effect on the corrosion resistance of the Mg alloy. The pH of SBF after 30 days of immersion for the bare alloy, anodized, and anodized plus HA-coated samples were 8.5, 7.8, and 7.6, respectively. The hydrogen evolution rate decreased after anodizing and applying HA, going from 45.8 per $\text{cm}^2 \text{ ml}$ to about 7.38 per $\text{cm}^2 \text{ ml}$ after 29 hours of immersion. Finally, nanostructured HA was successfully deposited, which can enhance the biomimetic surface by creating active sites.

Kaur et al. (2018) studied samples' surface characteristics, microstructure, and in-vitro corrosion behavior in Hank's solution. They used the high-velocity flame spray to deposit HA (30 microns) coatings and HA/TiO₂ coating onto a steel plate. TiO₂ (5-22 microns) was used as a bond coat, while HA was the top coat in HA/TiO₂ coating. They analyzed the specimens' morphology and feedstock powders using XRD and SEM coupled with EDS. They determined the surface roughness using a roughness tester at a cutoff length of 0.8 mm and conducted micro-hardness tests using a Wilson micro hardness apparatus. After immersion, XRD showed that the HA-coated steel had HA

as the major peak, along with tricalcium phosphate (TCP) and calcium hydrogen phosphate hydrate. The HA/TiO₂ coating showed major peaks of HA along with minor peaks of TCP and calcium phosphate hydrate. Even after immersion in SBF (Hank's solution), no cracks were found on the surface of the as-sprayed samples. EDS mapping observations supported the claim that both fully retained their adherence and identity. The average coating thickness of the HA coating was 181 μm, and for HA/TiO₂ coating, it was 230 μm. The surface roughness of HA was lower (7.37 μm) than the coating with a bond coat (9.35 μm). The increase in roughness may be due to the presence of TiO₂. The flame-sprayed bond coating exhibited lesser porosity and higher microhardness and surface roughness than the HA coating. The average microhardness of the HA coating was found to be 254 HV, and that of the HA/TiO₂ coating was found to be 280 HV. HA/TiO₂ coating provided the maximum resistance to electrochemical corrosion testing due to the formation of TiO₂.

Singh et al. (2014) conducted a comprehensive study on the effects of different particle sizes of HA coatings on the biocompatibility and bond strength of 316L SS and Ti-6Al-4V specimens. The coatings were examined using X-ray diffractometry, SEM, EDS, and X-ray mapping techniques. The coatings with 10 μm particle size (HA-A) were amorphous. In contrast, those with. In comparison, that size (HA-B) had crystalline HA with minor tetra-calcium phosphate and tricalcium phosphate phases. The bond strength of the HA-A and HA-B coatings was significantly higher than other thermal spray HA coating techniques reported in the literature. The HA-B coatings exhibited higher surface roughness than the HA-A coating. Moreover, *in vitro*, biocompatibility studies revealed that the HA-B-coated specimens had good biocompatibility with a human osteosarcoma cell line KHOSNP (R-970-5). The study concluded that the particle size of HA powders significantly affects the phase composition, microstructure, roughness, and biocompatibility of deposited coatings. The HA-B coatings were found to be more for biomedical applications than HA-A coatings.

Gadow et al. (2010) conducted a study to compare the mechanical and morphological properties of hydroxyapatite (HA) coatings on titanium-grade 2 plates. The coatings were obtained through three different techniques: atmospheric plasma spraying (APS), high-velocity oxygen fuel (HVOF) spraying, and high-velocity suspension flame

spraying (HVSFS). Two types of HA suspension were used: nano-HA in water and in diethylene glycol dispersion. The APS and HVOF experiments were carried out in a 2-level fractional factorial design, while a full factorial experiment was used for the HVSFS experiments. The researchers used scanning electron microscopy to determine powder size and coating thickness, a stylus profilometer to measure surface roughness, and digital image analysis to measure coating porosity. X-ray diffraction patterns were used to identify the phases of the raw powder and coatings. The researchers found that coatings deposited using diethylene glycol-based suspensions were denser than those deposited using water-based suspensions. HVOF coatings had un-melted submicron-sized particles and well-flattened lamellae. In contrast, APS coatings had a lower amount of un-melted submicron-sized particles and well-flattened lamellae due to the high temperature of the plasma jet. The HVOF coatings were smoother than the APS coatings due to the higher kinetic energy of the particles. The roughness of the HVSFS-HA coatings was significantly higher than that of the HVOF and APS coatings due to fine re-solidified spherical droplets and un-melted agglomerates concentrated around the asperities of the coating surface. The Vickers hardness of the HVOF coatings was higher than that of the APS coatings. The highest bond strength was measured for HVSFS and APS-HA coatings, with HVOF and APS coatings adhesively failing at the substrate interface and coating. The HVSFS coatings showed a cohesive failure mechanism. The researchers found that decreasing the spray distance and increasing the fuel and oxygen flow rate led to higher bond strength for the HVOF coatings. The deposition efficiency was higher for the APS and HVOF processes than for the HVSFS process. The deposition efficiency for the HVSFS process ranged between 11% and 26%, while for the APS process, it was between 52% and 62%, and for the HVOF process, it varied between 40% and 80%.

Hasan and Stokes (2011) sought to enhance the crystallinity and purity of HVOF-sprayed HA coatings through process parameter optimization. They used a feedstock powder HA (Plasma Biotal CAPITAL 60-1) with a size of 45 μm . The experiment used a two-level factorial design for five process parameters: Oxygen flow meter reading, Propylene flow meter reading, Air flow meter reading, Spray distance, and Powder feed rate. The minimum and maximum possible settings for each parameter were tested in

32 experiments based on DOE. The analysis of variance (ANOVA) was used to evaluate the DOE model. SEM was used to analyze the microstructure of the HA and coating, while XRD peaks were used to determine the coating's crystallinity (Rutland Method) and purity. The results revealed that all samples showed crystalline peaks and traces of an amorphous phase in the XRD pattern. The coating's crystallinity was highest at 93.81%, and the coating's purity was 99.09% when Oxygen was set to 45 FMR, Propylene was set to 40 FMR, Air was set to 50 FMR, SOD was set to 150 mm, and PFR was set to 45 g/min. The spray distance (SD) had the most significant effect on coating crystallinity.

Despite the clinical success of being brittle, synthetic HA exhibits inferior mechanical and tribological properties as compared to bone, especially showing inferior surface mechanical properties such as low fracture toughness, bending strength, bonding strength, tensile strength, and wear resistance. HA-modified biomaterial surfaces are also susceptible to bacterial colonization. Hence, researchers in this domain would face many challenges and opportunities while manufacturing HA composite coatings to meet desired properties and overcome the gaps in HA coatings.

2.2.2 HA reinforced alumina coatings

Alumina is considered a bio-inert material, but this is not entirely true, as no material is entirely immune to reactions with body fluids. Hench (1998) considered alumina to be a nearly bio-inert material with excellent mechanical properties like high strength, low friction coefficient, shallow surface roughness, resistance to dynamic impact fatigue, sub-critical crack growth, flexural bond compatibility, high hardness, corrosion, and wear resistance. Al_2O_3 is used in the manufacturing of biomaterials for hip and knee replacements, corneal replacements, bone screws, segmental bone replacements, alveolar ridge (jaw bone), ossicular (middle ear) replacement, maxillofacial reconstruction, blades, and screws (Viswanath and Ravishankar 2006). Mittal et al. (2013) plasma-sprayed 0, 10, 20, and 30 wt% Al_2O_3 / HA composite powders on a titanium substrate. Increasing the alumina content enhanced surface roughness, porosity, microhardness, tensile strength, and wear resistance. The tensile strength of HA coatings (28.4 MPa) increased with increasing alumina content as

follows: 10 wt% Al₂O₃/HA (32.7 MPa), 20 wt% Al₂O₃/HA (38.1 MPa), and 30 wt% Al₂O₃/HA (43.6 MPa). Tercero et al. (2009) produced plasma-spray 0, 20 wt% Al₂O₃/HA composite powders on a titanium substrate with 158% fracture toughness improvement (from 0.71 ± 0.19 MPa m^{1/2} to 1.83 ± 0.11 MPa m^{1/2} for 0 to 20 wt% Al₂O₃/HA coatings, respectively). Nearly 30 times higher thermal conductivity of alumina (36.16 W/m K) compared to HA (0.7 W/m K) allowed a lower cooling rate for HA splats. It reduced the CTE mismatch between the substrate and the coating. Also, alumina provided a lubricating effect to the HA matrix, leading to higher wear resistance. However, corrosion resistance was compromised by increasing the alumina content due to increased porosity.

Widantha et al. (2021) investigated the impact of HA and HA/alumina (15wt%) coatings on the corrosion and dissolution behavior of NiTi substrates in Phosphate Buffer Saline (PBS) and Ringer's lactate solutions. The researchers also examined these coatings' microstructure, phases, and hardness. During the study, the team used HA powder synthesized via the biogenic method and deposited it on NiTi substrates using the HVOF spray technique (TECKNOTHERM HVOF 2007, Hipojet-2700 spray gun). The synthesized HA had a low Ca/P ratio of 1.52 and an irregular porous structure. The results of the electrochemical tests showed that both coatings significantly improved the corrosion resistance of the NiTi substrates, as demonstrated by the Tafel polarization curves. After 21 days of immersion in both solutions, the ICP-MS analysis revealed a low dissolved nickel amount, which supported the findings. The levels of nickel in the solutions from all samples, including the bared substrate or coated samples, were below the maximum limit for human body allergies. The study's immersion testing demonstrated that the HA and HA/alumina layers acted as a barrier, maintaining their morphology in PBS solution but undergoing slight changes in Ringers.

To summarize, adding alumina may enhance the mechanical qualities of HA coatings, except for flexural strength and toughness. However, it is essential to note that alumina is not entirely resistant to the release of toxic ions in the body environment, and the potential for fatigued failure may arise in Al₂O₃ implants when used for extended periods.

2.3 Carbon nanotubes in medical implants

Carbon nanotubes (CNTs) are widely regarded as super-nanomaterials with remarkable properties that make them ideal for various applications. CNTs possess excellent mechanical properties and can withstand high strain, displaying superplasticity (Figure 2.1) despite their sp^2 bonding (Huang et al. 2006). This superplasticity is due to kink nucleation and movement and atomic movement to heal vacancies. As a result, CNTs are suitable as reinforcement for creating nanocomposites with improved mechanical properties. CNTs also have a cylindrical structure with an outer surface that interacts with host materials in biological environments. Due to their unique physical, chemical, mechanical, and biological characteristics, CNTs have been used in medicine, diagnostics, and other applications. In comparison to HA, CNTs have superior elastic modulus (0.8–1.2 TPa), tensile strength (11–63 GPa), and thermal conductivity (3000–5000 W/ m K). CNT/HA composites have been shown to improve fracture toughness and indentation hardness, aid human osteoblast cell proliferation, and allow apatite to precipitate and mineralize in composite coatings (Tercero et al. 2009). Thermally sprayed carbon nanotubes have sparked much attention in the scientific community over the last decade. In a study by (Facca et al. 2011; Lahiri et al. 2011), fracture toughness ($3 \text{ MPa m}^{1/2}$), elastic modulus ($88 \pm 10 \text{ GPa}$), and hardness ($2.43 \pm 0.02 \text{ GPa}$) of the 4.0 wt% MWCNT/HA composite coatings were reported, showing significant improvement as compared to unreinforced HA coating with $0.64 \text{ MPa m}^{1/2}$, $51 \pm 10 \text{ GPa}$, and $1.30 \pm 0.01 \text{ GPa}$, respectively. Balani et al. (2007b) and Lahiri et al. (2011) investigated the role of CNTs in HA and reported the increase in mechanical and biocompatibility of the coatings. The size of the HA particles appears to significantly impact the mechanical and biological characteristics of thermally sprayed composite coatings. Another research group, Mohajernia et al. (2018), plasma-sprayed the CNT/HA composite coating on the AZ31 Mg alloy substrate. The study indicated that the stress corrosion cracking ability decreased from 26.8% (HA coating) to 9.8% (CNT/HA composite coating). Also, the 4 wt% CNT/HA composite coating's crystallinity and fracture toughness were 71.1% and $2.13 \pm 0.29 \text{ MPa m}^{1/2}$, respectively, showing a marked increase as compared to those of the pure HA coating, 55.4%, and $0.91 \pm 0.16 \text{ MPa m}^{1/2}$. The increased fracture toughness was attributed to the CNT

bridging HA splats, and the number of secondary phases such as CaO, TCP, and TTCP reduced in the CNT/HA composite coating. Osorio et al. (2011) who have reported a maximum fracture toughness of $2.47 \text{ MPa m}^{1/2}$ by adding 0.5 wt.% CNTs in the HA matrix, while Li et al. (2007) have found an increase in the fracture toughness from 0.32 to $2.40 \text{ MPa m}^{1/2}$ with the addition of 3 wt—% CNTs. Zhan et al. (2003) added 10% single-walled CNTs to a nano- Al_2O_3 sample. The hardness of the composites was 16.1 GPa after 3 min of discharge plasma sintering at $1500 \text{ }^\circ\text{C}$. Zanello et al. (2006) showed osteoblasts can grow and proliferate on CNTs. Pandey et al. (2018b) studied the bacterial and tribological properties of grade-5 titanium alloy coated by HA/CNT/Ceria/Ag composite. The hardness, fracture toughness, elastic modulus, and wear resistance of the coated Ti improved significantly. They also found that the HA/CNT/Ceria/Ag composite coating was cytocompatible.

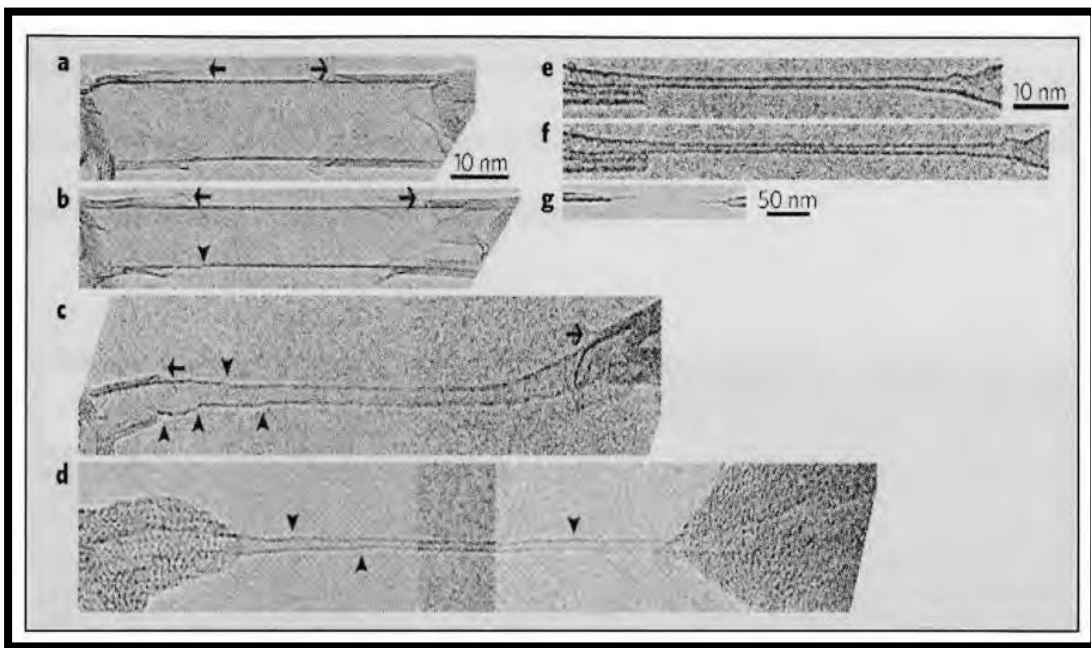


Figure 2.1 In-situ tensile elongation of single-walled carbon nanotubes (Huang et al. 2006).

Although carbon nanotubes (CNTs) have many advantages, researchers using CNT-reinforced coatings face two significant challenges during processing. The first challenge is that CNTs tend to agglomerate because of their high surface energy, which causes inhomogeneous mixing with the matrix phase. This results in poor dispersion centers and stress concentration levels that degrade the coating's properties.

Additionally, inhomogeneous dispersion weakens the anchoring between splats, limiting the capacity for load transfer. The second challenge is the decomposition of CNTs during high-temperature processing, resulting in the presence of oxidized CNTs that weaken the ensemble and lead to a coating with poor mechanical properties.

Mukherjee et al. (2014) have developed a simple shear mixing technique for producing HA-CNT nano-composite and investigated the effect of reinforcement on the physical, mechanical, in-vitro bioactivity, and biological properties of the HA. HA was prepared via wet chemical method using ortho-phosphoric acid (H_3PO_4) and calcium hydroxide ($Ca(OH)_2$) (S.D. Fine-ChemLtd., India) as reagents. MWCNTs (>95% purity, 10–30 nm diameter, and 1-10 μm average length) were procured from Nanoshel LLC, USA. HA and CNTs (0.5-5%) with a ball-to-powder weight ratio of 10:1 were mixed counterclockwise in a high-energy planetary ball mill (Fritsche Pulverisette 5, Germany) at 300 rpm for 5 h in acetone. Pellet samples (12 mm diameter x 4 mm thick) were made from sieved powder in a uniaxial press (PEECO, India) at 150MPa for 2min. The composite then went under the sintering process in two stages: first, temperature increased to 700 °C at a heating rate of 3 °C/min, and then again, temperature was increased to 1250 °C at a heating rate of 6 °C/min at an argon atmosphere. The apparent porosity (A.P.) and bulk density (B.D.) of the sintered specimens were estimated using Archimedes' water displacement method. X-ray diffraction (XRD, Ultima III Rigaku, Japan) and Fourier transform infrared spectroscopy (FTIR, IR Prestige 21, 200VCE, Shimadzu, Japan) were used to characterize the prepared composites. The microstructure and morphology of the nanocomposites were studied using field emission scanning electron microscopy (FESEM, Hitachi, S4800, Japan) and high-resolution transmission electron microscopy (HRTEM, JEOL, JEM 2100, Japan). The hardness and fracture toughness (K_{IC}) of the polished sintered samples (< 0.02 μm Ra) were evaluated using an automated Vickers hardness testing machine (LECO, LV-700AT, MI) via the indentation method (ASTMC1327). The flexural strength of the nanocomposites was evaluated using a universal testing machine (Instron4204) by three-point bending following ASTM C 1674, and fractography images were obtained using an FESEM. The hemocompatibility of the nanocomposite samples was studied as per ASTM 756 to determine the cytotoxicity effect of the composites. The in-vitro

bioactivity of the composites was investigated by immersing disc specimens in simulated body fluid (SBF). The findings revealed that the composites' bulk density (B.D.) initially increased with the addition of up to 1% CNT but then decreased with the addition of up to 5% CNT. Conversely, the composites exhibited a contrasting trend in apparent density (A.P.). The composites containing 5% CNTs primarily contained uniformly distributed nanosized particles and exhibited good density and ~9% porosity. XRD results measured no new peaks due to the addition of different CNT concentrations. FESEM microstructure showed fine-hair-like CNTs attached to the HA grains. The nanocomposites were observed to possess a porous microstructure, which is highly favorable for cellular growth. For the composite containing 5% CNTs, the CNT chains were observed to occur in an agglomerated state (in bundles) along the boundaries of the HA grain. The 1% CNT composite result showed 2% porosity and 2.93g/c.c B.D, and exhibited a substantial improvement in toughness (120%) without significantly compromising its hardness (2.8GPa) and flexural strength (26MPa). This also exhibited lower internal crystal strain (0.14) and an average crystallite size of 102 nm. This 1% CNTs showed enhanced apatite formation when exposed to SBF for up to 24 weeks, with 1.15% hemolysis; hence, it was highly hemocompatible per ASTM-F756 standards.

Balani et al. (2007a) conducted a study with alumina-2-8 wt% CNT powders to examine how the powder preparation methodology affected CNT dispersion and the coatings' mechanical properties. They synthesized the powder feedstock using simple mechanical blending in a ball mill and spray drying. They observed that CNT agglomerates were found to separate along the splat boundaries in the coating produced from the blended powder. Meanwhile, homogeneous dispersion in the spray-dried powders improved CNT anchoring across the neighboring splats, ensuring superior mechanical properties. The coating obtained from the spray-dried powder had almost twice the indentation fracture toughness of the other coating.

2.4 Functionalization and dispersion of CNT

One limitation of CNT is its poor dispersion characteristic. The nanotubes tend to form aggregates due to Van der Waal's force of attraction. Better dispersion of CNTs in the

matrix can be achieved by dispersing them in an appropriate medium to form a colloidal solution. For this purpose, it is necessary to functionalize the CNT by adding suitable functional groups such as OH or COOH on the inert wall of pristine CNT. There are several methods for functionalization, one of which involves keeping pristine CNT in a mixture of H₂SO₄ and HNO₃ (3:1 by volume ratio) at 40° C for 4 hours to attach a COOH functional group on the surface (Jambagi et al. 2015).

When mixed with an organic solvent like acetone, this functionalized CNT does not settle to the bottom of the container. It forms a stable colloid where CNTs remain suspended in the liquid, owing to a repulsive electrostatic force among the suspended elements. Unlike its dry, agglomerated, and pristine counterpart, this CNT, already dispersed in a colloid, can be easily dispersed in a ceramic or any other powder. Hence, functionalized CNTs are used in ceramic matrices as reinforcement. Several researchers have proposed that well-dispersed functionalized CNTs in the matrix can be achieved if the constituents, CNTs, and the powder are processed in the colloidal state (Jiang et al. 2011).

The stability of a dispersed phase in a colloidal suspension is characterized by its zeta potential. The Zeta potential of a solid particle suspended in a medium is defined as the potential difference between the dispersion medium and the electrical double layer of ions that are formed around the said particle. It is a function of surface charge. Higher zeta potential values (either positive or negative) imply a higher stability of the suspension in the colloid (Sun and Gao 2003).

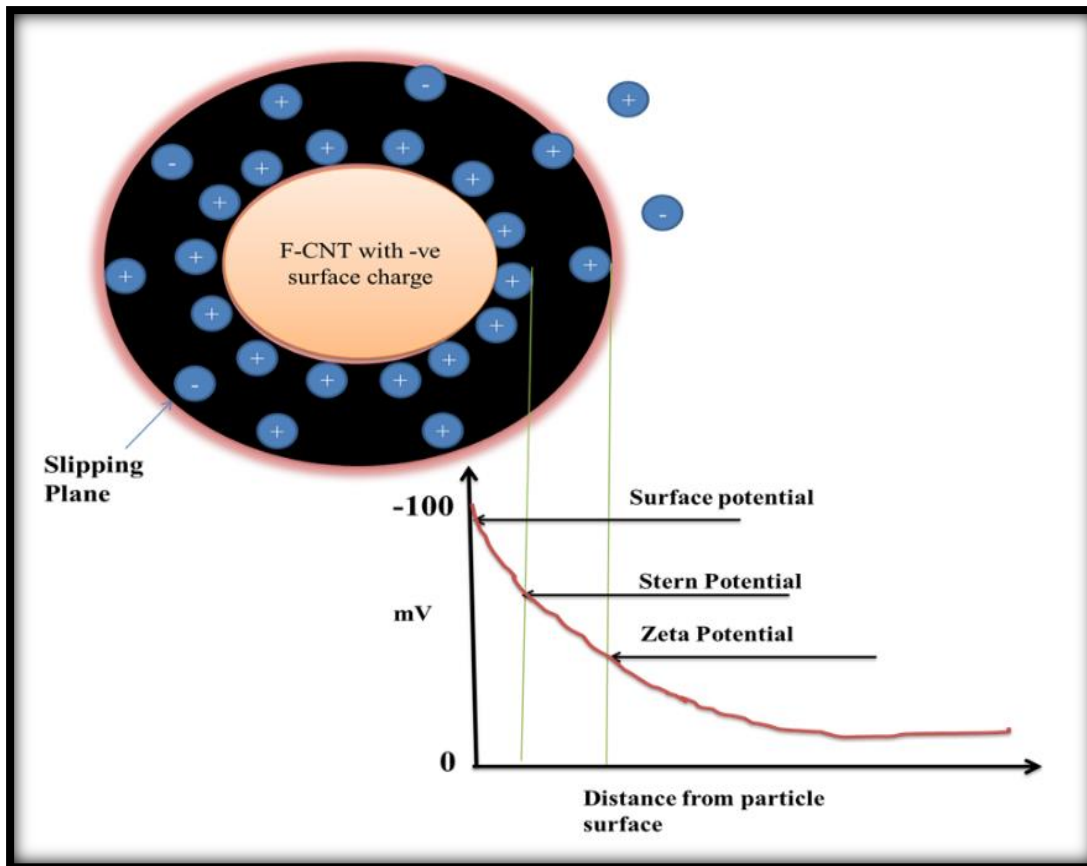


Figure 2.2 Schematic representation of zeta potential (Tengku Mohd et al. 2016).

Heterocoagulation is a technique where an intimate homogenized mixture of ceramic and CNT is achieved using colloidal processing. The process involves three steps. First, the matrix phase, i.e., the ceramic powder, is well-dispersed in water, and its pH is adjusted by adding an alkali or acid to get a zeta potential greater than ± 30 mV. Next, functionalized CNTs are dispersed in an appropriate surfactant (anionic or cationic) to get a zeta potential of the same order. However, the polarity of the zeta potential of the two components (powder and CNT) should be opposite. Finally, the matrix powder suspension is added to the CNT suspension slowly and dropwise. Owing to the Brownian movement of solute particles, they collide and adhere to each other by electrostatic attraction, and the average surface charge of the particles in the resulting suspension assumes a value intermediate between the zeta potential of the component colloids before mixing and the composite particles, i.e., CNT attached on matrix particles. The zeta potential of composite particles reached zero and settled down to the bottom of the container (Jambagi et al. 2015).

It may be noted that surfactants are organic compounds that reduce the interfacial tension between a liquid and a solid and thus improve the wettability of the solid surface by the liquid. These molecules comprise a long hydrocarbon chain terminated in a polar (cationic or anionic) or sometimes neutral functional group. Sodium dodecyl sulfate (SDS) and Cetyl triammonium bromide (CTAB) are typical anionic and cationic surfactants. The physical properties of these two surfactants are shown in Table 2.1. The effectiveness of a surfactant depends on its concentration in the liquid medium in which it is dispersed. Beyond a concentration level, the surfactant molecules form a characteristic agglomerated structure known as micelle. The corresponding concentration is known as Critical Micelle Concentration (CMC). Beyond CMC, the wettability of surfactant molecules onto the surface of solid particles increases considerably, owing to a steep decrease in the surface tension (Chibowski et al. 2007).

Table 2.1 Physiochemical properties of the surfactants (Lin 2004).

Surfactant	Empirical formula	CMC (mM) in water at 25°C	Type	Molar mass (g/mol)	Melting point (°C)	Density (g/cm ³)
CTAB	C ₁₉ H ₄₂ BrN	0.92-1	Cationic	364.45	248-251	1
SDS	NaC ₁₂ H ₂₅ SO ₄	8.2	Anionic	288.38	184-187	1.01

Very few authors have reported using the heterocoagulation technique in preparing composite powder; some are listed below.

Sun et al. (2002) investigated the role of the heterocoagulation process in creating a homogeneous mixture of 1 wt% carbon nanotube (CNT) in nano-sized alumina particles with an average particle size of 30 nm. CNT was treated with NH₃ for functionalization and then suspended in polyethyleneimine (PEI) to make its zeta potential positive (40 mV at pH=8). Nano-sized alumina particles were suspended in deionized water along with Polyacrylic acid (PAA) to give it a negative zeta potential (-45mV at pH=9.5). This alumina suspension was added to the CNT suspension

dropwise, and during mixing, the species of opposite charges got attached and lost charges, leading to heterocoagulation. The final composite powder was used for the spark plasma sintering (SPS) process. The indentation fracture toughness of the composite increased from 3.7 to 4.9 MPa m^{1/2}, attributed to the CNT bridging between alumina particles.

A similar powder processing technique was described for BaTiO₃ (with 1wt% CNT) and TiN (with 5 wt% CNT) composite powders. The nanocomposites were synthesized by spark plasma sintering technique, and improvements in indentation fracture toughness by factors of 2.4 and 1.6 were reported for BaTiO₃/CNT and TiN/CNT composites, respectively (Gao et al. 2006).

Another study investigated the role of the heterocoagulation process while forming a homogeneous mixture of 1-2wt% CNT with agglomerated alumina, crushed alumina, and crushed titania. The mixtures were prepared by ball milling under dry and wet (acetone) conditions and compared for degree of dispersion and flowability. For heterocoagulation, CNT was treated with HNO₃ and H₂SO₄ (in a 1:3 volume ratio) for functionalization. CNT was given a positive charge using CTAB, and SDS provided a negative charge to the alumina particles. The heterocoagulated composites showed good flowability and an excellent degree of dispersion for CNT compared to other powder mixing methods (Jambagi et al. 2015).

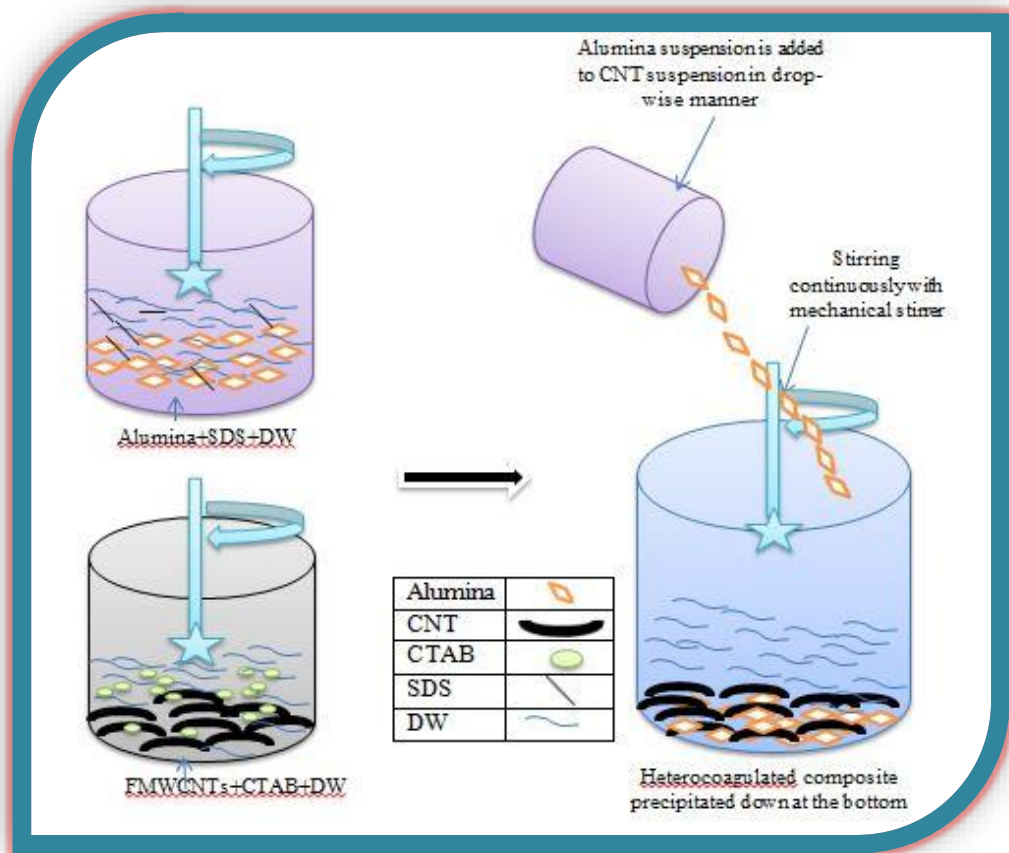


Figure 2.3 Heterocoagulation of Alumina and CNT particles with corresponding surfactant.

2.5 Mechanical properties of the coatings

HA coatings are widely used in orthopedic and dental implants due to their excellent biocompatibility and osteoconductive properties. The mechanical properties of HA coatings play a crucial role in determining their performance as an implant material. The mechanical properties of HA coatings depend on various factors, such as the deposition technique, the microstructure of the coating, and the composition of the coating material. HA coatings possess excellent biocompatibility, but their mechanical properties are inferior to alumina ones. Alumina coatings have high hardness and wear resistance (Rattan et al. 2022) but low bioactivity. CNTs, on the other hand, have excellent mechanical properties and biocompatibility, making them an ideal candidate for reinforcing HA and alumina coatings (Guan et al. 2019). The addition of CNTs has been shown to significantly improve the mechanical properties of the HA, including

hardness, adhesion strength, and wear resistance, making them suitable for use in load-bearing applications. For instance, a study found that adding CNTs to HA coatings improved their mechanical properties, such as hardness and wear resistance. Another study by Mukherjee et al. (2014) also reported that the incorporation of CNTs in HA coatings resulted in an improvement in their toughness (120%) without significantly compromising their hardness (2.8 GPa) and flexural strength (26 MPa). Various researchers observed the drastic change in the coating properties of HA due to the effect of reinforcements and the use of different coating techniques, which are discussed below.

Saber-Samandari et al. (2018) investigated the impact of preheating and annealing processes on the micromechanical properties of oxy-acetylene-fueled flame-sprayed HA coatings on fine polished CP-Ti substrate. They used HA powder with particle size 20-40 μm , which was passed through a powder feeder and then into a flame spray torch with air as the carrier gas at a flow rate of 50 g/min and SOD as 15 cm onto pre-heated (300°C) substrate. Four different samples were prepared to study the effect of heat treatment: S1 (Room Temp), S2 (Room Temp, with annealing at 700°C), S3 (Pre-heating at 300°C), and S4 (Pre-heating with annealing). The nanoindentation tests were performed using a nano-based indentation system (Ultra Micro-Indentation System, UMIS-2000, CSIRO, Australia) with a calibrated Berkovich indenter (three-sided pyramidal). The elastic modulus and hardness were determined using UMIS software based on the Oliver-Pharr method. The XRD profiles of coated S1 and S3 samples illustrated the presence of an amorphous phase and the decomposed components such as α -TCP, TTCP, and calcium oxide (CaO). However, for annealed samples S2 and S4, the amorphous phase and decomposed components for both coatings were transformed into crystalline HA. The SEM image of before and after annealing the coated sample displayed micro-cracks and open pores due to the high percentage of partially melted/unmelted particles due to the low temperature and high particle velocity. For S1, the size of the pores is around 0.9-2.5 μm . In the case of S2, larger open pores (approximately 11.4 μm) were also formed on different splats. A partially melted shape of the particle and open pores in the splats are also observed for the 300°C preheated substrate before (S3) and after (S4) the heat treatment at 700°C, where the size of the

pores reached 0.2-1.4 and 0.4-7.5 μm , respectively. The HA coatings exhibited a mean thickness of around 78.8, 82.8, 70.8, and 62.8 μm for S1, S2, S3, and S4, respectively. The Ra and Rt values for S1, S2, S3, and S4 are 22.5 ± 1.1 and 70.0 ± 3.3 μm , 17.5 ± 0.8 and 72.0 ± 3.6 μm , 5.0 ± 0.2 and 42.0 ± 2.1 μm , and 2.5 ± 0.1 and 52.5 ± 2.6 μm , respectively. The coatings on preheated substrates showed lower roughness than those at room temperature, which can be attributed to the increased spreading of melted particles in the coatings. The 300°C preheated sample after annealing at 700°C has a maximum elastic modulus of 108.1 ± 6 GPa and hardness of 5.97 ± 0.3 GPa, almost 3% lower and 171% higher than the bare substrate, respectively. The annealing process at 750°C is favorable for enhancing adhesive strength and shear strength, as well as the fracture toughness of HA coatings.

Khanal et al. (2016) have investigated the effect of reinforcements (carboxyl functionalized single-walled carbon nanotubes (CfSWCNTs) and nylon) in improving the fracture toughness of HA. They prepared a series of HA samples (S1-S8) with varying CfSWCNT concentrations (0 to 1.5 wt.%) with and without nylon addition. The sample solutions were quenched on a steel plate, and part was poured into a mold to make a block. The samples were characterized for phase determination and microstructure using XRD and TEM equipped with EDS. A three-point bending test was performed to measure the fracture toughness of the samples using a VC 750 and Zwick/Roell. The XRD patterns for samples S1-S4 (HA, 0.5-1.5% CNT) showed a well-crystallized material that becomes less crystallized as the CfSWCNT content increases. The diffraction peaks broadened after adding nylon, indicating less crystallized material. The SEM image for sample S1 showed homogeneity in particle shape and size, which was reduced for samples S2 and S4 due to CNT addition. Sample S3 (1% CNT) displayed the most uniform distribution of CNTs in the HA matrix. SEM images from sample S7 (1 wt.% CfSWCNTs and nylon) displayed an amorphous nylon and a nonhomogeneous crystallite distribution over the nylon surface. The highest fracture toughness ($3.6 \pm 0.3 \text{ m}^{1/2}$) was found for sample S7, which contains 1 wt: % CfSWCNTs and nylon. The addition of nylon was critical in achieving K_{1c} values that are comparable to those of cortical bone. It was found that the increase of the CfSWCNT content above 1 wt.% results in a decrease in the fracture toughness and

work of fracture, loss of crystallinity, and formation of secondary phases.

Gopi et al. (2013) have investigated and studied the surface characteristics, microstructure, mechanical properties, and in-vitro assessment of HA-CNT coating on titanium substrate using the electro-deposition coating technique. The pure titanium samples (99.99%) of the size 10 *10*3 mm were embedded in epoxy resin, leaving an area of 1 cm² for exposure to the solution. The electrolyte for deposition was prepared by mixing a solution containing 0.042 mol/L of Ca (NO₃)₂.4H₂O and 0.025 mol/L of K₂HPO₄ under constant stirring for two hr. The different concentrations (0–2 wt.%) of the functionalized CNTs were gradually added to the solution. The pH was maintained at 4.7 using NaOH or HCl. The electro-deposition was performed in an individual cell using a three-electrode configuration. Titanium serves as a cathode, and platinum electrode acts as an anode. A saturated calomel electrode (SCE) was used as the reference electrode. The composite coatings' surface morphology and elemental composition were examined using SEM (JEOL JSM-6400, Japan) equipped with EDX. The Fourier transform infrared spectroscopy of the samples was recorded using Nicolet 380 FTIR Spectrometer (Perkin Elmer, USA) over the frequency range from 4000 cm⁻¹ to 400 cm⁻¹ with several 32 scans and spectral resolution of 4 cm⁻¹. The phase composition and crystallinity of the composite coatings were identified by XRD (Bruker D8 advance diffractometer), Cu K α incident radiation, tube voltage of 40 kV, and a current of 30 mA with scanning angle ranging from 20° to 60°, at a scan rate (2 θ) of 0.02°. The electrochemical measurements such as open circuit potential (OCP), Potentio-Dynamic Polarisation (Ecor) and Electrochemical Impedance Spectroscopic (EIS) studies were carried out to access the anticorrosive characteristics of the coatings. The standard scratch tester and indentation evaluated the adhesion strength between the composite coating and substrate using a Universal Instron Mechanical Testing system (Instron 5565, Instron Co.) according to ASTM F 1044-05 standard. Nanoindentation tests were performed by MTS Nanoindenter XP (MTS Corporation, nanoinstruments innovation center, TN), comprising a three-sided pyramid (Berkovich) diamond indenter. For in-vitro studies, mouse fibroblasts (L929) cells (National Centre for Cell Science (NCCS), Pune, India) cultured in essential media (Hi-Media Laboratories) supplemented with 10% Fetal Bovine Serum (FBS), Streptomycin (100 U/mL) and

Penicillin (100 U/mL) (Cistron laboratories) were used. MTT assay was performed to determine cell viability. The SEM morphology of 1 wt% CNT showed slanting and perpendicular flakes covering the entire titanium surface. For 2 wt% CNTs, this flakes-like structure grows outwardly and disorderly, forming a macroporous structure over the surface that covers the way for the detachment of the composite coating from the titanium surface. The EDX spectrum for the CNTs–HA coating indicates the presence of C, O, P, and Ca. This result confirms the existence of CNTs and Ca/P (HA) on the surface of titanium. The OCP value of 0 wt.% CNTs–HA-coated titanium was measured as -0.44 ± 0.005 V vs. SCE, whereas for 0.1 and 1 wt.% CNTs coated titanium, the values were found to be (-0.41 ± 0.004) and (-0.17 ± 0.007) V vs. SCE, respectively. For 2 wt. %, the OCP value becomes (-0.19 ± 0.003) V vs. SCE, which is more negative than 1 wt. % CNTs. This immediate shift of potential for 1wt%-CNT towards the noble direction indicates the improved corrosion-protective nature of the coating. The E_{corr} values for 0.1 wt. % CNTs and 1 wt. % CNTs coated samples were found to be -0.02 ± 0.007 and 0.02 ± 0.003 V vs. SCE, respectively. A more positive shift in OCP value was observed for the 1 wt% CNTs coated titanium with respect to 0 wt. % CNTs and uncoated titanium. A negative shift in the OCP value was observed for 2wt. %CNTs. This may lead to coating detachment over the surface of titanium, thereby indicating the lowest corrosion performance of the composite coating. The lowest i_{corr} value for 1 wt. % CNTs ($0.05 \pm 0.006 \mu\text{A}/\text{cm}^2$) represent the well-dispersed structure of CNTs and the coherence between CNTs and HA in the composite. The adhesion strength showed an appreciable improvement when the amount of CNTs in the HA composite was enhanced to 1wt. % (24.2 ± 0.8 MPa) is even higher than the adhesion strength of 2wt. % CNTs (22.4 ± 0.6 MPa) composite coating. For 2 wt.% CNTs, the cohesive strength is slightly decreased due to the crystalline nature of the composite coating, which may lead to the detachment of the coating over the titanium substrate. CNTs–HAP composite depicts excellent anti-corrosion resistance in SBF solution. The highest hardness (7.22 ± 0.52 GPa) and elastic modulus (130.50 ± 5.24 MPa) value was measured for the 2 wt. % of the CNTs composite. The 0 wt.% CNTs coated sample showed 46.6% viability, while the viability of 72.5% was observed for 1 wt—% CNTs, indicating the less/non-toxic nature of CNTs.

Gaona et al. (2007) conducted a study on the microstructure, morphology, and mechanical properties of composite coatings made of nano-structured titania/HA (CAPTAL 30 SD, Plasma Biotal, UK) deposited by high-velocity oxy-fuel (HVOF) (Diamond Jet 2700-hybrid, SulzerMetco, Westbury, NY, USA) spraying. The feedstock powder mixtures consisted of TiO_2 (5–20 μm) + 20 wt% HA (CAPTAL 30 SD) and TiO_2 –10 wt% HA. The feedstock powders were blended mechanically in a planetary mill (P5, Fritsch GmbH, Germany). The coatings were studied for their morphology, phases, porosity, hardness, and bond strength. Vickers microhardness measurements (Micromet II, Buehler, Lake Bluff, IL, USA) were taken under a 300 g load for 15 s on the polished cross-section of the coatings. The bond strength of the coatings was tested using the ASTM standard C633-01 to determine the adhesion or cohesion strength of thermal spray coatings (Method 2001). The average particle temperatures and velocities were 1874–1881° C and 651–686 m/s. The SEM images of the coating showed that HA appears as lamellae in a titania matrix, with some spherical HA particles. The porosity levels of the nanostructured TiO_2 + 10 wt% HA and nanostructured TiO_2 + 20 wt% HA coatings were less than 1%. The TiO_2 + 20wt% HA coating exhibited the highest roughness, which suggests that the roughness may be dominated by the HA splats since the topography of the titania is partially masked. XRD analysis did not detect tricalcium, tetra calcium phosphate, or CaO, which are commonly produced due to the thermal decomposition of HA. The Vickers hardness result and the adhesion tests showed that the addition of HA weakened the mechanical properties of the titania coatings. Nano-structured titania and nano-structured TiO_2 + 10 wt% HA coatings failed at the epoxy glue during bond strength testing (ASTM C633). As these samples had a glue failure, the bond strength of the nanostructured titania and nanostructured TiO_2 + 10 wt% HA coatings were higher than the strength of glue (77 MPa). However, the nanostructured TiO_2 + 20 wt% HA coatings showed an adhesive-cohesive failure and an adhesion value of 68 ± 14 MPa.

Balani et al. (2007a) conducted a study to analyze the microstructural, mechanical, and in-vitro properties of plasma-sprayed HA reinforced with CNT. They mixed irregular HA powder (10-50 microns) with 4wt.% multi-walled CNT (95%+ pure, OD=40-70 nm, L=0.5-2 microns) in a jar mill for 18 hours. The powder was then plasma-sprayed

on a Ti-6Al4V bioimplant substrate using a Praxair SG-100 gun. For cell culture, human osteoblasts (ATCC, CRL-11372) were cultured on coated HA samples (with and without CNTs) in Dulbecco's Modified Eagle Media (DMEM) without phenol red (Gibco, 31053-028) supplemented with 10% FBS (Hyclone, SH30071), and 1% penicillin/streptomycin/glutamine (PGS) (Gibco, 15140-122). The fibroblasts were grown under standard culture conditions (37°C and 5% CO₂—95% air) for 3 days. X-ray diffraction (Siemens D-500) and FESEM JEOL JSM 6330 F were used for phase determination and microstructural properties. The microhardness and fracture toughness of the coatings were estimated using a Shanghai Taiming Optical Instruments HXD-100 TMC Lenovo Vickers microhardness tester. The indentation toughness of the coatings was calculated using the Antsis equation for a load of 100 g for a dwell time of 15 s. The results showed that the thickness of the HA coating was 150 microns, while for the HA-CNT coating, it was 110 microns. The microstructural analysis of the HA coating revealed surface microcracks due to the brittle nature of HA. In contrast, the HA-CNT coatings had rough surfaces due to melt-resolidified fine and nodular HA particles. XRD showed a lower crystallinity of 53.7% for the HA coating, which increased to 80.4% when CNTs were added. The addition of CNTs also improved the fracture toughness by 56% ($0.61 \pm 0.09 \text{ MPa m}^{1/2}$) compared to the HA coating ($0.39 \pm 0.09 \text{ MPa m}^{1/2}$). In-vitro assessment of HA-4% CNT showed good spreading of the hFOB 1.19 osteoblast cells, which grew unrestrictedly along CNT-abutting surfaces. This suggests that the CNTs are non-toxic in the body environment.

Khor et al. (2003) investigated the microstructure and mechanical properties of hydroxyapatite (HA) splats and coatings sprayed using HVOF as a function of the proportion of melting in HA particles. The study also examined the behavior of HA splats and coatings using Kokubo SBF (pH-7.40) in vitro. Fine sieving was conducted to prepare the HA powders of different particle sizes, and their size range distribution was analyzed using a laser particle size analyzer (22, Fritsch GmbH, Germany). The powders and coatings' structure was characterized using scanning electron microscopy (SEM, JEOL JSM-5600LV) and transmission electron microscopy (TEM, JEOL, JEM-2010) at 200 kV. Additionally, the phase composition of as-sprayed coatings was qualitatively determined through X-ray diffraction (XRD) analysis (MPD 1880,

Philips, the Netherlands). The melt fractions of HVOF-sprayed HA powders were experimentally determined through image analysis. The Young's modulus and microhardness of the sprayed particles were determined through a nano-indentation test on Nano-Indenters XP equipment, and the samples were finely polished using 1 mm diamond paste after grinding. Furthermore, Young's modulus was evaluated via a 3-point bend test, and fracture toughness via a micro-indentation test. The adhesive bonding strength testing was conducted according to ASTM C633-79 using the universal Instron machine with a 1 mm/min tensile rate. The study found that the melt fraction significantly influenced the phase composition of as-sprayed HA coatings in HVOF-sprayed particles. The study suggested that the spray parameters and starting powder size influenced the melt fraction of the particles. Raman spectroscopy qualitative inspection on the sprayed HA particles (partially melted) revealed that thermal decomposition occurred within the melted part rather than the unmelted zone. The resolidified zone of the sprayed HA particles exhibited an average Young's modulus value of 41.25 GPa, with measured values ranging from 23.1 to 65.3 GPa. The unmelted part of the HA powders showed a markedly narrower range, with Young's modulus value of 83.9 ± 9.4 GPa recorded for this region. For small HA particles, 25 nm, the resulting splat virtually disappeared, thus indicating complete dissolution before any precipitation. In vitro investigation of individual HA splats made from different HA particles revealed a decisive role of local phase composition in influencing their dissolution/precipitation behavior during the test.

Lima et al. (2005) investigated the mechanical properties, microstructure, and in vitro analysis of HA coatings on Ti-6Al-4V substrates fabricated using the HVOF technique. The feedstock and coating's nanostructure and microstructure were analyzed using a field-emission scanning electron microscope, and the coating porosity was measured using image analysis. The phase composition and crystallinity were determined using X-ray diffraction (XRD) with a step of 0.01° and a step time of 2.0 s. The Vickers microhardness of the coatings was measured by performing ten indentations in the cross-section (centerline) using a 300 g load for 15 s. The bond strength was determined using a universal testing machine following a standard procedure (ASTM C633-01). The in vitro test was conducted in Kokubo SBF (pH = 7.40) over seven days in a

continuously stirred bath containing distilled water with a stable temperature of 37°C. Each sample was incubated in 70 ml SBF contained in a polyethylene bottle. The study found that the average particle velocity was 638±82 m/s, while the average particle temperature was 1826±346°C. The bond strength of the HVOF-sprayed HA coating was 24±8 MPa (n=5), which is higher than the bond strengths of HA coatings deposited via air plasma spray. The HVOF-sprayed HA coating from a nanostructured feedstock exhibited high crystallinity levels (84%) and low degradation without TCP, TTCP, or CaO phases. The HVOF-sprayed HA coating from the nanostructured feedstock featured high density and microstructural uniformity. A uniform layer of apatite (~35 microns) was formed on the HA coating after 7 days of incubation in SBF, which is much higher than that of plasma spray (~20 µm).

2.6 Wear resistance of the coatings

Friction and wear properties are important in load-bearing bioceramic implants' long-term in vivo performance, especially when used to substitute hip and knee joints (Dey et al. 2014). Due to the human body's complex biomechanical and biochemical environment, the implanted bioceramics are subjected to constant friction and wear, which is the main reason for generating wear debris and implant loosening (Suñer et al. 2012). In addition, excessive abrasion causes a reduction of the implant's mechanical properties, contributing to the device's early failure. The short lifespan of artificial joints is related to stress shielding, which is affected by the elastic modulus of materials used in fabricating bioimplants. Materials with an elastic modulus similar to natural bone would suffer fewer damages caused by stress shielding, like titanium alloy (Geetha et al. 2009). Also, titanium-based artificial joints have the potential to cause less damage to natural bones, increasing the survivorship of bioimplants in the human body. Hence, its excellent mechanical strength makes titanium alloys well-accepted for fabricating femoral stems of artificial hip joints (Jambagi and Malik 2021). However, the wear resistance of titanium alloys is relatively low, restricting its application in the field of bearing surfaces. One of the main reasons for the poor tribological properties of titanium alloys is their low thermal conductivity (Chauhan and Dass 2013). This is due to the disruption of fragile, low-shear strength oxide film, consisting mainly of titanium dioxide (TiO₂), which results in both de-passivation and subsequently accelerated wear

of the metallic surface due to the displaced particles of oxide, giving rise to three-body abrasive wear. In addition, the poor tribological behavior of titanium alloy is characterized by high coefficients of friction, severe adhesive wear with a strong tendency to seize, and low abrasion resistance (Lahiri et al. 2011).

Wang et al. (2022) investigated the tribological properties of laser-grooved titanium alloy under dry and SBF environments. The study was recorded using a tribometer (UMT-3, Bruker). The test module was a reciprocating ball–plate module with parameters such as room temperature, applied load 1 N, frequency 1 Hz, amplitude 2 mm, and test time 1800 s. The counter-body was a Si₃N₄ ball (6 mm), with a Ra of 0.02 μm and a Vickers hardness of 1500 HV. The tribological performance results showed that introducing the microgroove structure can significantly reduce the friction coefficient of the titanium alloy in dry friction. Besides, the wear resistance under both lubrications on the titanium alloy surface was improved considerably. Among them, the wear rates of titanium alloys were reduced by 87% under dry friction and 85% in SBF lubrication after texturing the microgroove structure with a 45 μm width. This was attributed to the increase of the microhardness due to the laser-grooved treatment and the function of storing abrasive particles of the grooved structure.

Further, HA-based implants are also prone to wear under load-bearing applications due to their poor fracture toughness and brittleness. A tribological study by Pandey et al. (2018b) investigated the wear properties of plasma sprayed-HA coating and reported a CoF of ~0.16 and a low wear rate of $176.1 \pm 7.0 \times 10^{-6}$ due to its low mechanical properties, including hardness = 1.88 GPa, $K_{Ic} = 0.68 \text{ MPa/m}^{1/2}$. The primary wear mechanisms involved during the HA coating wear were extensive delamination, cracks, and pits.

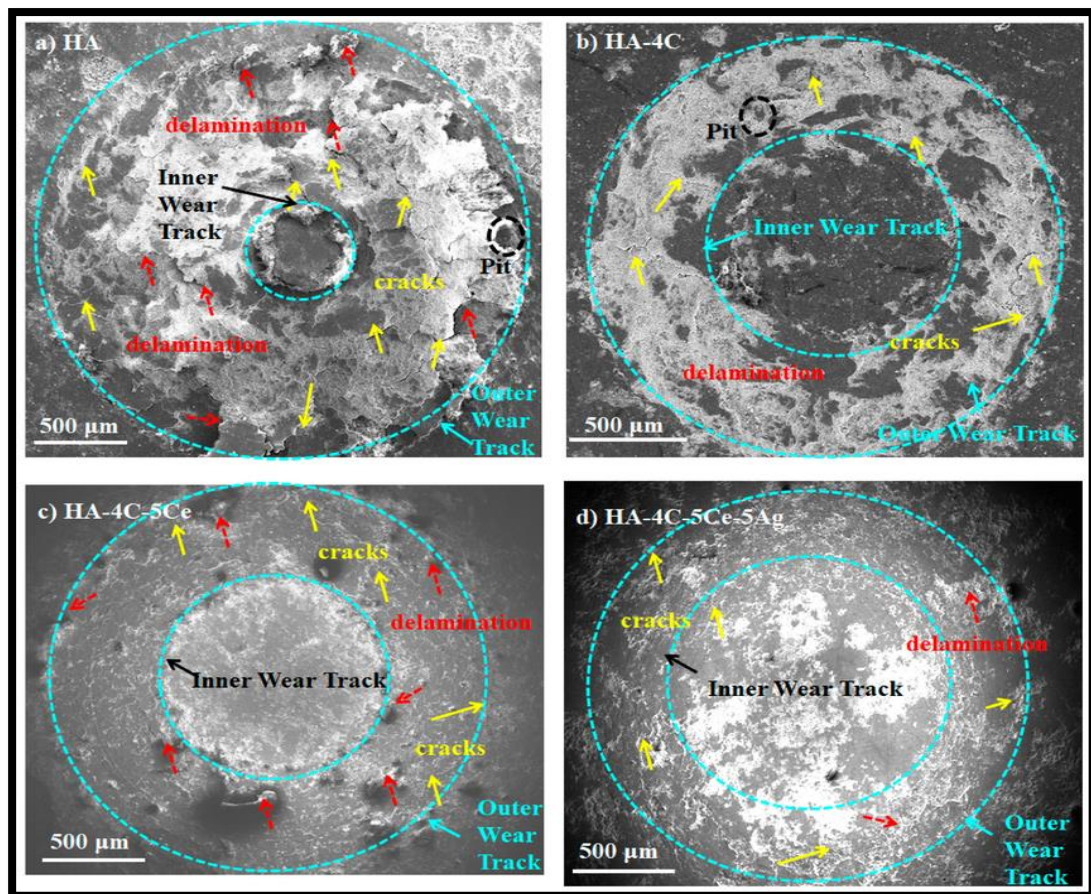


Figure 2.4 Micrographs showing the worn surface scar of (a) HA, (b) HA-4C, (c) HA-4C-5Ce, and (d) HA-4C-5Ce-5Ag (yellow and red arrows show cracks and delamination, respectively) (Pandey et al. 2018b).

Jagadeeshanayaka et al. (2023) investigated the wear resistance of high-velocity air fuel (HVAF)-sprayed HA coating. The fretting wear behavior was analyzed by using a ball-on-flat setup tribometer (TRB3, Anton Paar), with a counter-body as a steel ball of 6 mm diameter. The reciprocating motion had a stroke length of 1.0 mm and a frequency of 9 Hz with an applied load of 1 N for 900 cycles. The extent of the wear area, wear depth, wear volume, and coating damage was determined using a 3D noncontact profilometer (ST400, NANOVEA, USA), HR-FESEM (GEMINI 300, Carl Zeiss, Germany), and FEGSEM 7610FPLUS, Jeol, Japan). They reported a CoF of ~ 0.64 and a $1.532 \times 10^{-3} \text{ mm}^3/\text{Nm}$ wear rate. The wear mechanism observed in the HA coatings under fretting conditions involved a combination of adhesive and abrasive wear. Further, EDS analysis showed minimal changes in the percentages of calcium (Ca),

phosphorus (P), and oxygen (O) elements in the fretted regions.

Chen et al. (2019) conducted a study on the wear of APS HA coating in sliding contact with Al₂O₃ abrasive paper, HA, polyurethane (PU), and polycarbonate (PC). The study was conducted under dry and SBF conditions with various applied loads. Results showed that at a load of 20 N and when sliding against different materials, the wear rates of the coating ranged from 0.05×10^{-2} to 24.09×10^{-2} mg/Nm in dry conditions and from 0.25×10^{-2} to 13.54×10^{-2} mg/Nm in SBF. The weight loss of the coating sliding on HA in SBF increased from 3.1 to 7.9 mg as the applied load increased from 5 N to 20 N. The wear rate of APS HA coating was highest when sliding on Al₂O₃ and lowest on PU. APS HA coating in SBF showed lower wear rates than in dry conditions, except when sliding against HA. Wear behavior mainly involved abrasive wear in plowing, gouging, and peeling off splats and adhesive wear in thin flakes. When sliding against Al₂O₃, the primary wear mechanism was abrasive wear in the form of gouging and peeling off. When sliding against PU or PC, adhesive wear mainly occurs in the form of flakes of debris wear. When sliding against HA in SBF, adhesive wear primarily happens in exfoliated debris with some deformation. Lastly, when sliding against HA in dry conditions, abrasive wear mainly occurs by plowing and peeling off splats.

Many research groups have made several efforts to enhance the properties of HA coatings by adding reinforcements such as carbon nanotubes (CNT), alumina (Al₂O₃), yttria-stabilized zirconia (YSZ), Ni₃Al, and Ti-alloys (Jagadeeshanayaka et al. 2022; Li et al. 2019; Rattan et al. 2022). Among these, the alumina reinforcement to hydroxyapatite (HA) matrix provides better mechanical stability and biocompatibility with surrounding cells and tissues (Tercero et al. 2009). Incorporating inert metal oxides, such as Al₂O₃, in HA composites acts as a crack arrester and increases their mechanical strength (Vignesh Raj et al. 2018).

Rattan et al. (2022) conducted a study to examine the wear characteristics of coatings made of HA (45.5 μm) and HA-15 wt% Al₂O₃ (8-10 μm) that were plasma-sprayed (Anod Plasma Limited in Kanpur, India) onto a pure titanium (cp-Ti) substrate. The SEM, EDX, and XRD techniques scrutinized the coated samples. The wear tests were carried out using a tribometer with a Ball on a disc assembly to evaluate the durability

of the coatings. Both coatings showed partially melted and completely melted particles on their surfaces. The XRD analysis revealed the presence of amorphous phases in both coatings. The average friction coefficient of the HA and HA-15 wt% Al₂O₃ coatings were 0.21 ± 0.04 and 0.4 ± 0.01 , respectively. The wear rate of composite coatings was better than that of HA coatings. The wear rate of HA+15 wt% Al₂O₃ coatings was 4.9×10^{-3} mm³/Nm, while that of HA coatings was 8.4×10^{-3} mm³/Nm. The results indicated that adding Al₂O₃ to the coatings significantly impacted their tribological properties, possibly due to the formation of a dense microstructure, enhanced bond strength, and alumina, which contributed to the high wear resistance of the composite coating.

Despite the advantageous properties of using alumina, many researchers have reported its limitations, such as its low tensile strength, fracture strength, and brittleness (Hernigou and Bahrami 2003). Further, CNTs have shown potential for enhancing HA coatings' mechanical and wear properties, but few researchers have explored this application (Balani et al. 2007b; Lahiri et al. 2011). Due to their lubricious characteristics, high stiffness ($E \sim 1$ TPa) (Tercero et al. 2009), and outstanding wear resistance, numerous studies have investigated the fundamental behavior of CNTs in tribological applications. A study by Kim et al. (2011) investigated using a CNT/Ag coating on a silicon surface. This coating was tested using a pin-on-reciprocating tribometer with a normal force of 20 mN. The results showed that CNTs have great potential in reducing surface wear by anchoring the splats. More recently, Dalili et al. (2022) reported an increase in hardness and adhesion strength for electrophoretic deposited-HA/CNT coating with enhanced cell viability, indicating the non-toxicity of CNTs. However, the coating's wear resistance property was not explored, a crucial parameter for determining implant longevity in the human body. Therefore, the current work uses CNTs' excellent mechanical properties to fabricate a bioceramic composite.

2.7 Biocompatibility of the powders and the coatings

The complexity of the human body makes it almost impossible to replicate the exact environment that implanted joints experience during in vitro testing. Bioreactivity assessments, including bone bonding, have generally been done through animal testing,

which has been done since 1829 (Baino and Yamaguchi 2020). Although various materials have been implanted, they have been isolated from surrounding bone tissue due to fibrous connective tissue at the interface between the bone and the implant. In 1972, researchers discovered the first man-made material that bonded to bone without fibrous tissue by developing bioactive materials that directly bond to living bone. These materials can form an apatite layer on their surfaces, reproducible in vitro using an acellular simulated body fluid (SBF). Researchers found that the bone-bonding capability of a material could be evaluated by examining the apatite-forming capability on its surface in SBF (Hench et al. 1971). Many researchers now use the SBF solution to investigate the apatite growth structure over the implant surface.

Titanium and its alloys have been widely used in blood-contacting devices, such as intra-osseous implants, prosthetic heart valves, cardiovascular stents, and circulatory assist devices. However, improper implant surface interactions with blood are likely to cause thrombosis, and this is a major complication that can lead to device failure and other serious complications (Manivasagam and Popat 2020). Thrombosis is an acute syndrome where the blood clots on the implant surface, and once the clotting cascade begins, it spreads rapidly, which can also increase the chances of mortality. To prevent this, patients are prescribed blood thinners such as aspirin, vorapaxar, etc. However, overuse of these medications can weaken the immune system, and during injuries, there is profound bleeding of blood (Adams and Bird 2009). Thrombosis is initiated due to the contact of blood with a foreign surface, such as a metal implant surface, and it starts with the adsorption of blood proteins onto the biomaterial surface, which can lead to a series of complex reactions that ultimately form the thrombus (Shankar et al. 2024a). A medical device usually made of titanium is a left ventricular assist device (LVAD). This mechanical pump is implanted in a human's chest to assist a weakened heart. The major limitations of these devices are thromboembolism, bleeding, hemolysis, infection, and renal failure. A case study on HeartMate II patients showed that 11% had thrombus formation in less than one year after implantation (Shankar et al. 2024b). Infection was also commonly found due to thrombus formation. In recent years, efforts have been undertaken to reduce the thrombogenicity of biomaterials and prevent these complications. The thrombogenicity of a material is directly related to its surface

properties and can be influenced by modifying the surface characteristics such as topography, chemistry, charge, etc. Therefore, many research groups are focusing on modifying the titanium surfaces to improve their hemocompatibility and prevent the failure of blood-contacting implants. Hemocompatibility (i.e., blood compatibility) is essential for any biomaterial used for blood-contacting medical devices (Sarath Chandra et al. 2012). Blood compatibility refers to a material's ability to control the thrombotic and inflammatory responses caused by contact with blood. To achieve this, researchers have focused on developing hemocompatible surfaces that can prevent blood reactions without affecting the material properties. Over the years, there has been extensive research to understand the physical chemistry involved in the interaction between biomaterials and blood, which can lead to thrombosis and inflammation. This has led to significant progress in developing novel surfaces for blood-contacting medical devices. There are two main approaches to enhance the blood compatibility of titanium: changing the surface chemistry and topography. By combining these strategies, researchers can tailor the surface characteristics, such as roughness, wettability, and surface charge, to make the surface more hemocompatible (Shankar et al. 2024b). Studies show surface roughness can influence protein adsorption, platelet adhesion and activation, and thrombus formation. Surface wettability is also essential in determining how a liquid behaves when interacting with a solid surface. Hydrophilic surfaces are desirable as they tend to reduce blood protein adsorption due to higher water-surface interaction (Weber et al. 2018). Blood compatibility is a material's ability to control the thrombotic and inflammatory responses induced by the foreign surface when in contact with blood. Since the interaction between the implant and blood happens only on the implant surface, intensive research has been conducted to develop hemocompatible, novel surfaces. Modifying the device surface effectively prevents blood reactions without altering the favorable bulk material properties.

Over the last few decades, intensive research has been conducted to understand the physical chemistry behind the biomaterial–blood interaction and how it leads to thrombosis and inflammation. This has promoted significant progress in developing novel surfaces for blood-contacting medical devices. Strategies to enhance the blood compatibility of titanium are based on two main approaches: changing the surface

chemistry and topography. By combining both strategies, it is possible to tailor the surface characteristics, such as roughness, wettability, and surface charge, to make the surface more hemocompatible (Wang et al. 2012).

In vivo/in vitro results have shown that surface roughness can influence protein adsorption, platelet adhesion and activation, and thrombus formation. Surface wettability is an important factor that quantifies how a liquid behaves when it interacts with a solid surface, and this is dictated by the intermolecular interaction of the liquid and solid surface and the cohesive force between the liquid molecules. Designing hydrophilic surfaces is desirable as a lower amount of blood plasma proteins adsorb on them than hydrophobic surfaces. Due to the higher water–surface interaction, hydrophilic surfaces tend to reduce blood protein adsorption (Shabalovskaya et al. 2013).

Various researchers have established different ways of determining the biocompatibility of biomaterials, some of them are discussed as follows:

Henao et al. (2020) studied and compared the in-vitro bioactivity and electrochemical interactions of HVOF-sprayed HA/TiO₂ coatings on Ti-grade 5 samples with the simulated body fluid (Hank's solution). Ti-64 samples (10 × 10 × 6 mm) were cut by water jetting from the sheet, and grit blasted using Al₂O₃ (grade 20) particles at a pressure of 8 bar, cleaned with ethanol. Commercial high-purity HA powder (CAPTAL, 30SD, Plasma Biotol, UK) and TiO₂ powder (METCO 102, Oerlikon Metco) were used as feedstock materials. These powders are mixed mechanically in (75/25) wt.% (HA/TiO₂) and (25/75) wt.% (HA/TiO₂) proportions. A Diamond Jet HVOF gun (DJ-2700 hybrid, Sulzer Metco, Westbury, NY) coupled with a rotary AT1200-HP powder feeding system (Thermach Inc. Appleton, WI) and mounted on a six-axis KUKA industrial robotic arm was employed to fabricate the graded coatings on the substrates. The coatings were produced by employing a raster speed of 1 m/s, a spray distance between 200-230 mm, a powder feed rate of 12 g/min, and a thickness of ~9 mm per pass. The HA/TiO₂ graded coatings comprise four coating layers starting at the bottom with pure TiO₂, followed by a second coating layer with a composition of 25/75 wt.% (HA/TiO₂), a third coating layer with a composition of 75/25 wt.%

(HA/TiO₂), and finally, pure HA in the outer coating layer. Scanning electron microscopy (FE-SEM-JEOL JSM-7200F), with 15 kV accelerating voltage and secondary electrons (SE) radiation, was employed to reveal the morphology of raw powders and coatings. X-ray diffraction (XRD-Rigaku DMax 2100) with CuK α radiation (wavelength of 1.5406 Å) operating at 30 kV and 20 mA was employed to identify the constituent phases in the feedstock materials and the coated samples. The in-vitro tests of the HA/TiO₂ graded coating were performed using Hank's balanced salt solution (Sigma Aldrich) and following the ISO 23317:2007 (E) standard. In-vitro electrochemical tests were conducted in Hank's balanced salt solution at body temperature (~36.5°C). A three-electrode cell follows the ASTM F2129 standard, employing the studied sample as a working electrode, a saturated calomel electrode (SCE) used as the reference electrode, and a graphite rod as the auxiliary electrode. Potentiodynamic polarization, open circuit potential, linear polarization resistance, and electrochemical impedance spectroscopy (EIS) measurements were performed in a Gamry Interface 1000E potentiostat/galvanostat. XRD patterns showed that the HA peak was predominant in the HA/TiO₂ mixture (75/25 wt.%), while rutile and anatase were the main phases for the TiO₂/HA (75/25 wt.%). SEM images of raw HA showed spherical morphology, while TiO₂ powder particles are angular and irregular in shape for all size fractions. SEM micrographs of the top area of the coatings showed irregular morphology with typical micro-features (i.e., hills and valleys, voids, limits between particles, and some cracks). The mean micro-roughness of the top surface area of the graded coatings (Ra) was $4.4 \pm 0.5 \mu\text{m}$. The mean thickness value of the coating (four coating layers) was $350 \pm 7 \mu\text{m}$. The SEM analysis also revealed that the coating porosity is higher at the top coating layer than at the bottom one, forming a sort of porosity gradient. Porosity values of the top, third, second, and bottom coating layers were 8%, 7%, 5%, and 2%, respectively. XRD pattern showed increased intensity in the (002) plane as a function of immersion time, a characteristic of bone-like apatite formation. The Ca/P ratio starts from 1.60 for the as-sprayed sample and reaches a value of 1.86 for the sample soaked in Hank's solution for 28 days, which is attributed to the ion exchange occurring between the coating surface and fluid; this fact is often related to the bone-like apatite layer formation kinetics.

Hermann-Muñoz et al. (2019) investigated the microstructure and in-vitro analysis of HVOF sprayed HA (25-44 μm) coatings and splats on 302 stainless steel (302 SS). The study involved an experimental approach based on the design of experiments and process maps to improve the biocompatibility of the coatings. Before the hydroxyapatite (HA) deposition, the substrates were coated with titanium oxide (TiO_2) to act as a bond coat. The researchers used a two-level design of three factors (23) to investigate the effect of fuel-oxygen ratio (F/O), stand-off distance (SOD), and powder feed rate (PFR) on the coating formation. An environmental scanning electron microscope (ESEM-Philips XL30) at 10 kV electron acceleration voltages and a secondary electron detector were used to characterize the powder and splat morphology and the coatings' microstructure. The study focused on selecting the most suitable deposition parameter combinations to obtain HA coatings with optimal crystallinity ($> 45\%$), Ca/P ratio (approx. 1.67), and phase content ($> 95\%$ of HA). These properties guarantee the coating's mechanical stability and biocompatibility. The DPV-evolution equipment (Tecnar) was used to measure the temperature, velocity, diameter, and flow of the in-flight particles during coating deposition. The coating behavior within simulated body fluid (SBF) and cell culture was studied to analyze the apatite layer formation and the cytotoxicity of the extracts on human osteoblasts, respectively. The results showed that the F/O ratio is the most significant factor in the temperature and velocity of the in-flight particles and, therefore, in the coating properties. The PFR did not significantly influence the in-flight particle conditions, splats formation, and coating properties. The combination of the shortest SOD (10 cm) and the highest F/O ratio (0.27) used parameters resulted in faster and colder particles with short residence times in the flame, leading to coating delamination. A disk-like splat morphology was obtained using the following combination of parameters: SOD=20 cm, F/O ratio=0.14, and PFR=16 g/min. The obtained coating showed a homogeneous surface, high crystallinity, and Ca/P ratio within the range established by the ISO-13779 standard. The coating also showed a bioactive behavior. The material released by the coatings during the cytotoxicity assays did not induce a cytotoxic response. The SBF results confirmed the formation of an apatite layer after 14 days of immersion. Finally, the mitochondrial activity measured by the MTS assay and cell membrane integrity measured by LDH liberation assays showed that the coating-released material does not

induce toxicity on the exposed cells.

Kowalski et al. (2022) studied the antibacterial properties, in-vitro biocompatibility, microstructure, and phases of hydroxyapatite (HA) coatings deposited on titanium-grade 2 substrates using plasma spray. The HA powder was deposited through axial powder injection using the Axial III system from Northwest Mettech Corp., Surrey, Canada, at three different distances (100, 120, and 140 mm). The surface structures and morphologies of the coatings and the adhesion of bacterial cells were studied using a JEOL scanning microscope from Peabody, MA, USA. The phase composition analysis of both the HA powder and the sprayed coatings was performed using a Bruker D-8 Advance diffractometer from Billerica, MA, USA. The Talysurf CCI-Lite 3D profilometer from Warrenville, IL, USA, was used to examine the surface topography of the sprayed coatings. Each implant's surface morphology was examined, and the direct contact cytotoxicity of each HA coating was evaluated according to norm ISO 10993-5:2009. The activation of the transcription nuclear factor was used to assess the response of monocytes to HA. All coatings had a lamellar structure, with the highest roughness and minimal phase change observed in the HA sprayed at a distance of 120 mm. The analysis of the research results showed that the plasma-spraying distance used during the HA coating process had a negligible impact on biocompatibility. A slight increase in the biological properties tested was observed in the results obtained for a distance of 120 mm. Moreover, HA coatings sprayed at different distances were not cytotoxic and did not stimulate the NF- κ B. Finally, it was observed that bare titanium was less susceptible to colonization by *Staphylococcus aureus* than HA-coated surfaces.

Vilardell et al. (2020) conducted a study to compare the surface microstructures and biological performance of Ti-6Al-4V alloy coated with HA (30 μ m) using different methods, including APS, HVOF, and Cold Spray (CS). The top surface of the HA coatings was evaluated using FESEM (JEOL JSM 7100F). Thickness and porosity values were measured by ASTM F1854 using Optical Microscopy (Leica DMI5000 M). Coating roughness was measured using Confocal Microscopy (Leica DCM3D). Phase identification was analyzed using an X'Pert PRO MPD diffractometer (PANalytical). MTS and LIVE/DEAD assays were used to test cell viability, alkaline phosphatase (ALP) quantification was used to measure cell differentiation, and FESEM

was used to analyze cell morphology. The FESEM images of APS and HVOF coatings showed irregular micro-featured morphologies due to the combination of melted and un-melted particles. However, the CS HA coating showed a more regular surface due to the compaction of the particles. The HA coatings showed an increase in HA crystallinity from 62.4% to 89%, but also an increase in hydrophilicity from $\sim 32^\circ$ to 0° , with the decrease of the operating temperature of the thermal spray techniques (APS > HVOF > CS). Moreover, APS HA coatings showed more surface micro-features than HVOF and CS HA coatings. Cells onto APS HA coatings showed faster attachment by acquiring osteoblastic morphology than the rounded cell morphology observed on CS HA coatings at 1 day of cell culture. HVOF-HA coatings also showed proper cell adherence but did not show extended filopodia as cells onto APS HA coatings. However, at 14 days of cell culture, higher cell proliferation and differentiation were detected on HA coatings with higher crystallinity (HVOF and CS techniques). Surface micro-features are suggested to favor cell attachment, along with moderate surface wettability. On the other hand, HA crystallinity and crystal size are thought to influence cell proliferation and differentiation highly.

Previously, many researchers have studied the toxicity of implants or wear debris through osteoblast cells; however, their compatibility with human blood was not explored, as human blood is the first fluid that comes into close contact with implants.

Nuswantoro et al. (2021) have studied the osseointegration and inflammatory response of HA-coated Ti-29Nb-13Ta-4.6Zr (TNTZ) sample in vivo on *Rattus norvegicus* Wistar rats (300g). The coating process was carried out using the electrophoretic deposition (EPD) method, and TNTZ implants with and without HA coating were installed on the rats' tibia. TNTZ rod with a diameter of 6 mm was turned by lathe machine into an M3 \times 0.5 screw type; the length of the screw section was 3 mm while the length of the head was 2 mm. The HA suspension was made by mixing 4 g of 10 μ m Sigma Aldrich HA powder into 100 mL of ethanol, which was then stirred using a magnetic stirrer at a room temperature of 27 $^\circ$ C. The EPD coating process was done by immersing a carbon rod (anode) and a TNTZ (cathode) with a power supply voltage of 7 V and a coating time of 5 min. A removal torque test was carried out on TNTZ screw samples mounted on the tibia of the animals. Inflammatory factor, TNF- α concentration

on rat's blood serum was measured using Bioassay Technology Laboratory Rat Tumor necrosis factor α ELISA kit Cat—no E0764Ra. The histological observation was made by photographing HA preparations with an optical microscope Olympus BX 51 at 200x and 1000x magnification (Objective 20x and 100x); this examined the granulation and callus tissues in the implant area. Statistical analysis of quantitative data was performed using R statistics software. HA coating on the surface of TNTZ improves bone osseointegration as indicated by the removal torque value of the coated implant (8.1 Ncm) is much higher than that of the non-coated one (1.7 Ncm), and reduces excessive inflammation as indicated by TNF- α levels of the coated implant (29.44 ng/L) is much lower than that of the non-coated one (36.16 ng/L) after two weeks experiment. Histopathological observations showed a significant increase in osteogenesis in the bone tissue fitted with coated TNTZ implants compared to tissues observed for a bare implant. This growth of bone tissues was characterized by high osteoblast activity and visible chondrocyte formation found on the coated implant after two weeks, while bone tissue at the bare implant was dominated by granulation tissue that indicates inflammation activity.

Bose et al. (2020) have investigated the mechanical, in-vitro, and in-vivo assessment of plasma-sprayed HA and reinforced coatings. This study also explained the role of oxide layer formation on the surface of Ti6Al4V samples by heating it at 600, 700, and 800 °C to increase coating crystallinity and to improve coating bond strength with the metal surface. Substrates with a 25.4 and 12.2-mm diameter were prepared by cutting Ti6Al4V plates (President Titanium, MA) using a water jet cutter for adhesive bond strength tests and other characterizations, respectively. Commercial grade HA powder (150–212 μm , Monsanto) was mixed with 0.5 wt % SiO₂ and one wt % MgO using a 1:1 powder to milling medium ratio for 2 h at 70 rpm. An induction RF plasma-spray system (Tekna Plasma Systems, Sherbrooke, Canada) with a supersonic nozzle and an axial powder feeding system was used to spray powders. Plasma sprayed HA coatings were prepared on Ti6Al4V (HA/Ti6Al4V), Ti6Al4V with oxidation at 600°C (HA/600TiO₂/Ti6Al4V), Ti6Al4V with oxidation at 700°C (HA/700TiO₂/Ti6Al4V), and Ti6Al4V with oxidation at 800°C (HA/800TiO₂/Ti6Al4V). MgO/SiO₂-HA coating was prepared on Ti6Al4V with oxidation at 800°C (MgO/SiO₂-HA/800TiO₂/Ti6Al4V)

to see the effects of MgO and SiO₂ on physical, mechanical, and biological properties compared to HA/800TiO₂/Ti6Al4V. The coatings obtained were approximately 80–100 μm thick. An X-ray diffractometer (Siemens D5000, Aubrey, TX) using Cu Kα radiation at 30 mA and 40 kV was used to identify the phase formation of different coatings, and the calculation was conducted by MDI JADE software. Adhesive bond strength of the coatings (~300 μm) was performed using an Instron tensile apparatus with a constant crosshead speed of 13 μm/s until failure. The testing procedures were performed based on ASTM C633. FESEM images of the coatings depicted details about the surface topography. An SBF solution, with pH 7.4, was used for the dissolution study of Ca²⁺ ions of plasma-coated samples. Primary human osteoblasts (PromoCell, Heidelberg, Germany) were cultured for in vitro characterizations. Samples were 12 mm in diameter, and cells were seeded at a density of 1 × 10⁴ cells/sample. MTT assay (Sigma, MO) was used to evaluate the osteoblast proliferation. An ALP assay kit (SensoLyte, Fremont, CA) was used to characterize the osteoblast differentiation. An in vivo rat distal femur model was studied using implants of Ti6Al4V control, HA/Ti6Al4V, and MgO/SiO₂-HA/Ti6Al4V to assess the osteogenic potential of adding the MgO/SiO₂ additives. Six male Sprague Dawley rats with an average mass of 300g (Simonsen Laboratories, Gilroy, CA) were implanted, producing duplicates of each composition, with half euthanized at 6 weeks and the other half euthanized at 10 weeks. Critically sized circular bone defects were formed using a drill with gradually increasing diameter bit sizes up to 3 mm diameter. Implants were tightly placed through both cortices with lengths of 5 mm. The result showed that the oxide layer at 800 °C further improves the crystallinity of plasma-sprayed HA coating from 64-75%, thus decreasing the dissolution, indicated by a lower quantity of Ca²⁺ release in SBF. The adhesive bond strength of plasma-sprayed HA coating was improved from 25.9 ± 2.3 (HA/Ti6Al4V) to 30.7±1.1 9 (MgO/SiO₂-HA/800TiO₂/Ti6Al4V) MPa due to the addition of an oxide layer. The presence of MgO and SiO₂ has negligible effects on the crystallinity and adhesive bond strength of plasma-sprayed HA coating. MgO and SiO₂ showed enhanced osteoblast proliferation and differentiation by observing higher MTT and ALP expression compared to HA-coated samples. The additive improves osteoblast proliferation and differentiation and significantly enhances osseointegration and bone mineralization in a rat distal femur model. Osseointegration was not only reinforced by

the MgO/SiO₂-HA coating compared to uncoated Ti6Al4V but was also improved compared to the HA coating alone, as shown in Figure 2.5.

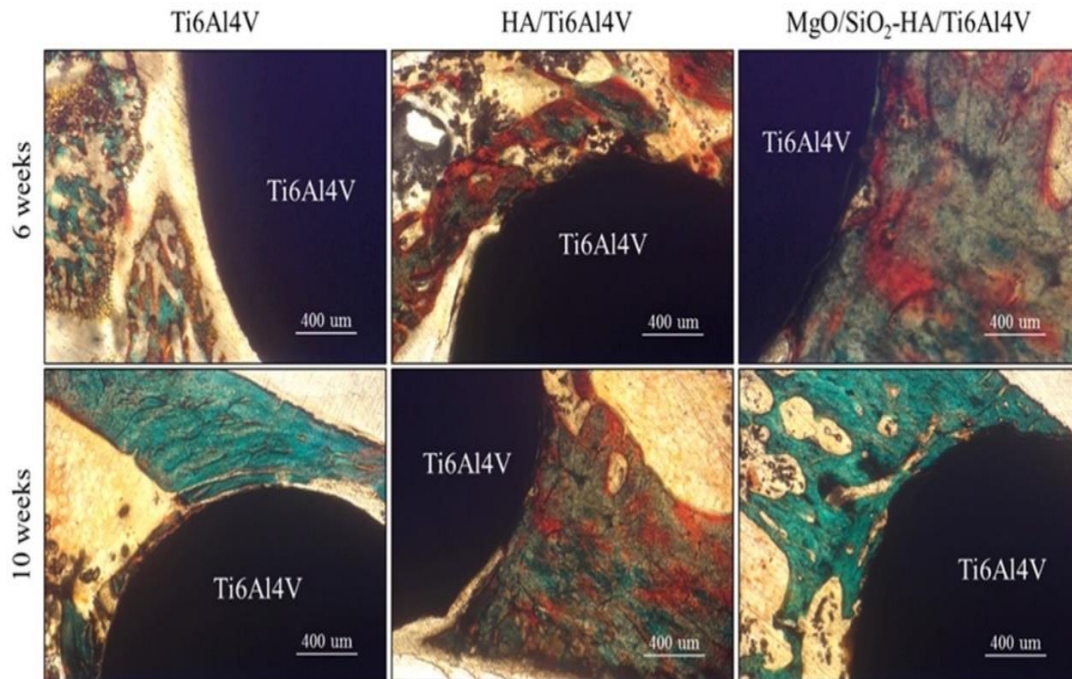


Figure 2.5 Microscope images of Ti6Al4V control, HA/Ti6Al4V, and MgO/SiO₂ HA/Ti6Al4V-sectioned implants stained by a modified Masson–Goldner trichrome stain. Larger gaps were observed between the Ti6Al4V implant surface with surrounding osseous tissue. The HA coating enhanced osseointegration between the implant surface and osseous tissue and was further enhanced by the MgO/SiO₂-HA coating. Osteoid formation is depicted in red/ orange, and mineralized bone in blue/green (Bose et al. 2020).

Ooi et al. (2019) investigated the hemocompatibility of nanoporous hydroxyapatite prepared using surfactant-templating method for adsorption-based biomedical applications. Pluronic P123 and F127 (surfactants) were used as soft templates for producing rod-like hydroxyapatite particles. Pluronic P123 has resulted in HAP with a larger surface area and pore volume than the HAF sample (using F127 surfactant) due to the agglomeration of its smaller rod-like particles. The percentage of hemolysis of the HAP and HAF samples at different concentrations ranges from 1.04 to 3.69%. The percentage of platelets adhered to HAP and HAF is 15.7 ± 11.8 and $14.6 \pm 10\%$, respectively, significantly lower than that of the collagen-coated glass ($88.6 \pm 8\%$, $p < 0.05$, $n = 3$). Further, they reported the round morphology of the platelets on the hydroxyapatite surfaces and silicon tube, indicating the non-activation of the platelets

(Figure 2.6). The absorbance values at 45 min for the HAP, HAF, glass, and baseline samples are 1.03 ± 0.38 , 1.46 ± 0.15 , 0.23 ± 0.06 , and 0.29 ± 0.09 , respectively. The absorbance values for the HAP and HAF samples are relatively higher than that of the reference materials (paired t-test shows a significant difference, $p < 0.05$, $n = 6$), indicating their non-thrombogenicity. The hemocompatibility evaluation suggested that both nanoporous hydroxyapatite samples are highly hemocompatible biomaterials, and they do not cause an adverse effect on blood components.

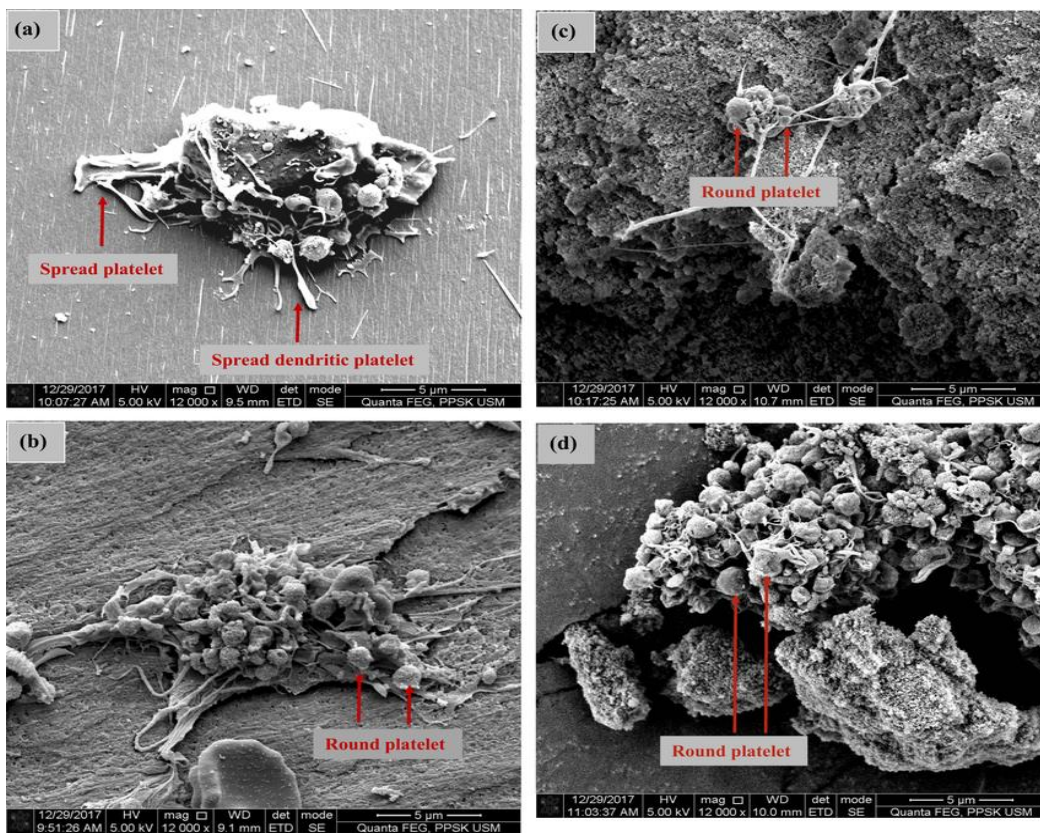


Figure 2.6 Morphology of platelets adhered on (a) collagen-coated glass, (b) silicone tube, (c) HAP, and (d) HAF samples (Ooi et al. 2019).

Laranjeira et al. (2016) characterized and compared the in vitro cytotoxicity and hemocompatibility of hydroxyapatite magnetic nanoparticles doped with different ions ($Gd^{3+}/Fe^{2+}/Fe^{3+}/Co^{2+}$) for MRI applications. The powders were produced by a well-controlled wet chemical precipitation method. 10% Gd-doped HA and 10% Fe-doped HA displayed the highest magnetic moment levels compared to Fe (II) and Co-doped HA, and the magnetic moment values were closest to those of a commercially available Gd-based MRI contrast agent composed of Gadoteric acid. The viability and

morphology of human dermal microvascular endothelial cells did not seem to be significantly altered after incubation with the synthesized materials. Regarding the hemolytic assay and hemostatic studies, it was shown that HA, Gd, and Fe doped HA showed no hemolytic activity up to the concentration of 4 mg/ml, with a hemolysis percentage less than 2%. Through SEM analysis, it was observed that nanoparticles did not activate platelets. The coagulation cascade activation assays and the whole blood kinetic clotting time showed that HA and Gd10-HA nanoparticles up to a concentration of 4 mg/mL did not interfere with the intrinsic or extrinsic coagulation pathways. However, results suggested that iron ions affected the coagulation cascade, indicating that Fe (III) doped HA nanoparticles are thrombogenic materials.

Li et al. (2013) investigated the hemocompatibility and cell toxicity of oxidized diamond nanocrystals for biomedical applications. The monocrystalline nanodiamonds (NDs) were synthesized by high-pressure-high-temperature (HPHT) methods and purified by air oxidation and strong oxidative acid treatments. The results indicated that the NDs have excellent hemocompatibility with negligible hemolytic and thrombogenic activities. Figure 2.7 (a) and (b) show the hemolytic activity of different nanoparticles of different sizes and types that were incubated with human RBCs at room temperature for 2 h, after which they were removed by centrifugation before colorimetric analysis. Irrespective of the particle size, all NDs showed no sign of RBC destruction at a concentration as high as 400 mg/mL. In contrast, the membrane of the RBCs incubated with GOs was substantially damaged, releasing free hemoglobin in the supernatant at a dose higher than 25 mg/mL. Cell viability assays with human primary endothelial cells suggested that the oxidized HPHT-NDs (dimensions of 35–500 nm) are non-cytotoxic. No significant elevation of IL-1b and IL-6 inflammatory cytokine levels was detected in mice after intravenous injection of the nanocrystals *in vivo*. Using a hindlimb-ischemia mouse model, they demonstrated that 35 nm NDs after covalent conjugation with polyarginine are helpful as a drug delivery vehicle of heparin for prolonged anticoagulation treatment.

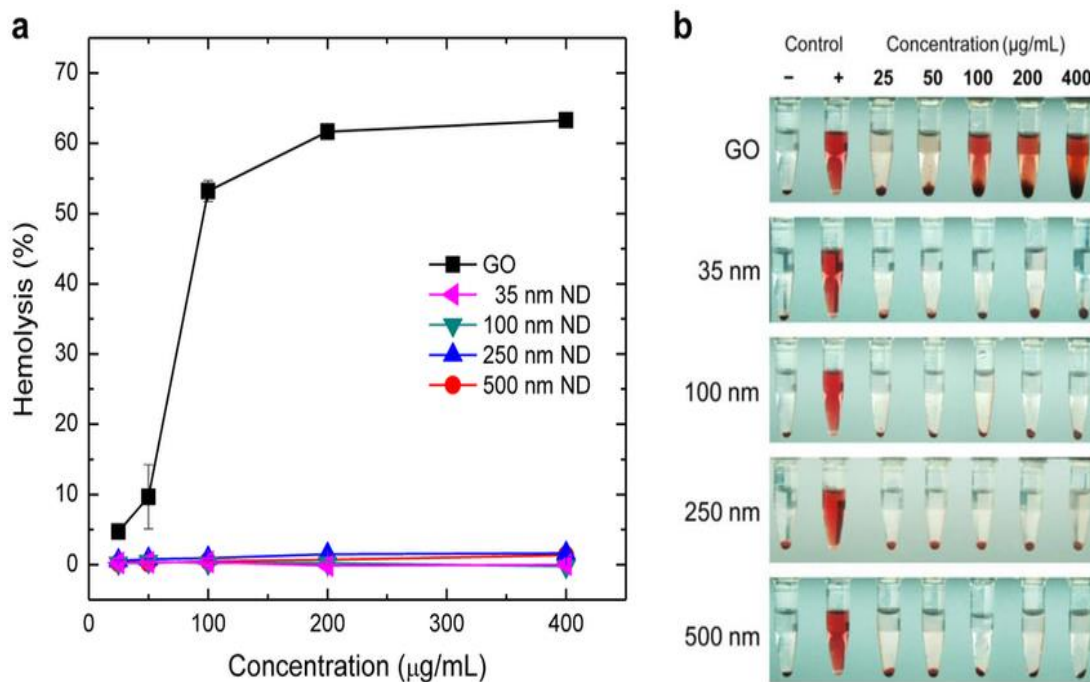


Figure 2.7 Hemolysis studies of GOs and oxidized NDs of different sizes with human RBCs. (a) Hemolysis percentages were measured at the 25–400 µg/mL concentration range for GOs and 4 different ND samples (35, 100, 250, and 500 nm in diameter) incubated with RBCs at 25°C for 2 h. GOs served as the positive control. (b) Photographs of human RBCs treated with GOs and NDs of 4 different sizes at 25–400 µg/mL concentrations range. The red color of the solution is due to the release of hemoglobin from the damaged RBCs, and the red pellets at the bottom of the Eppendorf tubes are intact RBCs precipitated by centrifugation. PBS and DDW were negative (-) and positive (+) controls, respectively. The experiments were repeated in triplicate (Li et al. 2013).

Sarath Chandra et al. (2012) investigated the in-vitro toxicity and hemocompatibility of Fe³⁺ (0-0.1wt%)-doped nHA synthesized by a combination of hydrothermal and microwave techniques. The in vitro bioactivity test of the material showed the deposition of the apatite layers on the samples; however, there was better apatite layer deposition on the Fe³⁺-doped nHA, attributed to the drastic reduction in particle size due to dopants. From EDS analysis, the Ca/P ratio was calculated to be 1.71, 1.70, 1.89, and 1.77 for 0Fe, 0.01Fe, 0.05Fe, and 0.1Fe, further suggesting the apatite layer growth. The proliferation of MG-63 cells in the presence of un-doped samples showed better cell proliferation with more than 90% of viable cells. In contrast, the doped 0.01Fe, 0.05Fe, and 0.1Fe show a significant increase in cell proliferation on day 3 compared to day 1, with the percentage of cell viability between 65% and 80% of viable cells.

0.01Fe nHA impregnated with antibiotic showed efficacy against the common pathogens *E. coli*, *S. epidermidis*, and *S. aureus* implicated for the long-term treatment in osteomyelitis. Further, the hemolytic assay showed that the undoped and doped samples did not cause hemolysis (<5%).

Facca et al. (2011) investigated the in-vivo study of plasma-sprayed CNT-reinforced HA coating on titanium implants embedded in rodent bone. Two geometries of Ti-6Al-4V alloy, with and without coatings, were implanted: spherical beads for mice and rods for rats. The spherical beads were 1 mm in diameter, whereas the rods were 10 mm long and 2.5 mm in diameter. Spherical titanium beads and rods were coated by plasma spraying (Plasma Forming Laboratory at Florida International University, Miami, USA). HA nanorods (length= 100-325 nm, diameter = 25-50 nm) and CNT were spray-dried together to form an agglomerate that served as the feedstock for plasma spraying. Titanium beads and rods had three different types of coatings: (i) uncoated titanium, (ii) HA coating, and (iii) HA/4 wt. % CNT coating. The coating thickness was 100-150 μm . Three groups of titanium implants were tested in the pull-out model for mice and rats: uncoated (group 1), HA coating (group 2), and HA/4 wt. % CNT composite coating (group 3). As a group control, a hole was made inside the femoral bone with no implant (group 4). Hysitron Triboindenter TI 900 was used to evaluate the newly grown bone's elastic modulus (E), and HA-based coatings in the retrieved implants were evaluated using nanoindentation. The clinical results showed that the implants from groups 1, 2, and 3 were well-positioned inside the external femoral condyle. None of the implants were ejected. Cortical bones were restored completely, and good healing was achieved for all four group bones after one month of implantation. The histological observations showed that implants (group 1&2) from mice and rats were fully removed from the bone using forceps. Still, it was most challenging to detach group 3 implants (HA-CNT), a qualitative indicator of the strong adherence of CNT-containing HA coating with the bone. TEM images (group 3) of the rats' bones showed normal bone cells and bony trabeculum without any inflammatory reaction. There was no tissue degeneration or neutrophil infiltration for HA-CNT-coated implants. The elastic modulus of the bone near the HA-CNT surface showed a higher value than the bone at the HA surface. CNT showed better osteoblast proliferation and viability due to the

absorption of favorable proteins on the CNT surface.

Further, the use of CNT in the biomedical field is always a topic of discussion, as mixed responses regarding its biocompatibility have been reported so far. Liu et al. (2008) reported a promising use of CNTs for in vivo cancer treatment in a mouse model. On the other hand, Vijayalakshmi et al. (2022) have reported that carboxylic functionalized single-walled carbon nanotubes (C-SWCNTs) have increased cytotoxicity effects on human neuronal LN18 cell lines compared to pristine single-walled carbon nanotubes (P-SWCNTs). The increased toxicity of C-SWCNTs was attributed to their oxidized form, which can readily couple to proteins, peptides, or oligonucleotides. Conversely, a recent study by the same research group Vijayalakshmi et al. (2023), has reported the nontoxicity of MWCNT-COOH compared to MWCNT in terms of cell viability, reactive oxygen species (ROS) and lipid peroxidation assays. This effect was observed for longer incubation periods and higher concentrations (20 and 40 $\mu\text{g mL}^{-1}$). Additionally, they have reported the nontoxicity of both CNTs at lower concentrations (5–10 $\mu\text{g mL}^{-1}$). Tercero et al. (2009) reported the biocompatibility for plasma sprayed - HA-18.6wt% Al_2O_3 -1.4 wt% CNT coating. CNT coating displayed a higher proliferation rate than HA- Al_2O_3 (20 wt%) and HA coating due to apatite crystallization on the CNT surface, which acts as a bioactivity booster promoting cell proliferation. Dalili et al. (2022) have reported the bioactivity of HA-CNT nanocomposite coating on anodized Ti6Al4V alloy. The results of the in vitro test showed that the cell viability increased with increasing the concentration of CNTs to 3 wt-% CNTs (74.7%). Mukherjee et al. (2014) also reported the bioactivity using the SBF immersion test and non-hemolytic behavior for HA-CNT (0.5-5wt%) sintered pellets.

Researchers have studied the toxicity of osteoblast cell lines for HA implants. However, it is crucial to understand the blood compatibility of metal-based implants before clinical application. Few studies have been conducted on the blood compatibility of titanium-based implants. Li et al. (2016) reported the blood compatibility behavior of pure and coated titanium after conducting hemolysis and platelet adhesion tests. Still, they did not analyze their thrombogenicity, a vital factor affecting implant longevity. Guan et al. (2012) established hemocompatibility by conducting a hemolysis study for

HA-coated and uncoated Mg-4Zn-1Ca-0.6Zr alloy, while Manivasagam and Popat (2020) conducted platelet adhesion tests and whole blood clotting assays for grade-5 titanium and reported its thrombogenicity. A case study on heart patients using HeartMate II, made of titanium, showed that 11% of the implants failed within a year due to thrombus formation on their surface. Another medical device typically made of titanium is a left ventricular assist device (LVAD), implanted in a human's chest to help a weakened heart. However, these devices have significant limitations, such as thromboembolism, bleeding, hemolysis, and infection, and the thrombogenicity of a material is directly related to its surface properties, such as microstructure, chemistry, and charge. Uncoated titanium lacks necessary blood-compatibility properties, and there are no reports on the hemocompatibility assessment of thermally sprayed HA implants. Therefore, extensive research is required before in-vivo and clinical usage of metal implants with human blood, especially for HA coatings for blood-related biomedical applications.

2.8 Basis of Objectives Formation

The preceding literature survey leads to construe the following:

This investigation aims to identify the optimal CNT-reinforced HA composition for coating medical implants through a carefully selected thermal process. This process begins with preparing powders that exhibit high crystallinity and biocompatibility. Several HA thermal spray processes will determine the ideal coating process. Following this, a series of primary coatings will be fabricated using the most biocompatible feedstock composition and appropriate thermal technique and tested for its suitability for clinical use by different in vitro and in vivo studies. This endeavor aims to determine whether the powders can produce coatings that meet the necessary criteria in terms of thickness, crystallinity, hardness, porosity, and biocompatibility for orthopedic implants.

The fracture toughness of HA ($1\text{MPa m}^{1/2}$) is significantly lower than the minimum reported value for cortical bone ($\sim 2\text{MPa m}^{1/2}$) (Balani et al. 2007a). Thus, to replace bone as an implant or coating, the fracture toughness of HA needs to be improved. Reinforcing biomaterials to HA gives promising results in enhancing implant materials'

mechanical & biological properties.

CNTs have been explored as a second-phase reinforcement for improving the fracture toughness of HA-based composite parts and coatings. However, homogenous dispersion of nano-materials like CNTs in the matrix phase is challenging (Jambagi et al. 2015). CNT has high surface energy and tends to agglomerate in the composite. An agglomerated lump of CNTs in the coating raises the stress concentration levels when a coated component is subjected to forces and exacerbates the properties (Bakshi et al. 2008). Inhomogeneous dispersion also results in weak anchoring between the splats. Better dispersion of CNT in the matrix is possible if it is dissolved and well dispersed in an appropriate solvent to form a colloidal solution.

There are several methods to disperse CNT in preparing CNT-dispersed thermal spray powders, including dry mechanical mixing and spray drying (Balani et al. 2007b; Tercero et al. 2009). Another option is to mix and homogenize CNT in a matrix powder by combining both components in a suitable liquid and shaking the mixture in a ball mill. Alcohol is an effective liquid medium for this purpose, as it can be easily removed and reportedly has a debundling effect (Gupta and Saleh 2011). Heterocoagulation, a colloidal processing technique, is yet another approach used for CNT dispersion. Sun et al. (2002) investigated its role in forming a homogeneous mixture of alumina and MWCNT (0.1 wt %), while Jambagi et al. (2015) studied its effectiveness in the homogenous dispersion of CNT into ceramics powder. However, no research is currently available on the HVOF spraying of CNT-bioceramics composite produced using the colloidal heterocoagulation technique for orthopedic applications.

To achieve a longer life of bio implant, the tensile strength, wear resistance, and hardness of the porous coating must be sufficient to hold the coating with the metallic substrate (Singh et al. 2011). The poor adhesion strength between hydroxyapatite coating and the substrate of metallic biomaterial needs to be improved for load-bearing applications (Spriano et al. 2018).

Previously, various deposition methods of bioactive coating were used, such as HA coating on metallic biomaterials. These methods were introduced over the years to

improve adhesion strength to the metallic biomaterial substrates for long-term stability. The phenomenon (poor adhesion strength) between the coating and the metallic substrate is correlated to bond strength and is considered a critical biocompatibility issue (Fiume et al. 2021).

Although the availability of coating techniques is huge, an optimal technique for biological application has not been developed. Currently, most of the implants available in the market are produced by plasma spray coating technique only (FDA approved method for applying HA coatings to the implant surfaces (Hussain et al. 2023)). Due to intrinsic high temperature (i.e., $T > 1500\text{ }^{\circ}\text{C}$) operation in plasma spraying, instability is observed in HA phases, which lead to the formation of secondary and tertiary phases, such as amorphous calcium phosphate (ACP), tricalcium phosphate (TCP), tetracalcium phosphate (TTCP) (Hermann-Muñoz et al. 2019; Vilardell et al. 2020). Some of the phases are bio-resorbable. These highly soluble phases in nature, compromise the long-term stability of the coating and critically affect blood components in the human body (Jagadeeshanayaka et al. 2022). Thermal spray techniques of low-temperature range, like HVOF/Flame spray, should be explored for producing HA implants. A comparative Table 2.2 of different thermal spray processes is presented here that directly influence the coating properties (Jagadeeshanayaka et al. 2022; Singh et al. 2014).

Furthermore, CNT reinforcement improves the bulk wear resistance of the brittle coating (e.g., HA/alumina). So far, no reports on the tribological properties of CNT-reinforced HVOF sprayed HA/alumina coating in a physiological environment are available.

Table 2.2 Comparison of atmospheric plasma-spray (APS), flame spray (FS), and high-velocity oxy-fuel (HVOF) techniques.

Characteristics	APS (FDA- approved)	FS	HVOF
Operating temperature	6000 and 15000 °C	2500-3500 °C	2200-3000 °C
Velocity	150-600 ms ⁻¹	100-300 ms ⁻¹	400-1000 ms ⁻¹
Coating splat	Fully melted, well-flattened lower particles,	Fully melted, well-flattened unmelted flattened lamellae	Unmelted well-flattened lamellae
Crystallinity	Low	Moderate to high	High

Further, biological evaluations are crucial when materials are intended for human use and biomaterial selection for medical applications is generally considered in terms of biocompatibility. When investigating orthopedic biomaterials, biological investigations by *in vitro* and *in vivo* tests are required to obtain a true overall picture of biocompatibility, and of osteogenetic and osteointegration properties. Hemocompatibility assessment is regarded as the most accepted way of establishing the biocompatibility of the newly developed biomaterials due to its close resemblance to the human body.

2.9 Objectives

The main objectives of the present investigation are:

1. To prepare the heterocoagulated alumina (19.5-18wt%)/carbon nanotube (CNT) (0.5-2wt%) powder followed by ball mixing with HA to study the retention and degree of dispersion of CNT in HA/alumina matrix.
2. Hemocompatibility assessment of carbon nanotube doped hydroxyapatite worn debris of low-temperature thermally sprayed implants.
3. A Comparative study of plasma spray, flame spray, and HVOF sprayed-HA coatings based on their physiochemical, mechanical, and biocompatibility.
4. Biocompatibility assessment of the reinforced implants obtained with a suitable

thermal spray process.

5. To determine and study the wear resistance of the best-performing reinforced coating using the ball-on-flat method.
6. In-vivo osseointegration and toxicity assessment of bio-ceramics coated titanium rods in rabbit femoral bone.

2.10 Summary

In this section, an overview of commercially utilized consumables in medical implants has been provided. The significance of consumables concerning hydroxyapatite as a coating material within the realm of surface engineering has been emphasized. Additionally, various coating techniques and the use of reinforcing materials like alumina and carbon nanotubes were explored to enhance the properties of the implants. The concept of functionalization and its critical role in composite coating was also discussed. Furthermore, the fundamental components of the coating, including their morphology and their impact on the coating's properties, were examined. Moreover, the mechanical and wear properties of the implants and their biocompatibility with cells, human blood, and in vivo studies were briefly assessed to comprehend the effect of the coating's properties. Lastly, based on prior research, the objectives for the current study were established. In the subsequent chapter, the experimental procedure and materials used in this research will be explained.

CHAPTER 3 MATERIALS AND METHODS

3.1 Introduction

This chapter describes the experimental methodology used in the current investigation. It includes a novel composite preparatory technique for orthopedics applications, i.e., heterocoagulation for homogenous dispersion of CNTs onto alumina, followed by ball mixing of Alumina-CNT (0-2wt %) and HA. The prepared feedstocks were then assessed for their hemocompatibility. Different thermal sprays used for producing HA implants were discussed and evaluated for their physiochemical and mechanical properties. Further, the effect of CNT reinforcement in the coating was assessed using scratch test. Coatings were characterized for their cross-section, phases, and wear resistance with and without CNT reinforcement. In-vitro & in-vivo assessments required for this study are discussed thoroughly. This chapter provides a thorough description of each experimental technique.

3.2 Powder preparation and their physiochemical characterization

3.2.1 Feedstocks used

The base material for orthopedic implants was a titanium Grade-5 alloy (Ti-6Al-4V) sheet cut into 20x20x3 mm³ coupons. Porous HA powder, CAPITAL 60-1 with diameter ranges from 10-60 μm, average particle size: ~40 μm, density: 3.2 g/cm³, and purity: 99.72%, was procured from Plasma Biotol Limited, Derbyshire, England. Crushed angular alumina with a purity of 99.61% and size ranging from -45+15 μm was obtained from Oerlikon Metco, Splat Solutions, Chennai, India. We obtained multi-walled CNT with a purity of ~ 99%, outer diameter ranging from 10 to 30 nm, length >10 μm, and a density of 0.14 g/cm³ from Adnano Technologies Private Limited, Karnataka, India. The present study favors MWCNTs over SWCNTs due to their superior strength, durability, and thermal stability, making them advantageous for high-temperature applications. Moreover, MWCNTs exhibit superior processability, uniform dispersibility, cost-effectiveness, and biocompatibility compared to SWCNTs (Carneiro and Simões 2020; Facca et al. 2011; Saifuddin et al. 2013). Further, to functionalize the MWCNT, the technique outlined in the report by Jambagi et al. (2015)

was followed. From now on, functionalized MWCNT will be referred to as CNT.

3.2.2 Processing of CNT

The use of pristine CNTs in coatings is hindered by their poor dispersion and adhesion properties, making functionalization necessary to improve their compatibility with matrix materials. Functionalization involves modifying the CNTs through covalent or non-covalent methods to create functional groups on their surface, which enhances their solubility, dispersion, and adhesion properties. To achieve this, 100 mg batches of MWCNT were functionalized using a 20 ml mixture of 6 M HNO₃ and H₂SO₄ (in a 1:3 volume ratio) for 4 hours at 40 °C inside an ultrasonic agitator. The formation of functional groups on the CNTs was detected using a Fourier Transform Infrared (FTIR) spectrometer (Spectrum 2 FTIR, Perkin-Elmer, Singapore). Afterward, the functionalized CNTs were extracted from the colloidal solution by filtration using filter paper and examined for any damages caused during functionalization under a high-resolution transmission electron microscope (HR-TEM) (JOEL 2010 F, Tokyo, Japan). A dispersion test was conducted with functionalized CNT to check for its dispersion behavior (Figure 3.1).

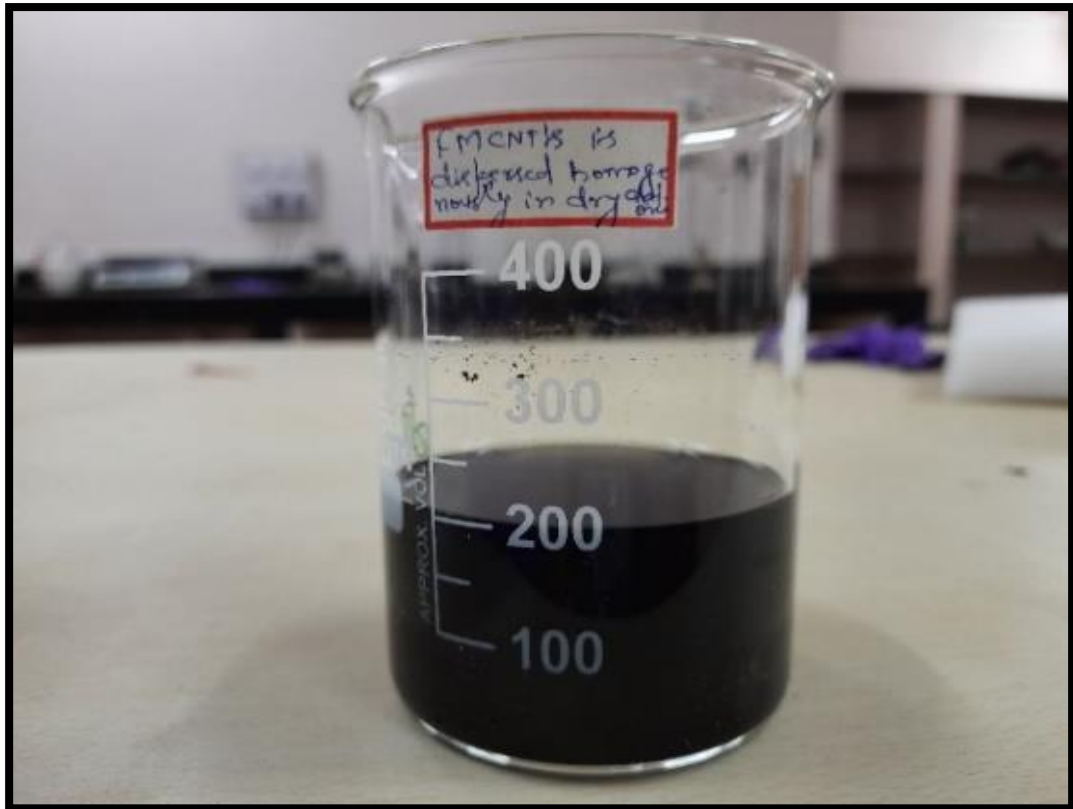


Figure 3.1 Photograph of functionalized MWCNT in acetone shows complete dispersion.

3.2.3 Size and morphology of powders

Field Emission Scanning Electron Microscope (FESEM) (7610F PLUS, Jeol, Japan) operating at 15 kV was used to examine the morphology of the feedstock and composites using backscattered electron images. Energy dispersive spectroscopy (EDS) equipped with FESEM was used to analyze the specimen's elemental composition and dot mapping (2% CNT composite). The degree of dispersion of CNTs in the matrix was determined by processing the FESEM images according to the procedure reported by Jambagi et al. (2015). For HA-based composites, Transmission Electron Microscopy (TEM) analysis was used in bright-field mode and operated at 200 kV (JOEL 2010 F, Tokyo, Japan).

3.2.4 Phase Identification and crystal size

X-ray Diffractometer (XRD), Empyrean 3rd Gn, Malvern PANalytical, Netherlands,

with CuK α radiation (wavelength of 1.54 Å) operating at 45 kV and 40 mA was used to identify the phase constituents of the powder samples. Data were acquired for 2 θ values between 20° and 60° with steps of 0.002°. The crystallinity % for the samples was determined using equation 3.1. The average crystal size was calculated for all the planes using the Scherrer equation (Sarath Chandra et al. 2012).

$$\text{Crystallinity \%} = (\sum A_c) / (\sum A_c + \sum A_a) \quad (3.1)$$

Where $\sum A_c$ = Sum of the areas of all HA crystalline peaks, $\sum A_a$ = Sum of areas under amorphous peaks.

3.2.5 Raman spectroscopy

Raman spectra were acquired under ambient conditions with a Compact Raman Spectrometer, Renishaw, UK, operating in 180° backscattering geometry. Spectra were collected through 532 nm excitation wavelength with laser power of 10%, a 50x objective focusing the excitation laser on a ~ 2 μ m diameter spot.

3.2.6 Fourier transform infrared spectroscopy (FTIR)

FTIR spectroscopy (Spectrum 2 FTIR, Perkin-Elmer, Singapore) was performed on samples (HA and HAC2) scanned from 4000 cm^{-1} to 500 cm^{-1} . To perform the analysis, ~200 mg of each powder was mixed with ~2 mg of potassium bromide (KBr), a binder, to maintain low humidity levels. Discs were produced in a hydraulic press (PCI Analytics, Maharashtra, India).

3.2.7 Zeta potential/Surface charge

The zeta potential (ZP) of all the bio-ceramic powders (Table 1) with and without respective surfactants were measured using Anton-Paar, LitesizerTM 500, Austria, equipped with a 40 mW semiconductor laser ($\lambda = 658$ nm). 10 mg of each sample (Table 1) was dissolved in 100 mL of 1 mM NaCl aqueous solution and sonicated for 15 minutes for complete dispersion. The pH of the solution was varied in the 2–12 range by adding dilute NaOH or H₂SO₄.

3.3 Hemocompatibility assessment of powders

Any newly developed biomaterial is first investigated for its hemocompatibility. The evaluation is done by ISO 10993-4, which essentially examines the suitability of biomaterials for clinical use (Weber et al. 2018). This ISO guideline for hemocompatibility evaluation is divided into many categories, out of which hemolysis, coagulation assays, platelet adhesion, and platelet activation are widely used and selected for the current study (Laranjeira et al. 2016).

3.3.1 Hemolysis study

A hemolysis test of the HA and its based composites (Table 4.1) with varying concentrations was performed with fresh human blood (Ooi et al. 2019). 3 mL of blood was collected from a healthy volunteer in an anticoagulated tube (K₃EDTA). The hemoglobin concentration of the sample was determined by an automated blood cell counter (Sysmex K350, Hamburg, Germany) to check for its quality. Five different concentrations (5, 10, 20, 40, and 80 mg/5 mL) of solutions were prepared in 10 mL sterile test tubes by adding the powders to the saline solution at a predetermined ratio. The test tube was then ultrasonicated to disperse powders in the solution completely.

100 µL of anticoagulated whole blood (WB) was pipetted to the tubes with prepared samples. For positive control, 100 µL of blood was added to the distilled water (DW) tube (100 µL blood/5 mL DW). For negative control, 100 µL of blood was added to the saline solution (100 µL blood/5 mL saline). All the tubes were then incubated for 60 minutes at 37°C. During the incubation time, tubes were gently agitated every 10 minutes. After incubation, the tubes were centrifuged for 10 minutes at 3000 rpm using a laboratory centrifuge (REMI R-8C BL, REMI Elektrotechnik LTD., India). This settles down the particles and the undamaged RBCs at the bottom of the tube to obtain a clear supernatant. The amount of free hemoglobin released from the rupture of RBCs in the supernatant was determined by measuring its absorbance value at 545 nm using a Microprocessor visible spectrophotometer (Model-2306, Electronics India). A pictograph explains the hemolysis study procedure (Figure 3.2). The % hemolysis was calculated using equation 3.2 (Komath and Varma 2003).

$$\% \text{ hemolysis} = (\text{OD}_{\text{test}} - \text{OD}_{\text{negative}}) / (\text{OD}_{\text{positive}} - \text{OD}_{\text{negative}}) \quad (3.2)$$

OD_{test} is the absorbance for powder samples, $OD_{negative}$ is the absorbance for the negative control, and $OD_{positive}$ is the absorbance of the positive control. As per the ASTM standard, if hemolysis induced by biomaterial is $<5\%$ = highly hemocompatible, within 10% = hemocompatible, and $>20\%$ = non-compatible.

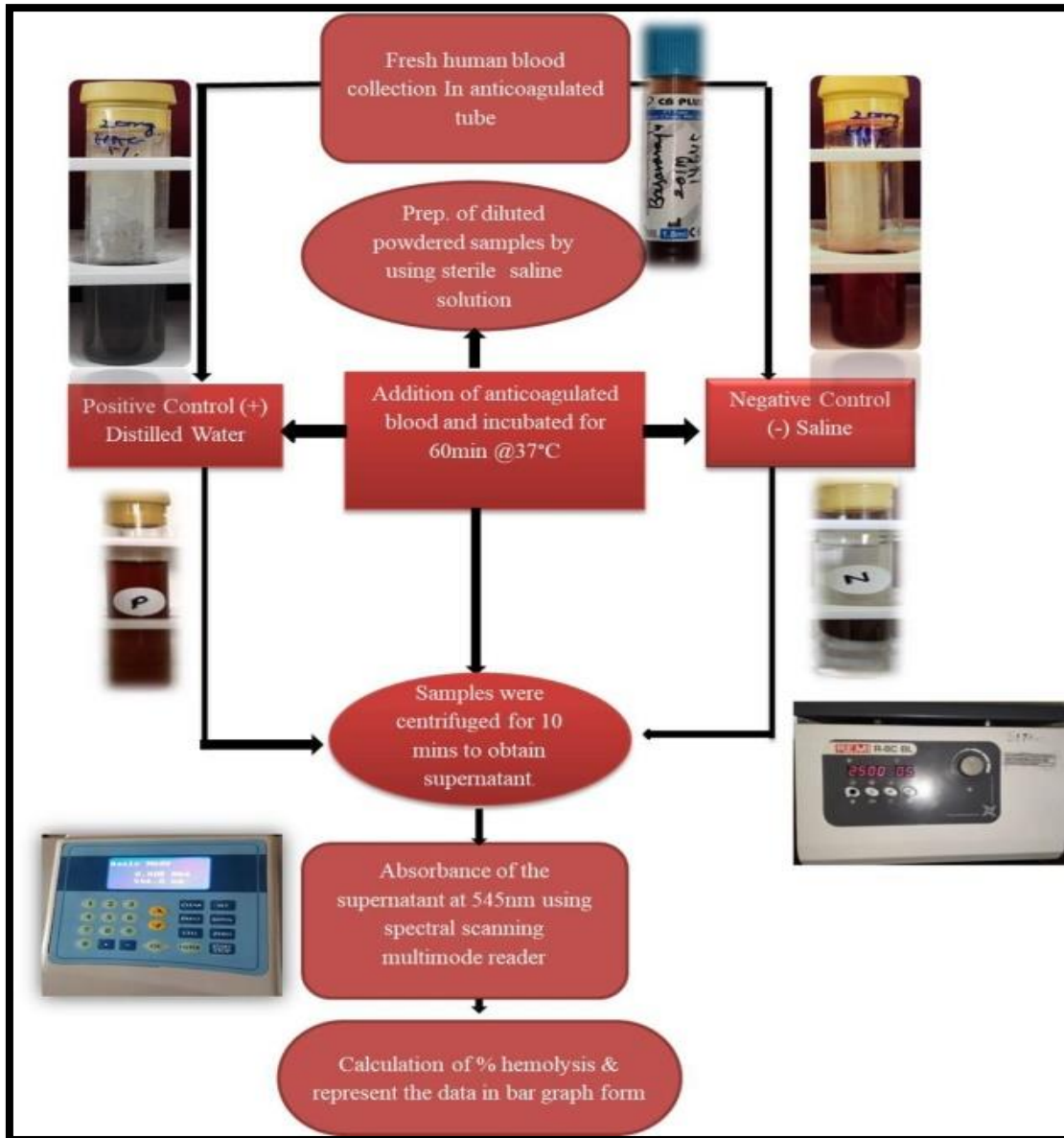


Figure 3.2 The pictograph shows the procedure for conducting a hemolysis test for HA and its based composites (Shankar et al. 2024a).

3.3.2 Whole blood clot study

The sample was assessed for its thrombogenicity using a whole blood clotting assay. Figure 3.3 represents the pictorial representation of the blood clotting assay procedure.

WB donated by the volunteer was collected in 2 mL sodium citrate tubes (Labtech Disposables, Gujarat, India) and tested for quality, with a total of 1.8 mL collected. The WB was mixed with 100 μ L of CaCl_2 solution (0.1M, AMD Labs, Bengaluru, India) to initiate the clotting effect. Test tubes were filled with 80 mg of various powders (Table 1) and a control sample (100 μ L CaCl_2 -blood without powders). Each sample tube was labeled with different timings, and 100 μ L of CaCl_2 -added blood was pipetted into the tubes. It was essential to ensure that the CaCl_2 -added blood was instant to prevent clotting before pipetting. Once the predetermined time (5, 15, 25, 35, and 45 minutes) had elapsed, the samples were mixed with 3 mL of distilled water and incubated for another 5 mins. The erythrocytes not trapped in the clot were lysed, releasing hemoglobin into the water. The water-added tubes were centrifuged at 3000 rpm for 10 minutes to obtain clear supernatant. The absorbance value at 540 nm using a Microprocessor visible spectrophotometer (Model-2306, Electronics India) was measured to assess the hemoglobin concentration of each sample. The absorbance value was inversely related to the blood clot formed on the sample (Manivasagam and Popat 2020).

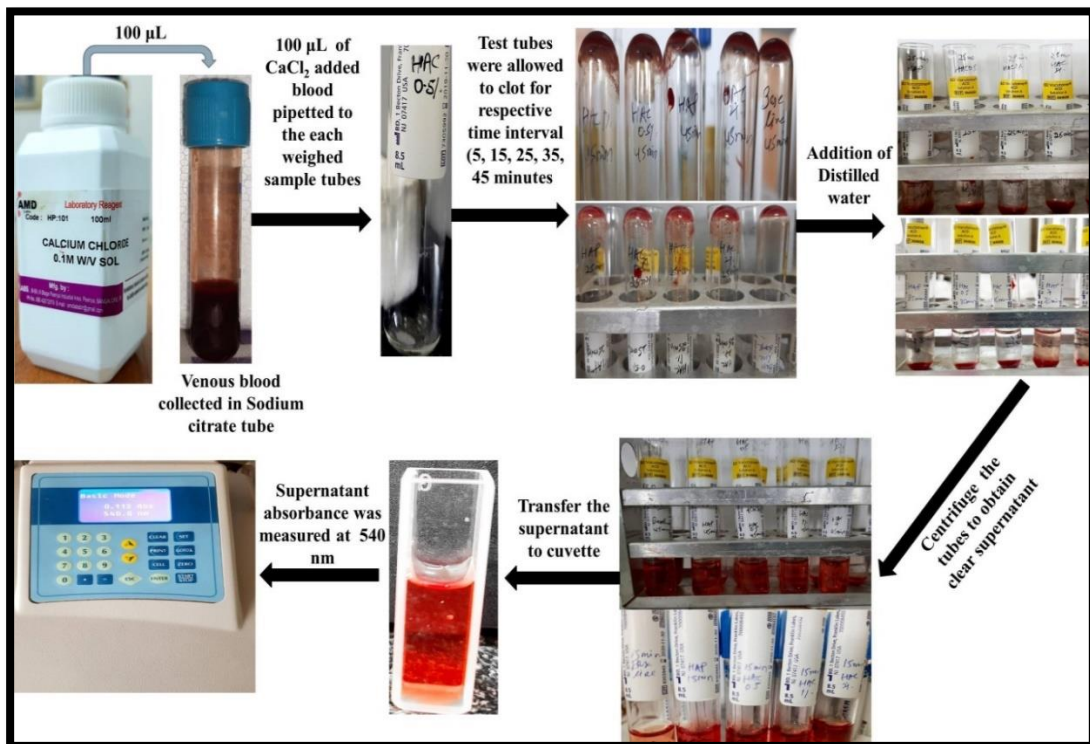


Figure 3.3 Pictograph depicts the procedure for conducting a whole blood clot test (Shankar et al. 2024a).

3.3.3 Platelet adhesion and activation study

Platelet-rich plasma (PRP) was created through a double centrifugation process using WB donated by volunteers. Figure 3.4 illustrates the method for generating PRP from WB and conducting the platelet adhesion test. Eppendorf tubes containing different concentrations (5, 20, and 80 mg) of powdered samples, collagen-glass beads (positive control), and polypropylene beads (negative control) had 600 μL of platelet-rich plasma (PRP) added to them and were incubated at 37 $^{\circ}\text{C}$ for 1 hour. After incubation, 600 μL of Phosphate-Buffered Saline (PBS) with a pH of ~ 7.4 was added to the tubes and incubated for 20 minutes to remove weakly adhered platelets. The PBS-platelet suspensions were counted twice with a hematology analyzer (Sysmex XN-350 Hematology Analyzer, Japan). The same procedure was repeated with PRP alone (600 μL PRP and 600 μL PBS; no sample).

This study aimed to measure the number of platelets adhered to the samples. The platelet adhesion % was estimated by quantifying platelet depletions from the PRP suspension using equation 3.3 (Amarnath et al. 2006).

$$\% \text{ Platelet adhesion} = (\text{PC}_{\text{initial}} - \text{PC}_{\text{samples}}) / (\text{PC}_{\text{initial}}) \times 100 \quad (3.3)$$

Where $\text{PC}_{\text{initial}}$ is the platelet count in the pure PRP with PBS without adding sample (number of platelets/ μL), $\text{PC}_{\text{samples}}$ is the platelet count in the PBS-platelet suspension with incubated samples (number of platelets/ μL). Platelet activation was studied by observing the changes in platelet morphology when adhered to the samples. The samples after the test were fixed with a mixture of buffered glutaraldehyde (2%) and formalin solution (to fix the adhered platelets) at room temperature for 30 minutes and rinsed three times with DW. Then, the samples were dehydrated at increasing alcohol concentrations (20, 50, 90, and 100%). The samples were immersed in each alcohol solution for 5 minutes and dried at room temperature. The samples were gold sputtered and observed for platelet structure using FESEM.

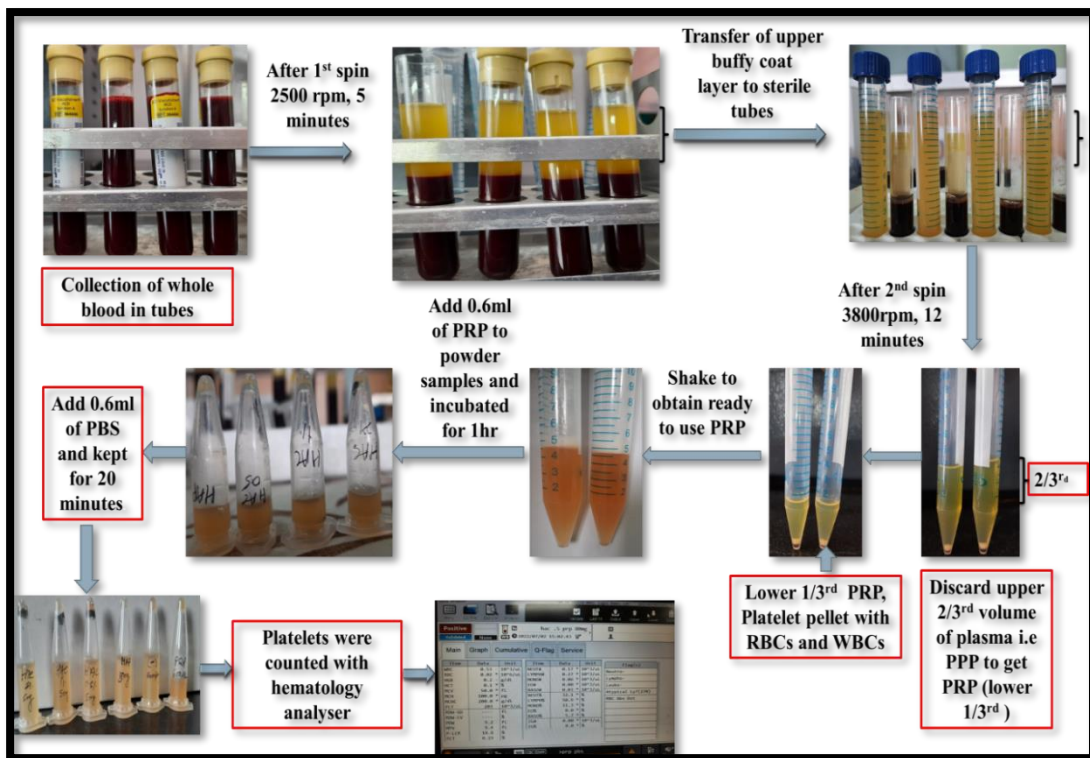


Figure 3.4 The pictograph shows the procedure for generating PRP from whole blood, followed by the platelet adhesion test methodology (Shankar et al. 2024a).

3.3.4 Coagulation Assays

Coagulation assays are functional bioassays that rely on comparison with a control. Most routine coagulation investigations are performed on platelet-poor plasma (PPP). Ideally, PPP should have a platelet count of less than $10000/\mu\text{l}$ (Raditya and Hernaningsih 2020). The two commonly used coagulation tests— Prothrombin time (PT) and the activated partial thrombin time (aPTT), have defined two pathways of coagulation activation: the extrinsic and intrinsic path, respectively.

Prothrombin time (PT)

PPP was created from WB using the process described in Figure 3.5. The platelet count was determined to be $9 \times 10^3/\mu\text{l}$ and was utilized as the PPP for PT and aPTT research. The PT assay measures the clotting time of the plasma that has been re-calcified (calcium restored) in an optimal concentration of tissue extracts (thromboplastin). It shows the overall efficiency of the extrinsic clotting system. A mixture of HA-based

samples (Table 1) with varying concentrations (5, 20, and 80 mg) and negative control (polypropylene beads) was prepared by combining 5 mg of the sample with 1 mL of PPP and then incubated for 1 hour. In this test, the first step is to add 200 μ l of the rabbit brain thromboplastin, PT reagent (Uniplastin, Tulip Diagnostics Private LTD. Goa, India), in a cuvette fitted with bead. The reagent was incubated for 180 seconds. After incubation, 100 μ l of plasma from the prepared suspension was added, and the clot was permitted to form. The results were recorded as the triplicate clotting time (in seconds) mean, using a 2-channel Hemostasis Analyzer, Hemostar XF 2.0, India (as shown in Figure 3.5 (a)).

Activated Partial Thrombin Time (aPTT) Study

This test helps to determine the duration of plasma clotting after the activation of contact factors, along with the addition of phospho-lipid and CaCl_2 , but without the addition of tissue thromboplastin. A mixture of HA, HAC0.5, HAC1, and HAC2 was prepared with varying concentrations of 5, 20, and 80 mg, along with a negative control (polypropylene beads). The sample (5 mg) was mixed with 1 mL PPP and then incubated for 60 minutes. 100 μ L of the sample's PPP was then pre-incubated for 3 minutes with a 100 μ l contact activator (Liquicelin-E, Activated Cephaloplastin reagent, Tulip diagnostics (P) LTD. Goa, India) in a cuvette having stirrer. This phase of the test activates FXIIa, which cleaves FXI to FXIa. However, coagulation does not proceed beyond this point without calcium. After the incubation, 100 μ L CaCl_2 (0.025 mol/L, AMD Labs, Bengaluru, India) was added. Once CaCl_2 restores calcium, FXIa activates FIX, and coagulation follows. The clotting time was recorded using the 2-channel Hemostasis Analyzer, Hemostar XF 2.0, India (Figure 3.5 (b)).

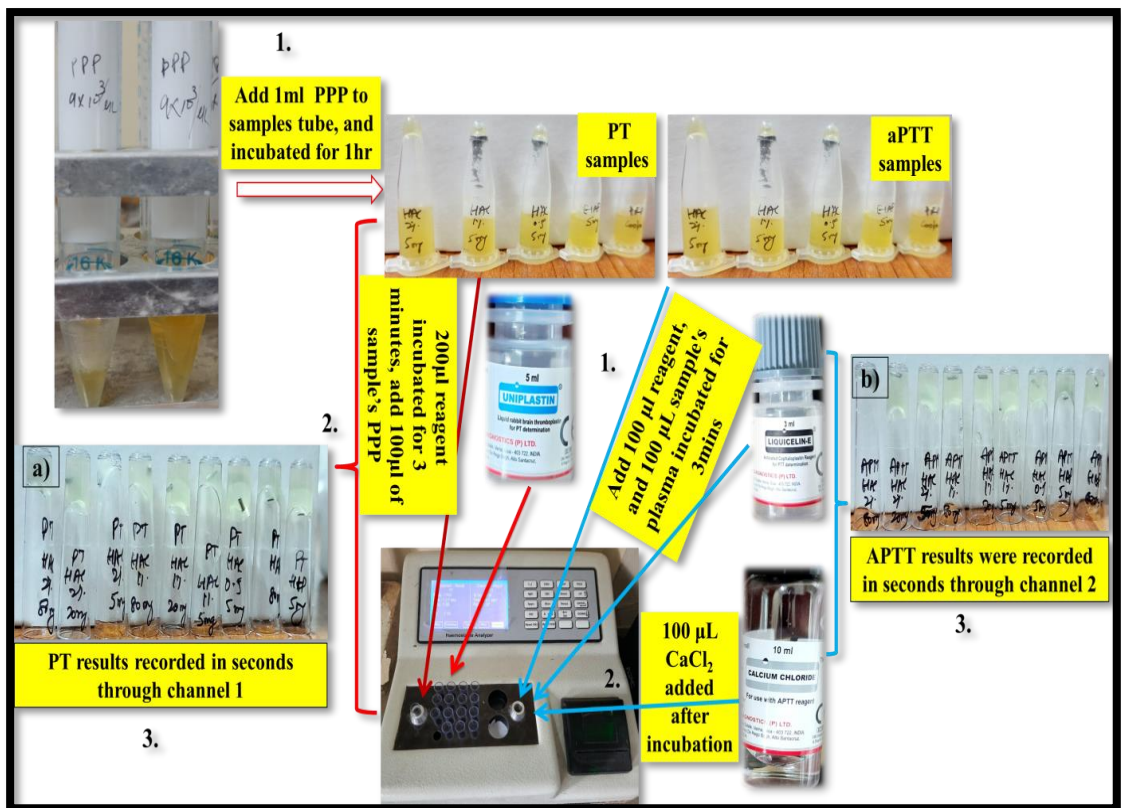


Figure 3.5 The pictograph depicts the procedure for conducting a coagulation assay with PPP (a) PT test and (b) aPTT test (Shankar et al. 2024a).

3.4 Coating deposition

Ti-6Al-4V sheets were cut into different sizes (3 x 10 mm disc and 20 x 20 x 3 mm) for various characterizations and used as substrate. The samples were coated with HA powder (CAPTAL 60-1) from Plasma Biotol, UK. The purity of the HA powder was 99%, as reported by the manufacturer, which is greater than the 95% requirement for HA powder. Further, APS is the only FDA-approved thermal spray technique for obtaining HA coating. Therefore, the current study aims to evaluate various processes among the thermal spray family that operate from very high to low temperatures to get a biocompatible and mechanically sound HA coating for clinical use. Titanium coupons were coated with three different thermal spray coating techniques: APS, FS, and HVOF. The rationale behind selecting these particular processes and equipment is explained here. First, APS was chosen for the current study as it is the only FDA-approved technique for producing HA implants and is therefore used as a reference for other methods. This study uses a 40 kW plasmatron Metco 3 MB, Westbury, NY, USA, to

obtain the HA coating, a well-established equipment for producing HA coatings as per the literature (Celik et al. 2005). However, the limitations associated with APS (phase change) are a major concern for HA coatings. Therefore, different low-temperature operated equipment are explored here. Flame spray (CERAJET, MECPL, Jodhpur) is selected as it is a high-velocity (~300 m/s) version of a flame spraying system with an operating temperature range of 2600-3500 °C (Singh et al. 2014), much lower than APS. It can potentially mitigate the phase changes of HA that directly impact the implant properties. Furthermore, HVOF spray has the lowest operating temperature and very high particle velocity (600-800 m/s), among other characteristics. This could provide a significant advantage in reducing the phase changes of HA, potentially enhancing the implant's properties. The current study utilized DJH 2600 from Sulzer Metco, Inc., Westbury, NY, a well-established equipment for producing HA coatings in the literature (Vilardell et al. 2020). The operating parameters for various processes have been adopted from prior literature, with some modifications based on preliminary experiments. This was mainly done for HVOF and plasma spray experiments to attain a high level of crystallinity. For instance, in HVOF spraying, the hydrogen-to-oxygen ratio has been reduced to mitigate the harsh temperature of fuel combustion (Hermann-Muñoz et al. 2019). From here onwards, bare titanium, Plasma-HA, Flame-HA, and HVOF-HA coatings will be referred to as Ti, APS, FS, and HVOF, respectively.

Table 3.1 Deposition parameters for Atmospheric Plasma Spray (APS) (Hadipour et al. 2015; Method 2018), Flame Spray (FS) (Singh et al. 2014), and High-velocity oxy-fuel (HVOF) (Vilardell et al. 2020) - HA coatings.

APS		FS		HVOF	
Parameters	Values	Parameters	Values	Parameters	Values
Argon flow (scfh)	80-90	Oxygen flow (slpm)	45	Oxygen flow (scfh)	30-34
Hydrogen flow (scfh)	15-18	Acetylene flow (slpm)	55	Hydrogen flow (scfh)	55-60
Current (A)	500	N ₂ Carrier gas (scfh)	20	PFR (g/min)	45-50
Voltage (v)	65.7	PFR (g/min)	35	-	-
PFR (g/min)	35	-	-	-	-
SOD (cm)	10	SOD (cm)	20	SOD (cm)	20

scfh = standard cubic feet per hour, slpm = standard liters per minute.

3.5 General characteristics of the deposited coatings

A Field Emission Scanning Electron Microscope (FESEM) (7610 FPLUS, Jeol, Japan) was used to examine the microstructural details of the HA powder and the coatings. The cross-sectional FESEM images were used to assess the thickness and porosity of the coatings with the help of Image J Software. The coatings' elemental composition was analyzed using energy-dispersive X-ray Spectroscopy (EDS) equipped with FESEM. The Image J software was used to process the FESEM images to determine the particle size distribution of HA particles. To achieve this, the diameter of 270 particles from the FESEM images was measured, and the size histogram was fitted with a log-normal function (Jalili et al. 2019; Paswan et al. 2021). The surface roughness (Ra) of the coating surface was measured using a 3D-Non-contact Profilometer (ST400, Nanovea, USA). The phase constituents of the samples were identified by using an X-ray Diffractometer (XRD), Empyrean 3rd Gn, Malvern PANalytical, Netherlands, with CuK α radiation (wavelength of 1.54 Å) operating at 45 kV and 40 mA. Data were collected for 2 θ values between 20° and 60° with steps of 0.002°. The fraction of crystalline HA phase in the coatings was calculated using equation 3.1. Raman spectra were collected to analyze the HA phases of the samples. The measurements were done using a Compact Raman Spectrometer made by Renishaw, UK. The zeta potential (ZP)

or surface charge of the HA powder was evaluated in physiological saline solution at pH-7.4. The measurements were carried out using Anton-Paar, Litesizer™ 500, Austria, equipped with a 40 mW semiconductor laser ($\lambda = 658 \text{ nm}$). The contact angle of the samples was measured using a sessile drop method with a Kyowa contact angle meter (DME-211, Kyowa Interface Science Co., LTD., Japan). For this, two μL of milli-Q- H_2O water was dropped on the surface and left for 10 seconds to stabilize. The adhesion strength of the coating was tested using a conventional progressive scratch tester (TR-101, DUCOM, India). Three scratches were made under a progressive load of 2 to 100 N with a scratch velocity of 0.1 mm/sec and a stroke length of 10 mm. The scratch tester had a Rockwell C-type conical indenter with an apex angle of 120° and a tip radius of 100 μm . The critical load of failures was assessed using the 3D profile of the scratch and the microscopic images. The polished cross-sectional area of the samples was subjected to an indentation load of 200 g (1.96 N) and a dwell period of 10 s using a Vickers microhardness tester (OMNITECH, S-Auto, India). The average value of ten indentations was taken to calculate hardness, which can be evaluated from the following relationship (Chavana et al. 2022).

$$H = \Psi \times 1.8544 P_L / (2a)^2 \quad (3.4)$$

Where P_L is the indentation load, Ψ is the calibration factor, and $2a$ is the diagonal length of the indentation impression (Figure 3.6). The data for each investigation were presented as mean \pm SD (standard deviation). The unpaired comparison t-test determined the significance of the results. P values of <0.05 (2-tailed) were considered as significant.

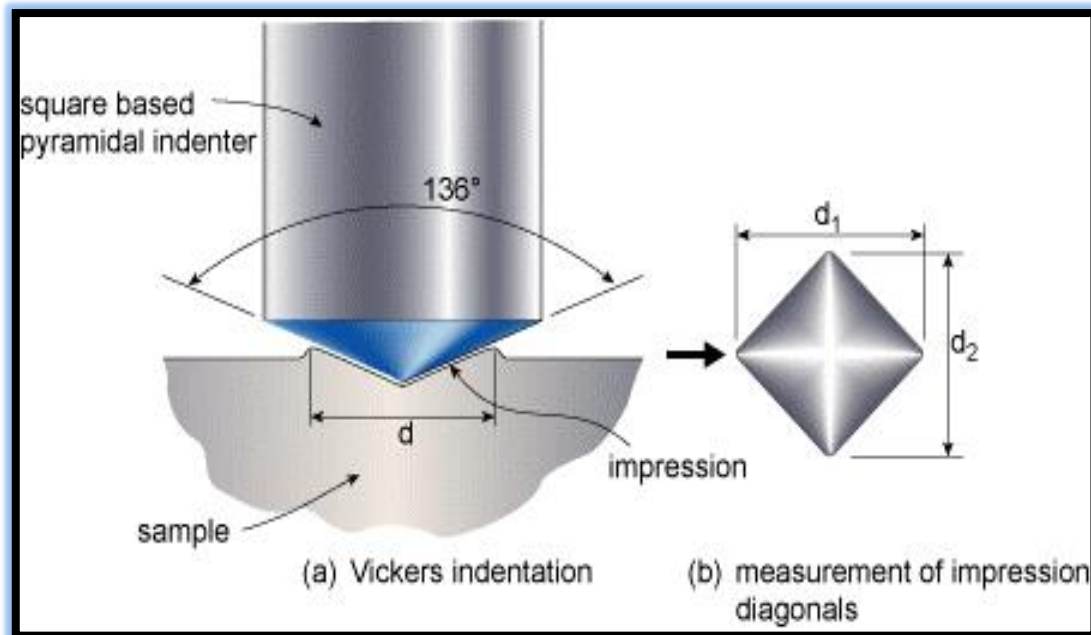


Figure 3.6 Schematic principles of operation of Vickers hardness machine (a) and Vickers hardness test (Kah et al. 2011).

3.6 Simulated Body Fluid (SBF) immersion test

A study was conducted to investigate the formation of bone-like apatite on samples using SBF prepared according to the procedure described in (Lima et al. 2005). The samples were weighed as W_1 before being immersed in 30 mL of SBF solution and incubated in sterile polyethylene containers at 37°C. The SBF solution was renewed every 48 hours to prevent saturation or absorption by the samples. The study was conducted for 15, 30, and 60 days, and after each time point, the samples were removed, washed twice with distilled water, and air-dried at 37°C. The weight gain % of the samples was calculated by $((W_2 - W_1) / W_1) \times 100$, where W_2 is the weight of the samples after apatite growth. The dried samples were then investigated using FESEM equipped with EDS to examine the grown apatite structures.

3.7 Hemocompatibility assessment of the coatings

3.7.1 In-vitro hemolysis study

The samples were kept in contact with human blood to verify their cytotoxicity effects

for their use as biomedical implants. 1.8 mL blood was collected and gently mixed with 0.2 mL sodium citrate in citrate tubes (Labtech Disposables, Gujarat, India). The samples were placed in sterile tubes containing 10 mL of saline and incubated at 37°C for 30 min for thermal equilibration. The blood was diluted with sterile saline to a ratio of 4:5. Then, 100 μ L of the diluted blood was added to the test tubes and mixed gently. Blood with distilled water (DW) served as a positive control (DW causes large-scale rupture of RBCs). For the negative control, a sterile saline solution was used (it does not rupture RBCs). All samples and controls were incubated at 37°C for 60 minutes. After incubation, all the tubes were centrifuged for 10 minutes at 3000 rpm using a laboratory centrifuge (REMI R-8C BL, REMI Elektrotechnik LTD., India). The centrifuging process settles down the denser elements at the bottom of the tube, leaving behind a clear supernatant. The absorbance/optical density (OD) of the free hemoglobin due to damaged RBCs in the supernatant was measured by a Microprocessor visible spectrophotometer (Model–2306, Electronics India) at a wavelength of 540 nm (Singhal and Ray 2002). The % hemolysis is calculated based on equation 3.2 (Sarath Chandra et al. 2012). The experiments were run five times, and the obtained values were compared with the ASTM standard (Manivasagam and Popat 2020).

Additionally, imaging was carried out using a biological microscope (CX21i, Olympus, India) to ascertain the condition of RBCs. For this, a drop of supernatant was smeared on the glass slide and allowed to dry off. The slides were covered entirely in Leishman stain and left for three minutes. Afterward, the NaCl buffer solution was poured over the slide and left for another seven minutes. Finally, the slides were rinsed with water, dried, and imaged.

3.7.2 Whole Blood (WB) clot assay

The quantity of free hemoglobin in unclotted blood was measured to determine the clotting ability of the blood samples. 1.8 mL of blood was collected in sodium citrate tubes and used immediately to begin the clotting process. The tubes were marked with different time points, such as 15, 30, and 45 minutes, and 0.1M CaCl₂ solution (AMD Labs, Bengaluru, India) was added in a 100 μ L amount. Following this, 100 μ L of CaCl₂-blood was pipetted onto the surfaces of the samples, which were then incubated

at 37°C for the designated time. After the predetermined time, 3 mL of DW was added to each tube to lyse the erythrocytes not entrapped in the blood clot formed. The tubes were further incubated for 5 minutes and then centrifuged at 3000 rpm for 10 minutes to obtain a clear supernatant. Using a microprocessor visible spectrophotometer (Model-2306, Electronics India), the amount of free hemoglobin in the supernatant released by the lysed red blood cells was measured at a wavelength of 540 nm. Five samples were tested for each time point for each condition. The absorbance value of free hemoglobin in the supernatant is inversely proportional to the blood clot-forming ability of the sample (Manivasagam and Popat 2020).

3.7.3 Platelet adhesion and activation study

Platelet-rich plasma (PRP) was generated using whole blood collected from young, healthy, non-smoking volunteers. A double centrifugation process was used to prepare the PRP. In the first step, the whole blood was centrifuged at 2500 rpm for 5 minutes (soft spin), which separated it into three distinct layers. The upper two layers (plasma, white blood cells, and platelets) were transferred to another sterile polypropylene tube. Then, a second centrifugation was performed at 3800 rpm for another 12 minutes (hard spin), which caused the denser elements (erythrocyte platelet) to settle at the bottom of the tube. The upper two-thirds portion is platelet-poor plasma (PPP) used for coagulation studies. The lower one-third plasma with platelet pellet was kept in a platelet agitator for 2 hours to obtain PRP. The platelet count was measured using a hematology analyzer (Sysmex XN-350, Hematology Analyzer, Japan). For this study, a disc of 10 mm diameter (n=3) was used, with no sharp edges. The samples were placed in Eppendorf tubes with 1 mL of PRP and incubated for 1 hour at 37°C. After incubation, the samples were rinsed three times with PBS to remove platelets that had adsorbed non-specifically on the surface. A hematology analyzer measured The platelet count twice, which counted the recovered PBS-platelet suspensions. The platelet adhesion % was estimated by quantifying platelet depletion from the PRP suspension using equation 3.3 (Amarnath et al. 2006).

Platelet activation was studied by observing changes in their morphology while adhering to the samples. After the test, the samples were fixed with a mixture of

buffered glutaraldehyde (2%) and formalin solution to set the adhered platelets, and then the plates were rinsed three times with distilled water. The samples were dehydrated in alcohol concentrations that increased gradually (20%, 50%, 90%, and 100%) for 5 minutes in each solution. After that, the samples were left to dry at room temperature. Finally, the samples were gold-sputtered and observed for platelet structure using FESEM.

3.7.4 Coagulation assays- PT and aPTT

Coagulation tests are bioassays that are practical and rely on comparison with a control. Platelet-poor plasma (PPP) is used for most routine coagulation tests, and PPP requires the platelet count to be ideally lower than 10,000/ μ L. The two most commonly used coagulation tests are PT and aPTT, which identify the extrinsic and intrinsic mechanisms of coagulation activation, respectively. To achieve thermal equilibrium, all samples are incubated with PPP at 37°C for 1 hour.

PT gauges the effectiveness of the extrinsic clotting system by measuring the clotting time it takes for the recalcified (restoration of calcium) plasma to clot in the presence of an optimal amount of tissue extracts (thromboplastin). This study is carried out in two steps. Firstly, 200 μ L of the rabbit brain thromboplastin, PT reagent (Uniplastin, Tulip diagnostics Private LTD. Goa, India), is added to a cuvette fitted with an iron bead and incubated for 180 seconds. After incubation, 100 μ L of plasma from each sample's tube is added, and the clot is allowed to form. The results are then expressed as the triplicate clotting time (sec) mean, recorded with a 2-channel Hemostasis Analyzer (Hemostar XF 2.0).

The aPTT study defines the intrinsic clotting time of the plasma after the activation of contact factors and the addition of phospho-lipid and CaCl₂ but without tissue thromboplastin. This study is conducted in three stages. First, 100 μ L of the contact activator (Liquicelin-E, Activated Cephaloplastin reagent, Tulip diagnostics (P) LTD. Goa, India) is added to a cuvette fitted with an iron bead and incubated for 180 seconds. Next, 100 μ L of the plasma sample is added to the cuvette and incubated for another 180 seconds. During this test phase, FXIIa is activated, which cleaves FXI to FXIa. However, coagulation does not proceed beyond this point without calcium. Finally, 100 μ L CaCl₂ (0.025 mol/L, AMD Labs, Bengaluru, India) is added and waited

for the clot to form. After the restoration of calcium by CaCl₂, FXIa activates FIX, and coagulation follows. Clotting time is recorded with 2-channel Hemostasis Analyzer.

3.8 Antimicrobial Analysis

An adapted disk diffusion approach was implemented to assess the qualitative antimicrobial effects of the HA coatings. The antimicrobial analysis was performed using *Escherichia coli* (*E. coli*, ATCC 25922) and *Staphylococcus aureus* (*S. aureus*, ATCC 25923), which are Gram-negative and Gram-positive bacteria. For the antimicrobial analysis, microbial suspensions were acquired for each strain and calibrated to an optical density of 0.5 McFarland (1.5×10^8 CFU/mL). The entire surface of the nutrient agar muller in Petri dishes was covered with suspensions. After injection, 10 mm sterile discs were placed on the surface of the inoculated agar, and the dishes were incubated for 24 hours at 37°C. Following incubation, the inhibition zone (mm) diameter was measured to determine the antimicrobial potential of the samples.

3.9 Tribological experiments

The performance of coated and uncoated implants was assessed under mode-I fretting conditions using a ball-on-flat setup tribometer (TRB3 Tribometer, Anton Paar, Austria), which created low-amplitude relative reciprocating tangential sliding conditions to mimic the contact conditions at articulating surfaces. The tribological study parameters were chosen carefully based on an orthopedic implant's wear and tear conditions within the human body and previous studies (Chen et al. 2019; Kataria et al. 2010; Lahiri et al. 2011). The samples, which were rectangular and measured 20 mm by 20 mm with a thickness of 3 mm, were affixed securely onto the sample stage. A steel ball, 6 mm ϕ , acted as the counter body. A 5 N load was applied to the samples with a sliding speed of 2.5 cm/s for a travel distance of 100 m. The experiments were conducted under dry and SBF conditions. The wear behavior was evaluated mechanically in dry conditions since they are more aggressive. At the same time, the SBF solution was used to simulate the wear condition of joints in the human body. The experimental setup for conducting a wear test under dry and wet conditions and the schematic illustration for the wear mechanism under the SBF environment are shown

in Figure 3.7 (a) and (b). Three wear tracks were made on each coating to increase the study's accuracy. The fretting tests were conducted at room temperature ($33\pm 4^\circ\text{C}$) with a relative humidity of $65\pm 15\%$. The wear track depth profile was collected using a 3D non-contact profilometer (ST 400, Nanovea, USA). The wear volume was determined from the wear track depth profile, and the wear rate (W_R) was calculated using equation 3.5. The extent of damage and imaging of the samples' worn surfaces were observed using FESEM. ImageJ software was used for quantitative particle size analysis in wear debris from FESEM images. Raman spectroscopy was utilized to study wear tracks and identify changes on the coating surfaces.

$$W_R = W_v / (P * S) \quad (3.5)$$

W_R is the wear rate ($\text{mm}^3\text{N}^{-1}\text{m}^{-1}$), W_v is the wear volume (mm^3), P is the applied load (N), and S is the sliding distance (m).

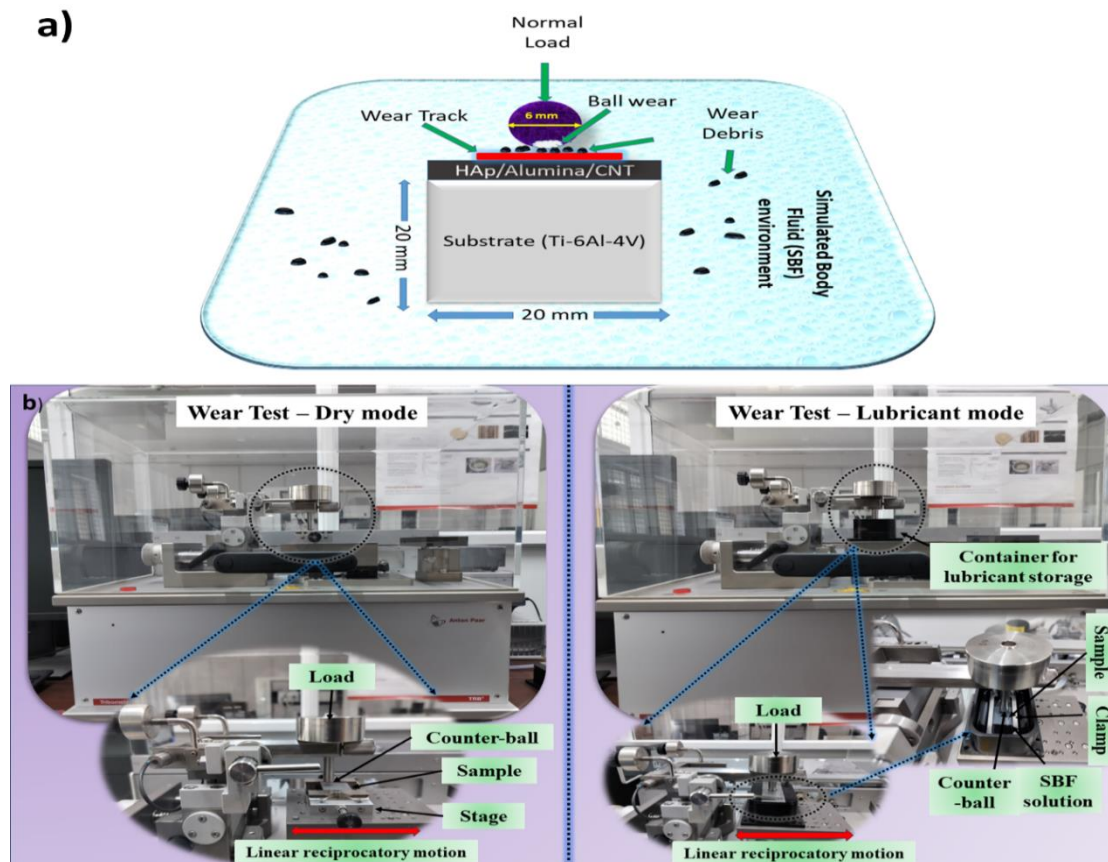


Figure 3.7 (a) Schematic illustration to show wear test mechanism under SBF environment, and (b) Experimental set-ups for wear test under dry and physiological (SBF) conditions.

3.10 In-vivo study

The methodology of this study was to implant best achieved coatings i.e., HVOF sprayed HA and HAC1 coated titanium rods in the distal femoral bone of New Zealand white rabbits to compare tissue, cell behavior, and bone interface around the implants using histological observations. 2 mm diameter x 6 mm length implants along with control- high-density polyethylene (HDPE) were implanted in the left and right femur bone, respectively.

A total of 4 female New Zealand White Rabbits were acclimatized for 6 days, and 3 females were used for implantation for one type of test sample. About 24 hrs before the surgery, the animal fur was closely clipped at the femur bone region of all 3 animals. No abrasion was found on the skin. On the day of surgery, all the animals were adequately anesthetized by intramuscular injection of ketamine and xylazine mixture (35 mg/kg and 5 mg/kg, respectively).

Three test item implants were implanted in the left femur bone of the first two rabbits, and 4 test item implants were implanted in the left femur bone of the third rabbit. Similarly, three control implants were implanted in the right femur bone of the first two animals, and 4 control implants were implanted in the right femur bone of the third animal, such that a total number of 10 test item implants were used. Animals were observed daily for clinical signs and macroscopic changes at implanted sites till termination day.

Individual animal body weight was measured on day 1 of acclimatization, day 1 of implantation, and after that on days 08, 15, 22, and at termination (29 days). All the animals were terminally sacrificed by giving a lethal dosage of sodium thiopentone, and a necropsy was performed for all the rabbits implanted sites along with surrounding bone tissue was collected and stored in 10% neutral buffer formalin (NBF) for histopathological examination. Gross pathology (external and internal) was performed. Figure 3.8 shows different stages involved in the in vivo implantation of HA-based implants in New Zealand white rabbits.

This study was performed as per the guideline ISO 10993-6:2016 - Biological

Evaluation of Medical Devices Part 6: Tests for local effects after implantation (Third Edition 2016-12), and following the ISO/IEC 17025:2017 and in compliance with OECD Principles of GLP. Further, the study follows the OECD Principles of GLP for testing of chemicals as specified by international [C (97)186/Final] legislation. Further, the use of animals for this study has been approved by Liveon Biolabs Private Limited, IAEC Approved Protocol No.: LBPL-IAEC-064-09/2023.

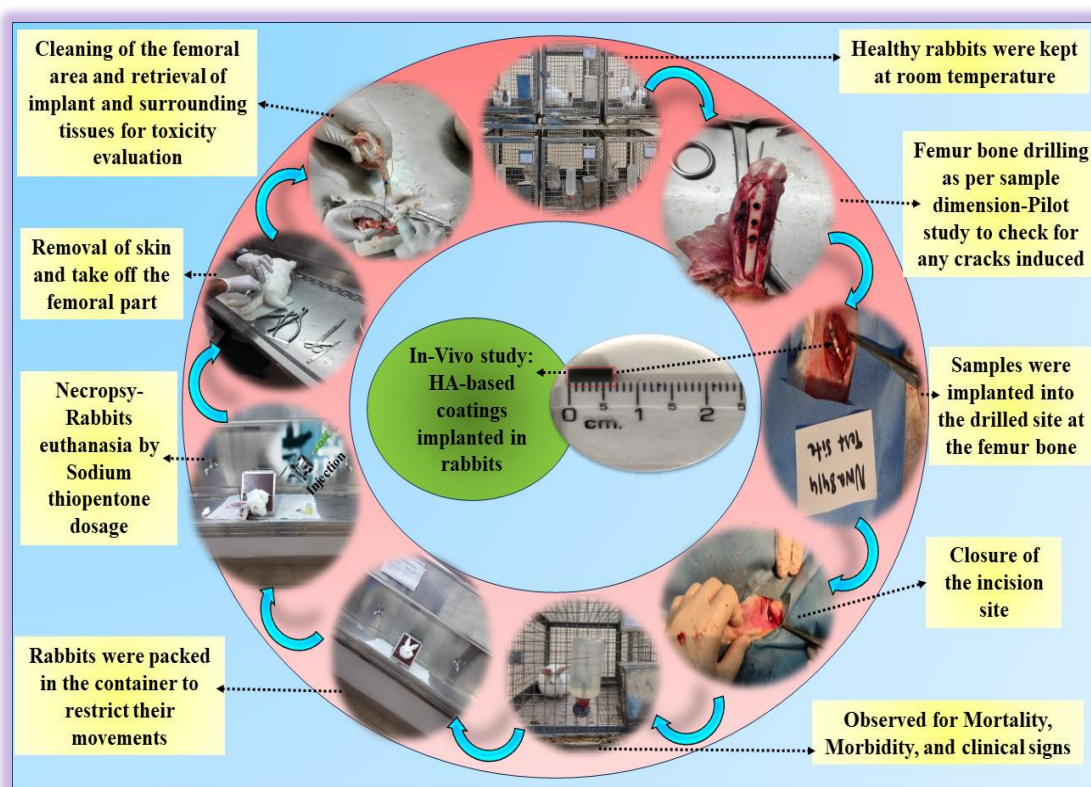


Figure 3.8 Different stages involved in the in vivo implantation of HA-based implants in New Zealand white rabbits.

3.11 Summary

This chapter dealt with the detailed experimental procedure followed in this research work. The procedures included the selection of feedstock and different methods used to assess their physiochemical properties, followed by their compatibility with human blood. Further, different HA coatings were observed for coating cross sections, phase changes, scratch, and hemocompatibility. One set of reinforced coatings was fabricated with the best thermal spray technique and tested for physiochemical, mechanical, wear, and biocompatibility properties. Finally, an in vivo study with rabbits was conducted

with HA-based implants. In the following chapters, results obtained from the experiments and the corresponding discussion are presented. The next chapter addresses the fabrication of composite powders and discusses their properties to find suitable compositions for further process.

CHAPTER 4 POWDER PREPARATION AND CHARACTERIZATION

4.1 Introduction

This chapter deals with the preparation of composite powders with various concentrations of alumina and CNT and analyzed for their morphology, the degree of dispersion and retention of CNT, the degree of crystallinity, phase determination, and crystallite size were evaluated and discussed. The feedstocks were then assessed for their biocompatibility with human blood.

4.2 Bio-ceramics composite preparatory method

Heterocoagulation of alumina and CNT was carried out based on the method described by (Jambagi et al. 2015). The zeta potential of all powders was measured with and without respective surfactants to gauge their net surface charge and determine the suspension's stability. The goal was to ensure complete dispersion of the electrostatically charged particles. Alumina was heterocoagulated with 1 wt.% CNTs in batches where 19 gm of alumina was suspended in 2 liters of distilled water (DW) and 800 mg SDS. The pH was adjusted to 8, causing the zeta potential to fall into the negative range (Figure 4.1 (a)). In another batch, 1 gm of CNT was suspended in 1 liter of DW with 1 gm CTAB, and the pH was adjusted to 8 using Dil. NaOH or Dil. H₂SO₄ (Figure 4.1 (b)). This caused the zeta potential to fall in the positive range, and at pH 8, the suspension showed maximum stability. It was discovered that both solutions were in maximum stable state at pH 8 ($> \pm 30$ mV, stable suspension) due to the electrostatic repulsion between their charged particles. The alumina suspension was then slowly added to the CNTs suspension with continuous stirring, triggering heterocoagulation and settling down the precipitate at the bottom of the container (Figure 4.1 (c)). The sediment was filtered and dried to obtain the powder. Other batches of different compositions (0.5wt.% and 2wt.%) were created using the same procedure. The heterocoagulated Alumina-CNTs composite was mixed (without balls) with HA at 300 rpm using isopropyl alcohol media for 12 hours in a Ball mill (Fritsch, Pulverisette 6, Fritsch, Germany). Alcohol facilitated the debundling of particles. The resultant powders obtained (Table 4.1) were dried for 120 hours at room temperature, stored in a vacuum, pathogen-free environment, and used for further studies.

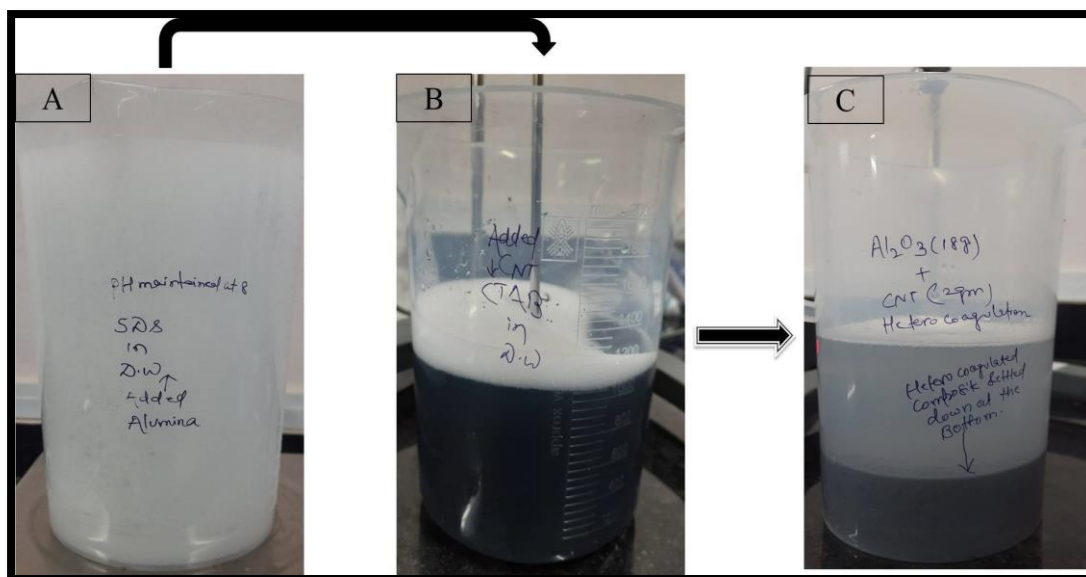


Figure 4.1 (a) Alumina suspended in DW with SDS surfactant at pH- 8, (b) FCNTs suspended in DW with CTAB surfactant at pH- 8, and (c) Heterocoagulated composite precipitated at the bottom of the container (Shankar et al. 2024a).

Table 4.1 Powders Designation with its processing description.

SL No.	Designation	Description
1.	HA	Hydroxyapatite
2.	AC0.5	Heterocoagulated 19.5 wt.% alumina and 0.5 wt.% CNTs (20 wt.%)
3.	AC1	Heterocoagulated 19 wt.% alumina and 1 wt.% CNTs (20 wt.%)
4.	AC2	Heterocoagulated 18 wt.% alumina and 2 wt.% CNTs (20 wt.%)
5.	HAC0.5	AC0.5 blended with 80 wt.% HA (alcohol media) in ball mill
6.	HAC1	AC1 blended with 80 wt.% HA (alcohol media) in a ball mill
7.	HAC2	AC2 blended with 80 wt.% HA (alcohol media) in ball mill.

4.3 Morphology

The powder labeled HA displayed a porous and spherical structure, with an average particle size range of approximately 40 μm (Figure 4.2 (a)). As noted in previous studies, this unique porous feature of HA is highly beneficial for cell growth and development. On the other hand, the particle size range of alumina varies between 20-55 μm and has an angular and blocky appearance (as seen in Figure 4.2 (b)). The TEM image reveals concentric walls and bulges. It grooves on the side wall and at the end of CNT tubes, which represents the $-\text{COOH}$ group's attachment and signifies the nanotube's functionalization (as depicted in Figure 4.2 (c)). In the heterocoagulated composite AC2, CNTs are readily adsorbed and cover the alumina surface due to their opposite charge (as seen in Figure 4.2 (d)). The CNT dispersion in the matrix should be uniform and consistent to ensure optimal results. FESEM images of the AC2 powder and the corresponding binary dot map are displayed in Figure 4.2 (e) and (f), respectively, and appear homogenous, with no large CNT patches found. Moreover, the average area % with a standard deviation from 96 segments was 29.35 ± 1.20 %. The standard deviation represents the degree of dispersion of CNTs in the ceramic powder, and the heterocoagulated powder (AC2) showed a dispersion index 1.20. In comparison, Jambagi et al. (2015) reported a dispersion index of 14 and 6 for the dry ball and wet ball mixed powders, respectively, for similar feedstocks, showcasing how heterocoagulation causes the debundling of agglomerated CNTs, leading to enhanced dispersion in the ceramic powder. Connections like V, Y, and T-junctions and bridging mechanisms, a characteristic of CNTs, can be seen in the HAC1 and HAC2 powders, as shown in Figure 4.2 (g) and (h). The images reveal hair-like CNT molecules (identified with black arrows) connected to the HA and alumina matrix via their end and side walls. This attachment occurs due to the electrostatic interactions between the ions, as illustrated in Figure 4.2 (i).

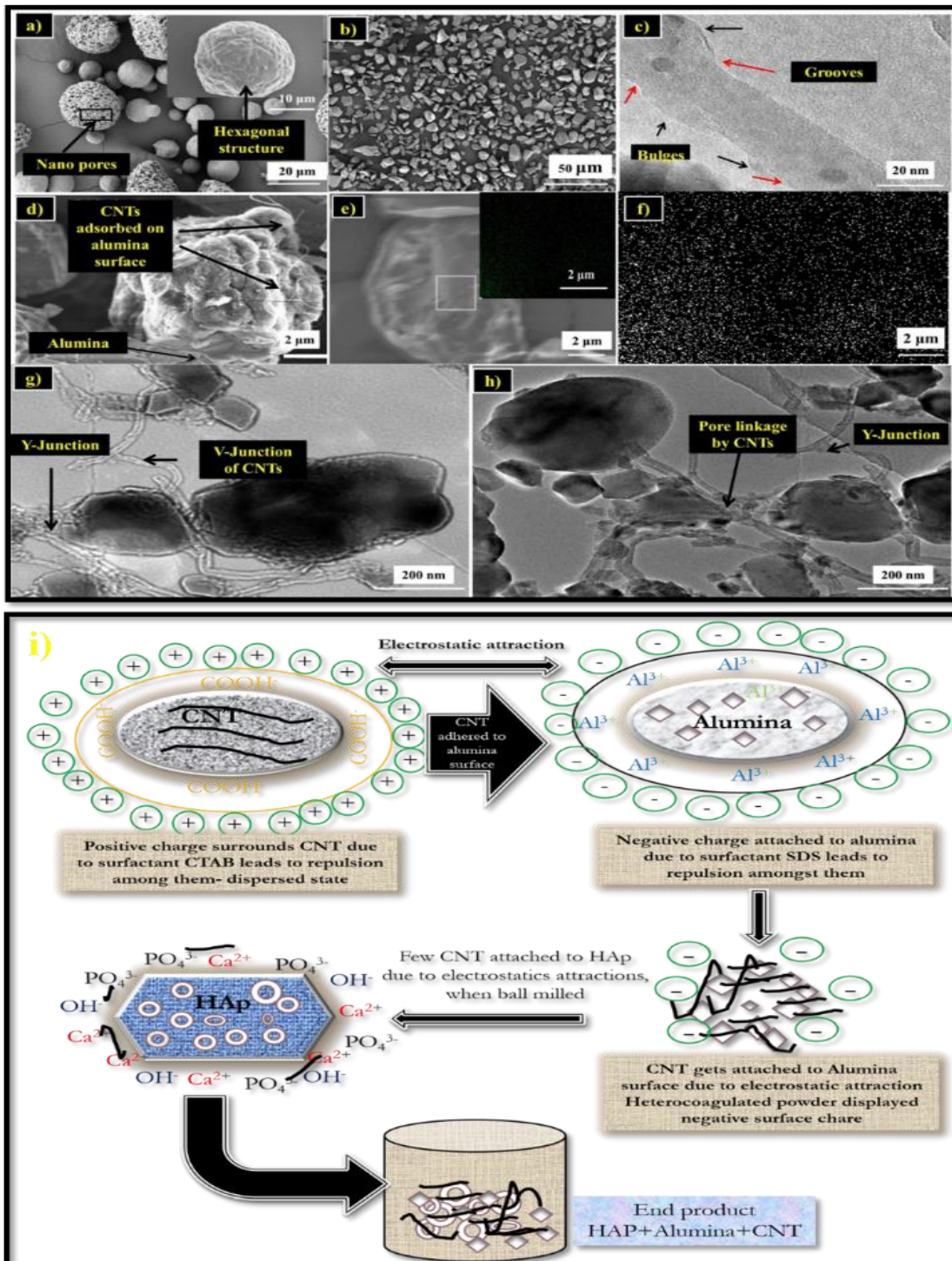


Figure 4.2 FESEM morphology for (a) HA, (b) Alumina, (c) TEM image for FCNT, (d) FESEM image for AC2 Composite, (e) Dot mapping for AC2, (f) Binary image for AC2 dot map shows the degree of dispersion of CNTs, (g and h) TEM image for HAC1 and HAC2, respectively showed different junctions formed by CNTs, and (i) schematic illustration to understand the electrostatic interaction between HA/Alumina/CNTs during powder preparation (Shankar et al. 2024a).

4.4 Phase identification and crystal size determination by XRD

Figure 4.3 (a-c) shows XRD patterns for the HA, AC2, and HAC2 powders. The hexagonal HA (ICDD PDF 072-1243) was confirmed by the peaks in Figure 4.3 (a). A minor trace of tetra calcium phosphate (JCPDS 025-1137) centered at 25.40° belonging to the (200) lattice plane was observed, consistent with a previous report. The peaks in Figure 4.3 (b) confirmed the presence of alumina particles (ICDD File No 046-1212), as reported by (Ferret et al. 2000). A high-intensity diffraction peak assigned to a graphite crystallographic (002) and (100) plane of CNTs was observed at 25.9° and 43.36° in Figure 2c (ICDD card No. 041-1487). As the CNT concentration in the composite increases up to 1wt.%, the peaks become sharper and more intense, indicating an increase in crystallinity with the reinforcement addition. However, a decrease in crystallinity was observed for the 2wt.% sample. The crystallinity % of the HA, HAC0.5, HAC1, and HAC2 composite was found to be 99.27, 99.69, 99.79, and 98.16 %, respectively, more than the required level (95%) (ISO 13779-:2000). The crystal size increased from 54.83 nm to 56.08 nm and 56.39 nm when 0.5% and 1% CNTs were added to the pure HA, respectively. As the CNT concentration increased from 0.5 to 1wt%, the crystal size didn't show much variation attributed to the small CNT concentration change. However, for the 2% CNTs sample, the crystal size was decreased to 52.74 nm. The change in crystal size may be attributed to the reinforcement effects (alumina/CNT). (Vignesh Raj et al. 2018) reported a decrease in the crystal size of the HA with the addition of alumina particles. The high degree of crystallinity observed in the synthesized sample made from the nanostructured feedstock surpasses those demanded by the standard, which is desirable for coating integrity.

4.5 Raman analysis

The Raman spectra of the feedstock powders and synthesized samples can be observed in Figure 4.3 (d-g). The study focuses on the region encompassing the phosphate (PO_4^{3-}) vibrational modes of HA. This is due to the structural significance of this area. The PO_4^{3-} peaks' ν_1 , ν_2 , ν_3 , and ν_4 modes were detected at 962, 400–490, 975–1150, and 560–620 cm^{-1} , respectively. A Raman spectrum that confirms peaks similar to those reported by Hermann-Muñoz et al. (2019) can be seen in Figure 4.3 (d). Alumina's

Raman spectra can be observed in Figure 4.3 (e), and the peak is very strong, with a frequency of about $\omega_0 = 470 \text{ cm}^{-1}$. Figure 4.3 (f) and (g) show two characteristic peaks of CNTs. The degree of disorder and the defects in the CNTs are depicted by the intensity ratio of D and G bands, which is 0.88 for COOH-CNT, confirming the presence of functionalized CNTs. (de Menezes et al. 2018) reported the ID/IG value as 0.72 for COOH-CNTs. The 'D' band of the first peak originates from the defects on the sidewalls and ends of CNTs, identified at 1331 cm^{-1} . The second peak of the G band is derived from the tangential stretching of the C-C bonds, located at 1582 cm^{-1} . Oxidation of CNTs breaks some of their bonds and inserts chemical groups (-COOH) that can be interpreted as structural defects. The HA, Alumina, and CNT bands can be seen in the same places, widths, and intensities for HAC2, demonstrating that reinforcements had no structural impact on HA.

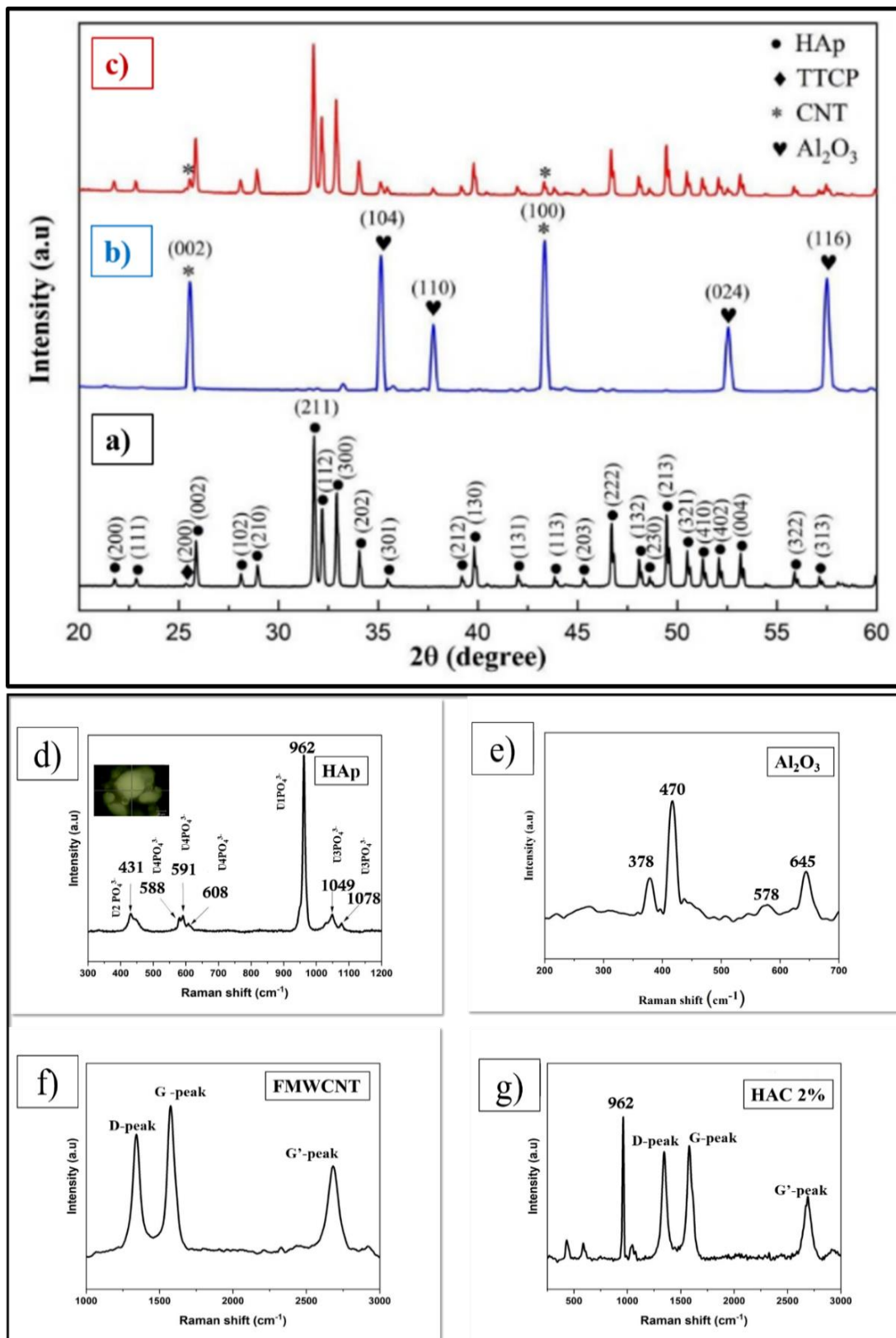


Figure 4.3 XRD spectra for (a) HA, (b) AC2, (c) HAC2, Raman spectra for (d) HA, (e) Alumina, (f) FMWCNT, and (g) HAC2 (Shankar et al. 2024a).

4.6 FTIR spectra analysis

Figure 4.4 depicts the FTIR spectra for HA and HAC2 powder. The spectra mainly identify the peaks for phosphate and hydroxyl groups of the HA. The bands found at 1051, 1095, and 961 cm^{-1} are the characteristic phosphate (PO_4^{3-}) stretching vibration bands. Further, due to O-P-O phosphate bending vibration, two bands can be identified at 571 and 461 cm^{-1} . The 633 and 3568 cm^{-1} absorption bands are assigned to the OH group's stretching and vibration modes, while the minor peak at 1635 cm^{-1} belongs to CO_2 . All the bands marked with black colored arrows confirmed the presence of pure HA. The pattern was comparable to other reported work (Ooi et al. 2019). The bands and wide stretched circles (green color) confirmed the functionalization of CNTs. The presence of the carboxylic group on the CNT wall was identified from the wide OH stretch in the 3750-3000 cm^{-1} range. Also, the carbonyl stretches (C=O, carboxylic group) range from 1700-1690 cm^{-1} , and an OH bend near 1000 cm^{-1} . Similar results for CNTs were reported by (Jambagi et al. 2015) and (Gupta and Saleh 2016). This indicates that the reinforcement addition does not change the basic structure of HA, and the same was confirmed with XRD and Raman spectra. These results align with the TEM observations, where no evident changes in nanoparticle morphology were observed.

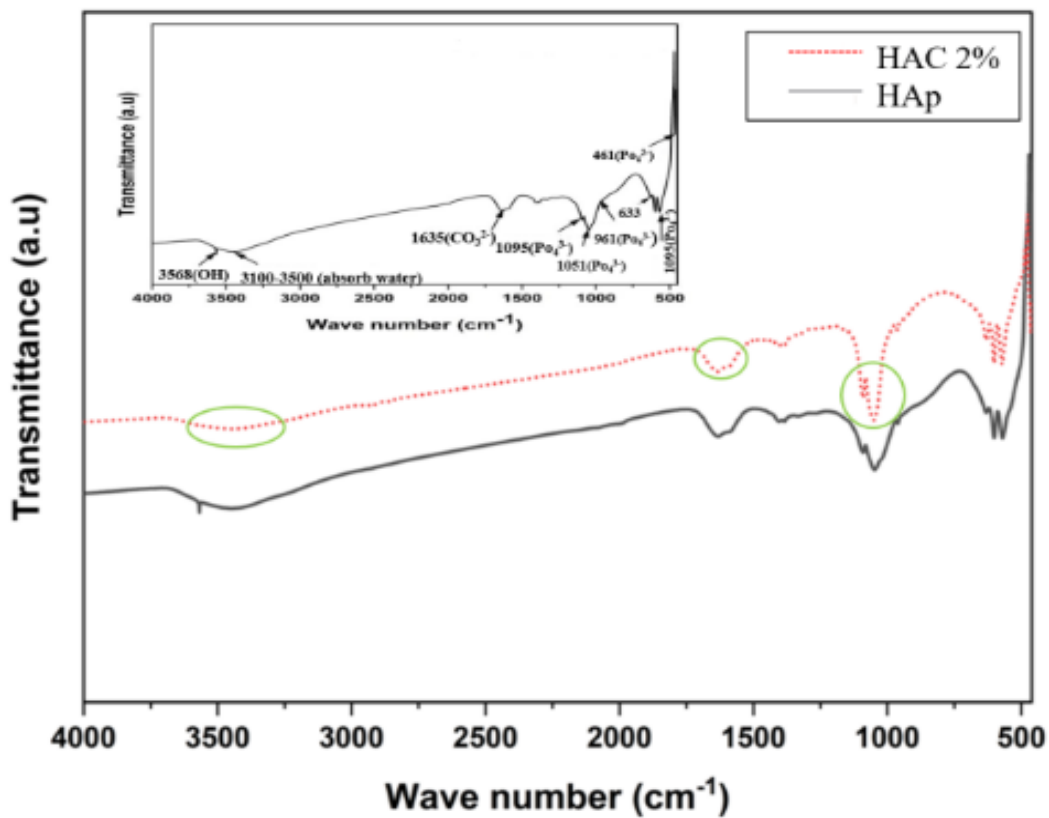


Figure 4.4 FTIR spectroscopy for HA and HAC2 powder (Shankar et al. 2024a).

4.7 Zeta potential/Surface charge of the powders

Figure 4.5 (a) shows the zeta potential variation with pH (2-12) for different powders (CNTs, Alumina) with and without surfactant and their corresponding heterocoagulated composites (AC1 and AC2), as reported by Jambagi et al. (2015). for CNT and alumina. The surfactant-coated CNTs and alumina particles have a zeta potential of over ± 30 mV at pH 8, which is considered a very stable suspension for mixing. Therefore, both particles disperse entirely at pH 8 due to electrostatic repulsion. Heterocoagulation is performed at pH 8, and the zeta potential for AC1 and AC2 is closer to the X-axis due to charge neutralization, thus indicating heterocoagulation. The same is evident from the AC2 composite pictograph (Figure 4.1 (c)), which shows particulates settling down at the bottom of the container, leaving clear water at the top.

Figure 4.5 (b) presents the ZP for HA and HAC composites in physiological

saline. HA powder shows negative ZP at a physiological pH of 7.4, consistent with already published results. Due to the breaking of oxide bonds, most ceramics have a net negative charge on the surface, which leaves unsatisfied oxygen ion charges on surfaces. In the case of ceramic like hydroxyapatite, the hydroxyl groups (-OH) are bonded to the calcium-phosphate lattice and can dissociate in aqueous environments to produce a negative surface charge. Further, the increase in the ZP values for the CNTs sample is due to a functional group (COOH) on its surface. To understand the electrostatic behavior of biomaterial with blood components, it is necessary to determine the surface charge of the biomaterial at a physiological pH of 7.4. At pH 7.4, the HA and composites (0.5–2 wt.% CNTs) have negative potential in the increasing order: $-2 \text{ mV} < -10 \text{ mV} < -11 \text{ mV} < -21.4 \text{ mV}$. Low protein adsorption (BSA) on HA particles is reported by (Lee et al. 2011; Miyake et al. 2013) due to their repulsive nature owing to their negative surface charge.

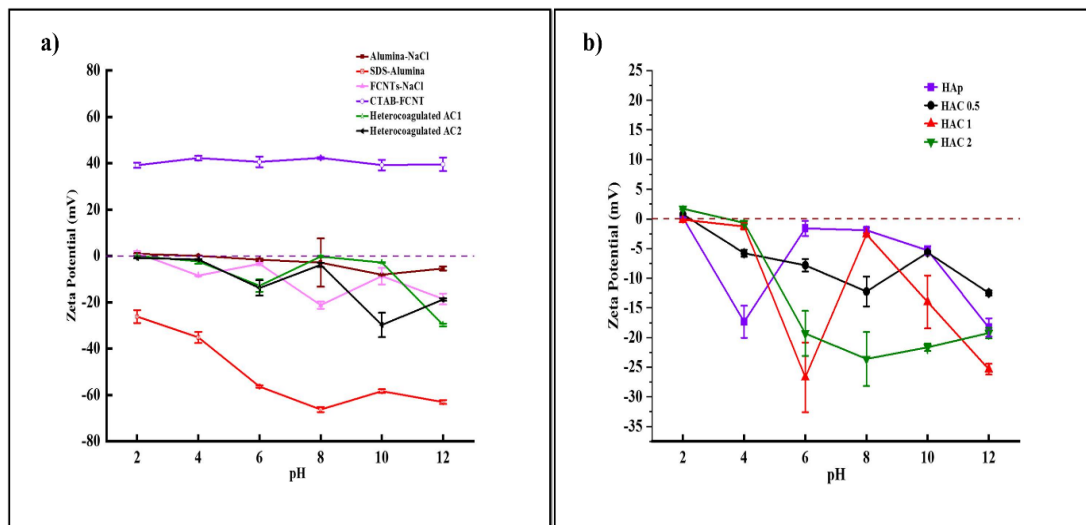


Figure 4.5 Variation of zeta potential with pH for (a) Alumina, Alumina with SDS, CNTs, CNTs with CTAB, and heterocoagulated sample (AC1 and AC2), and (b) HA and HAC composites (n=3) (Shankar et al. 2024a).

4.8 Hemocompatibility assessment of the powders

4.8.1 Hemolysis study

Extensive research should be conducted to determine the compatibility of new biomaterials that come into direct contact with blood, such as artificial implants. The

hemolysis percentage for bioactive HA and HAC composite powders with varying concentrations from 5 to 80 mg is shown in Figure 4.6. The positive control sample demonstrated 100% rupture of erythrocytes, while the negative control sample showed 0%. The hemolysis percentage did not significantly increase with the increase in HA concentration, as depicted by Figure 4.6 (a). The colorimetric image also displayed a transparent white saline solution (Figure 4.6 (e)). Nano-hydroxyapatite particles with a concentration range of 1-16 mg have been reported to have hemolysis between 1.04% to 3.69% by (Ooi et al. 2019). Thus, RBCs were not ruptured by the bioactive HA powder. The hemolysis percentage for the HAC0.5 composite was less than 5%, as shown in Figure 4.6 (b), and RBCs were not ruptured even at higher concentrations (80 mg), which was confirmed by the colorimetric image (Figure 4.6 (f)). The hemolysis percentage varied from 2.07% to 7.22% for the HAC1 powder, as shown in Figure 4.6 (c). This composite was highly hemocompatible (<5%) up to 40 mg, while at a concentration of 80 mg, it exhibited a hemocompatible nature (<10%). The colorimetric image corroborated this, displaying almost white saline up to 40 mg and light red-colored saline at 80 mg concentration (Figure 4.6 (g)). For HAC2, the hemolysis percentage varied from 2.73% to 10.43%, indicating significant RBC damage at a dose higher than 20 mg (Figure 4.6 (d)). Figure 4.6 (h) confirmed this, displaying a deep red-colored saline solution at 40 and 80 mg concentrations. The increased contact surface area due to the increased CNT concentration may have caused slight RBC damage by HAC2, rupturing the RBCs. Moreover, the HA and HAC composites rupture fewer RBCs than positive control (complete RBCs rupture). In summary, CNT-reinforced coatings exhibited good hemocompatibility.

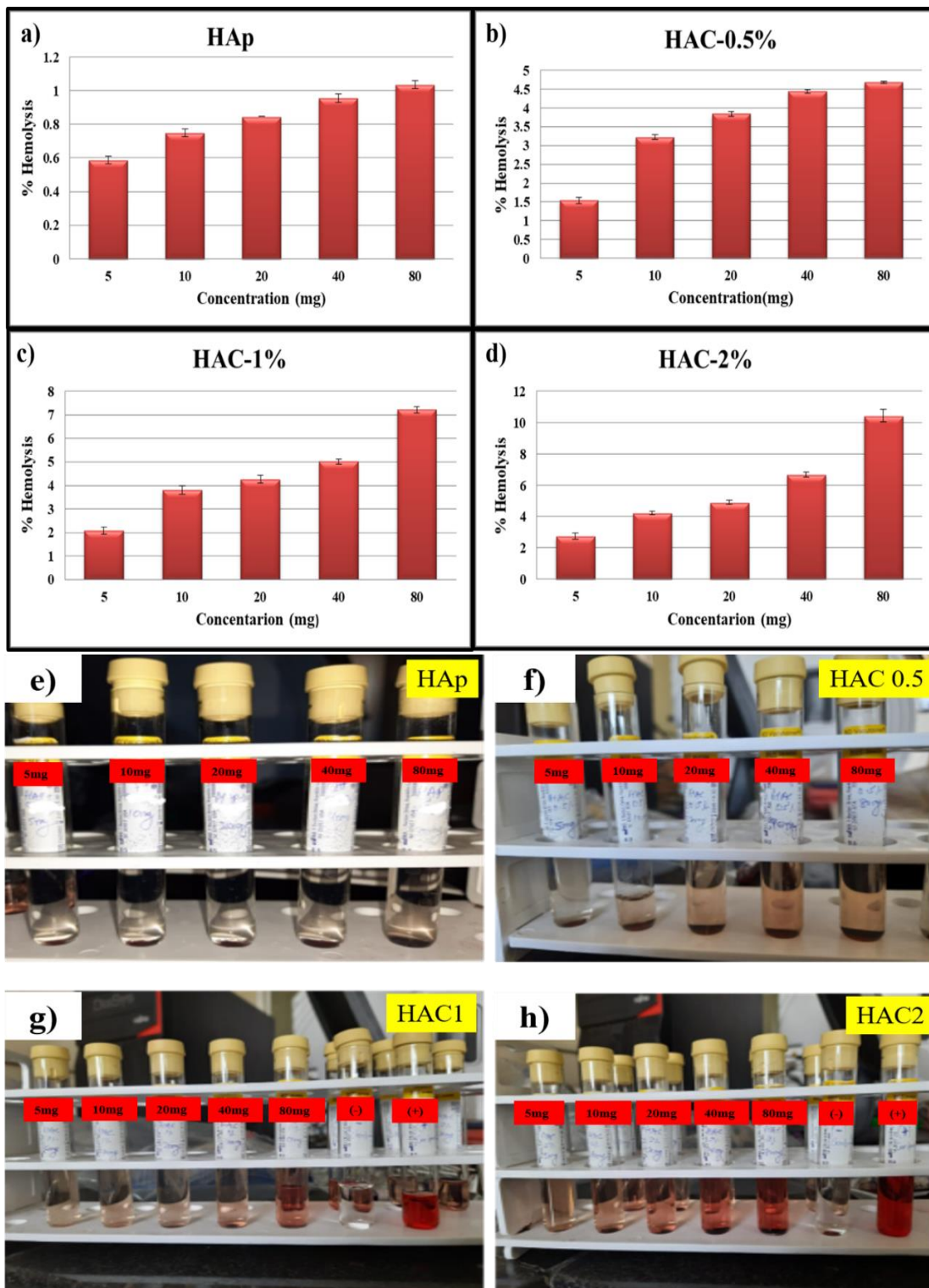


Figure 4.6 A bar graph shows the percentage hemolysis of different powders with varying concentrations for (a) HA, (b) HAC0.5, (c) HAC1, and (d) HAC2, colorimetric image to show RBC damage by (e) HA, (f) HAC0.5, (g) HAC1, and (h) HAC2. The white and light red colored tubes represent non-hemolytic, and the dark red colored solution depicts hemolytic behavior (Shankar et al. 2024a).

4.8.2 Whole blood clot study

Thrombogenicity is a major cause of failure in medical devices that come in contact with blood. This study provides information on the thrombogenicity and pro-coagulative behavior of each biomaterial. The clotting times of the samples were evaluated using blood from a healthy donor (Hgb= 14.8g/dL). Figure 4.7 (a) displays the blood clotting profile for the different samples and control (Only WB), and WB was used as reference material and incubated to form clots for 45 minutes. The tendency of the sample to form a clot is inversely proportional to the absorbance value. Laranjeira et al. (2016) reported a similar clotting profile for the HA powder (4 mg). As time increased, blood incubated with CNT samples showed relatively higher absorbance than the control (n = 3). HAC1 and HAC2 showed 1.15 and 1.40 times more absorbance than the control samples, respectively, indicating that they are non-thrombogenic. The absorbance value for the CNT samples increases as its weight % increases: HA < control < HAC 0.5 < HAC1 < HAC2. This suggests that the CNT samples release more erythrocytes from the clot formed. RBCs have a negative zeta potential (-15 mV) on their surface due to carboxyl groups of sialic acid. Therefore, RBCs repel the adjacent negative surface, not allowing themselves to get entrapped. Thus, the functionalized CNTs and the negatively charged HA are crucial in increasing the absorbance value. Figure 4.7 (b) shows the schematic illustration of the blood clot formation on the foreign materials. The negatively charged surface of particles could potentially minimize non-specific binding with the cell membrane and decrease abnormal protein binding. Protein interaction with Ca-P mainly depends on the electrostatic force, and the adsorption of surfaces occurs due to positive Ca^{2+} and negative $\text{PO}_4^{-3}/\text{OH}^-$ sites. These charges could bind the protein's negative acidic groups (COO^-) and positive amino groups (NH_3^+). Zhu et al. (2007) reported that the negative surface charge of the HA preferred to adsorb more basic protein lysozyme (LSZ) than acidic protein BSA at pH 7.4. A polymeric biomaterial polytetrafluoroethylene (ePTFE), used for prosthetic vascular grafts, has an absorbance value of $0.90 \pm 0.03.36$ (Shankar et al. 2024a). The thrombogenicity for the samples (HAC1 and HAC2) is significantly lower than the clinically used biomaterial. Thus, the CNT particles restrict clot formation.

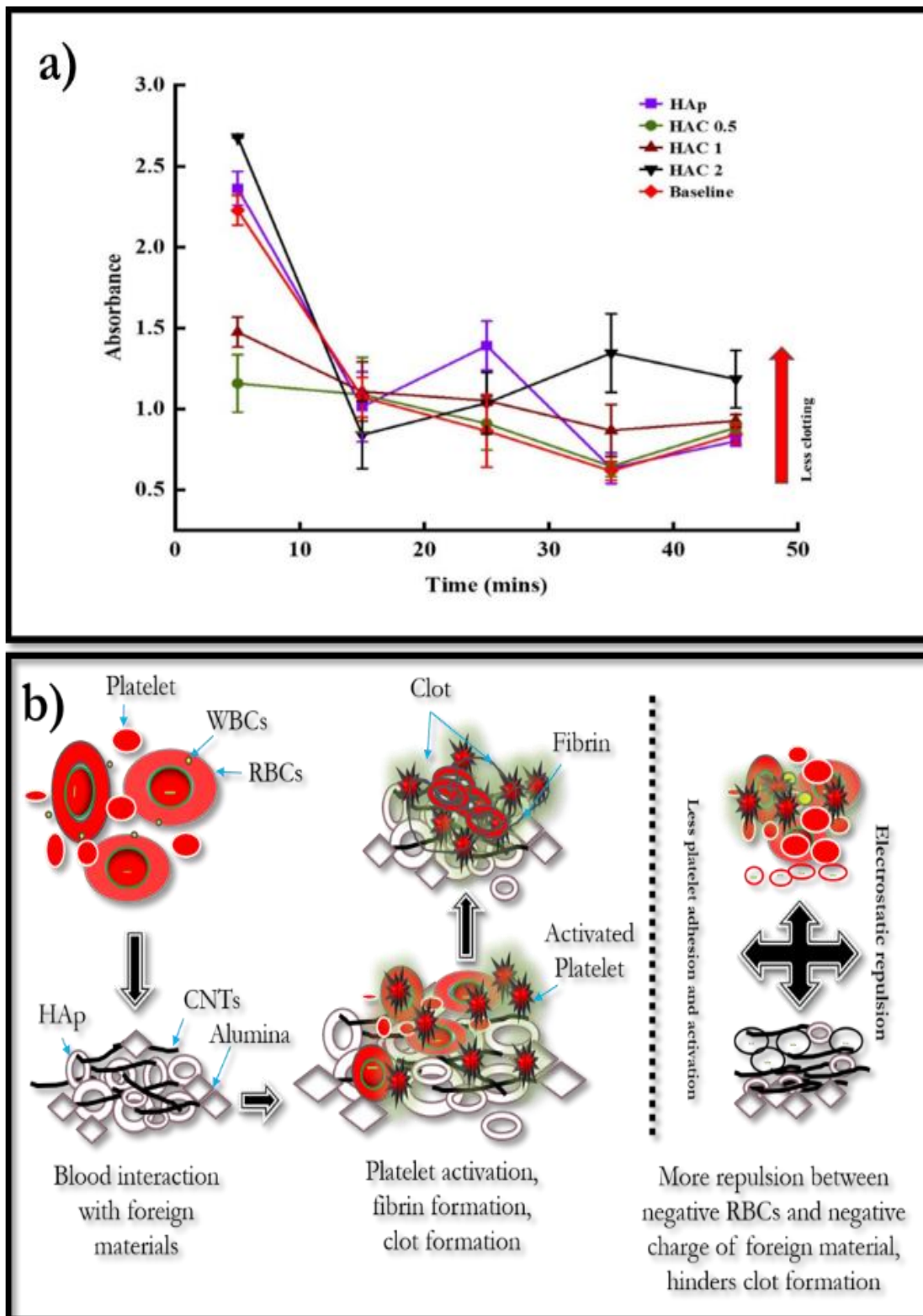


Figure 4.7 Absorbance vs. Time graph for whole blood clotting time measurement for the samples and the control, $n=5$, and (b) schematic diagram to illustrate clot formation when triggered by foreign material, and negative charge for HAC composites repels adjacent blood components, hinders clot formation (Shankar et al. 2024a).

4.8.3 Platelet adhesion and activation study

Platelet spreading and aggregation indicate damage caused to the interior surface of blood vessels by foreign substances. When in direct contact with blood, the implant surface activates platelets, the coagulation system, and white blood cells, affecting the implant surroundings. Figure 4.8 (a) displays the percentage of platelet adhesion on HA-based composites and controls. The negative control shows much lower platelet adhesion than the positive control. The percentage of platelet adhesion for all samples, up to 80 mg/mL, is significantly lower than that of collagen-glass beads. With an increase in concentration, HA, HAC0.5, and HAC1 showed a decreasing trend of platelet adhesion. However, HAC2 exhibited an increased tendency for the adhesion of platelets, indicating its poor hemocompatibility.

Furthermore, the sample HAC1 exhibited the most negligible platelet adhesion, i.e., 5.67 ± 0.359 %, with its maximum concentration in the plasma. This trend may be due to the combined effect of high negative surface charge and low sample surface area. However, the trend of increased platelet adhesion for HAC2 could be due to the high surface area and higher CNT concentration. The effect of the surface area of materials on protein adsorption has been reported by Wang et al. (2022). The more exposed surface area provides more interaction sites for protein adsorption. The mechanism underlying platelet activation and change in platelet morphology is shown in Figure 4.8 (b). Rouahi et al. (2006) reported an increase in protein adsorption with the increase in the surface area of the HA powder. Dextran (Dx) is a biopolymer that can lower surface platelet deposition, as reported by (Shoenfeld et al. 1987). This property of Dextran arises from its negatively charged molecules that repel platelets. The platelet membrane is rich in glycoproteins and glycolipids contributing to the surface charge. These molecules often carry negatively charged sialic acid, which imparts a negative charge to the platelet surface (EYLAR et al. 1962) and repels the adjacent negative charge biomaterials surface like Dextran. The result showed that the synthesized composite is highly hemocompatible, except for HAC2, as the particles did not activate the aggregation of platelets compared to the negative control.

The FESEM images were used to analyze the morphology of the platelets on

the sample surfaces and control. The negative control surface displays round platelets (red circle), as shown in Figure 4.8 (c). Similar observations were made for HA and HAC composites (red circle) at different concentrations (Figure 4.8 (d–g)). Additionally, the HAC2 composite at a concentration of 80 mg showed some pseudopodial extensions (black circle) with flattened morphology (Figure 4.8 (g)), which was previously correlated with a low activation state (Laranjeira et al. 2016). Figure 4.8 (h) shows fully spread platelets (yellow arrows) and dendritic platelets (black arrows), indicating complete platelet activation on the positive control. Furthermore, the platelet shape for all samples was almost similar to the polypropylene surface used as a non-thrombogenic biomaterial (Laranjeira et al. 2016).

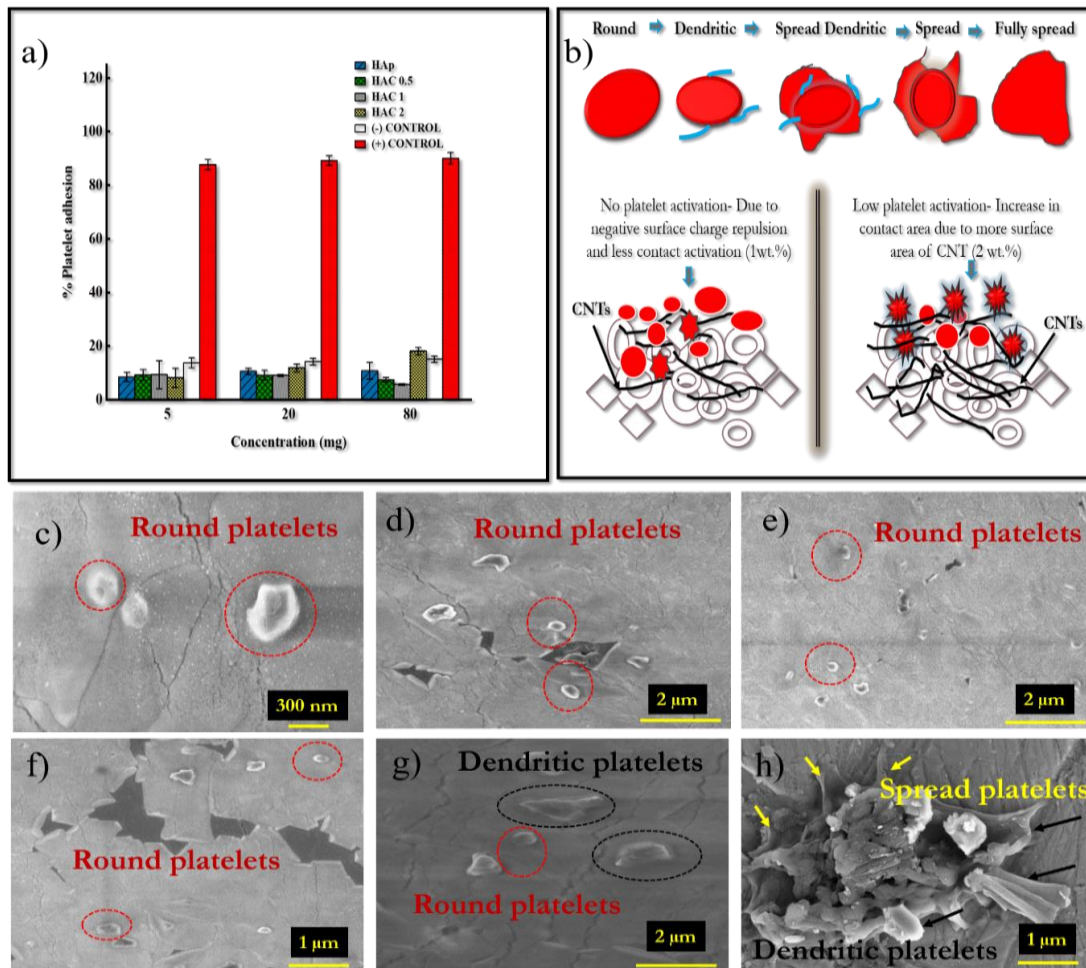


Figure 4.8 (a) Percentage of platelet adhesion on HA-based composites, negative and positive control, n=5, (b) Schematic diagram that shows the change in platelet morphology when in contact with foreign materials, FESEM images of platelets adhered on (c) Negative control, (d) HA, (e) HAC0.5, (f) HAC1, (g) HAC2, and (h) Positive control (Shankar et al. 2024a).

4.8.4 Coagulation assays: PT and aPTT

Clinical tests such as aPTT and PT are used to evaluate the anticoagulant potential of biomaterials. This study examined coagulation factor activation by measuring PT and aPTT for samples incubated with PPP. During the aPTT test, plasma is mixed with a contact activator; calcium ions are added to initiate coagulation, and clot formation time is observed. The aPTT study reflects the activity of coagulation factors of the intrinsic and common pathways (XII, XI, IX, VIII, and X). The PT clotting time assesses the action of the extrinsic and final common coagulation pathways (TF VIII, V, and X). Both coagulation pathways eventually lead to the formation of thrombin. Except for the HAC2 sample, none of the samples showed significant changes regarding PT & aPTT results (Figure 4.9 (a) and (b)). Santos et al. (2018) reported that rod-like HA nanoparticles tested up to 10 mg/mL in human PPP had little interference with these assays. Laranjeira et al. (2016) reported similar observations for HA but with 4 mg of HA powder. The study observed an increased PT and aPTT value with an increased concentration of CNT. For the HAC1 and HAC2 samples at 20 mg/mL, prolonged PT and aPTT values were observed, which exhibited significant anticoagulant activity. Moreover, a dramatic increase in PT and aPTT values was observed for HAC2 at 80 mg/mL particle concentrations. The PT values for HAC1 and HAC2 at 80 mg/mL were increased by approximately 1.04 and 1.31 times, respectively, and the aPTT value for the same was 1.006 and 1.426 times the control. This increase in coagulation time may be due to carboxyl groups attached to CNT samples. Li et al. (2013) reported similar observations for graphene oxide, which exhibited a dramatic increase in aPTT with an increase in particle dose due to the high density of the carboxyl group on their surfaces, which does not allow the protein to get readily adsorbed and delayed clotting time. The PT and aPTT for HA and HAC0.5 showed lower values than the control, which may be ascribed to the electrostatic attraction between the powder's Ca^{+2} , Al^{+3} , and C^{+4} cations and negatively charged proteins.

The study found that CNT samples up to 1 wt.% with human blood showed non-hemolytic and non-thrombogenic properties with low platelet adhesion and activation. Overall, CNTs with HA could be an ideal bio-ceramic coating for artificial implants. The study concludes that CNTs have advantageous bio properties provided its

concentration is kept within a limit.

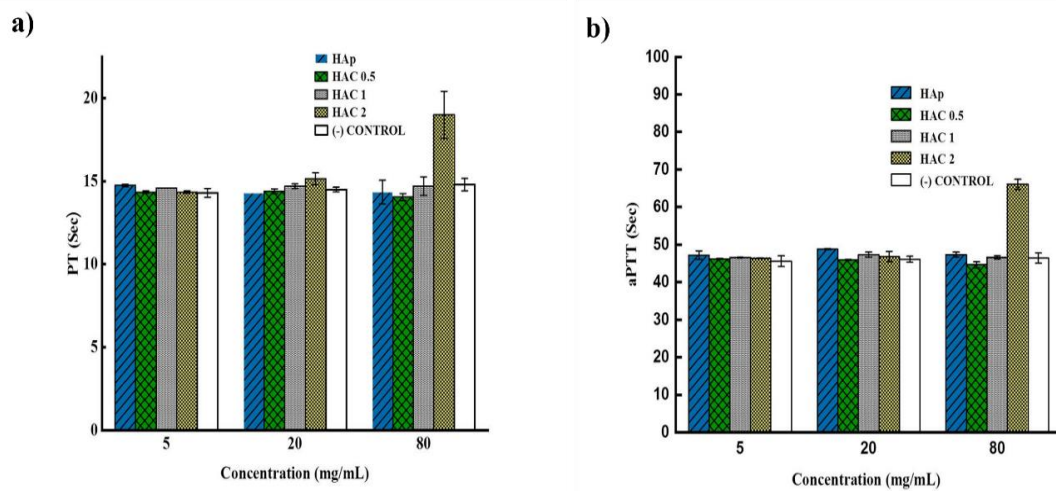


Figure 4.9 Coagulation assays (a) PT and (b) aPTT coagulation time of PPP incubated with different concentrations of HA-based composites at 5, 20, and 80 mg (n = 5) (Shankar et al. 2024a).

4.9 Summary

In this chapter, various feedstocks were explored in the context of the study. The process of creating bio-composites using the heterocoagulation colloidal technique was explained in detail, focusing on the characterization of powders for their morphology, surface charge, and dispersion of CNT within the matrix. The biocompatibility of the powders was also tested using human blood to identify the appropriate composition for orthopedic implant coating. Interestingly, when CNTs were used in low concentrations, they were found to be uniformly dispersed within the matrix, leading to excellent hemocompatibility. The next chapter will delve into different thermal spray techniques to determine the most suitable one for future coating processes. It is worth noting that some of the findings presented in this chapter have been published in a reputed publication (Shankar et al. 2024a).

CHAPTER 5 HA COATINGS BY DIFFERENT THERMAL SPRAY

5.1 Introduction

This chapter explores various thermal spraying techniques to determine the optimal method for creating HA-based coatings. The resulting samples were thoroughly analyzed for factors such as morphology, phase changes, crystallinity, and surface wettability to evaluate the impact of different surface properties on the hemocompatibility and bioactivity of the coatings. Additionally, the bond strength and hardness of the coatings were assessed to gauge their suitability for use within the human body.

5.2 Microstructural properties of the coatings

Figure 5.1 (a) displays the HA feedstock, which is composed of various nanosized HA particles aggregated together (Figure 5.1 (b)). The size distribution of the HA particles was determined by measuring the diameter of the spherical HA particle images captured from FESEM. The particle size distribution histogram was fitted with a log-normal distribution function, as seen in Figure 5.1 (j). Most particles are in the 10-50 μm range, while the average particle size is 39.79 μm with a standard deviation of 5.42 μm . The top surface microstructure of the APS coating is presented in Figure 5.1 (c), showing various intersplat cracks, flat-appearing melt surfaces, and partially fused particles due to the high temperature of the plasma spray. The surface has a rough profile (Figure 5.1 (c) and 5.2 (a)), with mostly partially melted and a few unmelted particles attached to the fully molten particles. Figure 5.1 (d) depicts the APS coating cross-section, showing a typical lamellar structure with no delamination from the substrate. The thickness of the HA coating ranges from $252 \pm 23.68 \mu\text{m}$, with distributed micrometer-size porosity and transverse and longitudinal cracks due to the plasma spray's rapid quenching characteristic (Kumari and Majumdar 2017). The cross-section's image processing analysis reveals the porosity to be $11.062 \pm 1.42\%$.

Figure 5.1 (e) displays the microstructure of the FS coating. The top surface exhibits some spherical particles in the matrix due to unmelted particles and an uneven

surface (Figure 5.1 (c) and 5.2 (b)), with partially melted and unmelted particles. The cross-section of the FS coating (Figure 5.1 (f)) has similar features (cracks/pores) to the APS coating, with a thickness range of $113\pm 13.22\ \mu\text{m}$ and a porosity of $13.204\pm 2.34\%$. The HVOF coating has a microstructure that is contrasting from that of the APS and FS coatings. It is composed of unmelted submicron-size particles and well-flattened lamellae. The unmelted submicron particles come from the raw powder material's crystallites and the low temperature involved in the process. The HVOF coating surfaces are mostly covered with several unmelted and partially melted particles that shattered upon impact with the high velocity of HVOF (Inset Figure 5.1 (g)). A smooth and homogeneous surface was observed, as confirmed by the surface roughness value (Figure 5.1 (c) and 5.2 (c)). The cross-section of the HVOF coating had a uniform thickness of $55.36\pm 2.05\ \mu\text{m}$, with very few pores and no microcracks observed (Figure 5.1 (h)). The porosity was determined to be $3.046\pm 0.45\%$, indicating a dense coating characteristic of HVOF coating. The HVOF coating displays a notably smoother texture (Figure 5.1 (c) and 5.2 (a)), which can be attributed to its dense microstructure, featuring low porosity, and a result of the high velocity utilized in the process. The EDS analysis (Figure 5.3) established that all three coatings contain Calcium (Ca), phosphorus (P), and Oxygen (O) elements, which are fundamental components of HA coatings. No impurities were introduced during the thermal spraying of HA, as no other elements were detected in any of the coatings. The Ca/P ratios of the APS and FS coatings were 1.56 and 1.51, respectively, indicating the formation of TCP phases (Manivasagam and Popat 2020). The HVOF coating had a Ca/P ratio of 1.7, confirming the presence of HA phases close to the theoretical Ca/P ratio of 1.67 (Ganvir et al. 2021).

The properties of a coating, such as its phases, crystallinity, and adhesion, are influenced by the precursor powder used (Khor et al. 2003). The shape of the powder also plays a role in ensuring good fluidity and continuous feeding of the powder (Hermann-Muñoz et al. 2019). The present study investigates using spherical porous hydroxyapatite (HA) as feedstock powder, which has a nanostructured spherical shape. Each particle comprises a collection of individual nanosized particles and an extensive nanopore network. The effect of the nano-pores in the HA feedstock on the coatings obtained by different thermal spray processes is intriguing to understand. The low

thermal conductivity of HA particles could be due to their nanopore network, which could reduce the degradation of HA and enhance its crystallinity (Lima et al. 2005). Different thermal spray processes produced coatings with distinct nanostructured zones. The HVOF coating had a porous zone similar to the porous structure of the HA feedstock particle, suggesting that the individual nanosized particles of the feedstock did not coalesce during spraying, thus retaining the porous structure of the agglomerated feedstock throughout the HVOF process. In contrast, the APS coating had densely packed nanosized, spherical particles embedded in the splat fibers, while the FS coating had rounded particles embedded in the fibers. The presence of completely or partially melted regions in the coatings indicates the degradation of HA, which directly affects the crystallinity and mechanical properties of the coating.

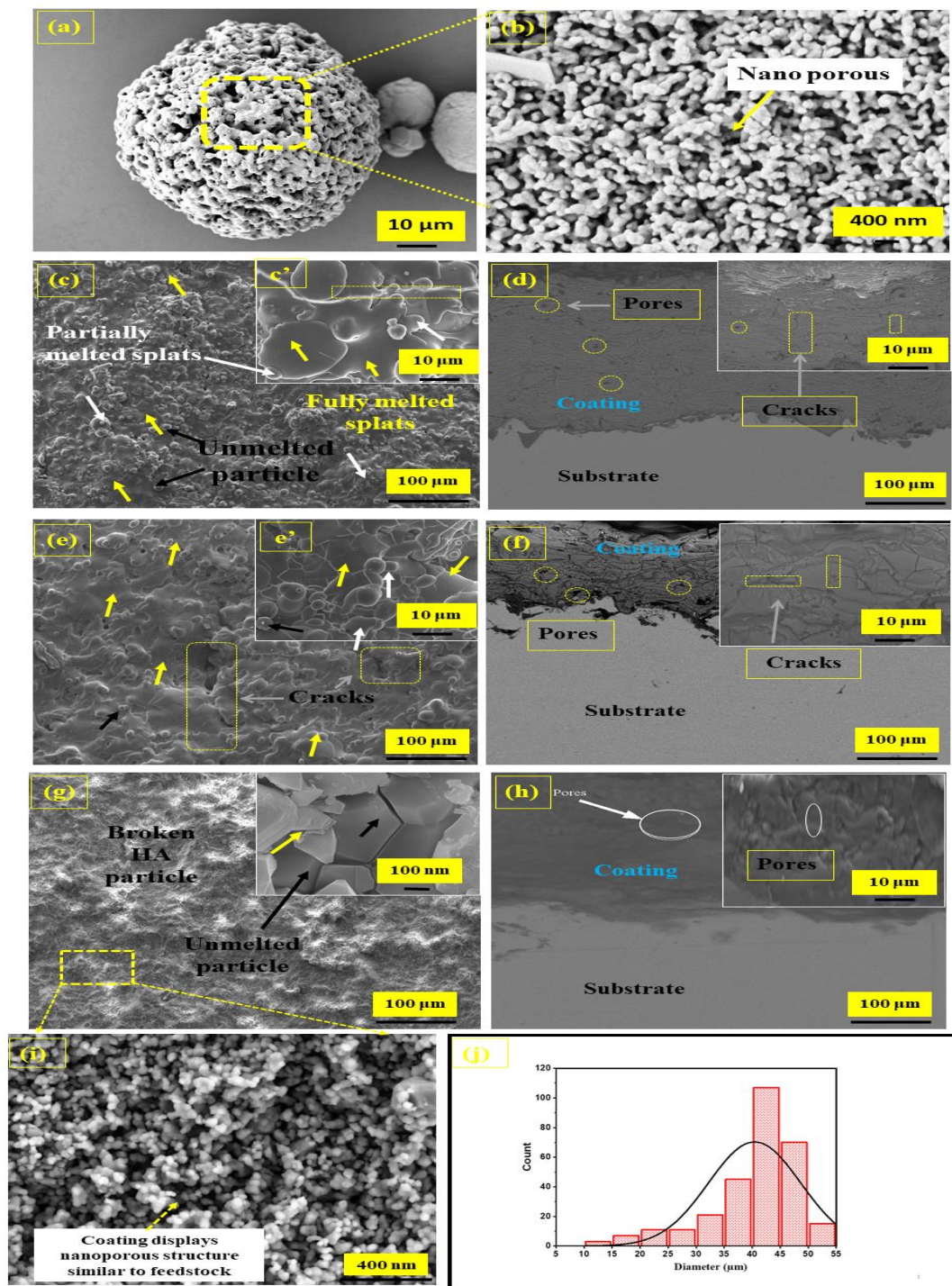


Figure 5.1 FESEM micrographs (a) HA powder, (b) nanoporous structure of individual HA particle. FESEM top surface morphology for (c) APS, (e) FS, and (g) HVOF-HA coatings. Cross-sectional microstructure of (d) APS, (f) FS, and (h) HVOF-HA coatings. The white arrow represents partially melting, the black arrow shows the unmelting, and the yellow arrow depicts the complete melting of HA. (i) The top surface microstructure showed a nanoporous structure of the HVOF coating, similar to HA feedstock. (j) Histogram shows particle size distribution for HA powder fitted with a log-normal distribution function (Solid black line) (Shankar et al. 2024b).

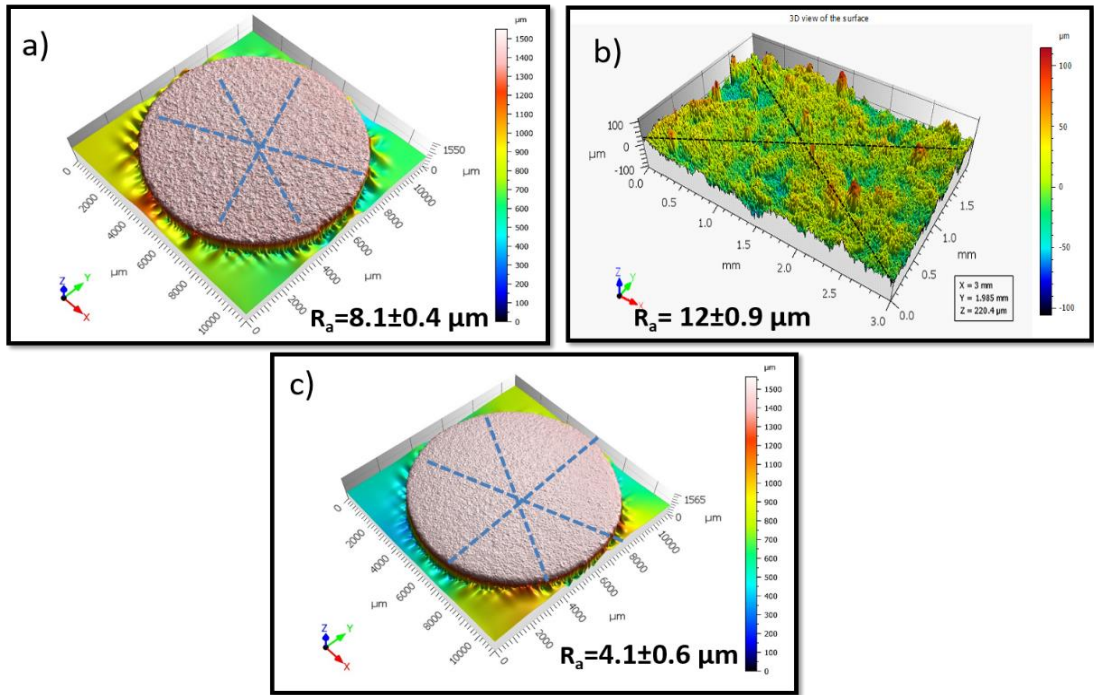


Figure 5.2 3D surface profiles of surface roughness (R_a) for (a) APS, (b) FS, and (c) HVOF-HA coatings (Shankar et al. 2024b).

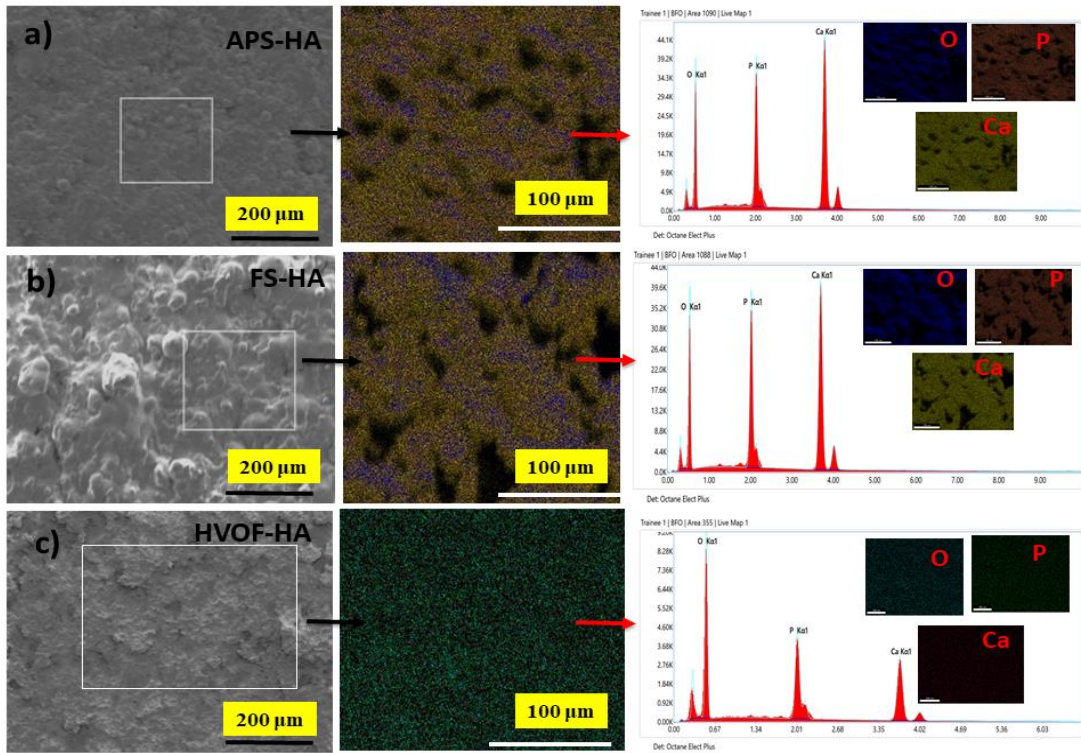


Figure 5.3 Top surface FESEM micrograph with corresponding EDS elemental mapping and EDS spectra shows Ca, P, and O as the coating elements for (a) APS-HA, (b) FS-HA, and (c) HVOF-HA coatings (Shankar et al. 2024b).

5.3 Phase identification and crystal size of the coatings

The feedstock's phases, crystallinity percentage, and coatings were identified using the diffraction pattern shown in Figure 5.4 (a), following ISO 13779-3 and ICDD files. The primary phase observed was HA, with a TCP peak at 25.36° (2θ) for the HA powder. The HA powder's crystallinity was 99.75%, indicating high crystallinity for thermal spray applications. HA crystallinity was observed as the technique's operating temperature decreased (APS < FS < HVOF), as higher temperatures and fast cooling rates can lead to HA decomposition. The analysis discovered TTCP, CaO, and TCP phases in the plasma and flame coatings. In contrast, HVOF coating showed no significant secondary phases, suggesting that most HA particles did not melt or undergo phase transformations during HVOF spraying. The crystallinity of the APS, FS, and HVOF coatings was determined by identifying pure HA and its secondary phases from XRD peaks and by using equation 3.1; the crystallinity % was found to be 67.8%, 81.2%, and 89.7%, respectively. As the operating temperature rose, the peak intensities decreased with the XRD peak broadening, which may be attributed to a decrease in the average crystallite size as well as due to the lattice strain.

The size of feedstock, high cooling rates, and operating temperatures significantly affect the crystallinity of HA coatings. The operating temperature for APS ranges from 6000°C to 15000°C , and under specific circumstances, inflight particles can reach a temperature between 2020°C and 2435°C (Cizek and Khor 2012). Flame spraying can operate at $2500\text{-}3000^\circ\text{C}$ (Singh et al. 2014), while the in-flight particle temperature ranges between $1200\text{-}1850^\circ\text{C}$ for HVOF spraying, with a higher particle velocity and shorter in-flame particle times. HA's melting temperature is 1550°C , and HA starts to decompose into α -TCP, β -TCP, and TTCP phases above 1050°C (Jagadeeshanayaka et al. 2022). In low-temperature thermal processes such as HVOF, the significantly reduced temperature can generate only lower levels of undesirable secondary phases. As a result, a high degree of crystallinity can be observed. Thus, low-temperature operated processes are preferred to produce HA coatings with high crystallinity.

The degree of crystallinity in the APS coating was 67.8% under present spraying conditions, but this value can vary according to process variables, chiefly gun power

and nozzle-sample distance (Tian et al. 2014). Tercero et al. (2009) reported a lower crystallinity (47.6%) for APS-HA coating. Though the operating temperatures are still too high to control the phase composition entirely, the coating achieved by FS has higher crystallinity than APS. As reported by Singh et al. (2014), secondary phases were present in the FS-HA coating, but the HA particles were 30 μm in size. The HVOF coating found optimal settings for high crystallinity, leading to better phase content and crystallinity. HVOF coating exhibited around 32% and 10% more crystallinity than APS and FS, respectively. Vilardell et al. (2020) reported 62.4% and 82% crystallinity for APS and HVOF coating, respectively. However, the decrease in crystallinity was attributed to smaller HA particle sizes (30 μm) and spraying conditions.

The bioactivity of HA-HVOF coating was studied by Lima et al. (2005) with the SBF immersion test, and they reported a crystallinity of 84%, which supports bioactivity. The low degree of crystallinity was due to the smaller HA particle size. Note that high crystallinity is crucial in maintaining coating integrity as it indicates a low percentage of secondary phases such as ACP, CaO, TCP, and TTCP that dissolve quickly in body fluids (Lima et al. 2005). In the case of HA coating, only pure HA peaks are considered crystalline, and the rest of the XRD peaks are considered secondary phases. The mechanical properties of coatings can be negatively affected by these secondary phases as ions from body fluids tend to degrade amorphous phases, resulting in rapid coating erosion, substrate surface corrosion, bacterial colonization, inflammatory responses, and ultimately, aseptic loosening and implant failure (Mittal et al. 2013).

The order of HA and secondary phase degradation when submerged in an organic fluid SBF was reported by (Khor et al. 2003; Surmenev et al. 2014). The order of degradation of different HA phases is arranged in descending order: CaO >> α -TCP > β -TCP > ACP > TTCP > oxyapatite >> HA. This equation provides valuable insight into the material behavior of HA implants (Jagadeeshanayaka et al. 2022), making it essential in academic and business settings where a comprehensive understanding of these materials is required. The crystallinity of HA directly impacts bioactivity and the stability of implants in vivo. Xue et al. (2005) examined the effects of HA coatings on in vivo activity produced through the APS and vapor-flame treatment process. Their

findings showed that the crystallinity of the APS and vapor-flame treatments was approximately 55% and 98%, respectively. It was concluded that the HA coating with higher crystallinity was better suited for long-term implantation based on the in vivo results. Therefore, in our situation, the HVOF with the highest crystallinity would have a greater chance of long-term survival and be considered a better candidate for clinical trials. It is known that the dissolution behavior of HA coatings is very sensitive to their crystallinity as secondary phases increase dissolution rates, which affects the longevity of the implants (Gadow et al. 2010). The degree of crystallinity also directly impacts mechanical strength and in-vitro hemocompatibility, which will be further discussed.

5.4 Raman Analysis of the feedstock and coatings

Figure 5.4 (b) demonstrates the Raman spectra of HA feedstock and various HA coatings. The peak for the phosphate ion was observed at 962 cm^{-1} in the HA powder, with other PO_4^{3-} ions modes detected between 577 and 613 cm^{-1} . The vibration modes ν_1 , ν_2 , ν_3 , and ν_4 exhibited higher intensity spectra with peak splitting between 200 - 1200 cm^{-1} , indicating a greater level of crystallinity.

The plasma and flame-sprayed coatings exhibited a broad peak with a slight shift, while the HVOF coating and feedstock showed a similar pattern. Although there was a minor variation in the ν_1 peak for all coatings, it was negligible due to the Raman spectrometer slit size. Both coatings (APS and FS) had a left shoulder broad peak at $\sim 950\text{ cm}^{-1}$, confirming the presence of amorphous calcium phosphate (Li et al. 2004). These coatings' low-intensity ν_2 and ν_4 peaks became more prominent and less distinct. This finding is consistent with previous studies that yielded similar results (Hermann-Muñoz et al. 2019; Saber-Samandari et al. 2013). The broadening of Raman peaks is due to the low degree of crystallinity resulting from the complete and partial melting of the powder during the plasma and flame spray process.

The HVOF coating's phosphate peaks had the same width, position, and intensity as the feedstock powder. A phase change was not observed, as unmelted particles were found in the HVOF deposits. Additionally, TCP ($\text{Ca}_3(\text{PO}_4)_2$) was absent as a left shoulder on the ν_1 peak (Saber-Samandari et al. 2013). Similar observations were also

made in XRD spectra (Figure 5.4 (a)).

Raman spectra further confirmed the difference in crystallinity due to phase transition among the coatings. Raman spectra for HVOF coating showed HA peaks similar to feedstock powder, indicating a high degree of crystallinity. Hermann-Muñoz et al. (2019) reported a similar Raman profile for HA coating. However, APS and FS coatings showed broad and wider Raman peaks, heralding at secondary phases, indicating a lower degree of crystallinity (Figure 5.4 (b)). These broad and featureless wide bands at different vibration modes (ν_1 to ν_4) typically represents amorphous calcium phosphate (ACP) structure (Li et al. 2004). These indicate the presence of secondary phases resulting from fully melted HA powders during the plasma and flame spray.

Furthermore, the morphology of the ceramic HA coatings that come in contact with blood components can be affected by the thermal history of the flame or gas stream particles. The APS coating process produces well-flattened splats due to the high temperatures and induces microcracks from the rapid quenching, leading to residual tensile stresses. Because of the inherent brittleness of HA, this can cause significant issues (Kowalski et al. 2022). In contrast, the HVOF technique uses lower temperatures and yields surface morphology similar to the original feedstock powder (Hermann-Muñoz et al. 2019). The FS coating, which uses temperatures between APS and HVOF, has a surface morphology composed of melted and non-melted particles (Singh et al. 2014). While XRD and Raman's results show that HA phases are retained in HVOF coatings, EDS observations show a decreased Ca/P ratio for APS and FS coatings (Figure 5.3).

5.5 Contact Angle/Surface Wettability

Different types of surfaces can be classified based on their wettability, with super-hydrophilic surfaces having an angle of about 0° , hydrophilic surfaces having an angle between 0 and 90° , hydrophobic surfaces having an angle greater than 90° , and super-hydrophobic surfaces with an angle greater than 150° (Rastegari and Salahinejad 2019). It was observed that the porous HA coating improved the wettability of titanium

surfaces to a greater extent, with the trend for contact angle being Ti>HVOF>APS>FS (Figure 5.4 (d)). All the coatings displayed hydrophilic characteristics with contact angles less than 90°, except for bare titanium, which displayed hydrophobicity due to its dense structure and/or may be due to an oxide layer formed on its surface. The wettability of a surface can be influenced by its topography, chemistry, charge, and liquid properties. APS and FS coatings showed lower contact angles ($\theta_{CA} < 15^\circ$) due to their porous structure and high surface roughness. In contrast, HVOF coating displayed a higher contact angle/lower wettability than other coatings with slight variation due to its dense, smooth, and homogenous structure.

The wettability of the bio-implant surface also plays a vital role in the adsorption of protein on the biomaterial surfaces (Fabre et al. 2018). Surface wettability results showed that porous HA improves the wettability of titanium to a greater extent as all the coated samples displayed $\theta_{CA} < 90^\circ$, indicating their hydrophilicity. Furthermore, HVOF coating exhibited a higher contact angle ($\theta_{CA} \sim 85^\circ$) than other coatings, owing to its dense morphology (porosity = ~3%). Similar hydrophilic behavior of HA coating by APS and HVOF spray was reported by Vilardell et al. (2020). However, they reported a much lower contact angle ($\theta_{CA} = 10.8 \pm 2.5^\circ$) for HVOF coating owing to a more significant amount of porosity (11-15%). In addition, the different contact angle values for the HA-coated samples (Figure 5.4 (d)) suggest the effect of HA structures on surface wettability and the importance of controlling HA structure due to the temperature effect on the implant. The variation in wettability also suggests different apatite morphologies, as seen from the SBF test (Figure 5.7 (a-1)). Hydrophilic surfaces are preferable to design because they absorb fewer blood plasma proteins than hydrophobic surfaces. Hydrophilic surfaces are believed to resist protein adsorption due to their ability to create hydrogen bonds with water molecules, building a water barrier. The hydrophilic surface demonstrates resistance to protein adsorption when the surface's propensity for proteins is insufficient to displace water molecules. On the other hand, hydrophobic surfaces, like pure titanium, are more likely to release water molecules and cause protein adsorption because they have low surface energy (Gessner et al. 2000). The absorption of protein on the implant surface is undesirable for the following reasons: 1) When proteins adsorb onto the surface of a bioimplant, they can

form a layer that may alter the surface properties. This protein layer can affect the subsequent interactions of the implant with surrounding tissues, potentially leading to inflammatory responses or adverse biological reactions like clot formation. 2) For implants intended to integrate with bone or other tissues, a protein layer can inhibit the attachment and proliferation of cells needed for integration. This can delay or prevent the desired biological response, such as osseointegration in bone implants. 3) Proteins on the surface of implants can also facilitate bacterial adhesion (Xu et al. 2014). Once proteins are adsorbed, they can serve as a binding site for bacteria, leading to biofilm formation and increasing the risk of infection (Wang et al. 2012). In summary, while some degree of protein adsorption might be unavoidable, excessive or uncontrolled protein adsorption on bioimplant surfaces can lead to inflammation, reduced biocompatibility, increased risk of infection, and compromised mechanical stability. Therefore, controlling or minimizing protein adsorption is crucial for ensuring bioimplants' long-term success and functionality. Previous investigations have demonstrated that polyurethanes and their derivatives, widely used in the medical field, dramatically reduce protein adsorption due to their hydrophilicity (Wu et al. 2009; Xie et al. 2018).

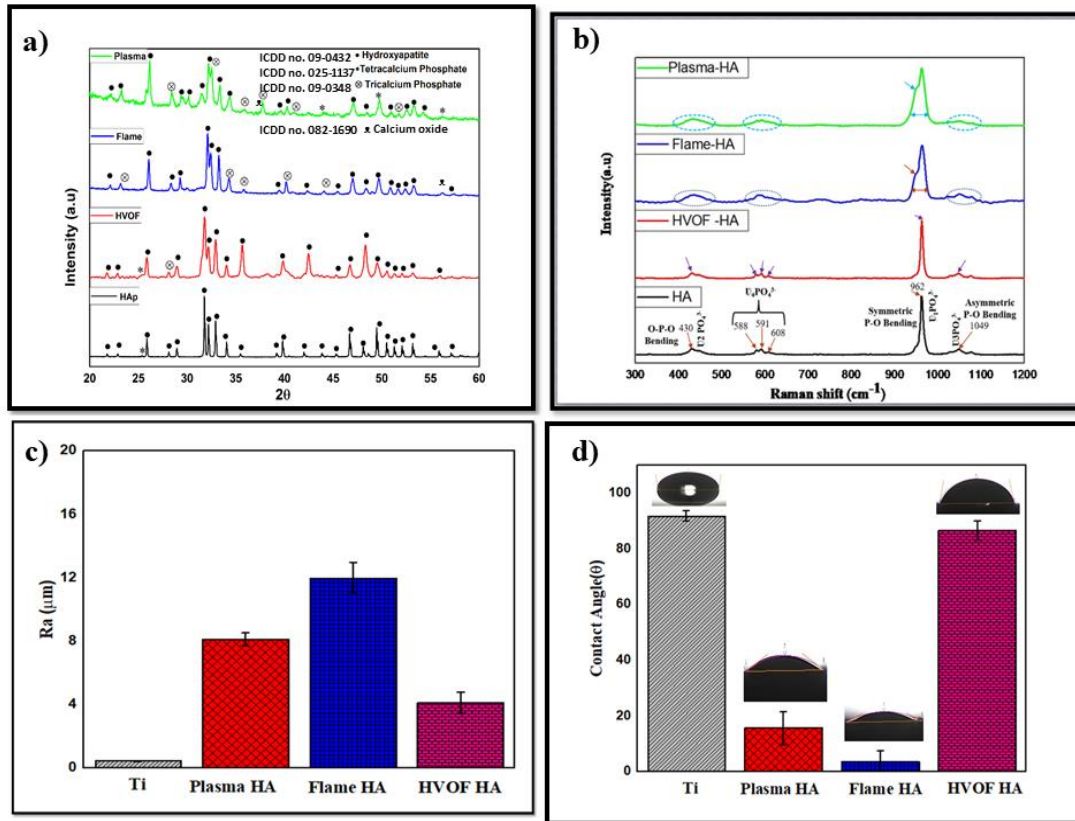


Figure 5.4 (a) XRD spectra of feedstock powder and all coated samples with corresponding ICDD file numbers for different phases of HA. (b) Raman spectral analysis shows different HA phases for feedstock and coatings. (c) The surface roughness (Ra) value for Ti and coated samples was obtained using a 3D profilometer ($n = 5$). (d) Contact angle and corresponding front-view photographs show hydrophilicity and hydrophobicity behavior for titanium and coatings ($n = 5$). The error bar represents the standard deviation (Shankar et al. 2024b).

5.6 Scratch Adhesion Strength and Hardness of the Coatings

A standard scratch test was conducted to study the adhesive properties of HA coatings. The thickness of the samples was grounded to approximately 50 microns. During the test, sensors monitored acoustic signals, friction force, tip position, and penetration depth. The coatings failed under loading, revealing distinct mechanisms resulting in sudden friction and acoustic emission changes. The critical load of failures was determined by analyzing microscopic scratch images (Figure 5.5) of the scratch track, 3D-profile images (Figure 5.6), and generated graphs. The initial cracks, corresponding to LC_1 , occurred suddenly, indicating a cohesive failure. This was followed by spallation and interfacial delamination at a second slope change corresponding to LC_2 , indicating

an adhesive failure. As the applied load increased, the track displayed the propagation of microcracks. The highest critical load value, L_{C3} , was reached when the film had sustained almost 50% damage. A bar graph (Figure 5.5 (m)) was used to compare the critical loads, which revealed that APS and HVOF coatings suffered less scratch damage than FS. Notably, the load value from L_{C1} to L_{C3} for the HVOF coating had significantly increased, with a substantial boost in the load for initial delamination (L_{C2}) compared to others, indicating improved adhesion.

The HA coatings' hardness also aligns with the scratch test results. Figure 5.5 (n-p) displays the indents carried out on the different coatings. The pyramids with diagonal D_1 and D_2 were longer for APS and FS coating than HVOF coating. The hardness of APS, FS, and HVOF sprayed HA coating was 282.08 ± 10.65 , 232.27 ± 16.72 , and 369.06 ± 13.37 HV, respectively ($n=10$, $p < 0.05$). A significant increase in hardness for HVOF coating was observed more than others, owing to its dense microstructure (porosity ~3%) and low thickness. The obtained hardness values are much higher than that of plasma sprayed HA coating, i.e., 1.88 ± 0.88 GPa (~209HV) (Pandey et al. 2018b), under the same loading conditions. Gadow et al. (2010) also reported an increase in hardness for HVOF-HA coating than plasma-HA coating, owing to the dense microstructure of HVOF coating.

Two aspects determine the adhesion strength between the coating and substrate: mechanical interlocking and chemical bonding. This study considers mechanical interlocking identical since the substrates had the same surface finish. Therefore, the increase in adhesion strength is attributed to stronger chemical bonds developed at the coating-substrate interface during deposition. The bond strength between the coating layer and the substrate is critical since separating the coating layer from the implant during service in the human body can adversely affect the implants and the surroundings. The HVOF coating has shown outstanding results with ~41% and ~48% increase in cohesion strength (L_{C1}) and ~34% and ~120% improvement in adhesion strength (L_{C2}) compared to APS and FS coating, respectively (Figure 3 (m)). Research has shown that crystalline coatings adhere better to substrates, and granular morphology crystals have a higher resistance to delamination (Clèries et al. 2000). The granular structure for the HVOF coating is believed to have helped in accommodating the

residual stresses. The residual stress determined by the XRD method was found to be compressive in nature for HVOF coating. However, the results are not presented here. The presence of compressive residual stress has a positive effect on mechanical properties, delaying crack initiation and extending the lifespan, which significantly impacts the coating's bond strength. Compressive residual stress may be attributed to factors such as coefficient of thermal expansion (CTE) mismatch and/or volume shrinkage mismatch between the substrate and powder (Yang 2011). Recent research on HAVF-sprayed HA coatings, similar to HVOF spray, also found compressive residual stress due to high velocity and impact with low-temperature in-flight particles (Jagadeeshanayaka et al. 2023). The low porosity of the HVOF coating with granular morphology aids in accommodating the residual stress, thereby increasing its adhesion strength compared to other coatings. Gadow et al. (2010) also reported decreased porosity's role in improving bond strength for HVFS-HA coating. The decreased inter-layer porosity and high crystallinity of the HVOF coating could be the prime reasons for the increase in the critical loads. However, the reduced adhesion strength for APS and FS coatings is due to micropores, micro-cracks, and secondary phases. Komath et al. (2011) conducted a micro-scratch test for pulsed laser-deposited (PLD)-HA coating on a Cp-Ti substrate. They applied a progressive load with a Rockwell Diamond indenter of 100 μm radius and reported a cohesion failure at 2.3N (L_{c1}) and adhesion failure at 5.42N (L_{c2}) for the as-deposited coating. However, due to the granular morphology, these values were significantly higher for hydrothermally treated samples ($L_{c1} = 4.4\text{N}$, $L_{c2} = 11.25\text{N}$).

Previous research has shown that HA coatings with a dense structure, characterized by low porosity and less amorphous phase, have a higher tensile adhesion strength than those with lower density (Kweh et al. 2002; Yang and Chang 2003). The APS and FS coating friction force graph showed significant fluctuations, suggesting material flaking off onto the scratch path, indicating low cohesiveness. However, HVOF coating exhibited consistent variation in friction force until the delamination stage, demonstrating its uniform and dense structure. The adhesion strength of the HVOF coating corresponds to its microstructure, as higher velocity leads to denser coatings with less interlayer porosity, resulting in a stronger bond. The mechanical

hardness test results for the HA coating follow a similar trend to the scratch test. The HVOF coating exhibited approximately 31% and 59% higher hardness than APS and FS coatings, owing to its high density (~97%). Increasing the hardness of thin coatings like HVOF coating is related to the rapid solidification of the first few lamellae of HA attached to the titanium substrate of higher thermal conductivity (6.7 W/m-k) compared to the HA (1.5 W/m-k) (Morks et al. 2007). The lower hardness of FS coating is attributed to incomplete densification (~87% dense) and poor inter-lamellar adhesion and cohesion abilities due to poor microstructural characteristics. Similar hardness results were reported for the HVOF-HA coating by (Gadow et al. 2010).

In a recent study, Jagadeeshanayaka et al. (2023) reported that low-temperature-operated HVAF-sprayed HA coating had a hardness of 334.33 ± 18.4 HV due to its dense structure. The coating thickness is also crucial in determining material strength and biocompatibility. ZHOU et al. (2023) investigated the effect of coating thickness on interfacial adhesion and mechanical properties of the Cr-coated zircaloy (Zr-4) substrate. They found that interfacial shear and adhesion strength decreased with increased coating thickness. This was attributed to the greater residual stress associated with thicker coatings, which results in the propagation of cracks along the interface and, ultimately, delamination of the coating. In this context, the proposed HVOF-HA coating thickness of around 55 μm with a very dense microstructure (~97%) is optimal for improving the osteogenesis function and regulating bone tissue metabolism for healing without compromising biocompatibility. Previous research has suggested that HA's optimal coating thickness should be 50-100 μm or less to enhance its biocompatibility (Li et al. 2014a). Furthermore, Morks et al. (2007) reported an increased hardness of HA coatings with decreased coating thickness. However, FS coating displayed the least adhesion strength, which may be due to its intermediate coating thickness and its porous microstructure. Future research is required to investigate the variations in coating thickness and compare their biocompatibility and mechanical strength.

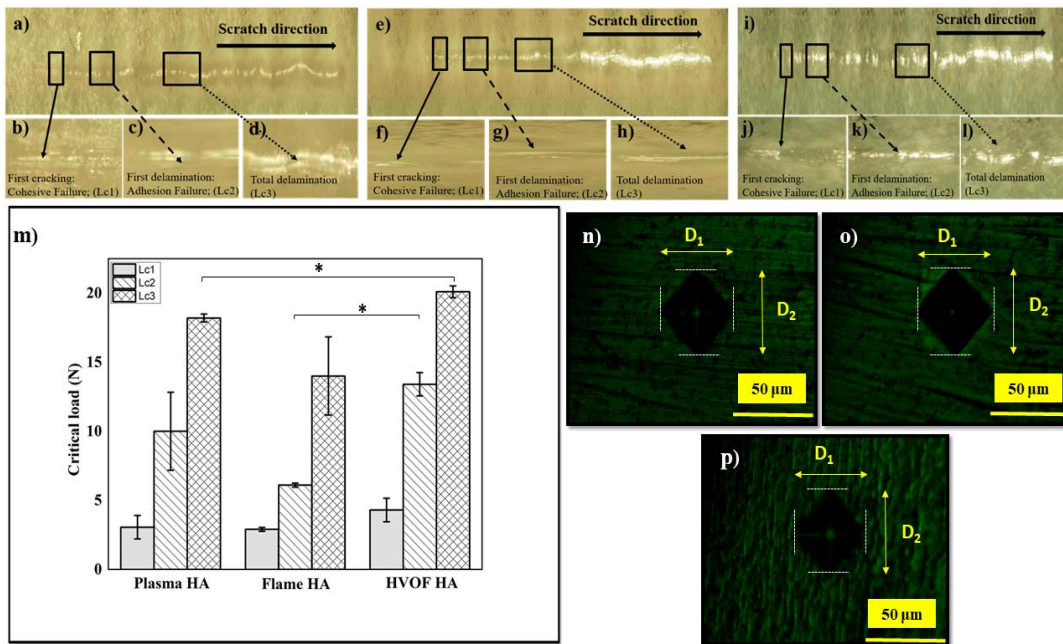


Figure 5.5 Optical micrographs of scratch tracks of as-deposited HA coating for APS (a) scratch track, (b) First cracking, (c) first delamination, (d) Total delamination, Flame spray (e) Scratch track, (f) First cracking, (g) First delamination, (h) Total delamination, HVOF spray (i) Scratch track, (j) First cracking, (k) First delamination, (l) Total delamination. (m) Bar graph shows the adhesion strength of the different HA coatings ($n = 3$; * p -values < 0.05). The error bar represents the standard deviation. Optical microscope image of the Vickers hardness indentation for (n) APS, (o) FS, and (p) HVOF-HA coating, where D_1 and D_2 are the horizontal and vertical diagonal lengths of the indentation (Shankar et al. 2024b).

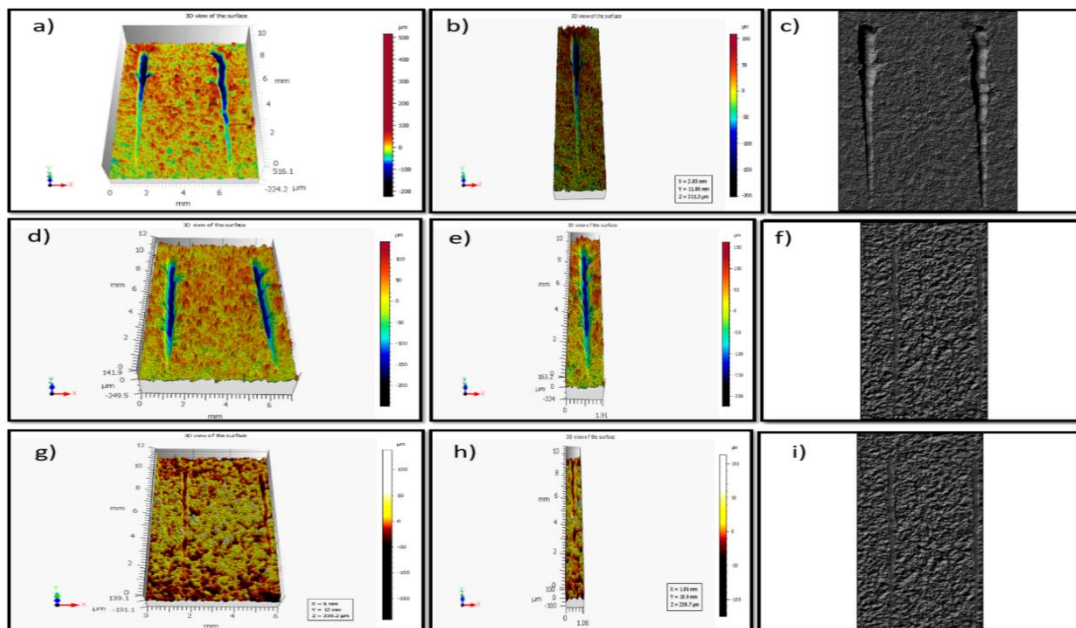


Figure 5.6 3D optical profilometer images show the coated samples' scratch track, (a-c) APS, (d-f) FS, and (g-i) HVOF-HA coatings (Shankar et al. 2024b).

5.7 In-vitro Simulated Body Fluid (SBF) Immersion Test

SBF was used to simulate blood plasma to evaluate the apatite development on the coated surfaces. Figure 5.7 (a-l) shows the changes in coating surface morphology after 15, 30, and 60 days of exposure to SBF. Different surface morphologies generated various nanocrystal HA that changed with time. The APS surface displayed a porous, honeycomb-like structure after 15 days of immersion. After 30 days, a dense honeycomb structure was observed. At the end of 60 days, a capsule-like structure was observed segregated over the coating surface. A cauliflower-like structure was noticed in most areas after 15 days of FS coating. After 30 days, these cauliflower structures were covered around the surface. Surprisingly, after 60 days, the coating displayed apatite structures similar to those observed on the APS surface. The apatite morphology of the HVOF coating was radically different from that of the APS and FS coatings. After 15 days, tiny needles and long interlinked filopodia structures could be observed all over the coating. However, after 30 days, a fine and dense hair structure had grown upright on the coated surface. After 60 days, fused capsule structures with a porous apatite layer surrounded the surface. The weight gain by the samples after each point of time supported the apatite layer deposition. X-ray diffractograms of the coatings after 15, 30, and 60 days of immersion further endorsed the apatite growth. The diffractograms' peak broadening (Figure 5.7 (n)) evidenced the apatite layer's development on the surface of the different coatings. Furthermore, the preferential apatite growth orientation in the 002 direction confirms the crystal orientation of natural apatite in the animal's hard tissue (Wang et al. 2017).

Blood plasma conditions were reproduced with SBF to study the in-vitro apatite growth on the coating surface. The changes in the coating surface morphology after 0, 15, 30, and 60 days of exposure to SBF are shown in Figure 5.7 (a-l). The formation of the superficial apatite surfaces for APS and FS has been reported previously (Clavijo-Mejía et al. 2020). The study showed the deposition of the apatite layers on all samples; however, there was better apatite layer deposition on the HVOF surface (Figure 5.7 (i-l)). The increase in the apatite layer deposited on the surface of HVOF coating may be due to its high degree of crystallinity and moderated hydrophilicity ($\theta_{CA} \sim 85^\circ$). Previously, other works argued that cell adherence and growth were better on

intermediate hydrophobic surfaces with contact angles of around 70° (Arima and Iwata 2007). Apatite layer deposition was further confirmed by the weight gain of the samples before and after soaking in the SBF (Figure 5.7 (m)). The development and the change in the apatite morphology of the samples over time were further established using X-ray diffractograms (Figure 5.7 (n)). XRD peaks for APS and FS coating showed a reduction of the mean width of the peaks after 15 days, and the intense peak at $2\theta = 31.8^\circ$ after 30 days of immersion probes that the coating interlayer delamination follows the apatite growth. However, an increase in the intense peak for HVOF coating over the period indicated the coating integrity followed by apatite growth. A similar XRD profile for the APS-HA coating was reported by Clavijo-Mejía et al. (2020) over different time intervals. The EDS analysis has also confirmed the testimony of the apatite growth. Apatite formation was observed to be low during the first two weeks due to dissolution/precipitation phenomena, which slightly improved after 15 days. The Ca/P ratio (after 30 days) was determined as 2.03, 2.25, and 2.3 for APS, FS, and HVOF coatings, respectively. After 60 days, the Ca/P ratio slightly changed to 2.05, 1.97, and 2.12. This increased Ca/P ratio confirms Ca-rich apatite formation on the surface of the SBF-soaked samples. The change in the Ca/P ratio is due to the interaction of the SBF and the HA ions. HA surface reveals a negative surface charge due to phosphate (PO_4^{3-}) and hydroxyl (OH^-) groups. The negative ions interact with the positive calcium ions (Ca^{2+}) from the SBF to form the Ca-rich ACP (amorphous calcium phosphate) layer, which gains a positive surface charge. The Ca-rich ACP again interacts with the negative phosphate ions in the SBF to form the Ca-poor ACP, which stabilizes by being crystallized into bonelike-apatite in the SBF (Sarath Chandra et al. 2012). Further, the SBF immersion study is one of the widely used methods in determining the biocompatibility of new biomaterials; the study may possess certain limitations, as it does not completely resemble the in-vivo or clinical environment. Conventional SBF and Dulbecco's Modified Eagle Medium (DMEM) may contain synthetic buffers that are not found in blood plasma. To simulate in vivo conditions accurately, modifying SBF solutions with biological molecules like amino acids, proteins, glucose, vitamins, and enzymes is recommended. Although the SBF composition differs slightly from the in-vivo environment, some studies have reported limitations of the SBF immersion test. It is, therefore, beneficial to determine its accuracy using previous literature. Materials

like β -tricalcium phosphate and natural calcite do not have apatite formation on their surfaces in SBF or in vivo (Kotani et al. 1991; Neo et al. 1993), but despite this, they were found to bond with living bone. The high resorbability of these materials was reported to be the reason behind this. In addition, a few studies have reported a mismatch in the results obtained from the SBF immersion study and the corresponding in-vivo study. Tan et al. (2010) reported the rapid degradation of a bone composite scaffold (nano-hydroxyapatite/collagen particles in an alginate hydrogel carrier) in SBF with no apatite gain, owing to the degradation of the alginate molecules. However, after eight weeks, the in vivo evaluation did not determine any obvious degradation. Despite the limitations of SBF, it has remained a powerful way of determining in vivo bone-bonding ability. Zadpoor (2014) reviewed 33 published articles in which the in vitro apatite forming ability and in vivo performance of two or more biomaterials were compared. They concluded that 75% of the SBF immersion studies successfully predicted the materials' relative in vivo bioactivity. However, ~25 % of the SBF test results contradict the in vivo results. Lopes et al. (2001) reported a comparative in-vitro SBF immersion and in-vivo study for CaO–P₂O₅ glass-reinforced hydroxyapatite (GR-HA) composites and sintered hydroxyapatite. None of the two materials showed apatite formation after four weeks of SBF immersion. However, the result of the in-vivo study with white male rabbits after 16 weeks exhibited a strong bonding between the composites and bone for GR-HA composite compared to sintered HA. The previous literature supports the SBF immersion study in evaluating new biomaterials; therefore, the current study results are reliable. However, further in-depth in-vivo studies will increase its accuracy.

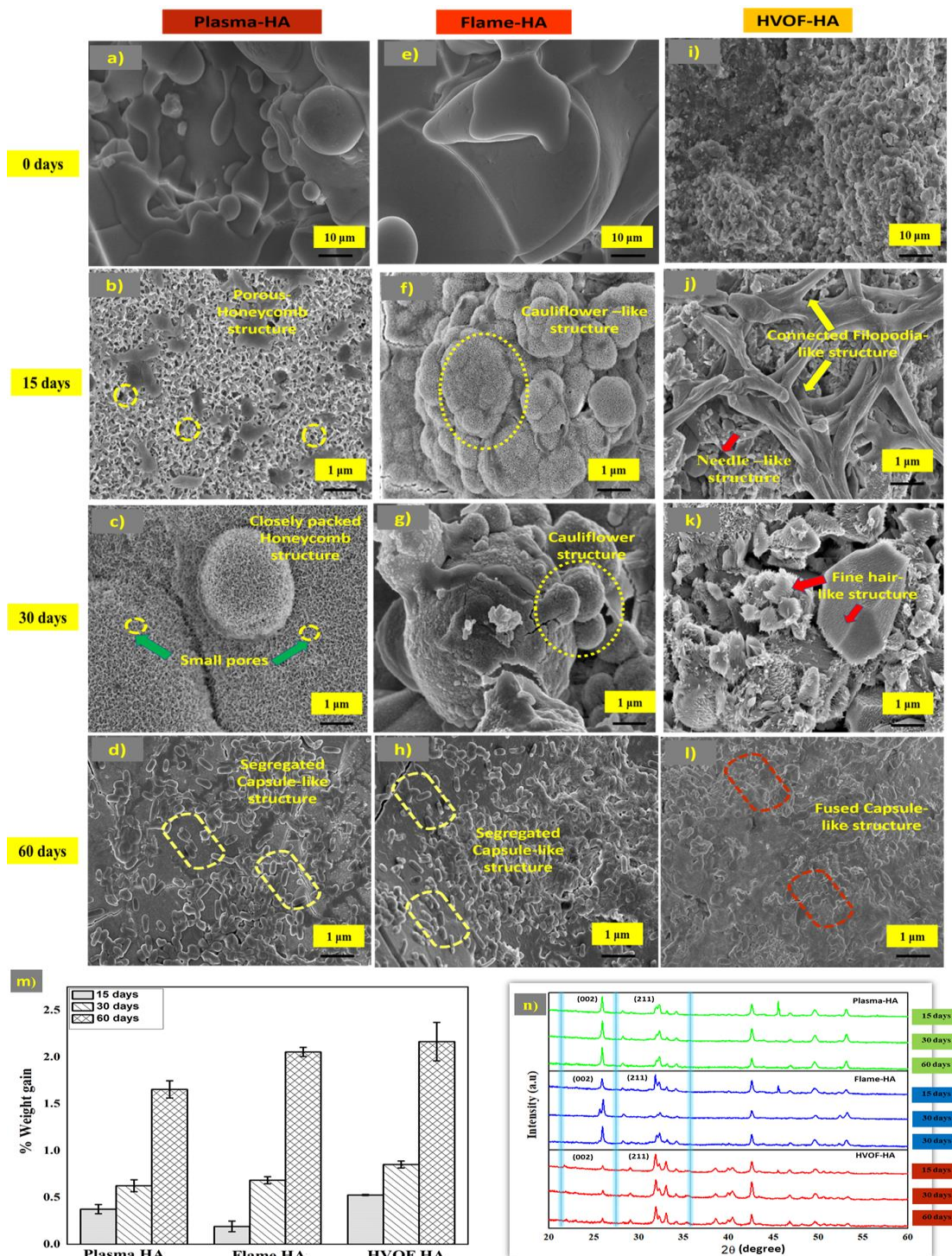


Figure 5.7 FESEM images show the change in apatite morphology on the surface of different HA coatings obtained after 15,30 and 60 days of immersion in SBF (a-d) APS, (e-h) FS, and (i-l) HVOF-HA coatings. (m) % weight gain by HA coatings as a function of the time immersed in SBF (n = 3). The error bar represents the standard deviation. (n) The XRD pattern shows the change in apatite growth observed over time in HA coatings (Shankar et al. 2024b).

5.8 Hemocompatibility assessment of HA coatings

5.8.1 Hemolysis study

Hemolysis is the release of hemoglobin from damaged red blood cells (i.e. erythrocytes). This test examines the interaction of materials with RBCs by measuring the released hemoglobin. As per the ASTM standard, if hemolysis induced by biomaterial is $<5\%$ = highly hemocompatible, within 10% = hemocompatible, and $>20\%$ = non-compatible (Sarath Chandra et al. 2012). The negative control showed no rupture of erythrocytes (0%); however, the positive control showed 100% hemolysis, suggesting a complete rupture of RBC cells. The same is confirmed by colorimetric images, which showed a completely white color solution for the negative control and a dark red color for the positive control (Figure 5.8 (b)). Microscopic images for the positive control (Figure 5.8 (f)) confirm the increase in the central pallor diameter of the RBCs. The RBC membrane is relatively weak, and water enters the cell by osmosis. The fragile cell membrane bursts as the volume and pressure increase due to water adsorption, releasing hemoglobin in the solution. The sample percentage hemolysis is displayed in a bar graph format, as seen in Figure 5.8 (a). The RBC rupture by the samples in decreasing order is $FS < APS < Ti < HVOF$. All samples exhibited less than 5% hemolysis, confirmed by the white color solution shown in (Figure 5.8 (b)). This suggests that the samples are non-hemolytic. Moreover, the HVOF coating exhibited the least absorbance of all the coatings, almost similar to the negative control. Further, HVOF coating showed a significant decrease in RBC rupture compared to other coatings. This indicates that HVOF coating has the potential to become a suitable implant candidate. Moreover, RBC's morphology and membrane integrity were unaffected by the released particles from the coatings (dotted red circles indicate intact RBC), demonstrated by microscopic pictures (Figure 5.8 (c-e)). Li et al. (2016) reported a hemolysis rate of less than 0.3% for electrophoretic-deposited silk fibroin/graphene oxide/hydroxyapatite coating on titanium. Guan et al. (2012) reported 4.12% and 4.35% hemolysis for uncoated and electrodeposited HA on Mg-4Zn-1Ca-0.6Zr alloy, respectively.

Hemocompatibility is the most basic requirement that a blood-contacting

material should meet for clinical use. This study is a way of identifying biomaterial's toxic nature toward red blood cells (RBCs). We have carried out the in-vitro toxicity evaluation of HA coatings to human erythrocytes according to ASTM: F756-00. The toxic element of new material damages the RBC membrane, which releases hemoglobin. All the coating displayed non-hemolytic behavior (<5% hemolysis). (Guan et al. 2012) studied the hemolysis assay with human blood for uncoated and electrodeposited HA coating on the Mg-4Zn-1Ca-0.6Zr substrate. The samples were reported to be blood compatible as the hemolysis % was <5%; however, the critical reason behind RBC rupture was not reported. The least non-hemolytic behavior shown by HVOF coating is due to their lower surface roughness and very high crystallinity. Increased roughness results in more surface area (Wang et al. 2012), providing more space for erythrocytes to interact with and leading to more RBC rupture. However, APS and FS samples showed higher absorbance than HVOF (Figure 5.8 (b)) due to their increased surface roughness and the low crystallinity of the coatings. The latter has a more dominating role in hemolysis (Wiessner et al. 1988). The findings of this assay indicate that low-temperature operated coatings, particularly HVOF coating, can effectively inhibit the rupture of RBCs and improve the hemocompatibility of Ti-6Al-4V alloy.

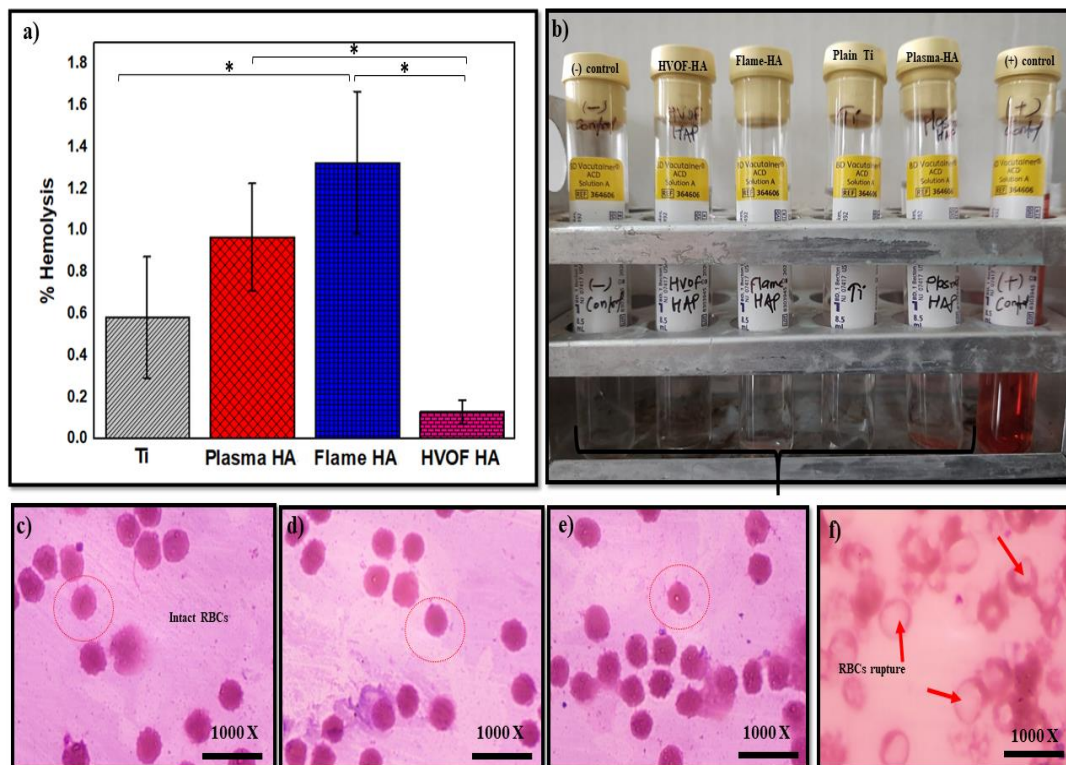


Figure 5.8 (a) Bar graph shows the percentage hemolysis for titanium and HA coatings ($n = 5$; $*p$ -values < 0.05). The error bar represents the standard deviation. All samples displayed less than 5% hemolysis, indicating their non-hemolytic behavior. (b) Colorimetric images showing RBC damage for positive control-DW, negative control-saline, and samples. The white-colored tube represents no rupture of RBCs, and the red-colored tube shows a complete rupture of RBCs. Microscopic stained images show the change in RBCs morphology for (c) APS, (d) FS, (e) HVOF coatings, and (f) Positive control (Shankar et al. 2024b).

5.8.2 Whole Blood Clotting Time Assay

In this study, the ability of samples to clot was evaluated by measuring the concentration of free hemoglobin released when unclotted RBCs interact with water. A higher hemoglobin concentration in the supernatant indicates less clotting by the sample. The results, depicted in Figure 5.9 (a), suggest that the clotting behavior on all coated surfaces was considerably lower than on titanium. Additionally, the thrombogenicity of titanium increased significantly between 15 and 45 minutes, possibly due to an increased number of entrapped RBCs within the clot. This aligns with the findings of Manivasagam et al. (2021) for uncoated Ti-6Al-4V. Furthermore, the HVOF samples displayed significantly higher non-thrombogenic behavior than the

APS and FS samples. The HVOF coating exhibited the lowest clotting behavior throughout each time point, as evidenced by its higher absorbance values than other samples. These results are supported by the colorimetric images displayed in Figure 5.9 (b-d).

The anticoagulant behavior of different samples was determined using the whole blood clotting assay. The absorbance value was used to measure the amount of blood clots formed on the sample. The higher the absorbance value, the lower the clotting behavior. The results indicated that the samples exhibited increasing clotting behavior at the end of 45 minutes in the following order: whole blood < HVOF < FS < APS < Ti (Figure 5.9 (a)). Uncoated titanium showed a high level of thrombogenicity (blood clotting behavior) because it lacked a repelling surface like HA. The HA powder used in the study had a negative surface charge ($-2.3 \text{ mV} \pm 0.82$) at physiological pH 7.4. Similarly, red blood cells (RBCs) also had a negative zeta potential on their surface due to carboxyl groups of sialic acid (EYLAR et al. 1962) repelling the adjacent negative surface, not allowing the erythrocytes to get entrapped. Therefore, all the coated samples showed higher absorbance than the uncoated ones. APS and FS coating showed almost 50% less absorbance value than unclotted blood during the first 15 minutes and significantly dropped over the period. This was attributed to the electrostatic interaction between proteins and Ca-P ions (Zhou et al. 2007). The adsorption of protein molecules on the HA surfaces occurs due to positive (Ca^{2+}) and negative ($\text{PO}_4^{-3}/\text{OH}^-$) sites. These charges could bind the protein's negative acidic groups (COO^-) and positive amino groups (NH_3^+). Research has shown that the negative surface charge of the HA preferred to adsorb more basic protein lysozyme (LSZ) than acidic protein BSA at pH 7.4 (Zhu et al. 2007). In addition to the surface charge, the high roughness and porosity of APS and FS coatings could be critical factors in displaying increased blood clotting. On the other hand, HVOF coating showed almost ~3 times higher absorbance value than a clinically used biomaterial, "polytetrafluoroethylene (ePTFE)," used for prosthetic vascular grafts (Motlagh et al. 2006).

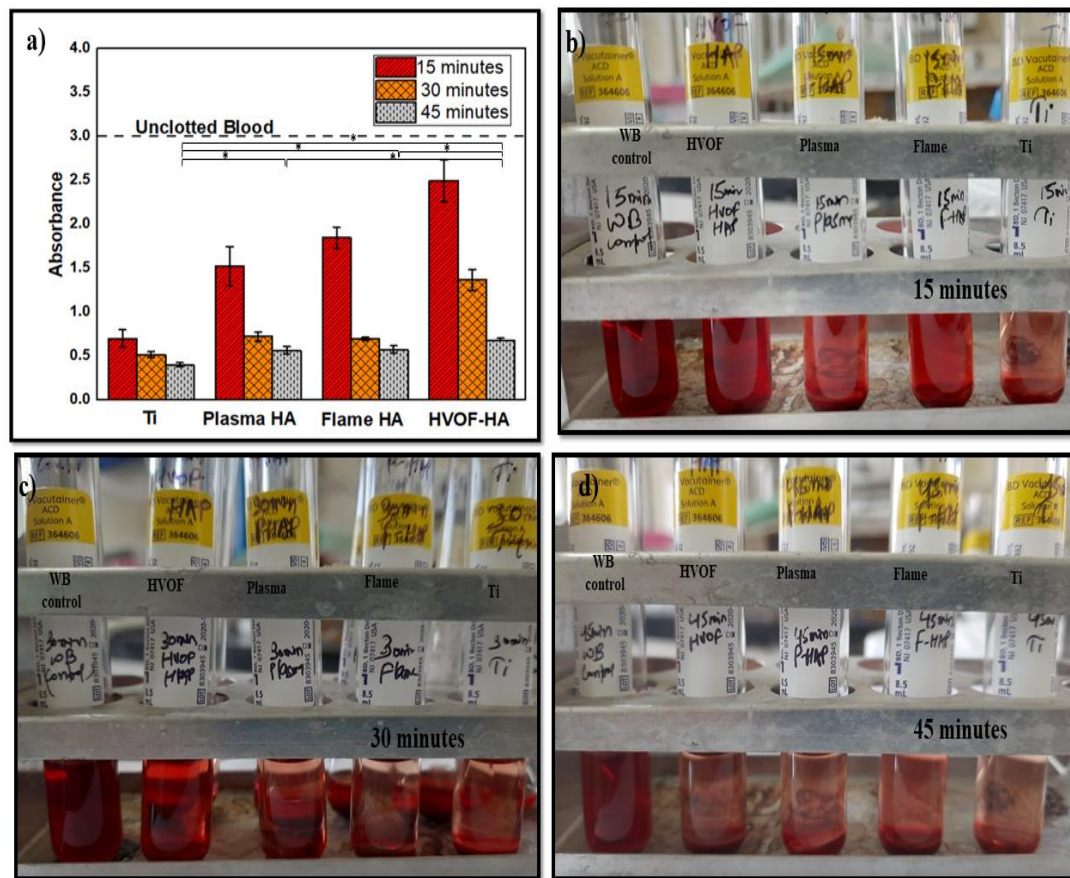


Figure 5.9 (a) Bar graph shows the absorbance value of the whole blood clot study at different time points (15, 30, 45 minutes) for titanium and HA coatings ($n = 5$; * p -values < 0.05). The error bar represents the standard deviation, and the dotted line represents the absorbance of free hemoglobin in unclotted blood. A significant increase in free hemoglobin is present on all coated surfaces compared to the uncoated titanium at respective time intervals. Colorimetric images of the samples after (b) 15 minutes, (c) 30 minutes, and (d) 45 minutes. The dark red tube shows the release of free hemoglobin, indicating that the samples are non-thrombogenic. On the other hand, the light red tube in color depicts the thrombogenicity of the samples (Shankar et al. 2024b).

5.8.3 Platelet adhesion and activation assay

A study investigated the effect of structural changes in the coating on platelet structure. The study used (PRP) with a platelet count of 7.21 lac platelets/ μ L, generated by centrifuging whole blood. The study observed that there was a more significant amount of platelets adhering to the coated surface than the uncoated titanium (Figure 5.10 (a)), with FS>APS>HVOF>Ti trend. FESEM images were used to analyze platelet structures (Figure 5.10 (b-f)). The adherent platelets were divided into five shapes to demonstrate varying degrees of platelet activation: round, dendritic, dendritic spread,

and fully spread. Figure 5.10 (g) illustrates the role of implant surface properties (zeta potential, wettability) on platelet adhesion and the mechanism underlying different stages involved in the change in platelet morphology and clot formation. Round platelets were seen on the control, Ti, and HVOF surfaces, indicating the non-activation of platelets due to their surface chemistry. However, APS and FS displayed pseudopodial extensions and spread dendritic platelets, indicating low platelet activation.

Platelet adhesion and activation are essential to evaluate biomaterial blood compatibility and the probability of thrombus formation. All the samples were incubated with PRP. Considering the surface properties of biomaterials is crucial as they significantly impact protein adsorption and blood component activation. A smooth and dense structure of titanium results in the least platelet adherence; however, a considerable amount of platelet was seen on its surface, owing to its hydrophobicity. Hydrophobic surfaces are more likely to release water molecules and cause protein adsorption because they have low surface energy (Gessner et al. 2000). APS and FS coating, on the other hand, demonstrate higher platelet attachment due to their uneven and porous structures. Further, the platelet morphology on Ti surfaces and the HVOF coating looks similar to the negative control (Figure 5.10 (c), (f), and (b)). However, the APS and FS coatings displayed low platelet activation, as shown by spread and pseudopodial platelets (Figure 5.10 (d) and (e)). A rough surface with pores and a larger surface area allows for more protein adsorption due to electrostatic force and wettability (Wang et al. 2012). Porosity and pore size also play a significant role in controlling surface area and protein adsorption. Zhu et al. (2009) reported higher protein adsorption on porous biphasic Ca-P (BCP) than on dense BCP surfaces. The surface charge of HA has significantly impacted protein adsorption with Ca^{2+} and $\text{PO}_4^{3-}/\text{OH}^-$ ions. acting as primary catalysts for protein binding. Acidic proteins contain negatively charged acidic groups, such as (COOH^-) , which are easily attracted to Ca^{2+} ions of HA. On the other hand, basic proteins have positively charged amino groups (NH_3^+) that can attract negative $\text{PO}_4^{3-}/\text{OH}^-$ ions (Shankar et al. 2024a). These surface charge interactions with plasma proteins help facilitate platelet adherence to coated surfaces.

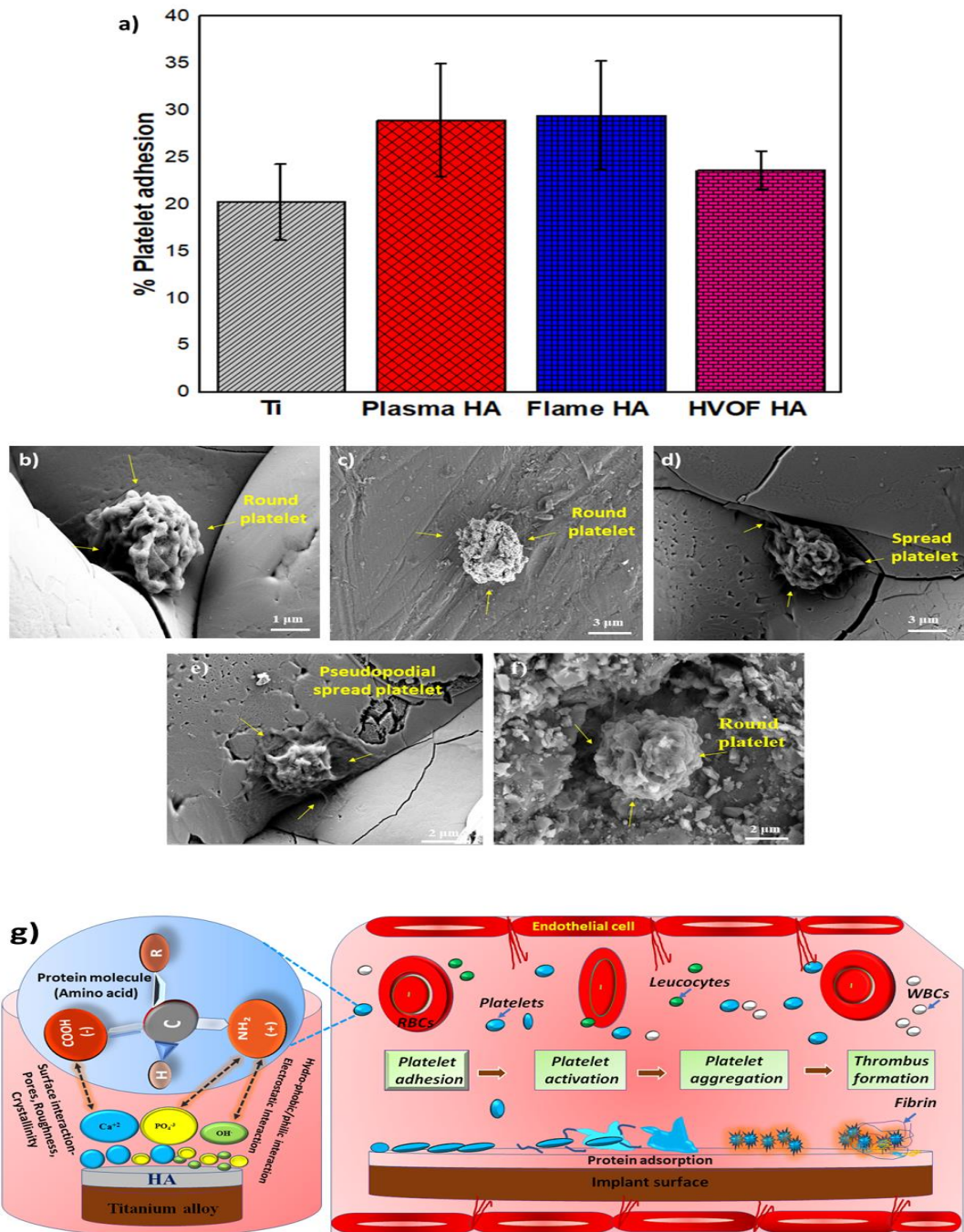


Figure 5.10 (a) Bar graph represents the percentage of platelets adhered to titanium and coated samples ($n = 3$; * p -values < 0.05). The error bar represents the standard deviation. FESEM morphology of platelets adhered on the surfaces of (b) Negative control, (c) Titanium, (d) APS, (e) FS, and (f) HVOF-HA coatings. (g) Schematic illustration shows the role of implant surface properties (zeta potential, wettability) on platelet adhesion and the mechanism underlying different stages involved in the change in platelet morphology and clot formation (Shankar et al. 2024b).

5.8.4 Coagulation assays

Clinical coagulation tests, such as PT and aPTT, are used to measure the anticoagulant potential of biomaterials. For this study, PPP with a platelet count of $9 \times 10^3/\mu\text{L}$ was generated from WB. The blood coagulation cascade involves different proteases that interact with each other to produce thrombin, followed by fibrin polymerization. It can be divided into two primary pathways: extrinsic (PT) and intrinsic (aPTT). These two systems are activated by different mechanisms and merge with the activation of factor X (FX) in the common pathway, where fibrin clot, the final product of the coagulation cascade, is produced. The bar graph in Figure 5.11 (a) shows the clotting time of the samples. Ti and FS coatings showed a slight decrease in PT results compared to the control, while APS and HVOF coatings showed a small increment in PT. The following trend was observed for the PT study: HVOF>APS>(-) control>FS>Ti. A similar trend was observed for the aPTT assay. A significant decrease in the aPTT value for Ti was observed, indicating its clotting behavior. Figure 5.11 (b) illustrates how implant surface properties, such as wettability and surface roughness, play a role in clot formation. HVOF coating slightly increased both PT and aPTT values, suggesting its non-thrombogenicity.

The coagulation assay (PT and aPTT) further confirmed the WB clotting time assay results. A prolonged PT and aPTT value for APS and HVOF coatings showed significant anticoagulant activity. However, Ti and FS coatings displayed reduced clotting time, indicating their thrombogenicity. Ti's hydrophobicity might be responsible for this behavior, allowing the plasma to clot quickly. The results suggested that the FS coating's porous structure and high surface roughness might activate the coagulation cascade and shorten PT and aPTT. Therefore, HVOF coating can be considered a better non-thrombogenic biomaterial. Table 5.1 compares HA coatings acquired through APS, FS, and HVOF thermal spray techniques based on their in vitro results.

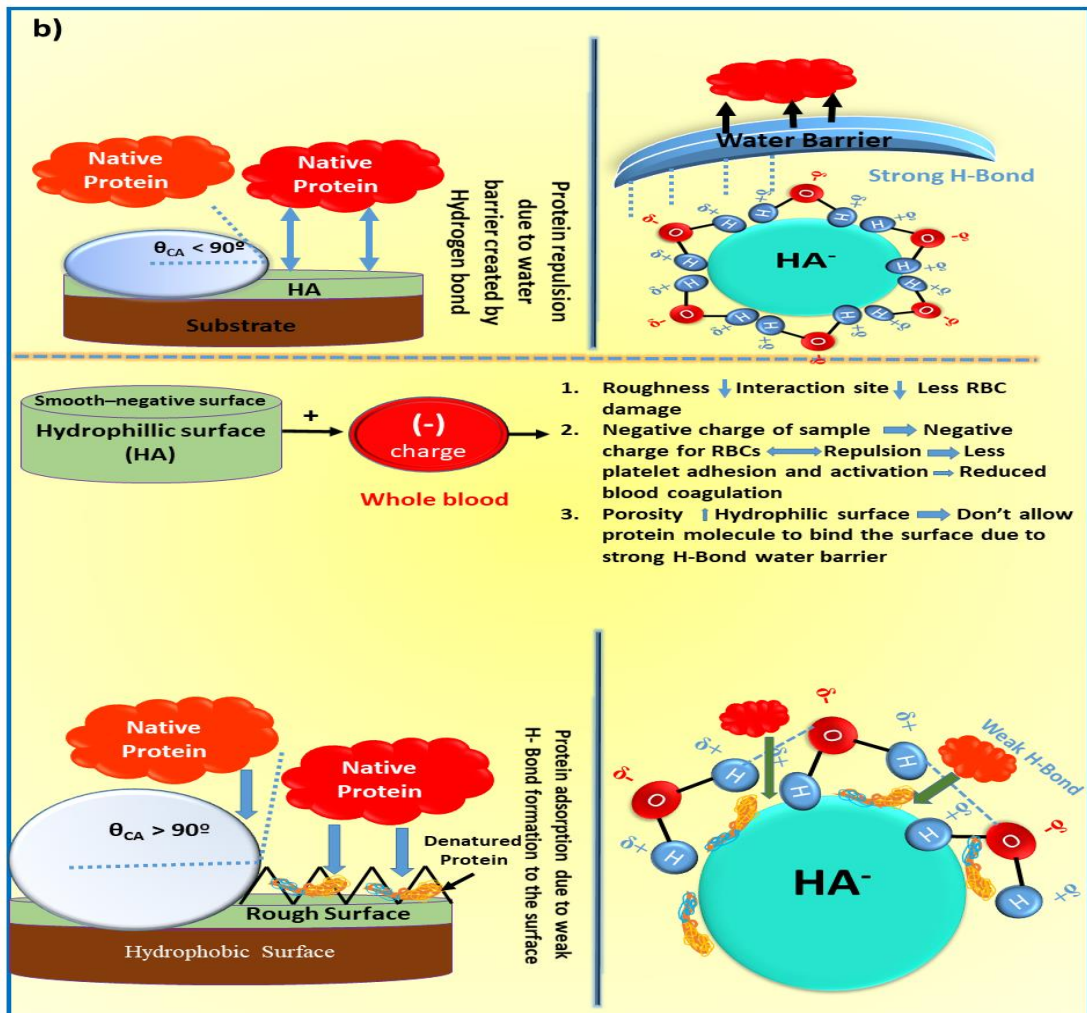
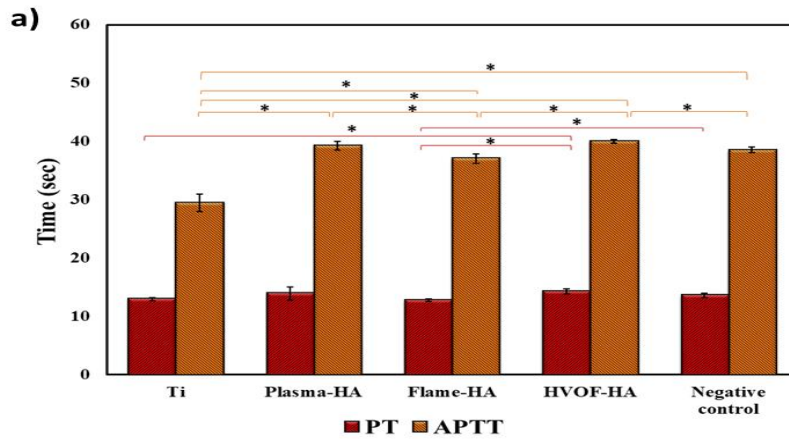


Figure 5.11 (a) Bar graph shows the coagulation time for different samples and a control incubated with PPP for 1 hour ($n = 5$; $*p$ -values < 0.05). The error bar represents the standard deviation. (b) A schematic illustration depicts the mechanism underlying the role of implant surface properties (wettability, surface roughness) in clot formation (Shankar et al. 2024b).

Table 5.1 Comparative analysis of HA coatings acquired through APS, FS, and HVOF thermal spray techniques based on their in vitro results (Shankar et al. 2024b).

In vitro studies	Surface properties influencing	FS	HVOF
SBF apatite growth (60 days)	Crystallinity, Wettability	+24.24%	+30.90%
Hemolysis	Roughness, Crystallinity	-37.11%	+86.59%
Blood clot (45 minutes)	Surface Charge, Roughness, and Porosity	+1.75%	+21.05%
Platelet adhesion %	Surface Charge, Roughness, Porosity, Wettability	-1.93%	+18.35%
PT	Wettability, Porosity	-8.63%	+2.87%
APTT	Wettability, Porosity	-5.61%	+2.04%

+ represents the increment, - represents the decrement. All the percentage (%) values are with respect to plasma sprayed HA coating.

5.9 Qualitative Antimicrobial Assay

The samples were tested for antimicrobial properties against Gram-positive and Gram-negative bacteria, and the results were validated. No activity was observed for either bacterium in the bare titanium and all coated samples, as evidenced by the lack of inhibition zone formation around the disc (Figure 5.12 (a) and (b)). This suggests that HA coatings have good osseointegration properties but poor antimicrobial properties. Scientists are currently exploring different methods and materials to improve the antibacterial effectiveness of coatings. However, it's important to note that simply having antibacterial properties alone is not enough for orthopedic implants. A recent study by Arjunan et al. (2021b) has identified a specific set of critical criteria that antimicrobial biomaterials intended for orthopedic purposes must fulfill. These prerequisites include stable mechanical performance, biocompatibility, effective antibacterial properties without causing toxicity, and sustained release during the "risk period." Therefore, it is crucial to investigate and develop biomaterials that satisfy these requirements. Previous research has demonstrated that metallic biomaterials, such as

silver, copper, zinc, gold, nickel, palladium, and selenium, possess exceptional antibacterial properties. CNTs are an intriguing prospect, as they have the potential to enhance the antimicrobial characteristics of HA coatings while simultaneously improving mechanical strength. The advantage of metallic components over other antimicrobial biomaterials is their complementary mechanical performance and ease of processing through established techniques. Consequently, reinforcements such as CNT/Ag/Cu are necessary to imbue HA with antimicrobial properties and enhanced mechanical strength and biocompatibility. However, these materials' long-term cytotoxicity and biocompatibility for clinical use are yet to be fully explored.

Preventing bacterial infections during joint replacement surgeries is crucial to avoid extended hospital stays, revision surgeries, and increased healthcare costs. The sample testing results revealed that none of them had any antimicrobial properties since no inhibition zone formation was observed around the disc (Figure 5.12). Similar results were also reported by Rameshbabu et al. (2007) for HA powder, which lacks antibacterial properties due to its strong affinity towards organic substances like proteins and amino acids that promote bacterial adhesion and replication. To address this issue, researchers are exploring different strategies to develop antibacterial biomaterials that can help prevent implant infections. The development of innovative biomaterials with inherent antibacterial properties, or the enhancement of biomaterial surfaces through bactericidal coatings such as copper, silver, and zinc, or bacteria-repellent coatings such as silicon ions and lotus leaf (Arjunan et al. 2021b) has become a cutting-edge research area. For instance, the Cu-W-Ag microporous architecture has shown antiviral solid behavior against SARS-CoV-2 with a virus inactivation rate of 99.2% (Robinson et al. 2021). Additionally, combining a ginger extract with iron oxide-magnesium oxide co-doped HA has demonstrated promising results in reducing bacterial cell count (by approximately 82%) with enhanced biocompatibility (Bhattacharjee and Bose 2023). Recent clinical studies have also suggested that thermally sprayed silver-HA composite coatings may potentially treat septic arthritis (Hashimoto et al. 2020), indicating the possibility of researching composite coatings for future generations. These findings suggest that future research should delve deeper into the potential of these antibacterial dopants or their combinations in HA for use in

orthopedic or dental implants. Furthermore, researchers have proposed the concept of smart coatings that can expand the capabilities of existing coating techniques by incorporating new functionalities such as enhanced tribological, osteointegration, and infection-causing bacterial detachment (Arjunan et al. 2021a).

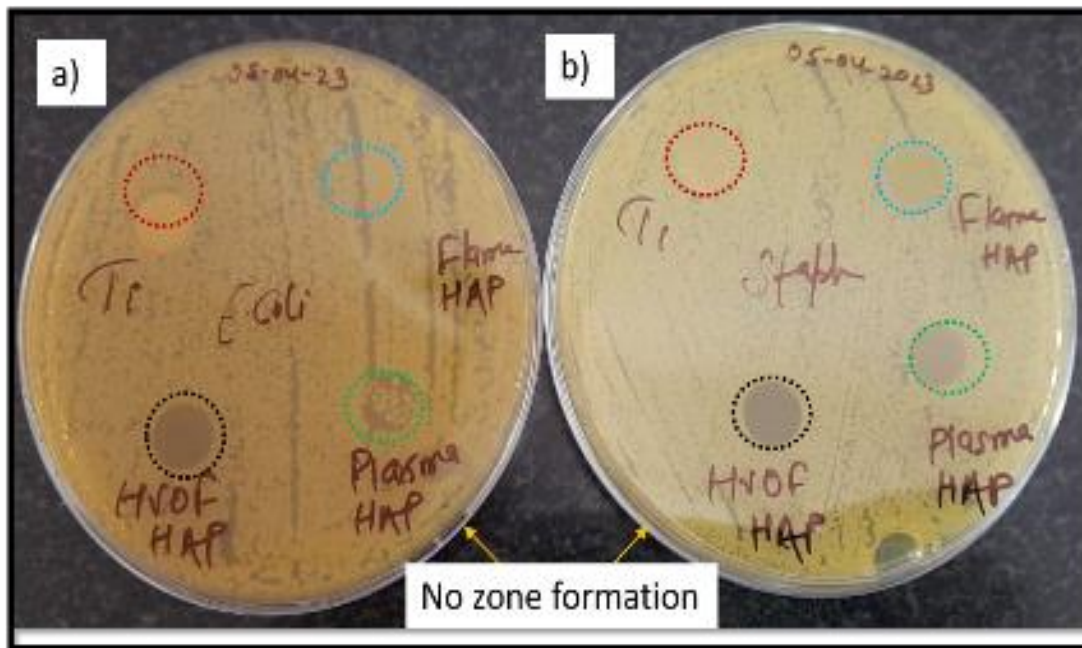


Figure 5.12 Agar diffusion test for the titanium and HA coatings with (a) Gram-negative *E. coli* and (b) Gram-positive *S. aureus* shows no inhibition zone formation around the discs. The dotted circle represents the formation of the no-inhibition zone around the discs, indicating the non-microbial property of HA (Shankar et al. 2024b).

5.10 Summary

This section delved into the distinct morphology, phases, and surface chemistry created by various thermal spray techniques across different temperature ranges. It also examined coating bond strength and hardness. Additionally, it explored how surface chemistry affects bioactivity, hemocompatibility, and anti-bacterial properties. The data presented in this chapter has been published in two reputable journals (Shankar et al. 2024b; a). The following section will discuss the coating's physiochemical, mechanical, tribological, and biological properties created through the most successful reinforced powder (HAC1) and best-performed thermal spray process (HVOF). Moreover, it will cover the in vivo implantation study of the best-achieved coatings.

CHAPTER 6 TRIBOLOGICAL AND IN VIVO STUDY OF THE COATINGS

6.1 Preamble

This chapter discusses the general characteristics of the HVOF sprayed coatings deposited using HA and CNT-reinforced HA powders. The microstructure and phases of the coatings were analyzed, and the retention of CNT was examined using Raman spectroscopy. The coatings were evaluated for their primary properties, such as porosity, roughness, degree of crystallinity, and phase change determination. Additionally, a scratch test was performed on the coatings to assess their adhesion strength to the substrate and to understand the role of CNT in improving the scratch resistance. The biocompatibility of the coatings was also evaluated using human blood and by implanting the coated titanium rods in the rabbit's femur bone. The coatings underwent a wear test to determine their durability and longevity. The main objective of this section is to compare the wear resistance and in vivo compatibility of the coatings.

6.2 Microstructure of feedstocks and coatings

The morphology of the feedstocks is explained in the previous section, 4.3. Figure 6.1 (g-n) illustrates the smooth surface of the bare titanium substrate used for coating and the top surface microstructure for HA and HAC1 coatings. The HA and HAC1 coatings exhibited flattened lamella with many unmelted particles of micron size and partially melted and fully melted splats spread over the surface. The submicron particles that have not melted are due to the crystallites present in the feedstock, indicating a significant level of crystallinity. Additionally, unmelted HA and alumina particles have retained their morphology. A few spherical particles of micron size similar to HA feedstock could be observed on the coating surface, most likely resolidified crystallites (Figure 6.1 (i), shown with a red dotted circle, and Figure 6.1 (l), shown with a yellow dotted circle).

Furthermore, let's compare the diameter of HA and HAC1-coated particles with that of feedstocks. It can be observed that most particles were in the range of 10-40 μm ,

present in the coating, similar to feedstock, thereby confirming the retention of HA phases. Some voids/pores with a few micro-cracks were observed on the HA surface, which can significantly reduce the hardness, ultimately resulting in the low wear resistance of the coating. Moreover, some microcracks were also observed on the HAC coating surface, but these cracks were arrested by the CNT bridging and hook mechanism, as seen in Inset Figure 6.1 (m). The density of the HA and HAC coatings was calculated as ~96% and ~97.2%, respectively, which is much higher than the values reported by (Kalmudia et al. 2010; Tercero et al. 2009) for plasma sprayed-HA and HA/alumina/CNT coating. The high density obtained in the present study is due to the inherent properties of HVOF spray. Moreover, the HAC1 coating showed greater density than the HA coating, which is attributed to the role of reinforcements, especially CNT, that arrest the microcracks and pores throughout the surface.

The unmelted and partially melted particles on the coating surfaces result from the synergistic effect of high crystalline feedstocks and the low operating temperature (~2500 °C) in the HVOF process. The high magnification images revealed submicron-sized broken and shattered particles (Figure 6.1 (i) and (m)), generated by the high velocity (600-1000 ms⁻¹) and kinetic energy involved in the HVOF process. The high-magnification images of the HAC1 coating in Figure 6.1 (m) showed the evenly distributed and embedded CNTs protruding from the HA/alumina matrix, indicating that the uniform distribution of CNTs during the powder stage is maintained in the coating. The heterocoagulation process employed for composite powder preparation is highly effective for achieving uniform CNT dispersion. CNT acts as a crack arrestor in the matrix, as seen in the inset Figure 6.1 (m), with surface precipitation (enclosed within the black rectangular box) and hook-like structure (shown with the enclosed arrow). The HAC1 coating had many small cracks compared to the HA coating, possibly due to secondary phases or unmelted particles in the matrix. The thermal stress mismatch between HA splats and secondary phases may be due to the difference in the thermal conductivity of the reinforcements. HAC1 coating has a higher likelihood of microcrack formation than HA coatings due to the higher thermal conductivity of CNTs, causing a steeper temperature gradient. However, microcrack formation in our case is much less significant than previous works reported for plasma-sprayed HA

coating. The high magnification image of the HAC1 coating (Figure 6.1 (l)) indicates that the coating has evenly distributed rough regions attributed to second-phase particles. The roughness of the coating can promote protein absorption on the surface, favoring cell attachment and improving biocompatibility.

It is essential to have a uniform distribution of reinforcements throughout the coating to achieve homogenous mechanical and biocompatibility properties. Thus, understanding the elemental distribution in the coatings becomes necessary to visualize the overall distribution of $\text{Al}_2\text{O}_3/\text{CNT}$ in the HA matrix. The EDS mapping (Figure 6.1 (j)) confirms that the HA coating contains its fundamental elements: Ca, P, and O. Furthermore, the HAC coating shows C, Al, O, Ca, and P, verifying the retention of reinforcements in the HA matrix (Figure 6.1 (n)). Both feedstocks were free of foreign elements, indicating no contaminants were introduced during the thermal spraying. The smooth regions in the corresponding backscattered image (Figure 6.1 (n)) are abundant in Ca and P, indicating the presence of HA. In contrast, the rough regions exhibit a high alumina concentration, suggesting the existence of second-phase particles, which supports the hypothesis of the formation of irregular morphologies in the secondary phase region. The Al-rich region mainly contains CNTs because they integrate with Al_2O_3 during heterocoagulation. EDS analysis also confirmed the homogenous distribution of CNTs throughout the bulk, as seen from the dot map image for carbon (Figure 6.1 (n), red dot mapping), where no chunks/patches of carbon can be seen. The microstructure of the coatings indicates that the HVOF spraying of HA-based feedstock and the heterocoagulation process could be an ideal approach for manufacturing implants with uniform surface properties with the retention of feedstock phases. Further confirmation for the phase retention will be carried out using XRD and Raman analysis, which will be discussed further in the next section.

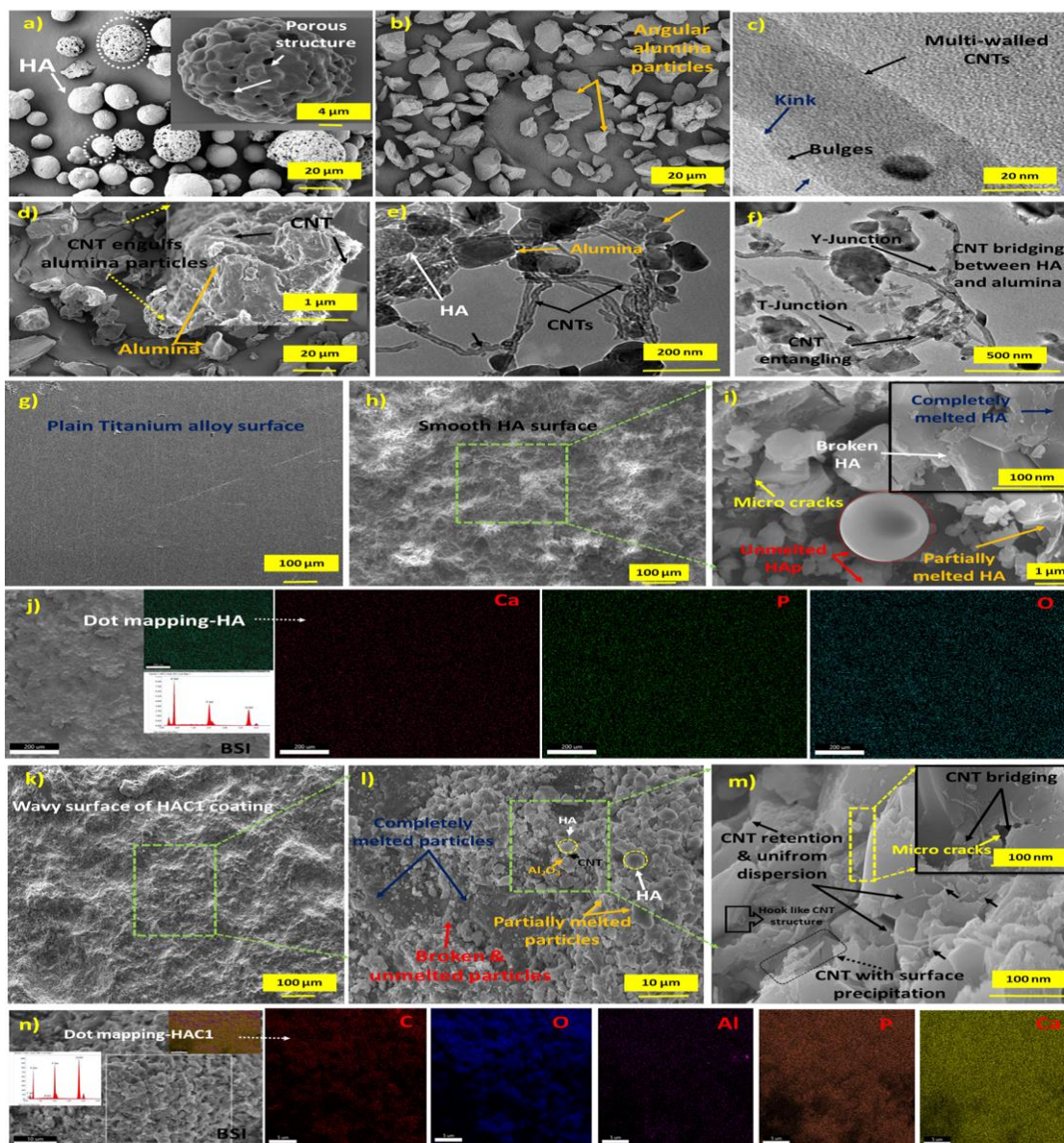


Figure 6.1 FESEM micrograph (a) spherical morphology for HA powder, (b) Angular and blocky structure for alumina particle, (c) Kink and bulges represents functionalization of CNT, (d) Heterocoagulated alumina/CNT shows CNT gets adsorbed and completely engulfed alumina particles, (e and f) TEM images showed various junctions of CNT attached to HA/alumina particles due to electrostatic interaction between the ions, FESEM micrograph (g) Plain smooth titanium surface, (h and i) Low and high magnification images showed top surface microstructure for HA coating displayed smooth surface with unmelted and partially melted HA particles, (j) Back scattered micrograph for HA coating with corresponding EDS analysis and dot mapping, (k and l) Low magnification images showed top surface microstructure for HAC1 coating, (m) High magnification image for HAC1 coating shows crack arresting, hook structure and homogenous dispersion and retention of CNT in HA matrix, and (n) Back scattered micrograph of HAC1 coating with corresponding EDS analysis and dot mapping, indicates no impurities were added during thermal spraying.

6.3 X-ray analysis of coatings for phase distribution and quantification

The diffraction pattern in Figure 6.2 (a') was used to identify phases, degree of crystallinity, and crystallite size of feedstock and coatings. ISO 13779-3 and ICDD files were used for reference. The transformation from powder to coating decreased crystallite size, resulting in a minor peak shift towards a higher angle and a slight broadening of peaks in both coatings. The main HA and HAC coating peak belonged to HA, with a small peak around 30° indicating HA's TTCP phase (ICDD File No. 01-070-1379). Due to the phase transition, i.e., α -TCP and β -TCP, HA's two primary secondary phases are considered here. β -TCP (JCPDS No. 009-0169) with the two highest peaks, $2\theta = 27.77^\circ$ and $2\theta = 31.02^\circ$, is absent in the coatings. Furthermore, α -TCP (JCPDS No. 009-0348) has no peaks at $2\theta = 30.71^\circ$, while the other peaks at $2\theta = 28.8^\circ$ and $2\theta = 34.2^\circ$ overlap with the peaks of HA at $2\theta = 28.93^\circ$ and $2\theta = 34.3^\circ$. Therefore, we could not detect α -TCP or β -TCP in both coatings. Additionally, the absence of the two humps at $2\theta = 25-35^\circ$ and $45-55^\circ$ indicates the lack of HA's amorphous phases (ACP) in both coatings. These observations show that most HA particles did not experience phase transformations or melting while being sprayed by HVOF. Moreover, HAC1 coating retains the alumina and CNT peaks with a slight shift, confirming their increased crystallinity. HA coating depicted crystallinity of 88.62%, owing to the low temperature of in-flight particles and high velocity (600 ± 350 m/s) involved in the HVOF process. The presence of second-phase particles and the built-in quality of the HVOF process resulted in a crystallinity of 91.23% for the HAC1 coating, which stands in contrast to other coatings. According to Vilardell et al. (2020), the HVOF-HA coating exhibited a crystallinity of 82%. The lower crystallinity percentage found in their study might be due to their utilization of smaller particle size for HA (~ 30 μm) and variations in the spraying conditions compared to our results.

The increase in the crystallinity for the HAC1 coating may be attributed to the huge difference in the thermal conductivity of reinforcements and the HA matrix. The high thermal conductivity of Al_2O_3 , which is approximately 30 times higher than HA's 0.7 W/m K, reduces the cooling rate of neighboring HA splats. This results in an increase in the crystallinity of HAC coating. Moreover, sharp peaks in HAC coating suggest that CNT also plays a role in increasing the crystallinity. The thermal

conductivity of CNTs (2890 W/m K) is much higher than Al₂O₃ (36.16 W/m K) by approximately 100 times and 4000 times higher than HA (Tercero et al. 2009). Previous research groups have reported a much lower degree of crystallinity for plasma sprayed-HA coatings. According to Ganvir et al. (2021), the plasma-HA coating exhibited a crystallinity of 66%. Meanwhile, Tercero et al. (2009) observed lower crystallinity levels of 47.6%, 51.4%, and 53.9% for plasma-sprayed HA, HA/alumina, and HA/alumina/CNT coatings, respectively. This reduced level of crystallinity was attributed to the high temperatures used during the plasma spray process. Moreover, they also reported an increase in crystal size with the addition of second-phase particles, similar to our findings. A recent study by Hussain et al. (2023) also reported crystallinity in the 46.15-65.22% range for plasma sprayed-HA coatings. It can be inferred from the XRD graphs that the HA crystalline characteristics of the coating were retained due to the severe plastic deformation of particles owing to high-velocity impact and the low temperature of in-flight particles. This suggests that HVOF spray could be a better option than plasma spray, which exhibited a high degree of crystallinity and directly affected mechanical, wear, and osseointegration properties.

6.4 Raman spectroscopy to determine the retention of the CNT in the matrix

The exposure of the feedstocks to a temperature of ~ 2500° C during HVOF-spraying makes it essential to check the retention of HA phases and the survival of alumina and CNT structure in the final coating. The Raman spectra for individual feedstocks, composite powders, and coatings are shown in Figure 6.2 (b'). The HA powder showed high-intensity spectra with peak splitting within the 200-1200 cm⁻¹ range, indicating a greater crystallinity level. The symmetric P-O stretching involving the triply degenerate mode of bending's ν_3 frequency was found at ~1046 cm⁻¹. Other PO₄³⁻ ions modes (ν_2 and ν_4) were detected between 425 and 610 cm⁻¹. In contrast, the phosphate ion's ν_1 peak was observed at ~960 cm⁻¹.(Shankar et al. 2024b). The Raman peak at 417 cm⁻¹ was observed in the feedstocks and coatings, representing a characteristic peak for alumina. The feedstocks and coatings showed D and G peaks for CNT, which confirms that the hexagonal carbon structure was retained in all powders and coatings.(Shankar et al. 2024a) The HA coating's phosphate peaks were similar to the feedstock powder in terms of width, position (~960 cm⁻¹), and intensity, and no phase change was

observed due to the low degree of melting. TCP ($\text{Ca}_3(\text{PO}_4)_2$) was also absent as a left shoulder near the ν_1 peak. The HAC1 coating showed a slight shift in ν_1 peak position ($\sim 956 \text{ cm}^{-1}$) compared to its feedstock, but no other characteristic peak shifts for HA in both coatings were observed, further establishing that no phase change occurred during coating. The G peaks in HAC coating around 1580 cm^{-1} indicate a highly pure graphitic structure, with the D peak around 1350 cm^{-1} originating from a disorder-induced mode in the graphite. The I_D/I_G ratio was increased to 1.01 for HAC1 coating compared to its feedstock (0.90), indicating an increase in the defect density in CNT due to thermal processing. A shift in the D and G bands towards lower wave numbers has also been observed after coating, possibly due to compressive stress in the coating generated during thermal spraying. Jagadeeshanayaka et al. (2023) recently reported a compressive residual stress for HVAF-sprayed HA coating. The characteristic Raman peak for CNT, along with the tubular structure visible on the surface of the coating (Figure 6.1 (m)), ensures the presence of CNT in the HVOF-sprayed composite coating. The survival of CNTs during HVOF spraying could be justified by the short exposure time to a low temperature, which does not oxidize or damage CNT. Raman's spectrum confirmed the pure crystalline nature of HA, the absence of secondary phases & retention of reinforcements in powder & coatings. These findings are consistent with the results obtained from XRD analysis.

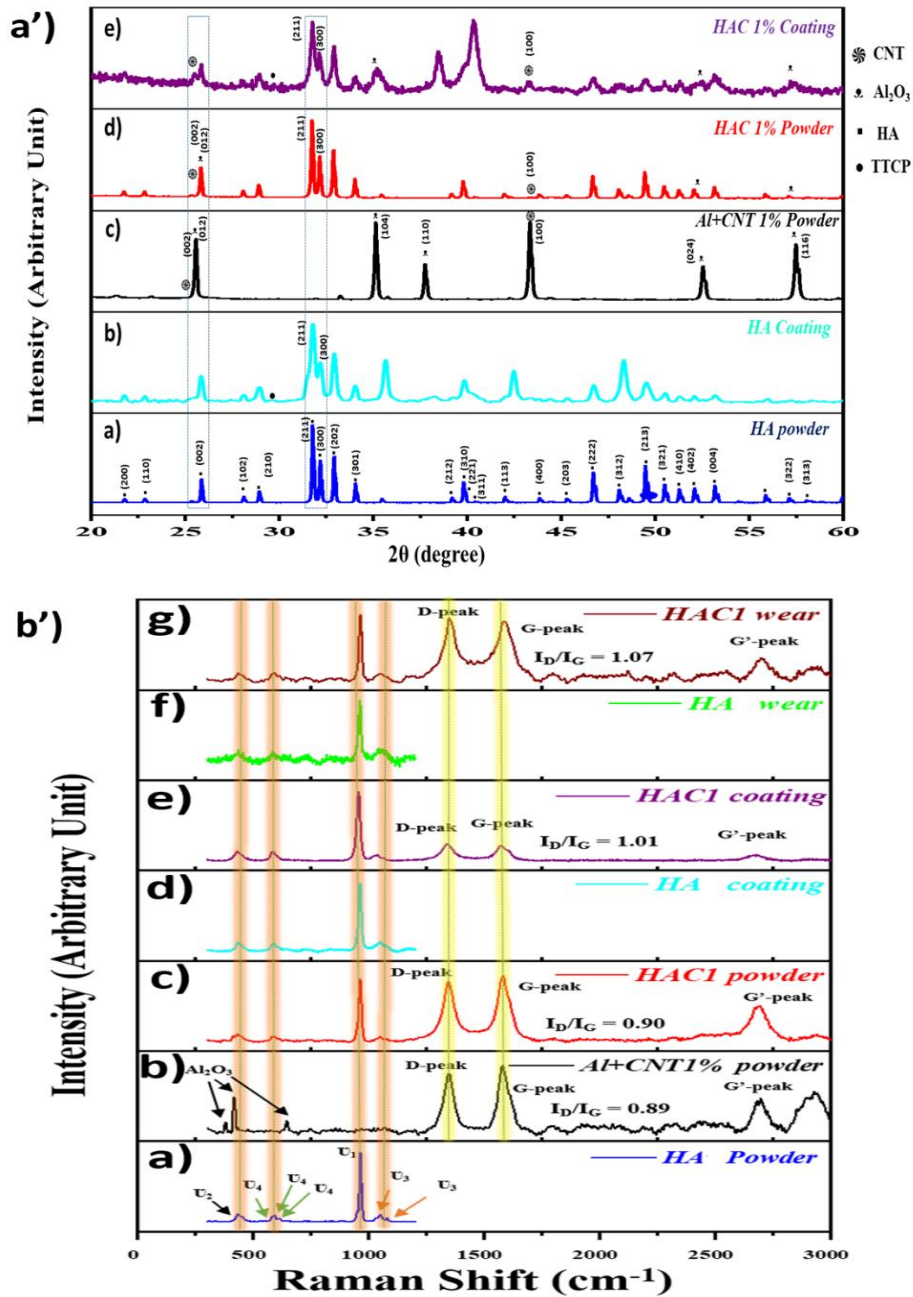


Figure 6.2 (a') X-ray diffraction spectra of the feedstocks and their corresponding coatings with the ICDD file numbers. The graph displays the retention of HA phases along with reinforcement elements (b') Raman spectra for feedstock powder and their HVOF-sprayed coating. The graph shows the retention of HA phases and D and G peaks for CNT in the coatings and the corresponding wear tracks.

6.5 Scratch adhesion strength and hardness of the coatings

The bond strength between a coating layer and an implant is crucial to prevent separation during use in the human body. A study was conducted to examine the bond

strength of HA-based coatings through a scratch test. The results revealed various failure mechanisms and critical loads of failures (L_{c1} and L_{c2}) from sudden changes in friction and acoustic emission graphs. However, determining the critical loads based solely on these graphs can be challenging. Therefore, the critical loads were determined using numerous FESEM, microscopic (Figure 6.3), and 3D profile images (Figure 6.4) of the scratch track, along with the generated graphs. The point of failure in a scratch test can be characterized as the initiation of microcracking, crazing, fish-scale formation, plowing, or the moment when the coating is penetrated, revealing the underlying substrate. In the study, it was found that HAC1 coating experienced less scratch damage than HA coating. The cohesion strength (L_{c1}) increased from 6 ± 0.7 N for HA coatings to 10 ± 0.49 N for HAC1 coatings, and the adhesion strength (L_{c2}) increased from 9.45 ± 0.77 N for HA coating to 22 ± 1.41 N for HAC1 coating. The load required for initial delamination increased significantly from L_{c1} to L_{c2} for the HAC1 coating. The HAC1 coating required almost twice the load than the HA coating to cause coating delamination. The adhesion strength of HAC1 coatings showed superior results compared to other processes, with a ~120% increment in adhesion strength (L_{c2}) than the HA coating. The increase in adhesion strength for HAC1 coating can be attributed to three significant factors. Firstly, due to the high degree of crystallinity and dense microstructure. Secondly, the hardness of alumina (~20 GPa). Harder ceramics like alumina can resist penetration by mechanically interlocking the HA splats when subjected to indenter stress during the test, thereby increasing the bond strength of the HAC1 coating. Lastly, when subjected to indenter stress, the energy adsorption by multi-walled CNT chains leads to the collapse of concentric C-layers. These findings indicate that even small amounts of CNT and alumina can significantly affect the bulk's mechanical properties. Li et al. (2014b) made a similar observation and reported increased adhesion strength for electrophoretic deposited graphene oxide/HA coating attributed to the graphene oxide. A study by Ahmed et al. (2020) reported an adhesion strength of ~10N for EPD coated-zein/HA-stainless steel substrate, nearly half the current HAC1 coating bond strength.

The observations made on the scratch track of the HA coating provide strong evidence of a deep plowing groove with multiple small cracks. This strongly suggests

that the indenter tip has penetrated the coating surface and caused micro-cutting. Additionally, the parallel cracks, also known as tensile cracks, that are perpendicular to the direction of the indenter's movement reinforce this interpretation. These observations are consistent with prior studies on thin films and thick coatings produced through thermal spraying (Jambagi and Bandyopadhyay 2017). The formation of these cracks is unequivocally due to the compressive stress ahead of the moving stylus and the tensile stress behind the stylus during scratching. When the stress exceeds the fracture toughness of the coating, cracks develop along the edges of the indenter tip to alleviate the stress, increasing the crack density and length. This ultimately leads to the formation of secondary cracks that run parallel to the scratching direction and cause the delamination of coating materials.

EDS analysis of the scratch area for the HA coating confirms the absence of HA elements in most of the area and the presence of Ti, V, and Al along the track. This indicates that the indenter has penetrated the coating. The scratch track for HAC1 coating is shallower than that of HA coating, with a lower crack density. However, fine surface cracks were observed along the scratch path, but the CNT bridging mechanism successfully arrested them. EDS analysis along the scratch area further confirms the toughening mechanism of CNT and alumina in the HA matrix.

Dot mapping clearly shows carbon's presence and uniform distribution in the scratch area along with Ca, P, and Al. This provides evidence of increased adhesion strength and hardness for the HAC1 coating. The improvement of ~120% adhesion strength for HAC1 than HA coating warrants further analysis of the role of CNTs in scratch toughening, which depends on the CNTs' dispersion in the matrix and their toughening mechanisms. The dispersion of CNTs in the HA matrix is uniform, thanks to the heterocoagulation colloidal technique, which significantly enhances bond strength for CNT coating.

A new toughening mechanism, the "bowline knot mechanism" by CNTs, is proposed here. The rebar reinforcement mechanism is also evidenced in the FESEM micrograph. These mechanisms act as a connecting bridge between the cracks. The results strongly suggest that the addition of CNT and alumina into the HA matrix has a

significant impact on the strength of the HA coating, enabling it to resist the stress concentration induced at the edge of the indenter tip. Furthermore, the addition of CNT significantly enhances the hardness and tribological properties of the CNT-reinforced HA coatings.

Figures 6.3 (k) and (l) display indents made on different coatings. The indentation sizes (D_1 and D_2) were more significant in the HA coating than in the HAC1 coatings, indicating that the HAC1 coating possesses a higher hardness value. The hardness values obtained for HA and HAC1 coating were 322.96 ± 15.96 and 469.60 ± 16.9 HV, respectively ($n=5$). The increase in hardness of HAC1 coating by $\sim 45\%$ compared to HA coating is attributed to the superior mechanical properties of reinforcements (alumina and CNT) and its dense structure ($\sim 97.2\%$). The CNTs exhibit high tensile modulus (~ 1 TPa) and behave as rigid reinforcement with excellent elastic recovery properties. (Balani et al. 2007a). Moreover, the uniform distribution of CNT is also a crucial factor in improving the hardness of HAC1 coating, which has been achieved in our study due to the heterocoagulation effect (see Figure 6.3 (m)). The hardness values obtained for the HVOF coatings in this study are excellent and superior to those of other processes. For example, Pandey et al. (2018b) reported a hardness of ~ 403 HV and ~ 209 HV for plasma sprayed-HA/4-CNT and HA coatings, much lower than the obtained hardness for HAC1 coating. Another recent study by Mittal et al. (2013) reported a hardness of ~ 400 HV for plasma sprayed-HA/20 wt.% alumina coating. Therefore, the improvement in hardness in the present study compared to previous literature is attributed to the presence of reinforcements, a high degree of crystallinity because of the low temperature involved in HVOF spray, and the hetero coagulation effect.

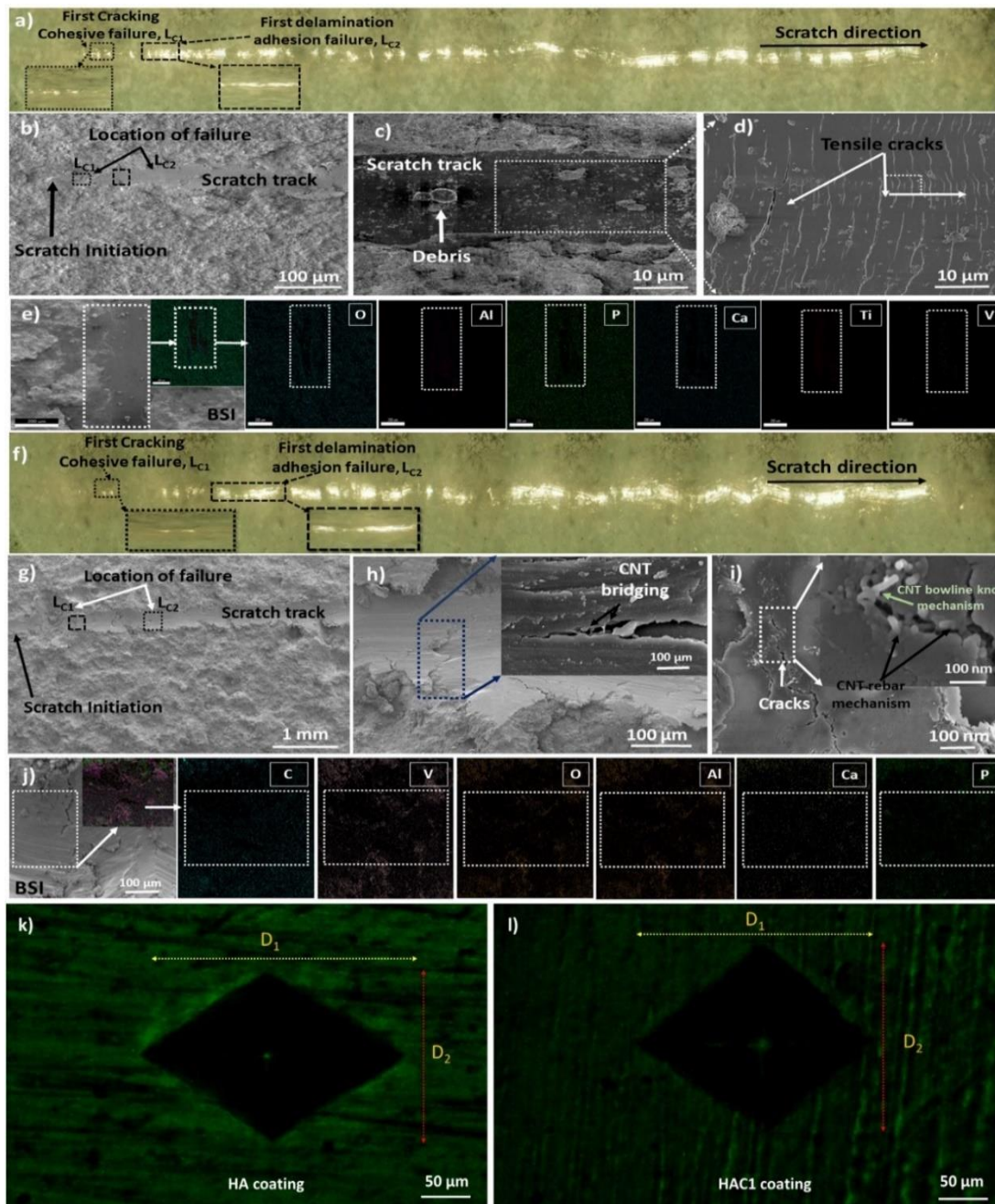


Figure 6.3 (a) Optical micrographs of scratch track for HA coating show different critical load of failures, (b-d) FESEM image of scratch track for HA coating shows critical loads and its failure mechanism, (e) EDS mapping shows the presence of Ti, Al, V along the scratch track for HA coating, indicates the penetration of indenter into the coating, (f) Optical micrographs of scratch track for HAC1 coating shows different critical load of failures, (g-i) FESEM image of scratch track for HAC1 coating shows different critical loads and bridging mechanism by CNT, (j) EDS mapping shows the presence C, Ca, P, Al, along the scratch track for HAC1 coating, indicates the toughening mechanism of CNT in the HA matrix, and Optical microscope image of the indentation for (k) HA (l) HAC1 coating shows horizontal (D_1) and vertical (D_2) diagonal lengths to determine Vickers hardness, $n=3$.

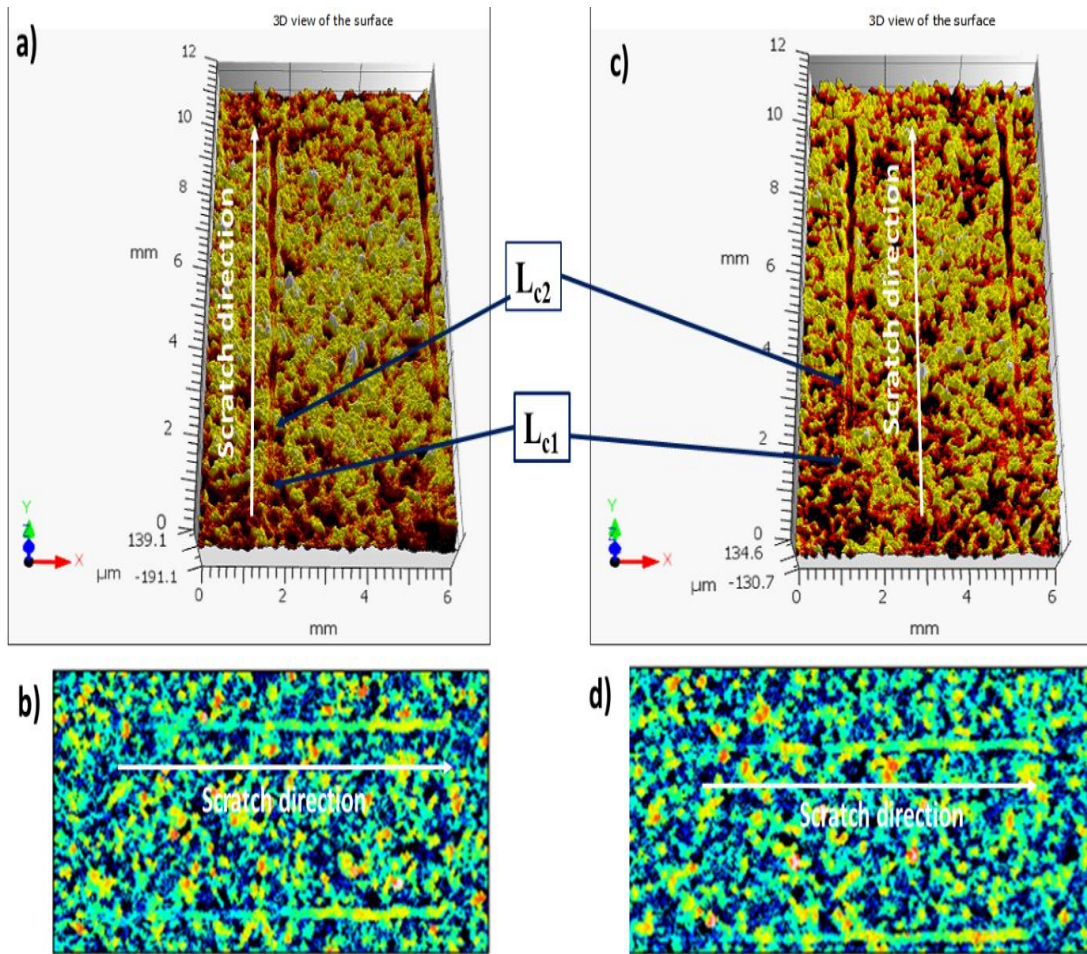


Figure 6.4 3D optical profilometer images show the HVOF-sprayed coated samples' scratch track, (a-b) HA, and (c-d) HAC1 coatings. L_{c1} denotes the critical load for cohesion failure, and L_{c2} denotes the critical load for adhesion failure.

6.6 In-vitro bioactivity study

The samples with coatings were immersed in SBF for a month to assess their bioactivity. Figure 6.6 displays the changes in the coating's surface after being immersed in SBF for different periods. After seven days of immersion in SBF, surface modification of the coating was observed due to the growth of a bone-like apatite layer (see Figure 6.6 (b) and (g)). The coating surface exhibited a noticeable apatite layer precipitation that spread across the surface after seven days, with several cracks and pores visible, acting as nucleation sites for Ca precipitation. These cracks are believed to result from diffusion and reaction between the coating surface and the SBF (Clavijo-Mejía et al. 2020). After 15 days, the HA coating showed a small needle-like structure (Figure 6.6 (c)), which transformed into a long hair-like structure covering and

spreading all over the surface after 30 days (Figure 6.6 (d)). In contrast, the HAC1 coating displayed a microstructure different from that of the HA coating. After 15 days, osteoblast cell-like structures were visible on most surfaces (Figure 6.6 (h)), which covered the entire surface after 30 days. Moreover, filopodia structures were visible on the surface, indicating good apatite growth (Figure 6.6 (i)). Additionally, the high-magnification image showed the precipitation of osteoblast cell structures on the surface of CNT and the nearby areas (Figure 6.6 (j)). Zanello et al. (2006) demonstrated that bone cells could grow, generate apatite granules as extracellular materials, and multiply on a CNT scaffold, making it an ideal candidate for bone engineering. The observations made in the current study confirm these results. Dalili et al. (2022) reported good apatite growth over the HA/CNT surface.

The growth of apatite was at its lowest during the first two weeks for both coatings due to dissolution and deposition phenomena in the initial stages, as indicated by the weight gain of the sample (Figure 6.5). At 15 days, increased apatite dissolution was observed in these two samples, caused by the replacement of PO_4^{3-} ions within the crystal structure of HA, which provides structural stability. Losing this group after 15 days results in faster dissolution. These observations were reported by (Mukherjee et al. 2014) during the initial days of immersion, and several studies have pointed out the importance of early dissolution/precipitation of HA coatings during the apposition of bony tissues onto the implants. The early adhesion of osteoblasts and direct deposition of bone matrix on the HA substrate proves that early precipitation can be beneficial, favoring bone apposition on the HA implant. However, after 30 days, apatite growth was highest for samples containing 1% CNT. Figure 6.5 shows that the HAC1 coating's high degree of crystallinity and moderated hydrophilicity ($\theta_{\text{CA}} \sim 88^\circ$) may have caused an increase in the apatite layer deposition. Previous research studies have suggested that intermediate hydrophobic surfaces with contact angles of around 70° are better for cell adherence and growth. The EDS analysis further confirms the apatite layer growth for both coatings. The decreasing intensity of Ca and P peaks indicates the formation of a Ca-deficient apatite layer on the coated surfaces after 15 days. However, after 30 days, the intensity of these elements increased more on HAC1 coating. A layer of calcium-rich apatite has formed on the coated surfaces, and the changes in the Ca/P ratio were

due to the electrostatic interaction between the ions present in the coatings (Ca^{2+} , Al^{3+} , PO_4^{3-} , COOH^-) and the ions present in the simulated body fluid. Functionalized carbon nanotubes with carboxyl groups promote the growth of hydroxyapatite. The negatively charged carboxyl groups (COOH^-) on the CNTs can adsorb calcium ions from the SBF and form a new layer of calcium-rich apatite. Alumina/CNT improved the bioactivity of the composites added to HA, according to the results presented in Figure 6.5 and 6.6. The current study confirms the non-toxicity of CNT, and Table 6.1 presents the microstructural, mechanical, and bioactivity properties of as-deposited coatings, which display better mechanical and bio properties for HAC1 coating.

The SBF immersion study is generally considered trustworthy but may have some limitations. One of its limitations is that the composition of SBF may not precisely match the clinical environment. To improve the accuracy of this study, it is recommended that more extensive research be conducted involving rodents or dogs. Despite these limitations, according to a study by Zadpoor (2014), SBF immersion studies had a 75% success rate in predicting materials' relative in vivo bioactivity. Therefore, this research can be used as a basis for predicting the non-toxicity of CNT.

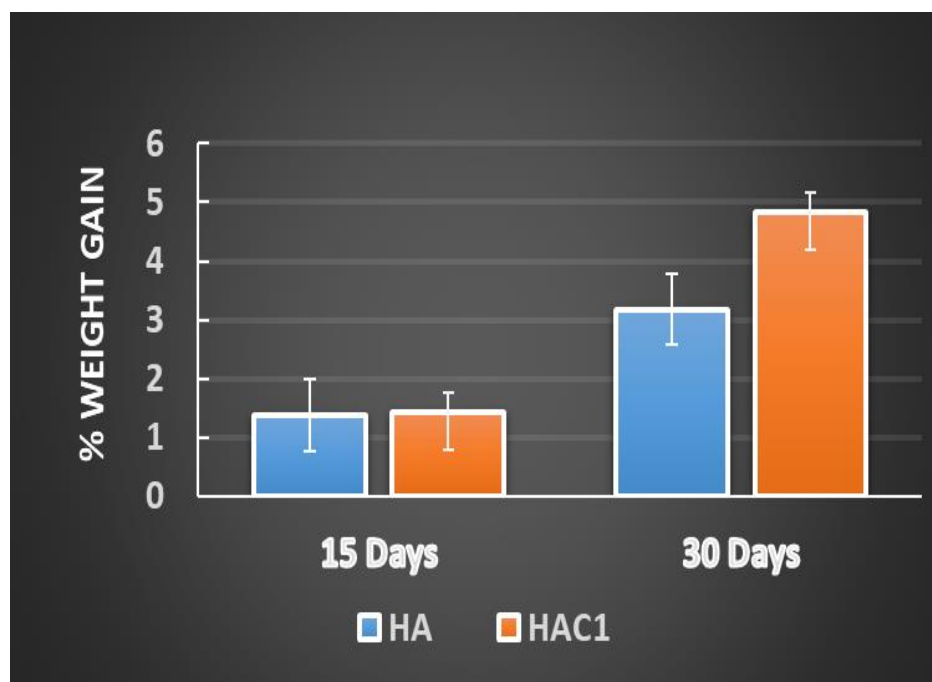


Figure 6.5 Percentage weight gain by HA coatings as a function of the time immersed in SBF ($n = 2$). The error bar represents the standard deviation.

Table 6.1 Microstructural, mechanical, and bioactivity properties of as-deposited coatings.

Samples	Roughness (μm)	Density %	Contact angle (θ)	Crystallinity (%)	Adhesion strength (L_c2) (N)	Vickers hardness (HV)	SBF weight gain (%)
Titanium	0.13 \pm 0.03	-	92.6 \pm 2.1	-	-	-	-
HA	4.11 \pm 0.67	95-96	83.6 \pm 1.8	88.62	10.15 \pm 0.49	322.9 \pm 15.6	3.18 \pm 0.60
HAC1	7.28 \pm 1.42	96.5-97.2	88.7 \pm 1.3	91.23	22.00 \pm 1.41	469.6 \pm 16.9	4.84 \pm 0.65

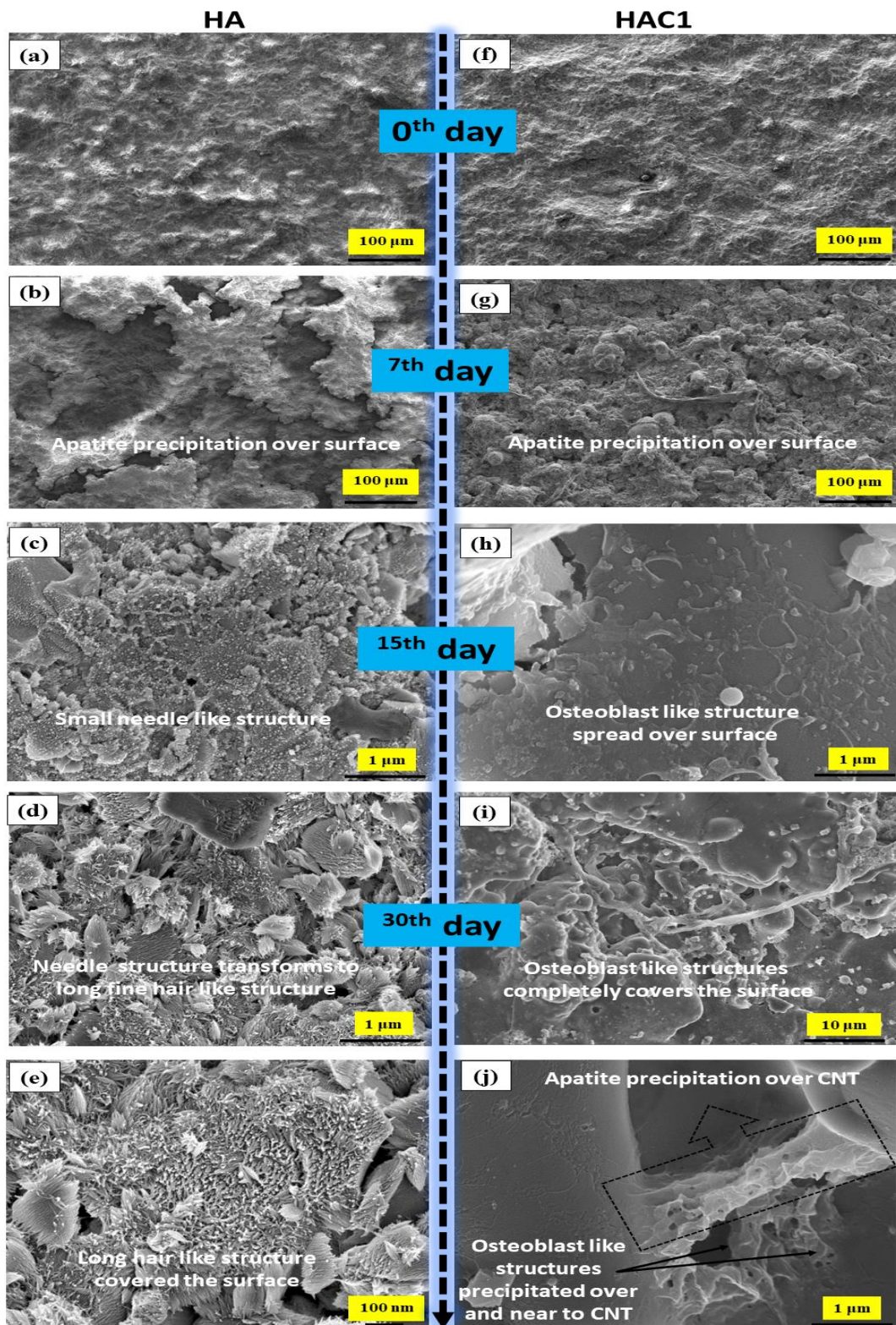


Figure 6.6 Apatite formation at the 0th, 7th, 15th, and 30th day for pure HA (a-e), HAC1 coating (f-j). The FESEM images show the apatite layer precipitation on the HA and HAC1 coatings, which testifies to the non-toxicity of CNT.

6.7 Blood-compatibility assessments

According to previous research, CNT can potentially be utilized as reinforcements in biomaterials for various biomedical applications. However, concerns have been raised about their hemolytic effects on red blood cells (RBCs), which may result in various health problems. Therefore, it is important to assess the hemocompatibility of CNT-based biomaterials before they can be employed clinically. According to the ASTM standard (Sarath Chandra et al. 2012), if the % hemolysis is $< 5\%$, the material can be considered highly hemocompatible and safe for human use, as demonstrated by the HAC1 coating, which exhibited a hemolysis ratio of 0.24 ± 0.03 , $n=3$. HAC1's non-hemolytic behavior is due to its high degree of crystallinity (91.23%). Additionally, previous research has shown that HA coating is also hemocompatible. Furthermore, the negative control indicated no RBC cell ruptures (0% hemolysis), and these findings were also validated by colorimetric images, which revealed a white color saline solution for both HAC1 coating and negative control (Figure 6.7 (a)).

The success of medical applications depends on the adhesion and activation of platelets, which can be affected by the structural changes in biomaterials. Therefore, it is essential to understand the mechanisms involved in platelet adhesion and activation and their responses to different biomaterials to create safer and more effective medical devices and implants. The HAC1 coating exhibited a considerably lower percentage of platelets adhered ($\sim 4.72\%$) than the negative control polypropylene ($\sim 13.5\%$), indicating its non-thrombogenicity. FESEM imaging revealed that platelets attached to HAC1 coating had a round morphology similar to the negative control (Figure 6.7 (b) and (c)). The HAC1 coating's low degree of platelet adhesion and activation on the surface is due to its hydrophilicity ($\sim 88^\circ$), dense microstructure ($\sim 97\%$), and negative surface charge (-11 mV). For instance, the biopolymer dextran repels platelets due to its negatively charged molecules. This study provides ample evidence to support the blood compatibility of CNT-based coatings, validating their usage as implant materials in orthopedic applications.

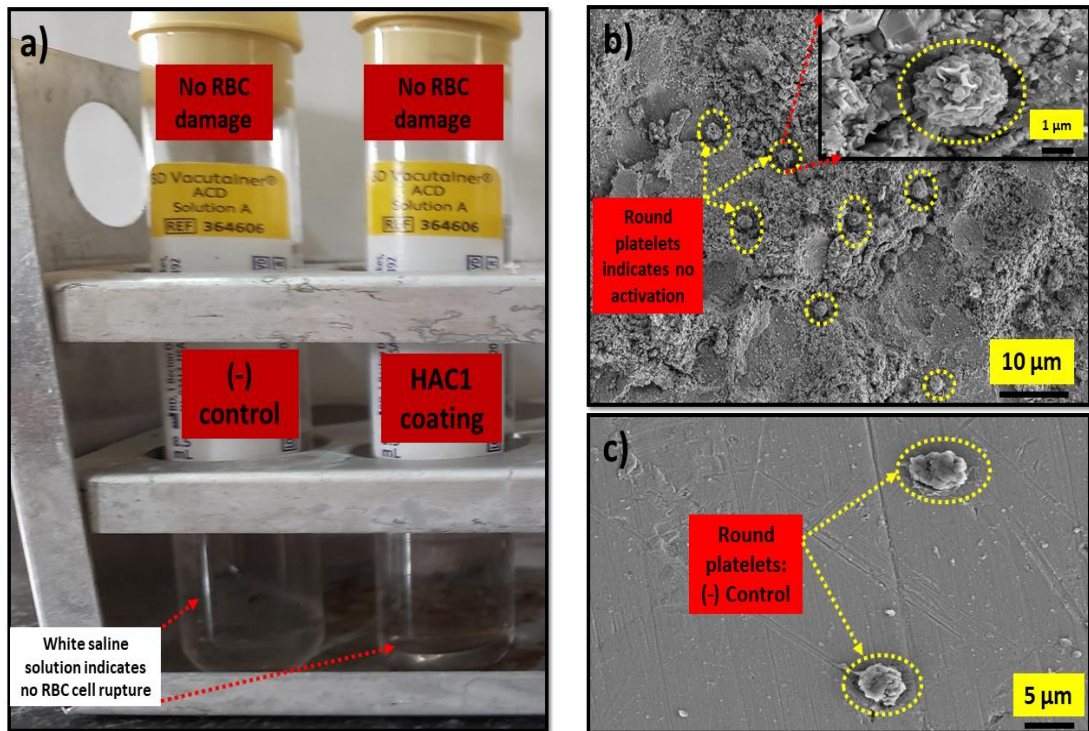


Figure 6.7 In-vitro blood compatibility assessments (a) colorimetric images show the non-hemolytic behavior of HAC1 coating similar to the negative control, FESEM morphology of the platelets adhered on to (b) HAC1 coating surface, and (c) negative surface. The dotted yellow circle indicates round platelets adhered to coatings similar to the negative control, indicating no sign of platelet activation.

6.8 Tribology studies for HA and HAC1 coatings in dry and wet environments

6.8.1 Analysis of the worn surface morphology of wear tracks

A wear test was conducted using a reciprocating fretting method to evaluate the tribological behavior of titanium-based implants. The wear tracks' morphology on the Ti substrate, HA, and HAC coatings were analyzed using FESEM images. The FESEM micrograph of the titanium alloy under a dry environment is shown in Figure 6.8 (a-c). Physical characterization of the worn surfaces indicated that the titanium alloy experienced more severe wear than the coated implants. The titanium alloy presented typical adhesive traces and abrasive furrows in a wet environment, and the worn surfaces became relatively rougher, with many ripped regions and abrasive furrows. Figures 6.8 (b) and (c) show a significant amount of debris spread over the surface, deep grooves, severe cracks, and delamination due to the brittle detachment of large

particles under dry conditions. The surface of the Ti alloy had suffered from substantial wear and tear, featuring deep scratches that imply low wear resistance in the underlying material. Moreover, the titanium substrate had undergone intense wear, resulting in a rough and extensive wear track. These characteristics suggest that the primary wear mechanism in titanium is likely two-body abrasive wear (Gang et al. 2018). The wear track's morphology under both dry and wet conditions for the Ti alloy surface showed deep scratches indicating low wear resistance of the base material. The wear behavior of the titanium alloy under dry and wet conditions was almost identical, as observed from the wear track's morphology. Chauhan and Dass (2013) reported similar morphological changes to titanium alloys in a dry environment, while Wang et al. (2022) reported comparable changes for the Ti-6Al-4V alloy under both dry and SBF environments.

The HA coating had a flat appearance in the wear areas, indicating that some of the material had been removed from the surface due to abrasive wear (Figure 6.8 (j-l)). Initially, it was believed that the delamination of the HA layer occurred due to brittle fracture. However, it is also possible that the high coefficient of friction could have caused high frictional shear stress, leading to brittle fracture of the implants. As a result, both abrasive wear and brittle fracture were the main mechanisms behind the wear of the HA coating, leading to a higher wear rate.

Interestingly, the HAC1 sample had a smaller wear track (Figure 6.9 (a) and (j)) than others, thanks to its higher surface hardness and better lubrication. This was achieved by removing the graphene layer from carbon nanotubes, which allowed the HAC1 sample to withstand the reciprocating ball better, removing fewer fine particles and fragments. To remove a single layer of graphite from a multi-walled carbon nanotube (CNT), a tensile force of ~ 11 GPa is needed along its axial direction. When a lateral force is applied during wear, it causes shear removal of mass on the surface, leading to tensile stress along the surface of the wear track (Lahiri et al. 2011). The current study's wear parameters are similar to previous research conducted by the Lahiri research group for HA-CNT composite, which calculated tensile stress of ~ 12 GPa in the wear track. This stress level is sufficient to remove the graphene layer from the CNT during wear (Lahiri et al. 2010). Further, the graphene layers from CNTs were separated and

smearred on the surface, which facilitated lubrication, separated opposing surfaces, thereby reducing wear and tear (Zalnejhad et al. 2021).

The HAC1 implant exhibited a piling-up effect on its wear track, which can be attributed to plastic deformation, with mass displacement towards the outer edge. Brittle ceramics like alumina and HA normally do not exhibit this behavior, and it is believed that the reinforcement of CNT in the alumina and HA matrix is responsible for it. On the HAC1 worn track, debris was observed, indicating a possible three-body abrasive wear mechanism resulting from the surface's micro-cutting. A significant amount of tribo-material is generated during sliding wear, but only a fraction undergoes selective delamination and is expelled from the system. Some particles become cold welded to the wear track, forming a glazed self-lubricating layer that reduces material loss by minimizing frictional coefficients. The exceptional mechanical properties of the HAC1 coating, including hardness and adhesion strength, make it highly wear-resistant. The CNT-reinforced composition helps prevent mass loss due to chipping and fracture during wear, where micro-cracks generated during the wear cycle are bridged and arrested, restricting the generation of microchips or large chunks and ultimately improving tribological properties. The uniform distribution and retention of CNT in the HA matrix through heterocoagulation are crucial in enhancing wear resistance for the HAC1 coating. Using SBF as a lubricant led to the same positive effects as expected, as the implants' wear rate, width, and depth of the track, coefficient of friction, and wear surface roughness in a wet condition demonstrated significantly superior outcomes to those in a dry environment, which will be elaborated on. The enhanced wear properties of the HAC1 coating under the SBF environment further support its potential for long-term clinical applications.

6.8.2 Topographical evolution of the worn surface

The wear resistance of the samples was assessed in dry and wet conditions using 2D and 3D profiles of the wear track, as shown in Figures 6.8 and 6.9. The width and depth of the wear track were determined from 2D profile images to measure the amount of material removed from each sample. The bar graphs in Figure 6.11 (c) and (d) indicate that Ti and HA coatings displayed larger wear track dimensions than HAC1 coatings

under dry conditions. Previous research by Qu et al. (2005) on the wear behavior of Ti-6Al-4V alloy under dry conditions reported a wear rate of $5.7 \times 10^{-4} \text{ mm}^3/\text{Nm}$. In comparison, the wear rate observed in this study for Ti-6Al-4V, HA, and HAC1 coatings was approximately 2, 4.5, and 5.5 times lower than that reported by Qu et al. (2005). Notably, the wear rate in the SBF solution was lower than that observed in the dry condition due to the intermediate medium acting as a lubricant. When the worn track results were analyzed in a wet environment, HAC-coated worn tracks were relatively narrow and minimal compared to other samples. The volume of material loss calculated from different samples is presented in Table 6.2. The results indicated that adding reinforcements to HA coatings increased the wear resistance of HAC coatings by up to approximately 32% under wet conditions and 17% under dry conditions. This was attributed to a decrease in the coefficient of friction and the strengthening of the HA coating with alumina/CNT reinforcement, which made it difficult for the counterpart to remove mass from the surface. Similar observations were made for the HA-CNT coating in previous research. The fretting wear properties of HVOF-sprayed HA-based coatings showed superior results compared to other processes. Perumal et al. (2013) studied the wear behavior of plasma-sprayed alumina and SiC coatings on Ti-6Al-4V alloy against alumina balls in Hank's solution environment. They reported the wear rates of $7.33 \times 10^{-5} \text{ mm}^3/\text{Nm}$ and $2.16 \times 10^{-4} \text{ mm}^3/\text{Nm}$, respectively. However, in our study, the HAC coating showed wear rates of $1.048 \times 10^{-4} \text{ mm}^3/\text{Nm}$ and $0.814 \times 10^{-4} \text{ mm}^3/\text{Nm}$ in dry and wet conditions. Therefore, composite coatings offer better wear resistance than alumina and SiC coatings. These results suggest that the HAC coating can decrease the volume of debris generated, thus reducing the probability of disturbance in the biological environment around the implant and prolonging the lifespan of artificial joints.

6.8.3 Sliding friction and wear behavior in dry and wet conditions

A counter ball was slid across the surface of various samples to measure the coefficient of friction (CoF). Under dry and wet conditions, Figure 6.11 (a) displays a bar graph that shows the CoF for different samples. The CoF for uncoated titanium was approximately 0.526 in dry conditions, which decreased to around 0.40 in the SBF environment. In dry conditions, Ti-6Al-4V reported a CoF of 0.6-0.7 using a ball-on-

flat set-up, as per (Fu et al. 1998). For HA coating, the CoF decreased from 0.58 ± 0.03 (dry) to 0.52 ± 0.01 (wet), while for HAC1 coating, it decreased from 0.50 ± 0.09 (dry) to 0.35 ± 0.14 (wet). Plasma-HA and CNT/HA coatings, as reported by (Lahiri et al. 2011), saw a decrease in CoF from 0.9 to 0.68, respectively. The CoF is reduced by almost 1.5 times for the HAC1 coatings, which is beneficial for enhancing the wear resistance of implants. In SBF conditions, a decrease in CoF values was observed for all samples due to the lubrication provided. However, for HA coatings, the CoF does not decrease significantly in SBF conditions, possibly because it is structurally saturated with OH ions/radicals and cannot bond with water molecules, failing to form a stable liquid film on its surface. The HAC1 coating reduced CoF by 1.16 and 1.48 times, respectively, compared to the HA coating in dry and wet conditions. The reduction in CoF seen with the HAC coating is due to the lubrication provided by the graphite layers that peel off from the CNT surface. Previous research indicates that separating graphite layers from the coating surface can lead to smoother sliding motion and less resistance, thus improving the overall durability and performance of the HAC1 coating by reducing CoF in the wear track (Lahiri et al. 2010). The decrease in CoF for HAC1 coating is further supported by Raman's analysis of the wear track, which is elaborated on in the subsequent discussion. Yang et al. (2022) also reported a 10% reduction in CoF for electrodeposited CNT/Ni versus Ni coating. Furthermore, they observed an improvement in wear resistance for the CNT/Ni coating, credited to the CNTs' exceptional mechanical strength and lubricating properties.

6.8.4 EDS analysis of the worn track

Under dry sliding conditions, the elemental analysis of titanium is presented in Figure 6.8 (h) and (i). The track exhibited the presence of carbon (C), iron (Fe), and molybdenum (Mo), which could have been transferred from the worn counterball. However, no oxide peaks were detected, indicating no oxides formed within the worn surface. This suggests that the wear particles produced were due to abrasive wear and the counter body's microplow (steel ball). The wear track for the HA and HAC1 coating revealed the presence of Fe, Ti, and C, along with a high-intensity oxygen (O) peak, suggesting the formation of an oxide tribo-layer on the coating's surface. The formation of an oxide layer on the coating's surface could be observed in the wear track of the HA

(Figure 6.8 (l) and HAC1 (Figure 6.9 (a) and (c) coatings. The oxide layer formed on the surface of the HA coating is beneficial in reducing the coefficient of friction (CoF) compared to uncoated titanium. In addition, the formation of mixed oxides of Fe, combined with the lubricating effect provided by the graphene layer and SBF solution in HAC1 coatings, further reduces the CoF, surpassing that of the HA coatings. (Lehmann et al. 2021) also observed a decrease in CoF due to the forming of a tribo-oxide layer of copper in the wear track. The reduced CoF is advantageous in enhancing the wear resistance of the coatings.

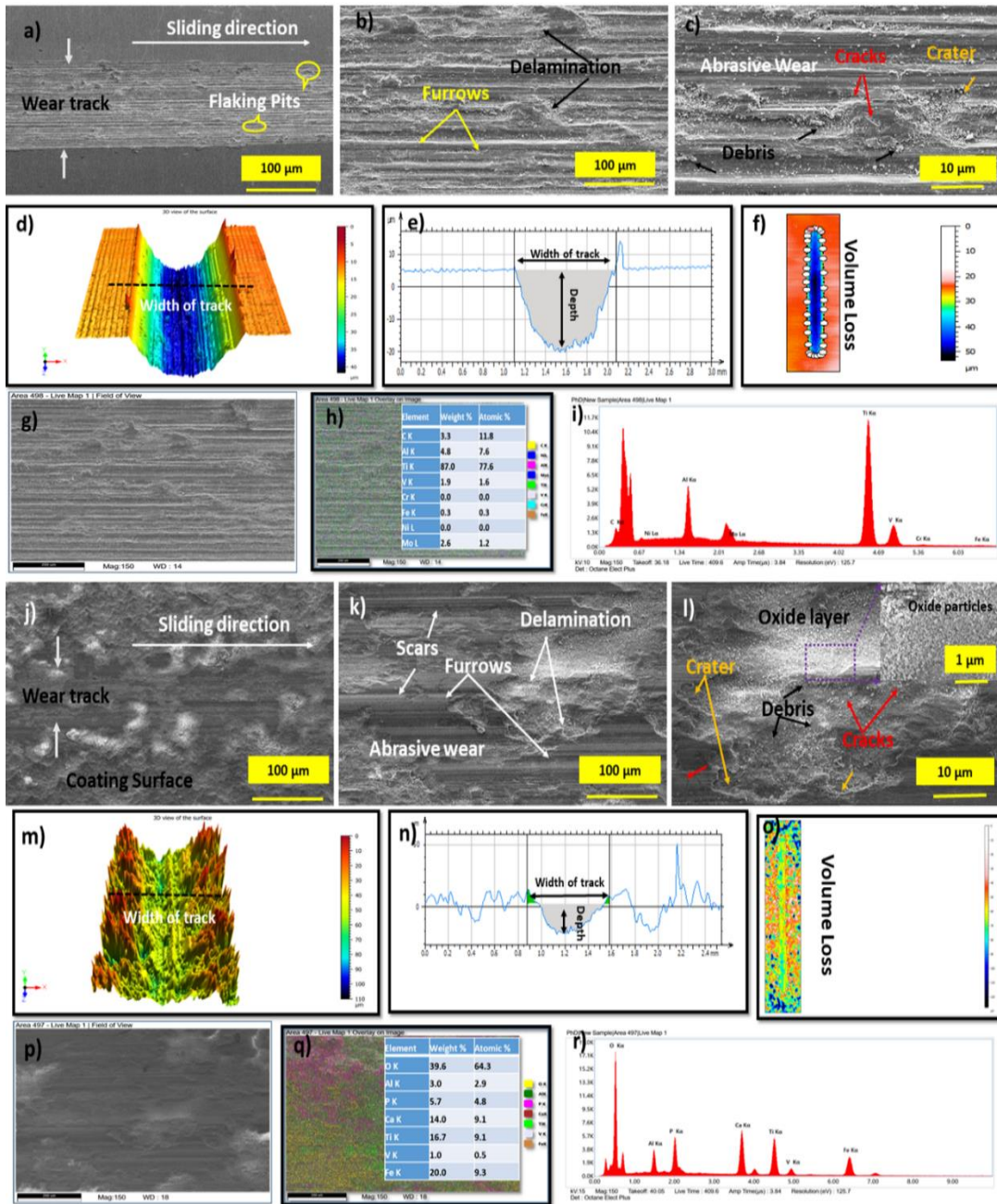


Figure 6.8 Wear profile for titanium alloy in the dry condition (a) FESEM images of wear track, (b) low magnification image shows scars on the wear track, (c) High magnification images show debris cracks and crater generated, (d-f) 3d profile images depicting the depth profile and the volume loss from the wear track, (g and h) wear debris size and its composition, (i) dot mapping with elemental analysis of wear track. Wear profile for HVOF-HA coating in dry condition (a) FESEM images of wear track, (b) low magnification image shows scars on the wear track, (c) High magnification images show debris cracks and crater generated, (d-f) 3d profile images depicting the depth profile and the volume loss of the wear track, (g and h) wear debris size and its composition, and (i) dot mapping with elemental analysis of wear track.

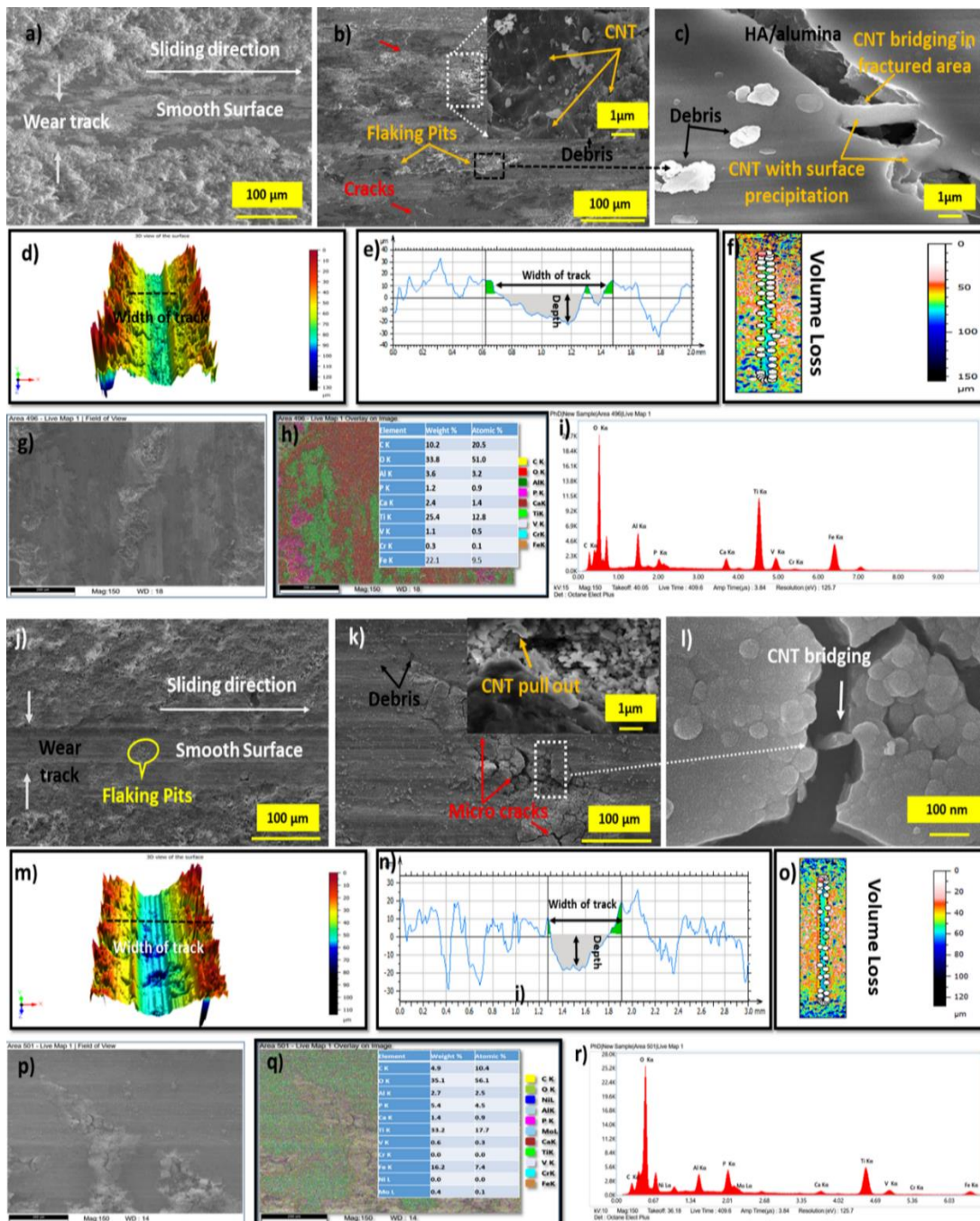


Figure 6.9 Wear profile for HVOF-HAC1 coating in dry condition (a) FESEM images of wear track, (b) low magnification image shows scars on the wear track, (c) High magnification images show debris cracks and crater generated, (d-f) 3d profile images depicting the depth profile and the volume loss of the wear track, (g and h) wear debris size and its composition, (i) dot mapping with elemental analysis of wear track. Wear profile for HVOF-HAC1 coating with SBF as lubricant (a) FESEM images of wear track, (b) low magnification image shows scars on the wear track, (c) High magnification images show debris cracks and crater generated, (d-f) 3d profile images depicting the depth profile and the volume loss of the wear track, (g and h) wear debris size and its composition, (i) dot mapping with elemental analysis of wear track.

6.8.5 Prediction of Wear Mechanisms Based on Wear Debris Size Distribution

The morphology of the wear debris generated from the samples was analyzed in both dry and SBF environments to identify the wear mechanism. However, it was challenging to collect the debris from the SBF solution. Ten wear tracks were created on each sample with the same parameters to generate sufficient collectible debris. The debris was then filtered and dried at room temperature for 24 hours. Later, it was oven-dried for an additional hour at 100°C to remove any remaining moisture content.

Figure 6.10 (a-d) displays the FESEM images of the wear debris generated from coated and uncoated titanium samples. The size distribution of the debris generated from different samples is statistically presented in a "box plot" in Figure 6.10 (e). The result indicates that the debris generated from the titanium substrate (~939 nm) and HA coating (~935 nm) have similar average-sized particles. However, it can also be observed that the lower and upper limits of debris particle size are larger for the titanium substrate (220.5 nm-2.4 µm) than for the HA coating (128 nm-1.98 µm). In contrast, the average debris size generated from the HAC1 coating in dry mode was much lower (~398 nm) than titanium and HA coatings. It had a smaller size range (25 nm-1.2 µm). Moreover, HAC1 coating observed much smaller debris under the lubrication effect (Figure 9d). The debris size for titanium and HA varies widely, suggesting that abrasion, fracture, and chipping govern the wear in these coatings (Lahiri et al. 2011). Abrasive wear generates finer particles, while fracture and chipping produce larger ones. On the other hand, most of the debris from the HAC coating is fine, indicating that the wear is predominantly abrasive. This observation agrees with the findings of (Lahiri et al. 2011) for HA/CNT coating.

The images of the wear track indicate that the HAC wear track has smaller craters and a larger abraded surface area compared to HA. The creation of the craters is due to fracture and chipping, while the rough surface is due to abrasive wear. The hardness and adhesion strength of the coating directly influences the mode of wear and debris size. Since the HA coating has many larger sizes and high-density flaws/cracks, they are more prone to fractures and chipping, resulting in more significant damage. Conversely, the HAC1 coating has better adhesion and hardness due to CNT bridging,

leading to smaller wear particles forming. The wear debris of the HAC1 samples contained HA/alumina crystals precipitated- CNTs (50-200 nm OD) of short length, which can potentially affect their cytotoxic response to blood components.

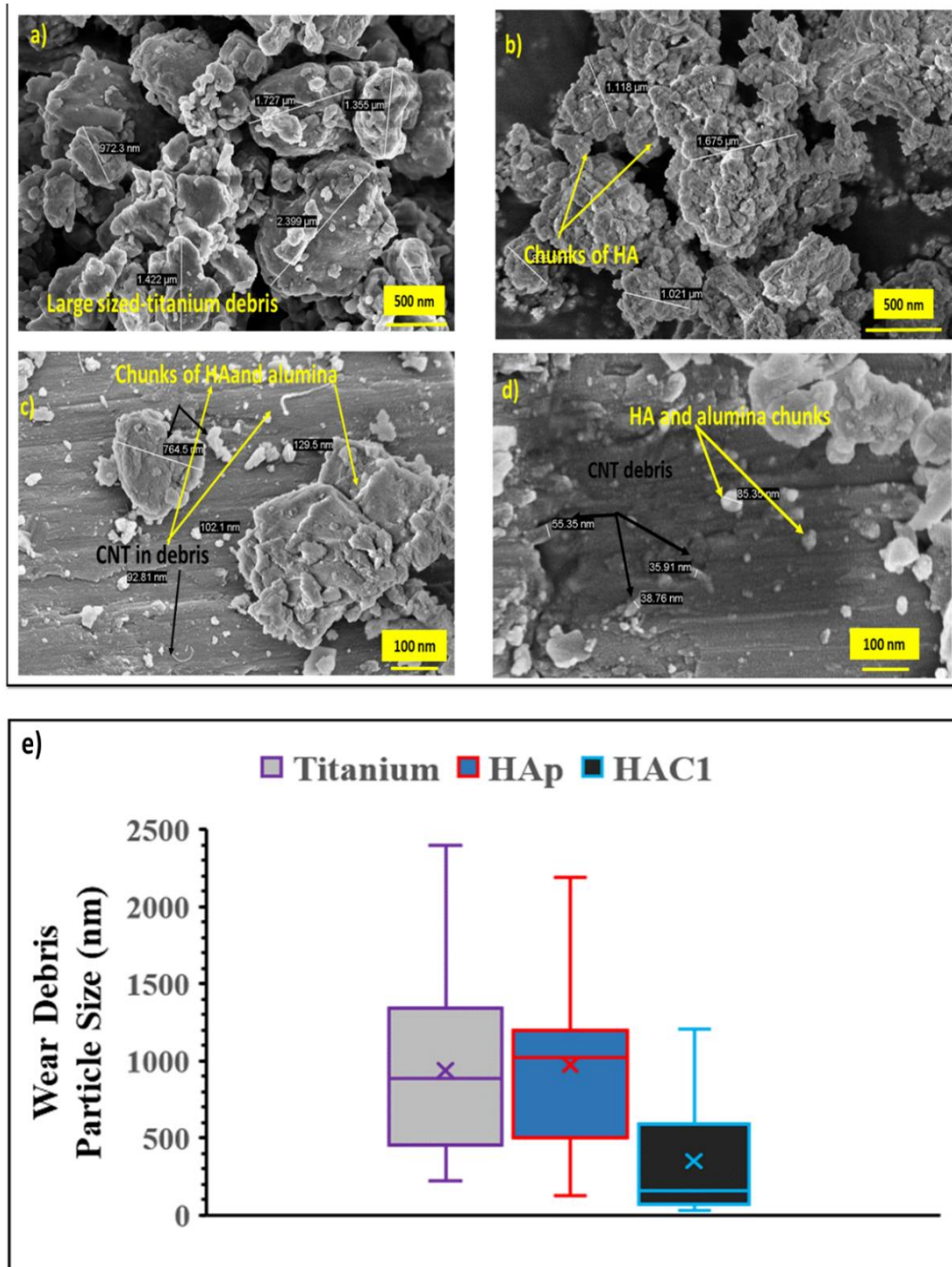


Figure 6.10 FESEM images show wear debris morphology generated from (a) Titanium substrate, (b) HA, (c and d) HAC1 coatings in dry and SBF environments, respectively, and (e) Box plot shows the wear debris size distribution for the samples.

6.8.6 Raman analysis of wear track

The Raman spectra plot of the wear track for both HA and HAC1 coatings is shown in Figure 6.2 (b'). During wear tests, there is typically an increase in the I_D/I_G ratio for carbon as new structural defects are generated. As shown in Figure 6.11 (a), the HAC1 coating displayed a decrease in CoF, suggesting a lubricant element in the wear track. This reduction in CoF can be attributed to the removal of the graphene layer from CNT in the HAC1 coating, which was subjected to shear force during wear. The observed change in the relative intensity of the D and G peaks of CNT strongly supports this assumption. For the HAC1 coating, the I_D/I_G ratio was 1.01, which increased to 1.07 in the same sample's wear track. This increase in the I_D/I_G ratio suggests that more defects are introduced into the CNT during wear, likely due to the tearing off of graphene layers, which reduces the CoF for the HAC1 coating. Hu et al. (2020) reported a similar I_D/I_G ratio increase for HA/1 rGO/1 CNT sintered pellets after wear. Moreover, the Raman plot shows that the G peak has shifted to a higher wave number, consistent with previous studies (Hu et al. 2020). This shift of the G peak to a higher wave number may be caused by an increased defect density in graphite when the coating was subjected to wear (Das et al. 2008). The bands belonging to HA did not significantly change their wave numbers before and after the wear tests in each coating. Additionally, no new peak was detected after the wear tests, indicating that the matrix material HA remained chemically stable, and there was no reaction between HA and the counter body in the wear tests.

6.8.7 Topographical analysis of the worn ball

The wear scars on the balls in contact with the coated and uncoated specimens under dry and wet conditions are shown in Figure 6.11 (e-p). The results demonstrate that the uncoated titanium surface, which slid against the ball in both environments, had a rougher surface and a larger wear track diameter than the HA and HAC1 coatings. This implies that the contact area between the ball and the coated specimens was smaller than that of the uncoated titanium. The smaller contact area of the coated specimen with the ball was due to its higher surface roughness, as illustrated in Figure 6.11 (b). Furthermore, Figure 6.11 (q) compares the wear volume of the corresponding ball. The

balls in contact with the coatings were more resistant to wear than those in contact with the uncoated titanium. The counterball against HAC1 coating decreased wear volume by around 70%, 52%, and 90.5% compared to HA's and uncoated titanium counterballs in dry and wet environments, respectively. Additionally, it can be observed from Figure 10r that HAC1's counter ball exhibited a decrease in surface roughness (S_a) of 57.9% and 75.7% compared to uncoated titanium in dry and wet conditions, respectively.

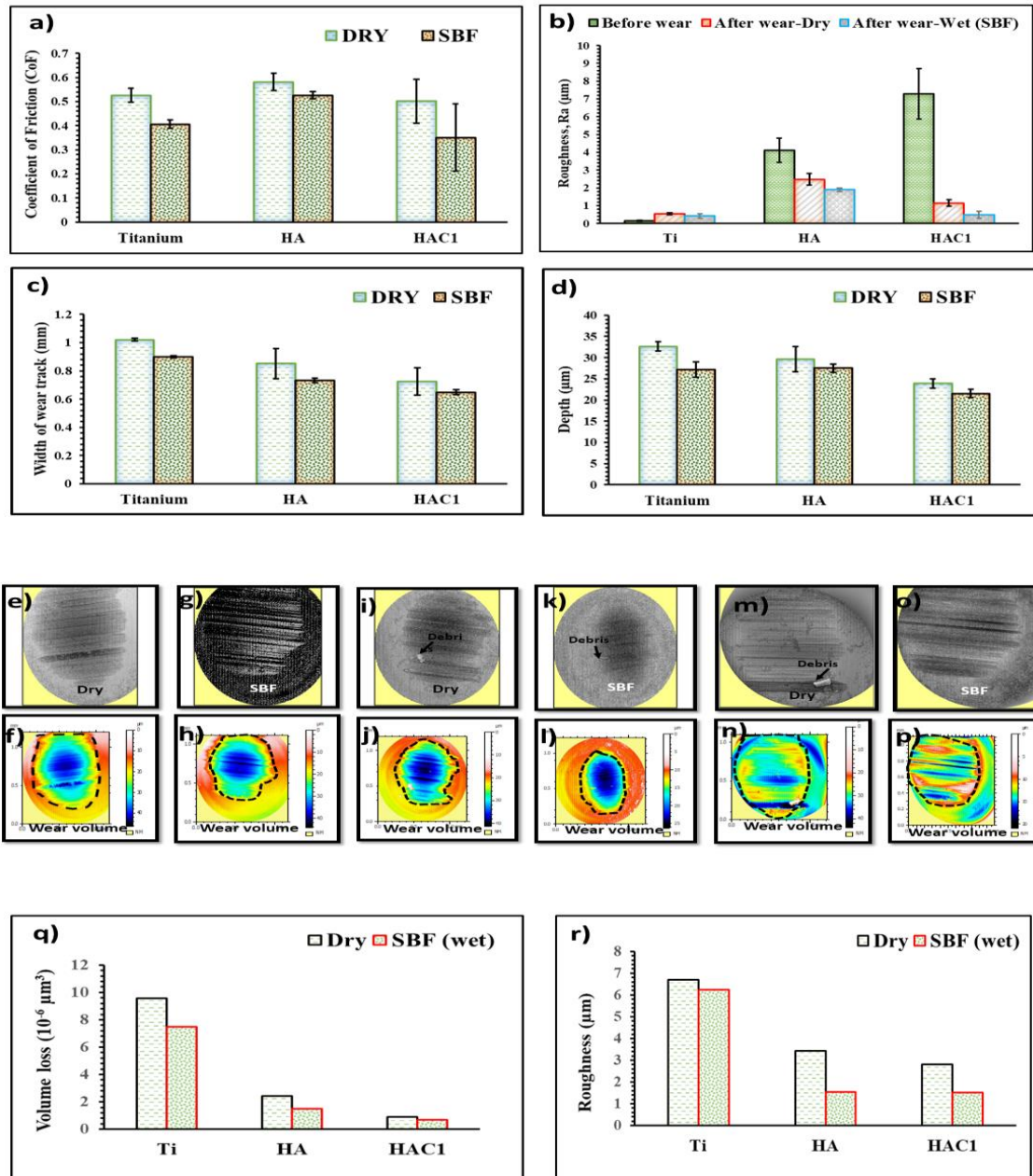


Figure 6.11 A bar graph shows (a) the Coefficient of friction generated during wear, (b) the Roughness of the samples before and after wear, (c) the width of the wear track generated after wear, (d) the Depth of the wear track, 3D profile images shows the wear of the counter-ball to determine the volume loss for (e-h) Titanium, (i-l) HA coating, (m-p) HAC1 coating.

(m-p) HAC1 coating, (q) Bar graph shows wear volume of the corresponding balls and r) Roughness of the counter-ball generated during wear. The error bar represents the standard deviation (n=3).

6.8.8 Effect of surface roughness (R_a) on wear

Figure 6.1 shows the surface microstructure of titanium, HA, and HAC coatings. The coatings of HA and HAC1 have more prominent surface waves than titanium's smoother textures. In addition, the roughness of the HA and HAC1 coatings is significantly higher than that of Ti-6Al-4V, indicating the formation of a complex surface topography during HVOF spraying. A bar graph in Figure 6.11 (b) depicts the surface roughness of the samples before and after wear in dry and wet conditions. The roughness of the coating decreases after wear in dry conditions and further decreases due to the lubricant effect provided by the SBF environment. The HA coating's average surface roughness (R_a) is marginally reduced from $\sim 4.11 \mu\text{m}$ to $\sim 2.47 \mu\text{m}$ in dry conditions and decreases to $\sim 1.88 \mu\text{m}$ in an SBF environment. The HAC coating significantly decreases roughness from $\sim 7.28 \mu\text{m}$ to $\sim 1.15 \mu\text{m}$ in dry conditions and reduces to $\sim 0.48 \mu\text{m}$ under SBF conditions. Balani et al. (2007b) reported similar findings regarding the wear roughness of plasma-sprayed HA and HA/4wt% CNT coatings in the SBF environment. Ti-6Al-4V exhibits a significant increase in surface roughness, going up from $\sim 0.13 \mu\text{m}$ to about $0.55 \mu\text{m}$ under dry conditions. In wet conditions, the surface roughness increases to $\sim 0.41 \mu\text{m}$. This increase in roughness is due to the adhesive wear of the material. Balani et al. (2007b) also noted an increase in surface roughness for Ti-6Al-4V, which they attribute to the zirconia pin causing adhesive wear.

The degree of surface roughness after wear can provide valuable insights into the underlying wear mechanism that caused it. Ti-6Al-4V is a relatively soft material compared to the counter-contact steel ball, which causes the ball to produce scratch marks as it penetrates the metallic substrate. This continuous abrasive wear increases surface roughness by approximately four times in dry conditions and three times in SBF environments. On the other hand, wear in the case of HVOF-sprayed ceramic coatings is caused by different mechanisms such as abrasion, brittle fracture, plastic deformation fragmentation, chipping, and plowing. The high surface roughness of HA and HAC

coatings provides a relatively small contact area for loading, which induces impact, resulting in surface fragments through cracking and delamination of splats. A higher surface roughness leads to surface protrusions coming into direct contact with the counter ball, causing severe splat chipping. These asperities fracture and separate from the coating and substrate in the form of debris when the sliding forces exceed the material's fracture or adhesion strength. The significant reduction in surface roughness for HAC1 coatings is attributed to the antifriction properties of CNT and the anchoring of delaminated splats via CNT anchoring and bridging mechanisms.

6.8.9 Effect of reinforcements on wear behavior

Incorporating alumina and CNT as reinforcement in HA coatings has improved their mechanical and wear resistance properties while retaining their bioactivity. Table 2 shows that the HAC coating has more excellent wear resistance than the HA coating and Ti substrate. The reduced wear rate for HAC coating is due to two factors: 1) mechanical strength from alumina and 2) CNT uniform distribution by heterocoagulation and splat bridging mechanisms. Alumina's high hardness initially reduces the coating's mass removal compared to HA coating, as seen from the wear results (HAC1 coating had the lowest wear volume, Table 6.2). Previous studies have shown that adding alumina to hydroxyapatite can improve lubrication, hardness, and strength properties (Mittal et al. 2013). Recently, Rattan et al. (2022) reported an increase of ~41% in wear resistance for HA/alumina (15 wt.%) - plasma coating compared to HA coating due to the reinforcement effect and density. CNT structures act as connectors, braces, reinforcement bars, and knots amidst the splats, enhancing the hardness, bonding strength, and, ultimately, the durability of the implants. Figure 6.9 (c) and (l) show how CNTs anchor the splats, locking them in place and reducing the release of wear debris by restraining the HA/alumina matrix through stretched CNTs. This implies that wear debris is secured by CNT anchors, which limits the damage to the coating via chipping. The presence of CNTs in the HAC coatings improves the hardness by up to 45%, confirming their ability to restrain and fasten the HA/alumina matrix by forming hooks and bridges. Previous studies have also shown that CNTs can provide lubricating conditions during severe abrasion between the counter ball and coatings, reducing the wear of ceramic coatings (Lahiri et al. 2010).

CNT reinforcements can provide substantial lubrication in specific areas that maintain cohesion with the matrix and safeguard the abraded surface. Another interesting observation is that CNTs distributed over the worn surface form a CNT pull-out structure (Figure 6.9 (k), shown with orange arrow) under the effect of repeated grinding of the counterpart. Embedded CNTs have strong cohesion with the matrix elements, while surface dangling CNTs act as energy-absorbing sources during abrasion. The increased thicknesses of CNT from 10-30 nm (original) to ~ 50-150 nm suggest that the CNTs were coated with HA during the thermal spraying. This surface protection with HA/alumina melt coating over CNTs results in a composite morphology ideal for sustained enhanced abrasion resistance. A study by Qi and Wu (2013) found that low wear resistance of implants is the primary cause of releasing toxic metal ions into the bodily environment. Therefore, it is critical to enhance implant wear resistance. The current study suggests that the HAC composite coating sprayed with the HVOF process can improve mechanical properties and biocompatibility and could be a potential synthetic replacement implant material under high load-bearing conditions.

Table 6.2 Characterization from a ball-on-disc test of Titanium and HA-based HVOF-sprayed samples under dry and wet (SBF) environments.

Samples	Volume loss (mm³)	Wear Rate (mm³. N⁻¹. m⁻¹)	Wear Resistance
Titanium	0.1483±0.003	2.965*10 ⁻⁴ ±0.071	Base
Titanium-SBF	0.127182±0.005	2.543*10 ⁻⁴ ±0.112	14.23% ↑
HA	0.063709±0.004	1.274*10 ⁻⁴ ±0.080	57.03% ↑
HA-SBF	0.06007±0.001	1.201*10 ⁻⁴ ±0.022	59.49% ↑
HAC1	0.052448±0.002	1.048*10 ⁻⁴ ±0.050	64.65% ↑
HAC1-SBF	0.040704±0.002	0.814*10 ⁻⁴ ±0.050	72.54% ↑

6.9 In-vivo assessment of implants in New Zealand white rabbits

Coated titanium rods were implanted inside the distal femoral bone of rabbits for one

month to determine their clinical implications using histopathological assessments. Titanium rods had two types of coatings: (i) HA coating and (ii) HAC1 coating. The coating thickness was 50-62 μm . A HDPE (clinically used material) was used as a group control. Different sets of implants were used with rabbits, as seen in Table 6.3. The animals showcased impeccable postoperative healing without any significant negative repercussions. Throughout the study, they displayed typical mobility with no signs of inflammation, infection, or allergic reactions at the surgical site. The interventional procedures had no discernible impact on the animals' overall health, behavior, or feeding habits, as seen by their weight gain. The weight gain by HA and HAC1 implanted animals measured at the end of 29 days were $11.23\pm 0.47\%$ and $12.45\pm 0.35\%$, respectively, indicating good healthy behavior during the test period. The test implants were firmly affixed, well positioned, and could not be manipulated manually, indicating exceptional osteointegration. Moreover, none of the implants were ejected.

Femoral bones were fully restored, and sound healing was achieved for all bone groups after 29 days of implantation. We observed good osseointegration, with no osteolysis or periosteal reactions around the implants in the rabbits. Periosteal tissue was restored without any inflammatory responses at the perforation location of the femoral bone. Femoral and marrow bones appeared normal around each implant, without any abnormal tissues. This includes CNT-based implants, which are of greater interest for this study. Figure 6.12 shows the histological observations of different implants embedded in rabbits. For HAC1 rods, bone tissues exhibited newly grown bone, hematopoietic marrow, and trabecular bones, which were synthesized with osteocytes into their lacuna. Similar results were observed for HA implants embedded in rats by Facca et al. (2011). After one month of surgery, the medullar cavity in both implants was fully restored. The femoral defect for all groups was also restored due to the formation of the neocortical bone.

Observations from clinical and histopathological studies have shown promising outcomes for implants based on CNTs. CNT-based implants showed an $\sim 11.4\%$ improvement in the histological values (such as Polymorphonuclear cells, lymphocytes, macrophages, plasma cells, fibrosis, necrosis, fatty infiltration, neovascularization, and

giant cells) from the microscopic images of the implant sites. These positive results are mainly due to CNTs and alumina, which accelerate bone growth, promote biomineralization, and inhibit osteoclastic bone resorption. CNTs stimulate osteoblast proliferation and adhesion, leading to faster bone repair. As a result, CNTs act as an effective nucleation surface to induce the formation of a biomimetic apatite coating, leading to better adhesion and anchorage. The higher surface area of CNTs promotes bonding with newly grown bone. In orthopedic surgery, the osseointegration of joint replacements remains a challenge in quality and duration. However, the addition, retention, and homogenous distribution of CNTs in the HA matrix could improve the recovery of joint replacements. In this study, heterocoagulation achieved uniform CNT distribution, and low temperature resulted in the retention of CNT and HA phases. Carbon nanotubes (CNTs) have been controversial due to their potential toxicity to tissues and cells. In particular, when used in orthopedic implants, nanotoxicological effects on human macrophage cells (Cheng et al. 2009) and phagocytes (Sakaguchi et al. 2008) could lead to increased inflammation and decreased wound healing. Studies have shown that unpurified multi-walled CNTs can cause a decrease in activity in human macrophage cells due to necrosis, which results from the uptake of CNTs. These CNTs may cause incomplete phagocytosis in vivo, leading to oxidative stress and cell death in vitro. However, the current study found that both implants showed a sign of fibrosis and a slight effect on lymphocytes. Still, there was no phenomenon of phagocytosis or necrosis, nor strong inflammation reactions near the implant/coating/bone interface in HAC1 and HA coatings. The lack of inflammatory response of nanotubes is due to enzymatic biodegradation, which does not trigger any inflammation. The lack of inflammatory response due to enzymatic biodegradation was assumed because of the absence of nanotubes and/or their by-products in the nearby cells/tissues of the implant area, as observed from histopathological images and the FESEM images (not shown here). Nanotubes seem to be actively ingested through phagocytosis in macrophages without a cytotoxic effect. However, further in-depth analysis is needed to confirm this phenomenon. The enhanced bio-properties of HAC1 coating may be attributed to the functionalization of CNT (Singh et al. 2016). The functionalization of CNTs improves their solubility (dispersion) and alters their cellular interaction pathways, resulting in much reduced cytotoxic effects and thereby

improving biocompatibility. Moreover, previous studies have shown that CNTs have decreased toxicity with higher functionalization on their sidewalls (Khan et al. 2021; Vardharajula et al. 2012), similar to the functionalization carried out in the present work.

Further, it is suggested that longer implantation (1 year) is needed to appreciate the quality of osseointegration further and to evaluate the safety of the coating before clinical application. This study can improve the healing time and osseointegration of biomedical materials for joint replacements with a fabricated composite coating.

Table 6.3 List of different types of implants embedded in the femoral bone of the rabbits.

Type of implants	Left Femur (Test item)	Right Femur (Control)	Total No. of Implants
HA	3	3	6
HA	3	3	6
HA	4	4	8
HAC1	3	3	6
HAC1	3	3	6
HAC1	4	4	8

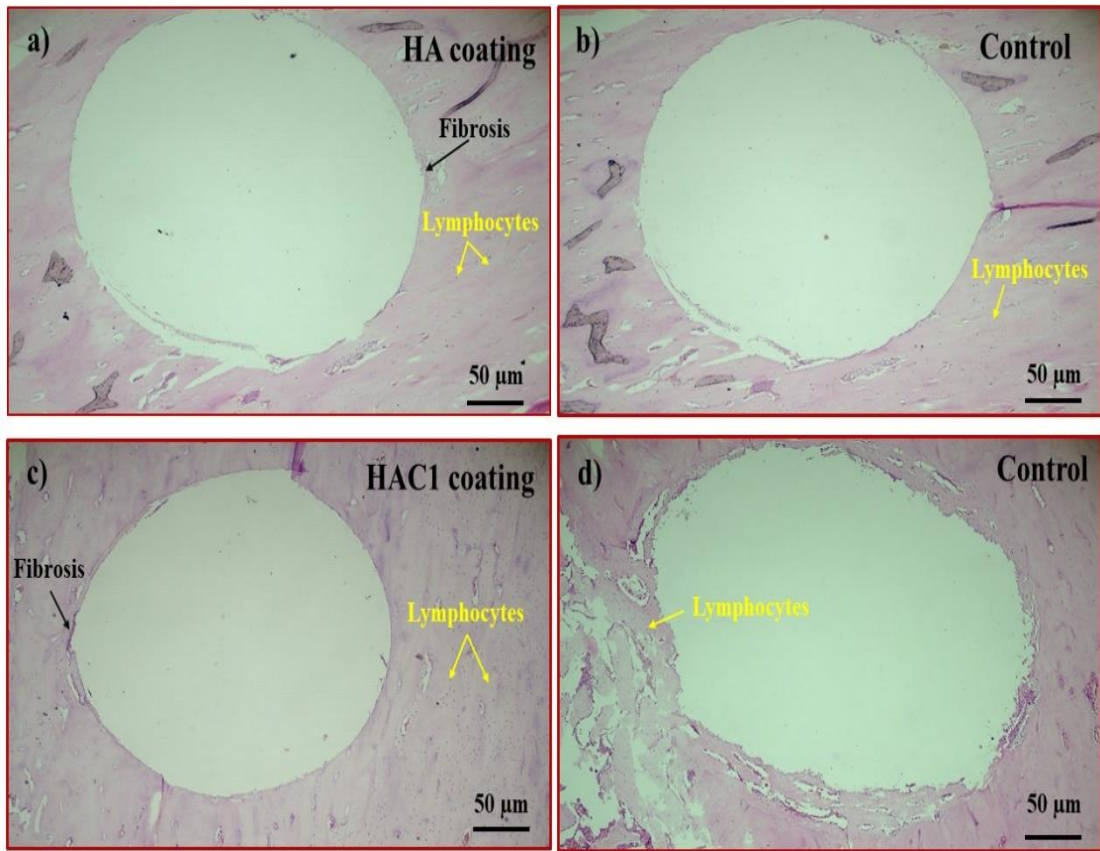


Figure 6.12 Histopathology images (a) HA coating, (b) HDPE (control), (c) HAC1 coating, and (d) HDPE (control) implanted in the femur bone of rabbits (n=10). The figure shows different inflammatory responses to the coatings.

6.10 Summary

In this chapter, the tribological performance of the coatings with and without reinforcement of CNT was compared in terms of relative volume loss and wear coefficient. The tribology test was conducted with a ball on a flat setup. A steel ball of 6 mm diameter was used as a counter body. The CNT-reinforced coatings had only one CNT concentration, 1 wt%, and performed better than others when used with human blood. The reinforced coatings showed much better tribological performance than the HA coatings. The underlying wear mechanism for each coating was identified from the test data and images of the worn surfaces. The 1 wt% CNT coating also displayed improved adhesion strength and biocompatibility, thus suggesting its use for the long term in orthopedic implants. The data based on the wear resistance of the implants presented in this chapter has been published by one reputed journal (Shankar and Jambagi 2024). Further, in-vivo osseointegration and cytotoxicity of the implants were

discussed. The next chapter presents the conclusions drawn from this investigation, the scope of future work, challenges, and limitations in the relevant direction.

CHAPTER 7 CONCLUSION

7.1 Preamble

This brief chapter deals with the concluding remarks, followed by the limitations, challenges, and scope of future work.

7.2 Conclusion

The study is divided into three stages: 1) Powder stage - The different concentrations of CNT (0.5-2 wt%) and alumina (19.5-18 wt%) were successfully produced by heterocoagulation, followed by ball milling with HA (80 wt%) and assessed for their biocompatibility to find out the most biocompatible composite powder suitable for orthopedic implant coating. 2) Coating stage - The HA coatings were fabricated by three different thermal spray techniques of different temperature ranges from high-moderate-low, namely APS, FS, and HVOF, and assessed for their compatibility with human blood, based on their surface chemistry to find out the most suitable thermal spray technique for producing biocompatible coating. 3) The powder with the best biocompatible properties from stage 1 (HAC1) was then sprayed with the best thermal spray coating technique (HVOF) determined from stage 2 to produce a coating on the titanium implant. The best-achieved coating (HVOF-HA/HAC1) was then assessed for its durability and longevity by wear test and finally studied its biocompatibility by implanting the coated rods in New Zealand white rabbits. Based on the above studies, the following observations were made:

The dispersion index of the powder containing 2% CNTs was 1.20, which resulted from the heterocoagulation colloidal technique. Therefore, the matrix exhibited a uniform carbon nanotubes (CNTs) dispersion.

XRD data of powders showed an increment in the crystallinity % up to 1 wt% and decreased for 2 wt% CNT. The same trend was observed for crystalline size. The sudden decrease of crystalline size at high concentrations can be attributed to the replacement of the Ca^{2+} ions by Al^{3+} or carbon cations.

All the powder samples showed a negative surface charge at a pH of 7.4, which is

favorable for blood interactions. Also, the surface charge of the CNT samples increases with the CNTs' concentration due to their functionalization. The zeta potential for HA, HAC.5, HAC1, and HAC2 was found to be ~ -2.1 mV, -10 mV, -11 mV, and -21 mV, respectively.

Regarding the hemolytic assay, HA, HAC0.5, and HAC1 powders showed no hemolytic activity up to 80 mg, with a hemolysis percentage of $<10\%$. However, HAC2 powder showed little hemolytic behavior at the same concentration with a hemolysis percentage greater than 10%.

The coagulation assays and the WB clotting time showed that HAC1 and HAC2 powder samples up to a concentration of 80 mg did not interfere with the intrinsic or extrinsic coagulation pathways and hence can be considered non-thrombogenic. The absorbance values for HAC1 and HAC2 powders were 0.927 ± 0.038 and 1.184 ± 0.128 , respectively, which were higher than HA and negative control, indicating its non-thrombogenicity.

The percentage of platelet adhesion on the HAC1 powder ($\sim 5.67\%$) showed a ~ 2.5 -fold decrement to the clinically used negative control ($\sim 13.73\%$). Moreover, microscopic images showed that none of the samples showed any platelet activation, except for HAC2 at 80 mg, which showed some pseudopodial extensions, indicating platelet activation.

These findings suggest that the 1 wt% CNT powder outperformed the others. Before conducting clinical trials and animal testing, selecting the appropriate biomaterial coating is a critical step. This approach reduces and eliminates using more lab animals, significantly saving time and money. Coatings of such powders could be employed in hip, knee, dental implants, and other medical components.

HA coatings were produced by three thermal spray technologies: APS, FS, and HVOF. An in-vitro assessment with human blood and SBF has been performed and analyzed based on surface chemistry, such as microstructure, surface roughness, phases, surface charge, crystallinity, and wettability.

HVOF coating displayed a $\sim 10\%$ and $\sim 32\%$ improvement in crystallinity

percentage compared to FS and APS coating. Raman spectra showed a broad and wide band near 962 cm^{-1} and a left shoulder at 950 cm^{-1} for APS and FS coatings due to amorphous phases, indicating their reduced crystallinity, unlike a narrower peak for HVOF coating similar to feedstock, indicating its higher crystallinity. The increased crystallinity for HVOF coating is due to the low temperature and high velocity involved in the process.

All the coatings showed negative surface charge and hydrophilic behavior ($\theta_{CA} < 90^\circ$), owing to nanoporous HA coating on the titanium substrate. These are the supportive factors for enhancing hemocompatibility. The negative surface charge for HA at physiological pH-7.4 repels the negatively charged RBCs that hinder platelet and protein adsorption and ultimately restrict clot formation. On the other hand, the hydrophilic surface creates a water barrier by forming a strong hydrogen bond and does not readily allow protein molecules to get adsorbed on the coatings.

HVOF-HA coating displayed a ~34% and ~120% improvement in adhesion strength compared to APS and FS coatings. The increased adhesive behavior for HVOF coating was attributed to its low porosity (~3%), high kinetic energy involved in the process, and low coating thickness.

HVOF-HA coating exhibited a ~31% and ~59% improvement in hardness compared to APS and FS coating, respectively, owing to the dense microstructure (~97%) and low coating thickness (~55 μm). A trend similar to scratch test results was observed for Vickers hardness (HVOF>APS>FS). The scratch adhesion and the Vickers hardness test results indicate that the HVOF coating possesses better mechanical strength and, therefore, has the potential to mitigate the issues associated with the aseptic loosening of implants when used clinically.

A capsule-like apatite structure over all the coatings was observed after 60 days of SBF immersion, and a considerable weight gain was measured over time, indicating their bioactivity. Moreover, a Ca-rich apatite on the HVOF coating ($\text{Ca/P}_{60\text{ days}} = 2.12$) at the end of 60 days was witnessed due to its high degree of crystallinity and moderated hydrophilicity ($\theta_{CA} \sim 85^\circ$).

All the samples showed non-hemolytic behavior with a hemolysis percentage of less than 5%, implying that the samples did not cause a rupture of the RBCs. Moreover, the HVOF coating demonstrated exceptional blood compatibility compared to APS and FS coating, with significantly lower hemolysis rates of ~8 and ~11 times, respectively. This decrease in hemolysis % for HVOF coating could be due to their smooth surface ($R_a \sim 4 \mu\text{m}$) and higher crystallinity. The smooth surface of HVOF coating results in less surface area, providing less space for erythrocytes (RBCs) to interact with and leading to less RBC rupture. On the other hand, the release and dissolution of secondary HA phases into the blood might have resulted in increased hemolysis for APS and FS coatings.

The coagulation cascade and the WB clotting time assays showed a delayed clotting time for HVOF coating compared to others. HVOF coating showed an absorbance value similar to unclotted blood during the first 15 minutes and a much higher absorbance value during each time point compared to other samples, suggesting its non-thrombogenicity. The non-thrombogenicity of HVOF coating is due to the synergy effect of coating properties like low porosity, smoothness, negative surface charge, and hydrophilicity.

The platelet adhesion percentage for the HVOF coating exhibited ~1.25-fold decrement compared to the APS and FS coatings. HVOF coating and titanium exhibited round platelet morphology, similar to the control. However, the APS and FS coatings displayed dendritic and spread dendritic platelet structures, indicating minimal activation. The change in platelet morphology and increase in platelet adhesion for APS and FS coating may be attributed to the combined effect of high porosity, rough surface, and electrostatic interaction between the protein molecule ($\text{COOH}/\text{NH}_3^+$) and HA ions ($\text{Ca}^{2+}/\text{PO}_4^{-3}/\text{OH}^-$).

Bare Titanium and coated samples showed poor antimicrobial properties due to their high affinity for organic substances, which promotes bacterial adhesion and replication. The antimicrobial properties can be improved with reinforcement like CNT, Ag, Cu, and tungsten, as well as smart coating, which can further augment the antimicrobial properties of HA.

The hemocompatibility evaluation (hemolysis test, platelet adhesion, platelet activation, blood clotting time measurement, and coagulation assays) revealed that the low-temperature HVOF-coated HA sample was highly hemocompatible biomaterials as it did not harm blood components (RBCs and platelets). Therefore, HVOF coatings can be the best alternative to other commonly used thermal sprayed coatings to increase biomedical devices' bioactivity, blood compatibility, and lifespan.

HA and HA+19wt.%Al₂O₃+1wt.%CNT coatings' deposition on Ti-6Al-4V substrates was achieved using low-temperature-operated HVOF spraying. The impact of the low temperature and incorporation of reinforcements into the HA coating was analyzed in relation to alterations in its physiochemical, in-vitro bioactivity, blood compatibility, and tribo-mechanical properties.

HVOF-sprayed HAC1 coating exhibited a very high crystallinity level (91.23%) compared to HA coating (88.62%) without major secondary phases. The obtained value is much higher than that of FDA-approved plasma-sprayed HA coatings reported in previous literature. The increased crystallinity for HVOF coating is due to the low temperature and high velocity involved in the process and the high thermal conductivity of reinforcements.

Raman's spectrum displayed distinct HA, D, and G peaks for CNT in HA and HAC coatings. The peaks were located in the same positions as the feedstocks and had the same width, indicating similar phases. A slight shift in the G-band was observed in the HAC1 coating, attributed to the compressive residual stress involved in the HVOF spray.

The HAC1 coating has shown a significant improvement in adhesion strength by approximately 62% and hardness by about 45% as opposed to the HA coating. This is due to the uniform distribution of CNT (carbon nanotube), a high degree of crystallinity at 91.2%, a dense microstructure at 97.2%, and excellent interfacial bonding. These factors have contributed to the exceptional tribomechanical properties of the HAC1 coating.

After 30 days of immersion in simulated body fluid (SBF), osteoblast cells and apatite

structures similar to filopodia were observed over the HAC coatings. This indicates their bioactivity, as considerable weight gain was measured over time. Additionally, a Ca-rich apatite on the coating (with a Ca/P ratio of 1.86) was witnessed due to its high degree of crystallinity and moderated hydrophilicity (with a contact angle of approximately 88 degrees). CNTs act as a bioactive booster, causing apatite to precipitate on their surface, while alumina particles remain bio-inert without affecting the biocompatibility of HA.

The study found that implants coated with HA and HAC1 powders showed significantly better wear resistance than uncoated Ti-6Al-4V. Additionally, reinforcing the HA coating led to a substantial increase in wear resistance for HAC1 coating, with improvements of around 32% and 17% under SBF and dry conditions, respectively. These improvements were attributed to a decreased friction coefficient and stronger splats thanks to CNT bridging. Notably, the HAC1 coating also showed a reduction in CoF value of 1.16 times and 1.48 times compared to HA coating in dry and wet conditions, respectively, attributed to the lubrication provided by the peeled-off graphite layers from the CNT surface.

Histopathological studies have revealed encouraging results for HAC1 implants implanted in rabbits. The CNT-based implants showed an improvement of approximately 11.4% in the histological values, including Polymorphonuclear cells, lymphocytes, macrophages, plasma cells, fibrosis, necrosis, fatty infiltration, neovascularization, and giant cells, as seen from the microscopic images of the implantation sites. These positive outcomes can be attributed to CNTs and alumina, which accelerate bone growth, promote biomineralization, and inhibit osteoclastic bone resorption.

It has been concluded that the HVOF-sprayed HAC1 coating effectively improves wear resistance by enhancing hardness and adhesion strength, thanks to the synergistic effect of reinforcements. Furthermore, the in vitro study with SBF solution indicates its bioactivity, and various studies with human blood indicate its hemocompatibility. Additionally, the in vivo studies of the HAC1 implants with rabbits demonstrated its potential for human use, confirming the results obtained from different in vitro studies.

These findings indicate that HAC1 is a potential and scalable candidate for load-bearing orthopedic applications.

7.3 Future scope, limitations, and challenges

The study in this field shall encompass the following to expand upon current work and possess certain limitations and challenges:

- The production of HA often faces issues related to reproducibility and scalability. Traditionally, wet precipitation methods have been used to develop HA-based biomaterials. However, these methods are limited by high particle agglomeration risk, significant property variation, and low scalability. As a result, researchers and industries are exploring new techniques that can offer better reproducibility and scalability.

Continuous production methods are emerging as a promising approach for producing high-quality HA-based composites. This technique provides several advantages, including better quality control, efficiency, scalability, cost-effectiveness, efficient use of reagents, better control over operating parameters, and the ability to modify product features. Continuous production methods have been reported to improve batch variability and fine-tuning of HA crystallinity, making it an effective strategy for easy scale-up (Gomes et al. 2008). For example, in the pharmaceutical industry, continuous production methods have been adopted for end-to-end production in a single, uninterrupted process line. Furthermore, researchers are also exploring ion doping to enhance the biological properties of HA and overcome the limitations associated with its properties, such as non-antibacterial and low mechanical strength. Recently, oscillatory flow devices have emerged as a promising continuous production approach for producing HA composites. This method allows better control over nucleation and crystal growth rates, opening new avenues for making tailored HA particles (Veiga et al. 2023). This technology has the potential to bridge the gap between academic exploration and large-scale industrial production, providing a consistent fabrication path for HA.

- To ensure good reproducibility, we established and followed standardized procedures for synthesis, including precise measurement of reactants and control of environmental conditions in the lab. Prior to full-scale production, many pilot studies were conducted to assess the scalability of the synthesis process and to identify potential issues with consistency and reproducibility. Multiple testing methods and replicated experiments were conducted to validate results and ensure accuracy. Additionally, detailed records of all experimental conditions, procedures, and results were maintained to aid in troubleshooting any issues and provide a basis for reproducibility.
- The current study has shown that the HVOF process is more effective than other thermal spray techniques for applying protective coatings to various industrial components. However, scaling up this process for industrial applications may pose challenges such as high cost, maintaining uniform coating thickness, and meeting market demand. Moreover, the scalability of the HVOF process, particularly for HA coating, poses a significant challenge, as it is subjected to regulation by the U.S. Food and Drug Administration (FDA).
- Challenges faced during HVOF spraying: To ensure a uniform coating, powders with a narrow size distribution were used. The powders were well-characterized, and when needed, sieving was done to maintain uniformity before coating to avoid issues with size variations. While coating, we have maintained a consistent spray distance using a robotic arm as, the manual spraying could lead to uneven coating thickness. Further gas flow rates were adjusted with the point of view of minimum melting with good adhesion, and the number of passes in both horizontal and vertical directions was fixed throughout to produce a coating with uniform thickness. Addressing these challenges required meticulous process control, thorough testing, and sometimes iterative adjustments to the process parameters to achieve a uniform and high-quality coating.

During the HVOF spraying of HA particles, a major issue encountered was the improper adhesion of the particles to the substrate. This resulted in

difficulties in achieving a uniform coating initially. Optimizing HVOF parameters for hydroxyapatite coatings posed a challenge, as finding the ideal balance between process parameters such as flame temperature, powder feed rate, spray distance, and gas flow rates was difficult.

- Generally, the US FDA needs a premarket review of the coated device to introduce a thermal spray-coated device in the market. The FDA does not clear or approve individual coatings or materials; rather, coatings and materials are evaluated as part of the final, finished medical device in the context of the specific device's technological characteristics and intended use. The FDA has two current guidance documents for orthopedic implants with modified metallic surfaces and hydroxyapatite coatings, which outline the FDA's recommendations for full characterization and testing of these coatings, respectively. Additionally, the standards organizations (e.g., ISO and ASTM) have developed many materials and testing standards for these coatings, recognized by the FDA, which the current research work has followed (Foy and Buch 2008).
- A new coating like HAC1 has an intended clinical use applied using a new thermal spray technique (HVOF), featuring new technologies, or utilizing a new characterization method; we have to submit a Pre-Submission report having the following steps to obtain the FDA's feedback: 1) **Consultation**: Engage in pre-submission meetings with the FDA to discuss the development plans, testing requirements, and potential concerns. This can help clarify expectations and guide the regulatory strategy. 2) **Preclinical Studies**: Conduct thorough preclinical studies, including in vitro and in-depth in-vivo tests with small to big-sized animals. These should assess biocompatibility, mechanical properties, and long-term performance using established protocols and standards, such as ISO 10993 for biocompatibility testing. The current study has followed the same protocols for in vitro and in-vivo studies. 3) **Clinical Trial**: Design and execute clinical trials to demonstrate the safety and effectiveness of the implants in human subjects. This involves phase I (safety), phase II (effectiveness), and phase III (comparison to existing treatments) trials. 4) **Regulatory Approval**:

Obtain Institutional Review Board (IRB) approval for clinical trials and ensure adherence to Good Clinical Practice (GCP) guidelines. 5) **Documentation and Submission:** Prepare a comprehensive regulatory submission that includes data from preclinical and clinical studies, manufacturing processes, risk assessments, and labeling information. 6) **Regulatory Pathway:** Determine the appropriate regulatory pathway (e.g., 510(k) for devices that are substantially equivalent to existing ones, or premarket approval (PMA) for high-risk devices) and follow the required steps. 7) **Post-Market Surveillance:** Implement a post-market surveillance plan to monitor the performance of the implants once they are on the market. This includes tracking adverse events, conducting follow-up studies, and responding to any issues. 8) **Continuous Improvement:** Use feedback from clinical trials and post-market surveillance to improve the HVOF process and the implant. Regularly review and update the processes to enhance quality and compliance. By addressing these challenges and following a structured approach to regulatory compliance, we can better navigate FDA regulations and increase the likelihood of successful approval for HVOF-sprayed hydroxyapatite implants (Sun 2018).

- The FDA should regulate any new thermal spray technique like HVOF spray used in the present study for producing hydroxyapatite implants to ensure its safety, efficacy, and compliance with the established standards and regulations for biomedical coatings.
- In-depth in-vivo studies with more big animals like dogs/sheep are required before clinical implementation of the implants.
- Future research should explore secondary reinforcements like Ag, Cu, Zirconium, alumina, and tungsten to address the HA coatings' limitations and further enhance the mechanical, tribological, and antibacterial properties.
- With the increasing demand for HA in biomedical applications, exploring natural and renewable alternatives for its production is essential. Animal bones and scales are promising for producing HA, ensuring sustainability, and

generating waste-to-value-added materials.

- One of the major issues of using CNTs is their agglomeration issue, as a high concentration of CNT in the matrix could increase the strength of the HA matrix; however, due to the Van der Waals force of attraction between CNTs, dispersion would be challenging, and that could critically affect the human body cells.
- The current hemocompatibility model's primary constraint is the absence of an endothelium in the circulating system. The endothelium produces cytokines and antithrombotic components and expresses adhesion molecules for thrombocytes, monocytes, and neutrophils. It plays a vital role in the interaction between circulating blood and artificial implants.
- The current hemocompatibility tests are conducted using blood from young, healthy donors who have not taken medication, which may not accurately represent the target population for the test materials. Comparative studies using blood from patients of various age groups and genders are necessary to enhance the accuracy of the current study findings.
- To study the level of osseointegration of the implants to bone cells, further study is needed to establish the mechanical properties of the implants. Therefore, the newly grown bone's elastic modulus (E) and HA-based coatings in the retrieved implants should be evaluated using the nanoindentation technique.

REFERENCES

- Aarik, L., Mändar, H., Tarre, A., Piirsoo, H. M., and Aarik, J. (2022). “Mechanical properties of crystalline and amorphous aluminum oxide thin films grown by atomic layer deposition.” *Surf. Coatings Technol.*, 438, 128409.
- Adams, R. L. C., and Bird, R. J. (2009). “Review article: Coagulation cascade and therapeutics update: Relevance to nephrology. Part 1: Overview of coagulation, thrombophilias and history of anticoagulants.” *Nephrology*.
- Ahmed, Y., Yasir, M., and Ur Rehman, M. A. (2020). “Fabrication and Characterization of Zein/Hydroxyapatite Composite Coatings for Biomedical Applications.” *Surfaces 2020, Vol. 3, Pages 237-250*, 3(2), 237–250.
- Al-Shalawi, F. D., Mohamed Ariff, A. H., Jung, D. W., Mohd Ariffin, M. K. A., Seng Kim, C. L., Brabazon, D., and Al-Osaimi, M. O. (2023). “Biomaterials as Implants in the Orthopedic Field for Regenerative Medicine: Metal versus Synthetic Polymers.” *Polymers (Basel)*, Multidisciplinary Digital Publishing Institute.
- Albee, F. H. (1920). “STUDIES IN BONE GROWTH: TRIPLE CALCIUM PHOSPHATE AS A STIMULUS TO OSTEOGENESIS.” *Ann. Surg.*, 71(1), 32–9.
- Amarnath, L. P., Srinivas, A., and Ramamurthi, A. (2006). “In vitro hemocompatibility testing of UV-modified hyaluronan hydrogels.” *Biomaterials*, 27(8), 1416–1424.
- Arima, Y., and Iwata, H. (2007). “Effect of wettability and surface functional groups on protein adsorption and cell adhesion using well-defined mixed self-assembled monolayers.” *Biomaterials*, 28(20), 3074–3082.
- Arjunan, A., Baroutaji, A., and Robinson, J. (2021a). “Introduction.” (June), 0–12.
- Arjunan, A., Baroutaji, A., Robinson, J., and Wang, C. (2021b). “Antibacterial Biomaterials in Orthopedics.” *Encycl. Smart Mater.*, 46–55.
- Baino, F., and Yamaguchi, S. (2020). “The use of simulated body fluid (SBF) for assessing materials bioactivity in the context of tissue engineering: Review and challenges.” *Biomimetics*.
- Bakshi, S. R., Balani, K., and Agarwal, A. (2008). “Thermal conductivity of plasma-sprayed aluminum oxide - Multiwalled carbon nanotube composites.” *J. Am. Ceram. Soc.*, 942–947.

Balani, K., Anderson, R., Laha, T., Andara, M., Tercero, J., Crumpler, E., and Agarwal, A. (2007a). "Plasma-sprayed carbon nanotube reinforced hydroxyapatite coatings and their interaction with human osteoblasts in vitro." *Biomaterials*, 28(4), 618–624.

Balani, K., Chen, Y., Harimkar, S. P., Dahotre, N. B., and Agarwal, A. (2007b). "Tribological behavior of plasma-sprayed carbon nanotube-reinforced hydroxyapatite coating in physiological solution." *Acta Biomater.*, 3(6), 944–951.

Ben-Nissan, B., Milev, A., and Vago, R. (2004). "Morphology of sol-gel derived nano-coated coralline hydroxyapatite." *Biomaterials*, 25(20), 4971–4975.

Bhattacharjee, A., and Bose, S. (2023). "Ginger extract loaded Fe₂O₃/MgO-doped hydroxyapatite: Evaluation of biological properties for bone–tissue engineering." *J. Am. Ceram. Soc.*, (September), 1–12.

Bose, S., Ke, D., Vu, A. A., Bandyopadhyay, A., and Goodman, S. B. (2020). "Thermal Oxide Layer Enhances Crystallinity and Mechanical Properties for Plasma-Sprayed Hydroxyapatite Biomedical Coatings." *ACS Appl. Mater. Interfaces*, 12(30), 33465–33472.

Budinski, K. G. (1988). "Surface engineering for wear resistance." 420.

Bulina, N. V., Makarova, S. V., Baev, S. G., Matvienko, A. A., Gerasimov, K. B., Logutenko, O. A., and Bystrov, V. S. (2021). "A study of thermal stability of hydroxyapatite." *Minerals*, 11(12), 1310.

Carneiro, Í., and Simões, S. (2020). "Effect of morphology and structure of MWCNTs on metal matrix nanocomposites." *Materials (Basel)*, 13(23), 1–16.

Celik, E., Ozdemir, I., Avci, E., and Tsunekawa, Y. (2005). "Corrosion behaviour of plasma sprayed coatings." *Surf. Coatings Technol.*, 193(1-3 SPEC. ISS.), 297–302.

Chandra Yadaw, R., Kumar Singh, S., Chattopadhyaya, S., Kumar, S., and C. Singh, R. (2018). "Tribological behavior of thin film coating-a review." *Int. J. Eng. Technol.*, 7(3), 1656.

Chauhan, S. R., and Dass, K. (2013). "Dry sliding wear behaviour of titanium (Grade 5) alloy by using response surface methodology." *Adv. Tribol.*, 2013.

Chavana, N., Bhajantri F, V., and Jambagi, S. C. (2022). "Improvement in Slurry Erosion and Corrosion Resistance of Plasma-Sprayed Fly Ash Coatings for Marine Applications." *ACS Omega*, 7(36), 32369–32382.

- Chen, Q. Y., Zou, Y. L., Fu, W., Bai, X. B., Ji, G. C., Yao, H. L., Wang, H. T., and Wang, F. (2019). “Wear behavior of plasma sprayed hydroxyapatite bioceramic coating in simulated body fluid.” *Ceram. Int.*, 45(4), 4526–4534.
- Cheng, C., Müller, K. H., Koziol, K. K. K., Skepper, J. N., Midgley, P. A., Welland, M. E., and Porter, A. E. (2009). “Toxicity and imaging of multi-walled carbon nanotubes in human macrophage cells.” *Biomaterials*, 30(25), 4152–4160.
- Chibowski, E., Holysz, L., Terpilowski, K., and Wiacek, A. E. (2007). “Influence of ionic surfactants and lecithin on stability of titanium dioxide in aqueous electrolyte solution.” *Croat. Chem. Acta*, 80(3), 395–403.
- Cizek, J., and Khor, K. A. (2012). “Role of in-flight temperature and velocity of powder particles on plasma sprayed hydroxyapatite coating characteristics.” *Surf. Coatings Technol.*, 206(8–9), 2181–2191.
- Claase, M. B., Vercoulen, P., and Misev, T. A. (2014). “Powder Coatings and the Effects of Particle Size.” Springer, Cham, 371–404.
- Clavijo-Mejía, G. A., Hermann-Muñoz, J. A., Rincón-López, J. A., Ageorges, H., and Muñoz-Saldaña, J. (2020). “Bovine-derived hydroxyapatite coatings deposited by high-velocity oxygen-fuel and atmospheric plasma spray processes: A comparative study.” *Surf. Coatings Technol.*, 381(April 2021), 125193.
- Clèries, L., Martínez, E., Fernández-Pradas, J. M., Sardin, G., Esteve, J., and Morenza, J. L. (2000). “Mechanical properties of calcium phosphate coatings deposited by laser ablation.” *Biomaterials*, 21(9), 967–971.
- Dalili, F., Aghdam, R. M., Soltani, R., and Saremi, M. (2022). “Corrosion, mechanical and bioactivity properties of HA-CNT nanocomposite coating on anodized Ti6Al4V alloy.” *J. Mater. Sci. Mater. Med.*, 33(4), 1–14.
- Das, A., Chakraborty, B., and Sood, A. K. (2008). “Raman spectroscopy of graphene on different substrates and influence of defects.” *Bull. Mater. Sci.*, 31(3), 579–584.
- Devi, R., and Gill, S. S. (2021). “A squared bossed diaphragm piezoresistive pressure sensor based on CNTs for low pressure range with enhanced sensitivity.” *Microsyst. Technol.*, 27(8), 3225–3233.
- Dey, A., Sinha, A., Banerjee, K., and Mukhopadhyay, A. K. (2014). “Tribological studies of microplasma sprayed hydroxyapatite coating at low load.” *Mater. Technol.*, 29(B1).

- Dorozhkin, S. V. (2015). "Calcium orthophosphate bioceramics." *Ceram. Int.*, Elsevier.
- Dorozhkin, S. V. (2023). "There Are over 60 Ways to Produce Biocompatible Calcium Orthophosphate (CaPO₄) Deposits on Various Substrates." *J. Compos. Sci.*, 7(7).
- EYLAR, E. H., MADOFF, M. A., BRODY, O. V., and ONCLEY, J. L. (1962). "The contribution of sialic acid to the surface charge of the erythrocyte." *J. Biol. Chem.*, 237(6), 1992–2000.
- Fabre, H., Mercier, D., Galtayries, A., Portet, D., Delorme, N., and Bardeau, J. F. (2018). "Impact of hydrophilic and hydrophobic functionalization of flat TiO₂ /Ti surfaces on proteins adsorption." *Appl. Surf. Sci.*, 432, 15–21.
- Facca, S., Lahiri, D., Fioretti, F., Messadeq, N., Mainard, D., Benkirane-Jessel, N., and Agarwal, A. (2011). "In vivo osseointegration of nano-designed composite coatings on titanium implants." *ACS Nano*, 5(6), 4790–4799.
- Feret, F. R., Roy, D., and Boulanger, C. (2000). "Determination of alpha and beta alumina in ceramic alumina by X-ray diffraction." *Spectrochim. acta, Part B At. Spectrosc.*, 55(7), 1051–1061.
- Ferrage, L., Bertrand, G., Lenormand, P., Grossin, D., and Ben-Nissan, B. (2017). "A review of the additive manufacturing (3DP) of bioceramics: Alumina, zirconia (PSZ) and hydroxyapatite." *J. Aust. Ceram. Soc.*, 53(1), 11–20.
- Fiume, E., Magnaterra, G., Rahdar, A., Verné, E., and Baino, F. (2021). "Hydroxyapatite for biomedical applications: A short overview." *Ceramics*, Multidisciplinary Digital Publishing Institute.
- Foy, J. R., and Buch, B. D. (2008). "Orthopaedic joint devices: the FDA's short answers to your questions." *J. Am. Acad. Orthop. Surg.*, 16 Suppl 1.
- Fu, Y., Batchelor, A. W., Wang, Y., and Khor, K. A. (1998). "Fretting wear behaviors of thermal sprayed hydroxyapatite (HA) coating under unlubricated conditions." *Wear*, 217(1), 132–139.
- Gadow, R., Killinger, A., and Stiegler, N. (2010). "Hydroxyapatite coatings for biomedical applications deposited by different thermal spray techniques." *Surf. Coatings Technol.*, 205(4), 1157–1164.
- Gang, S., Fengzhou, F., and Chengwei, K. (2018). "Tribological Performance of

Bioimplants: A Comprehensive Review.” *Nanotechnol. Precis. Eng.*, 1(2), 107–122.

Ganvir, A., Nagar, S., Markocsan, N., and Balani, K. (2021). “Deposition of hydroxyapatite coatings by axial plasma spraying: Influence of feedstock characteristics on coating microstructure, phase content and mechanical properties.” *J. Eur. Ceram. Soc.*, 41(8), 4637–4649.

Gao, L., Jiang, L., and Sun, J. (2006). “Carbon nanotube-ceramic composites.” *J. Electroceramics*, 17(1), 51–55.

Gaona, M., Lima, R. S., and Marple, B. R. (2007). “Nanostructured titania/hydroxyapatite composite coatings deposited by high velocity oxy-fuel (HVOF) spraying.” *Mater. Sci. Eng. A*, 458(1–2), 141–149.

Gautam, S., Bhatnagar, D., Bansal, D., Batra, H., and Goyal, N. (2022). “Recent advancements in nanomaterials for biomedical implants.” *Biomed. Eng. Adv.*, 3, 100029.

Geetha, M., Singh, A. K., Asokamani, R., and Gogia, A. K. (2009). “Ti based biomaterials, the ultimate choice for orthopaedic implants - A review.” *Prog. Mater. Sci.*, 54(3), 397–425.

Gessner, A., Waicz, R., Lieske, A., Paulke, B. R., Mäder, K., and Müller, R. H. (2000). “Nanoparticles with decreasing surface hydrophobicities: Influence on plasma protein adsorption.” *Int. J. Pharm.*, 196(2), 245–249.

Gkomoza, P., Vardavoulias, M., Pantelis, D. I., and Sarafoglou, C. (2019). “Comparative study of structure and properties of thermal spray coatings using conventional and nanostructured hydroxyapatite powder, for applications in medical implants.” *Surf. Coatings Technol.*, 357, 748–758.

Gomes, J. F., Granadeiro, C. C., Silva, M. A., Hoyos, M., Silva, R., and Vieira, T. (2008). “An investigation of the synthesis parameters of the reaction of hydroxyapatite precipitation in aqueous media.” *Int. J. Chem. React. Eng.*, 6.

Gopi, D., Shinyjoy, E., Sekar, M., Surendiran, M., Kavitha, L., and Sampath Kumar, T. S. (2013). “Development of carbon nanotubes reinforced hydroxyapatite composite coatings on titanium by electrodeposition method.” *Corros. Sci.*, 73, 321–330.

Guan, K., Zhang, L., Zhu, F., Sheng, H., and Li, H. (2019). “Surface modification for carbon/carbon composites with Mg-CaP coating reinforced by SiC nanowire-carbon nanotube hybrid for biological application.” *Appl. Surf. Sci.*, 489, 856–866.

- Guan, R. G., Johnson, I., Cui, T., Zhao, T., Zhao, Z. Y., Li, X., and Liu, H. (2012). "Electrodeposition of hydroxyapatite coating on Mg-4.0Zn-1.0Ca-0.6Zr alloy and in vitro evaluation of degradation, hemolysis, and cytotoxicity." *J. Biomed. Mater. Res. - Part A*, 100 A(4), 999–1015.
- Gupta, V. K., and Saleh, T. A. (2016). "Synthesis of Carbon Nanotube-Metal Oxides Composites ; Adsorption and Photo-degradation." (July 2011).
- Gupta, V., and Saleh, T. A. (2011). "Syntheses of Carbon Nanotube-Metal Oxides Composites; Adsorption and Photo-degradation." *Carbon Nanotub. - From Res. to Appl.*, InTech.
- Hadipour, M., Hafezi, M., and Hesarak, S. (2015). "Preparation and characterization of plasma-sprayed nanostructured- merwinite coating on Ti-6Al-4v." *J. Ceram. Process. Res.*, 16(3), 287–290.
- Hasan, S., and Stokes, J. (2011). "Design of experiment analysis of the Sulzer Metco DJ high velocity oxy-fuel coating of hydroxyapatite for orthopedic applications." *J. Therm. Spray Technol.*, 20(1–2), 186–194.
- Hashimoto, A., Sonohata, M., Kitajima, M., Kawano, S., Eto, S., and Mawatari, M. (2020). "First experience with a thermal-sprayed silver oxide-containing hydroxyapatite coating implant in two-stage total hip arthroplasty for the treatment of septic arthritis with hip osteoarthritis: A case report." *Int. J. Surg. Case Rep.*, 77, 434–437.
- Heimann, R. B. (2016). "Plasma-Sprayed Hydroxylapatite-Based Coatings: Chemical, Mechanical, Microstructural, and Biomedical Properties." *J. Therm. Spray Technol.*, Springer.
- Henao, J., Sotelo-Mazon, O., Giraldo-Betancur, A. L., Hincapie-Bedoya, J., Espinosa-Arbelaiz, D. G., Poblano-Salas, C., Cuevas-Arteaga, C., Corona-Castuera, J., and Martinez-Gomez, L. (2020). "Study of HVOF-sprayed hydroxyapatite/titania graded coatings under in-vitro conditions." *J. Mater. Res. Technol.*, 9(6), 14002–14016.
- Hench, L. L. (1998). "Bioceramics." *J. Am. Ceram. Soc.*, 81(7), 1705–1728.
- Hench, L. L., Splinter, R. J., Allen, W. C., and Greenlee, T. K. (1971). "Bonding mechanisms at the interface of ceramic prosthetic materials." *J. Biomed. Mater. Res.*, 5(6), 117–141.
- Heness, G., and Ben-Nissan, B. (2004). "Innovative bioceramics." *Mater. Forum*,

104–114.

Hermann-Muñoz, J. A., Rincón-López, J. A., Clavijo-Mejía, G. A., Giraldo-Betancur, A. L., Alvarado-Orozco, J. M., Vizcaya-Ruiz, A. De, and Muñoz-Saldaña, J. (2019). “Influence of HVOF parameters on HAp coating generation: An integrated approach using process maps.” *Surf. Coatings Technol.*, 358(November 2018), 299–307.

Hernigou, P., and Bahrami, T. (2003). “Zirconia and alumina ceramics in comparison with stainless-steel heads.” *J. Bone Jt. Surg. - Ser. B*, 85(4), 504–509.

Hu, H., Li, Z., Sun, W., Li, R., Li, H., and Khor, K. A. (2020). “Friction and Wear Behaviors of Reduced Graphene Oxide- and Carbon Nanotube-Reinforced Hydroxyapatite Bioceramics.” *Front. Mater.*, 7, 564624.

Huang, J. Y., Chen, S., Wang, Z. Q., Kempa, K., Wang, Y. M., Jo, S. H., Chen, G., Dresselhaus, M. S., and Ren, Z. F. (2006). “Superplastic carbon nanotubes.” *Nature*, 439(7074), 281.

Hussain, S., Shah, Z. A., Sabiruddin, K., and Keshri, A. K. (2023). “Characterization and tribological behaviour of Indian clam seashell-derived hydroxyapatite coating applied on titanium alloy by plasma spray technique.” *J. Mech. Behav. Biomed. Mater.*, 137(August 2022), 105550.

Iijima, S. (1991). “Helical microtubules of graphitic carbon.” *Nature*, 354(6348), 56–58.

Jagadeeshanayaka, N., Awasthi, S., Jambagi, S. C., and Srivastava, C. (2022). “Bioactive surface modifications through thermally sprayed hydroxyapatite composite coatings: a review of selective reinforcements.” *Biomater. Sci.*

Jagadeeshanayaka, N., Kele, S. N., and Jambagi, S. C. (2023). “An Investigation into the Relative Efficacy of High-Velocity Air-Fuel-Sprayed Hydroxyapatite Implants Based on the Crystallinity Index, Residual Stress, Wear, and In-Flight Powder Particle Behavior.” *Langmuir*, 39(48), 17513–17528.

Jalili, H., Aslibeiki, B., Varzaneh, A. G., and Chernenko, V. A. (2019). “The effect of magneto-crystalline anisotropy on the properties of hard and soft magnetic ferrite nanoparticles.” *Beilstein J. Nanotechnol.*, 10, 1348–1359.

Jambagi, S. C., and Bandyopadhyay, P. P. (2017). “Plasma sprayed carbon nanotube reinforced splats and coatings.” *J. Eur. Ceram. Soc.*, 37(5), 2235–2244.

Jambagi, S. C., and Malik, V. R. (2021). “A Review on Surface Engineering

Perspective of Metallic Implants for Orthopaedic Applications.” *Jom*, 73(12), 4349–4364.

Jambagi, S. C., Sarkar, N., and Bandyopadhyay, P. P. (2015). “Preparation of carbon nanotube doped ceramic powders for plasma spraying using heterocoagulation method.” *J. Eur. Ceram. Soc.*, 35(3), 989–1000.

Jeong, J., Kim, J. H., Shim, J. H., Hwang, N. S., and Heo, C. Y. (2019). “Whitlockite verification.pdf.” 1–11.

Jiang, L., Fan, G., Li, Z., Kai, X., Zhang, D., Chen, Z., Humphries, S., Heness, G., and Yeung, W. Y. (2011). “An approach to the uniform dispersion of a high volume fraction of carbon nanotubes in aluminum powder.” *Carbon N. Y.*, 49(6), 1965–1971.

Kah, P., Väst, H., Layus, P., Kah, P., Martikainen, J., and Layus, P. (2011). “Methods of evaluating weld quality in modern production (Part 2).” *Proc. 16th Int. Conf.*, (March 2011), 7–8.

Kalmodia, S., Goenka, S., Laha, T., Lahiri, D., Basu, B., and Balani, K. (2010). “Microstructure, mechanical properties, and in vitro biocompatibility of spark plasma sintered hydroxyapatite-aluminum oxide-carbon nanotube composite.” *Mater. Sci. Eng. C*, 30(8), 1162–1169.

Kataria, S., Kumar, N., Dash, S., and Tyagi, A. K. (2010). “Tribological and deformation behaviour of titanium coating under different sliding contact conditions.” *Wear*, 269(11–12), 797–803.

Kaur, S., Bala, N., and Khosla, C. (2018). “Characterization of Thermal-Sprayed HAP and HAP/TiO₂ Coatings for Biomedical Applications.” *J. Therm. Spray Technol.*, 27(8), 1356–1370.

Kaur, S., Bala, N., and Khosla, C. (2019). “Characterization of Hydroxyapatite Coating on 316L Stainless Steel by Sol–Gel Technique.” *Surf. Eng. Appl. Electrochem.*, 55(3), 357–366.

Kaya, C., Singh, I., and Boccaccini, A. R. (2008). “Multi-walled carbon nanotube-reinforced hydroxyapatite layers on Ti6Al4V medical implants by Electrophoretic Deposition (EPD).” *Adv. Eng. Mater.*, 10(1–2), 131–138.

Khan, F. S. A., Mubarak, N. M., Khalid, M., Walvekar, R., Abdullah, E. C., Ahmad, A., Karri, R. R., and Pakalapati, H. (2021). “Functionalized multi-walled carbon nanotubes and hydroxyapatite nanorods reinforced with polypropylene for biomedical

application.” *Sci. Rep.*, 11(1), 1–10.

Khanal, S. P., Mahfuz, H., Rondinone, A. J., and Leventouri, T. (2016).

“Improvement of the fracture toughness of hydroxyapatite (HAp) by incorporation of carboxyl functionalized single walled carbon nanotubes (CfSWCNTs) and nylon.” *Mater. Sci. Eng. C*, 60, 204–210.

Khor, K. A., Li, H., and Cheang, P. (2003). “Processing-microstructure-property relations in HVOF sprayed calcium phosphate based bioceramic coatings.” *Biomaterials*, 24(13), 2233–2243.

Kim, D. E., Kim, C. L., and Kim, H. J. (2011). “A novel approach to wear reduction of micro-components by synthesis of carbon nanotube-silver composite coating.” *CIRP Ann.*, 60(1), 599–602.

Koch, C. F., Johnson, S., Kumar, D., Jelinek, M., Chrisey, D. B., Doraiswamy, A., Jin, C., Narayan, R. J., and Mihailescu, I. N. (2007). “Pulsed laser deposition of hydroxyapatite thin films.” *Mater. Sci. Eng. C*, 27(3), 484–494.

Komath, M., Rajesh, P., Muraleedharan, C. V., Varma, H. K., Reshmi, R., and Jayaraj, M. K. (2011). “Formation of hydroxyapatite coating on titanium at 200.C through pulsed laser deposition followed by hydrothermal treatment.” *Bull. Mater. Sci.*, 34(2), 389–399.

Komath, M., and Varma, H. K. (2003). “Development of a fully injectable calcium phosphate cement for orthopedic and dental applications.” *Bull. Mater. Sci.*, 26(4), 415–422.

Kotani, S., Fujita, Y., Kitsugi, T., Nakamura, T., Yamamuro, T., Ohtsuki, C., and Kokubo, T. (1991). “Bone bonding mechanism of β -tricalcium phosphate.” *J. Biomed. Mater. Res.*, 25(10), 1303–1315.

Kowalski, S., Gonciarz, W., Belka, R., Góral, A., Chmiela, M., Lechowicz, Ł., Kaca, W., and Żórawski, W. (2022). “Plasma-Sprayed Hydroxyapatite Coatings and Their Biological Properties.” *Coatings*, 12(9).

Kumar, R., and Agrawal, A. (2023). “Micro-hydroxyapatite reinforced Ti-based composite with tailored characteristics to minimize stress-shielding impact in bio-implant applications.” *J. Mech. Behav. Biomed. Mater.*, 142, 105852.

Kumari, R., and Majumdar, J. D. (2017). “Microstructure and surface mechanical properties of plasma spray deposited and post spray heat treated hydroxyapatite (HA)

- based composite coating on titanium alloy (Ti-6Al-4V) substrate.” *Mater. Charact.*, 131(March), 12–20.
- Kweh, S. W. K., Khor, K. A., and Cheang, P. (2002). “An in vitro investigation of plasma sprayed hydroxyapatite (HA) coatings produced with flame-spheroidized feedstock.” *Biomaterials*, 23(3), 775–785.
- Lahiri, D., Benaduce, A. P., Rouzaud, F., Solomon, J., Keshri, A. K., Kos, L., and Agarwal, A. (2011). “Wear behavior and in vitro cytotoxicity of wear debris generated from hydroxyapatite-carbon nanotube composite coating.” *J. Biomed. Mater. Res. - Part A*, 96 A(1), 1–12.
- Lahiri, D., Ghosh, S., and Agarwal, A. (2012). “Carbon nanotube reinforced hydroxyapatite composite for orthopedic application: A review.” *Mater. Sci. Eng. C*, Elsevier.
- Lahiri, D., Singh, V., Keshri, A. K., Seal, S., and Agarwal, A. (2010). “Carbon nanotube toughened hydroxyapatite by spark plasma sintering: Microstructural evolution and multiscale tribological properties.” *Carbon N. Y.*, 48(11), 3103–3120.
- Laranjeira, M. S., Moço, A., Ferreira, J., Coimbra, S., Costa, E., Santos-Silva, A., Ferreira, P. J., and Monteiro, F. J. (2016). “Different hydroxyapatite magnetic nanoparticles for medical imaging: Its effects on hemostatic, hemolytic activity and cellular cytotoxicity.” *Colloids Surfaces B Biointerfaces*, 146, 363–374.
- Lee, K. W., Bae, C. M., Jung, J. Y., Sim, G. B., Rautray, T. R., Lee, H. J., Kwon, T. Y., and Kim, K. H. (2011). “Surface characteristics and biological studies of hydroxyapatite coating by a new method.” *J. Biomed. Mater. Res. - Part B Appl. Biomater.*, 98 B(2), 395–407.
- Lehmann, J. S., Schwaiger, R., Rinke, M., and Greiner, C. (2021). “How Tribo-Oxidation Alters the Tribological Properties of Copper and Its Oxides.” *Adv. Mater. Interfaces*, 8(1), 2001673.
- Levingstone, T. J. (2008). *Optimisation of Plasma Sprayed Hydroxyapatite Coatings*.
- Li, A., Sun, K., Dong, W., and Zhao, D. (2007). “Mechanical properties, microstructure and histocompatibility of MWCNTs/HAp biocomposites.” *Mater. Lett.*, 61(8–9), 1839–1844.
- Li, H. C., Hsieh, F. J., Chen, C. P., Chang, M. Y., Hsieh, P. C. H., Chen, C. C., Hung, S. U., Wu, C. C., and Chang, H. C. (2013). “The hemocompatibility of oxidized

- diamond nanocrystals for biomedical applications.” *Sci. Rep.*, 3(1), 1–8.
- Li, H., Ng, B. S., Khor, K. A., Cheang, P., and Clyne, T. W. (2004). “Raman spectroscopy determination of phases within thermal sprayed hydroxyapatite splats and subsequent in vitro dissolution examination.” *Acta Mater.*, 52(2), 445–453.
- Li, H., Sun, X., Li, Y., Li, B., Liang, C., and Wang, H. (2019). “Preparation and properties of carbon nanotube (Fe)/hydroxyapatite composite as magnetic targeted drug delivery carrier.” *Mater. Sci. Eng. C*, 97, 222–229.
- Li, H., Zhu, R., Sun, L., Xue, Y., Hao, Z., Xie, Z., Fan, X., and Fan, H. (2014a). “Effect of thickness of HA-coating on microporous silk scaffolds using alternate soaking technology.” *Biomed Res. Int.*, 2014.
- Li, M., Liu, Q., Jia, Z., Xu, X., Cheng, Y., Zheng, Y., Xi, T., and Wei, S. (2014b). “Graphene oxide/hydroxyapatite composite coatings fabricated by electrophoretic nanotechnology for biological applications.” *Carbon N. Y.*, 67, 185–197.
- Li, M., Xiong, P., Mo, M., Cheng, Y., and Zheng, Y. (2016). “Electrophoretic-deposited novel ternary silk fibroin/graphene oxide/hydroxyapatite nanocomposite coatings on titanium substrate for orthopedic applications.” *Front. Mater. Sci.*, 10(3), 270–280.
- Li, Q., Liu, J., and Xu, S. (2015). “Progress in Research on Carbon Nanotubes Reinforced Cementitious Composites.” *Adv. Mater. Sci. Eng.*, 2015.
- Lima, R. S., Khor, K. A., Li, H., Cheang, P., and Marple, B. R. (2005). “HVOF spraying of nanostructured hydroxyapatite for biomedical applications.” *Mater. Sci. Eng. A*, 396(1–2), 181–187.
- Lin, C. E. (2004). “Determination of critical micelle concentration of surfactants by capillary electrophoresis.” *J. Chromatogr. A*, J Chromatogr A.
- Liu, Z., Chen, K., Davis, C., Sherlock, S., Cao, Q., Chen, X., and Dai, H. (2008). “Drug delivery with carbon nanotubes for in vivo cancer treatment.” *Cancer Res.*, 68(16), 6652–6660.
- Lopes, M. A., Santos, J. D., Monteiro, F. J., Ohtsuki, C., Osaka, A., Kaneko, S., and Inoue, H. (2001). “Push-out testing and histological evaluation of glass reinforced hydroxyapatite composites implanted in the tibia of rabbits.” *J. Biomed. Mater. Res.*, 54(4), 463–469.
- Manivasagam, V. K., and Popat, K. C. (2020). “In Vitro Investigation of

- Hemocompatibility of Hydrothermally Treated Titanium and Titanium Alloy Surfaces.” *ACS Omega*, 5(14), 8108–8120.
- Manivasagam, V. K., Sabino, R. M., Kantam, P., and Papat, K. C. (2021). “Surface modification strategies to improve titanium hemocompatibility: A comprehensive review.” *Mater. Adv.*, Royal Society of Chemistry.
- Mardali, M., SalimiJazi, H. R., Karimzadeh, F., Luthringer, B., Blawert, C., and Labbaf, S. (2019). “Comparative study on microstructure and corrosion behavior of nanostructured hydroxyapatite coatings deposited by high velocity oxygen fuel and flame spraying on AZ61 magnesium based substrates.” *Appl. Surf. Sci.*, 465, 614–624.
- Menezes, B. R. C. de, Ferreira, F. V., Silva, B. C., Simonetti, E. A. N., Bastos, T. M., Cividanes, L. S., and Thim, G. P. (2018). “Effects of octadecylamine functionalization of carbon nanotubes on dispersion, polarity, and mechanical properties of CNT/HDPE nanocomposites.” *J. Mater. Sci.*, 53(20), 14311–14327.
- Method, S. (2018). “Hydroxyapatite / silica Nanopowders Deposition on Ti Substrate by Plasma Hydroxyapatite / silica Nanopowders Deposition on Ti Substrate by Plasma Spray Method.” (November).
- Method, S. T. (2001). “Standard Test Method for Adhesion or Cohesion Strength of Thermal Spray Coatings 1.” *Current*, 03(2008), 1–7.
- Miri, Z., Haugen, H. J., Loca, D., Rossi, F., Perale, G., Moghanian, A., and Ma, Q. (2024). “Review on the strategies to improve the mechanical strength of highly porous bone bioceramic scaffolds.” *J. Eur. Ceram. Soc.*, Elsevier.
- Mittal, M., Nath, S. K., and Prakash, S. (2013). “Improvement in mechanical properties of plasma sprayed hydroxyapatite coatings by Al₂O₃ reinforcement.” *Mater. Sci. Eng. C*, 33(5), 2838–2845.
- Miyake, N., Sato, T., and Maki, Y. (2013). “Effect of zeta potentials on bovine serum albumin adsorption to hydroxyapatite surfaces.” *Bull. Tokyo Dent. Coll.*, 54(2), 97–101.
- Mohajernia, S., Pour-Ali, S., Hejazi, S., Saremi, M., and Kiani-Rashid, A. R. (2018). “Hydroxyapatite coating containing multi-walled carbon nanotubes on AZ31 magnesium: Mechanical-electrochemical degradation in a physiological environment.” *Ceram. Int.*, 44(7), 8297–8305.
- Morks, M. F., Kobayashi, A., and Fahim, N. F. (2007). “Abrasive wear behavior of

sprayed hydroxyapatite coatings by gas tunnel type plasma spraying.” *Wear*, 262(1–2), 204–209.

Motlagh, D., Yang, J., Lui, K. Y., Webb, A. R., and Ameer, G. A. (2006).

“Hemocompatibility evaluation of poly(glycerol-sebacate) in vitro for vascular tissue engineering.” *Biomaterials*, 27(24), 4315–4324.

Mukherjee, S., Kundu, B., Sen, S., and Chanda, A. (2014). “Improved properties of hydroxyapatite-carbon nanotube biocomposite: Mechanical, in vitro bioactivity and biological studies.” *Ceram. Int.*, 40(4), 5635–5643.

Neo, M., Nakamura, T., Ohtsuki, C., Kokubo, T., and Yamamuro, T. (1993). “Apatite formation on three kinds of bioactive material at an early stage in vivo: A comparative study by transmission electron microscopy.” *J. Biomed. Mater. Res.*, 27(8), 999–1006.

Nicholson, J. W. (2020). “Titanium Alloys for Dental Implants: A Review.” *Prosthesis*, 2(2), 100–116.

Nuswantoro, N. F., Manjas, M., Suharti, N., Juliadmi, D., Fajri, H., Tjong, D. H., Affi, J., Niinomi, M., and Gunawarman. (2021). “Hydroxyapatite coating on titanium alloy TNTZ for increasing osseointegration and reducing inflammatory response in vivo on *Rattus norvegicus* Wistar rats.” *Ceram. Int.*, 47(11), 16094–16100.

Ogawa, K., and Seo, D. (2011). “Repair of Turbine Blades Using Cold Spray Technique.” *Adv. Gas Turbine Technol.*

Ong, J. L., and Chan, D. C. N. (2000). “Hydroxyapatite and their use as coatings in dental implants: A review.” *Crit. Rev. Biomed. Eng.*, Crit Rev Biomed Eng.

Ong, K. L., Yun, B. M., and White, J. B. (2015). “New biomaterials for orthopedic implants.” *Orthop. Res. Rev.*, 7(September 2015), 107–130.

Ooi, C. H., Ling, Y. P., Abdullah, W. Z., Mustafa, A. Z., Pung, S. Y., and Yeoh, F. Y. (2019). “Physicochemical evaluation and in vitro hemocompatibility study on nanoporous hydroxyapatite.” *J. Mater. Sci. Mater. Med.*, 30(4).

Osorio, A. G., Santos, L. A. Dos, and Bergmann, C. P. (2011). “Evaluation of the mechanical properties and microstructure of hydroxyapatite reinforced with carbon nanotubes.” *Rev. Adv. Mater. Sci.*, 27(1), 58–63.

Pandey, A., Midha, S., Sharma, R. K., Maurya, R., Nigam, V. K., Ghosh, S., and Balani, K. (2018a). “Antioxidant and antibacterial hydroxyapatite-based biocomposite for orthopedic applications.” *Mater. Sci. Eng. C*, 88, 13–24.

Pandey, A., Patel, A. K., Ariharan, S., Kumar, V., Sharma, R. K., Kanhed, S., Nigam, V. K., Keshri, A., Agarwal, A., and Balani, K. (2018b). “Enhanced tribological and bacterial resistance of carbon nanotube with ceria-and silver-incorporated hydroxyapatite biocoating.” *Nanomaterials*, 8(6).

Paswan, S. K., Kumari, S., Kar, M., Singh, A., Pathak, H., Borah, J. P., and Kumar, L. (2021). “Optimization of structure-property relationships in nickel ferrite nanoparticles annealed at different temperature.” *J. Phys. Chem. Solids*, 151(January), 109928.

Perumal, G., Geetha, M., Asokamani, R., and Alagumurthi, N. (2013). “A comparative Study on the Wear Behavior of Al₂O₃ and SiC Coated Ti-6Al-4V Alloy Developed Using Plasma Spraying Technique.” *Trans. Indian Inst. Met.*, 66(2), 109–115.

Qi, H., and Wu, H. Y. (2013). “Effect of surface modification of pure Ti on tribological and biological properties of bone tissue.” *Surf. Eng.*, 29(4), 300–305.

Qian, W., Yu, H., Wei, F., Zhang, Q., and Wang, Z. (2002). “Synthesis of carbon nanotubes from liquefied petroleum gas containing sulfur [4].” *Carbon N. Y.*, 40(15), 2968–2970.

Qu, J., Blau, P. J., Watkins, T. R., Cavin, O. B., and Kulkarni, N. S. (2005). “Friction and wear of titanium alloys sliding against metal, polymer, and ceramic counterfaces.” *Wear*, 258(9), 1348–1356.

Raditya, P. P. R., and Hernaningsih, Y. (2020). “Platelet counts analysis of platelet-poor plasma (Ppp) produced by several centrifugation techniques.” *Indian J. Forensic Med. Toxicol.*, 14(3), 1211–1215.

Rameshbabu, N., Kumar, T. S. S., Prabhakar, T. G., Sastry, V. S., Murty, K. V. G. K., and Prasad Rao, K. (2007). “Antibacterial nanosized silver substituted hydroxyapatite: Synthesis and characterization.” *J. Biomed. Mater. Res. - Part A*, 80(3), 581–591.

Rastegari, S., and Salahinejad, E. (2019). “Surface modification of Ti-6Al-4V alloy for osseointegration by alkaline treatment and chitosan-matrix glass-reinforced nanocomposite coating.” *Carbohydr. Polym.*, 205(June 2018), 302–311.

Rattan, V., Singh Sidhu, T., and Mittal, M. (2022). “Wear studies on plasma-sprayed pure and reinforced hydroxyapatite coatings.” *Mater. Today Proc.*, 60, 1731–1735.

Robinson, J., Arjunan, A., Baroutaji, A., Martí, M., Tuñón Molina, A., Serrano-

- Aroca, Á., and Pollard, A. (2021). “Additive manufacturing of anti-SARS-CoV-2 Copper-Tungsten-Silver alloy.” *Rapid Prototyp. J.*, 27(10), 1831–1849.
- Rouahi, M., Champion, E., Gallet, O., Jada, A., and Anselme, K. (2006). “Physico-chemical characteristics and protein adsorption potential of hydroxyapatite particles: Influence on in vitro biocompatibility of ceramics after sintering.” *Colloids Surfaces B Biointerfaces*, 47(1), 10–19.
- Roy, M., Bandyopadhyay, A., and Bose, S. (2011). “Induction Plasma Sprayed Nano Hydroxyapatite Coatings on Titanium for Orthopaedic and Dental Implants.” *Surf. Coat. Technol.*, 205(8–9), 2785.
- Saber-Samandari, S., Alamara, K., Saber-Samandari, S., and Gross, K. A. (2013). “Micro-Raman spectroscopy shows how the coating process affects the characteristics of hydroxylapatite.” *Acta Biomater.*, 9(12), 9538–9546.
- Saber-Samandari, S., Baradaran, S., Nasiri-Tabrizi, B., Alamara, K., and Basirun, W. J. (2018). “Microstructural evolution and micromechanical properties of thermally sprayed hydroxyapatite coating.” *Adv. Appl. Ceram.*, 117(8), 452–460.
- Saifuddin, N., Raziah, A. Z., and Junizah, A. R. (2013). “Carbon nanotubes: A review on structure and their interaction with proteins.” *J. Chem.*
- Sakaguchi, N., Watari, F., Yokoyama, A., and Nodasaka, Y. (2008). “High-resolution electron microscopy of multi-wall carbon nanotubes in the subcutaneous tissue of rats.” *J. Electron Microsc. (Tokyo)*, 57(5), 159–164.
- Santos, C., Turiel, S., Gomes, P. S., Costa, E., Silva, A. S., and Quadros, P. (2018). “Vascular biosafety of commercial hydroxyapatite particles : discrepancy between blood compatibility assays and endothelial cell behavior.” *J. Nanobiotechnology*, (March).
- Sarath Chandra, V., Baskar, G., Suganthi, R. V., Elayaraja, K., Ahymah Joshy, M. I., Sofi Beaula, W., Mythili, R., Venkatraman, G., and Narayana Kalkura, S. (2012). “Blood compatibility of iron-doped nanosize hydroxyapatite and its drug release.” *ACS Appl. Mater. Interfaces*, 4(3), 1200–1210.
- Shabalovskaya, S. A., Siegismund, D., Heurich, E., and Rettenmayr, M. (2013). “Evaluation of wettability and surface energy of native Nitinol surfaces in relation to hemocompatibility.” *Mater. Sci. Eng. C*, 33(1), 127–132.
- Shankar, D., and Jambagi, S. C. (2024). “Improvements in bioactivity, blood

compatibility, and wear resistance of thermally sprayed carbon nanotube reinforced hydroxyapatite-based orthopedic implants.” *Tribol. Int.*, 197(April).

Shankar, D., Jambagi, S. C., Gowda, N., Lakshmi, K. S., Jayanthi, K. J., and Chaudhary, V. K. (2024a). “Effect of Surface Chemistry on Hemolysis, Thrombogenicity, and Toxicity of Carbon Nanotube Doped Thermally Sprayed Hydroxyapatite Implants.” *ACS Biomater. Sci. Eng.*, 10(3), 1403–1417.

Shankar, D., Jayaganesh, K., Gowda, N., Lakshmi, K. S., Jayanthi, K. J., and Jambagi, S. C. (2024b). “Thermal spray processes influencing surface chemistry and in-vitro hemocompatibility of hydroxyapatite-based orthopedic implants.” *Biomater. Adv.*, 158(December 2023), 213791.

Shoenfeld, N. A., Eldrup-Jorgensen, J., Connolly, R., Callow, A. D., Valeri, C. R., Ramberg, K., Mackey, W. C., and O’Donnell, T. F. (1987). “The effect of low molecular weight dextran on platelet deposition onto prosthetic materials.” *J. Vasc. Surg.*, 5(1), 76–82.

Singh, B., Lohan, S., Sandhu, P. S., Jain, A., and Mehta, S. K. (2016). “Functionalized carbon nanotubes and their promising applications in therapeutics and diagnostics.” *Nanobiomaterials Med. Imaging*, 455.

Singh, D., la Cinta Lorenzo-Martin, M. de, Gutiérrez-Mora, F., Routbort, J. L., and Case, E. D. (2006). “Self-joining of zirconia/hydroxyapatite composites using plastic deformation process.” *Acta Biomater.*, 2(6), 669–675.

Singh, G., Singh, S., and Prakash, S. (2011). “Surface characterization of plasma sprayed pure and reinforced hydroxyapatite coating on Ti6Al4V alloy.” *Surf. Coatings Technol.*, 205(20), 4814–4820.

Singh, T. P., Singh, H., and Singh, H. (2014). “Characterization of thermal sprayed hydroxyapatite coatings on some biomedical implant materials.” *J. Appl. Biomater. Funct. Mater.*, 12(1), 48–56.

Singhal, J. P., and Ray, A. R. (2002). “Synthesis of blood compatible polyamide block copolymers.” *Biomaterials*, 23(4), 1139–1145.

Spriano, S., Yamaguchi, S., Baino, F., and Ferraris, S. (2018). “A critical review of multifunctional titanium surfaces: New frontiers for improving osseointegration and host response, avoiding bacteria contamination.” *Acta Biomater.*, Acta Materialia Inc.

Stokes, J. (2003). “Production of Coated and Free-standing Engineering Components

Using the HVOF (High Velocity Oxy-Fuel) Process.” *PhD Thesis*.

Sun, J., and Gao, L. (2003). “Development of a dispersion process for carbon nanotubes in ceramic matrix by heterocoagulation.” *Carbon N. Y.*, 41(5), 1063–1068.

Sun, J., Gao, L., and Li, W. (2002). “Colloidal processing of carbon nanotube/alumina composites.” *Chem. Mater.*, 14(12), 5169–5172.

Sun, L. (2018). “Thermal Spray Coatings on Orthopedic Devices: When and How the FDA Reviews Your Coatings.” *J. Therm. Spray Technol.*, 27(8), 1280–1290.

Suñer, S., Tipper, J. L., and Emami, N. (2012). “Biological effects of wear particles generated in total joint replacements: Trends and future prospects.” *Tribol. - Mater. Surfaces Interfaces*.

Surmenev, R. A., Surmeneva, M. A., and Ivanova, A. A. (2014). “Significance of calcium phosphate coatings for the enhancement of new bone osteogenesis - A review.” *Acta Biomater.*, 10(2), 557–579.

Tan, R., Feng, Q., She, Z., Wang, M., Jin, H., Li, J., and Yu, X. (2010). “In vitro and in vivo degradation of an injectable bone repair composite.” *Polym. Degrad. Stab.*, 95(9), 1736–1742.

Tanaka, K., Yamabe, T., and Fukui, K. (1999). “The science and technology of carbon nanotubes.” 191.

Tengku Mohd, T. A., Jaafar, M. Z., Ali Rasol, A. A., and Hamid, M. F. (2016). “Measurement of Streaming Potential in Downhole Application: An Insight for Enhanced Oil Recovery Monitoring.” *MATEC Web Conf.*, EDP Sciences.

Tercero, J. E., Namin, S., Lahiri, D., Balani, K., Tsoukias, N., and Agarwal, A. (2009). “Effect of carbon nanotube and aluminum oxide addition on plasma-sprayed hydroxyapatite coating’s mechanical properties and biocompatibility.” *Mater. Sci. Eng. C*, 29(7), 2195–2202.

Tian, P., Hu, H., Wang, H., Liu, X., and Ding, C. (2014). “TiO₂/CaF₂ composite coating on titanium for biomedical application.” *Mater. Lett.*, 117, 98–100.

Usui, Y., Aoki, K., Narita, N., Murakami, N., Nakamura, I., Nakamura, K., Ishigaki, N., Yamazaki, H., Horiuchi, H., Kato, H., Taruta, S., Kim, Y. A., Endo, M., and Saito, N. (2008). “Carbon nanotubes with high bone-tissue compatibility and bone-formation acceleration effects.” *Small*, 4(2), 240–246.

Vardharajula, S., Ali, S. Z., Tiwari, P. M., Eroğlu, E., Vig, K., Dennis, V. A., and

Singh, S. R. (2012). "Functionalized carbon nanotubes: Biomedical applications." *Int. J. Nanomedicine*.

Veiga, A., Madureira, S., Costa, J. B., Castro, F., Rocha, F., and Oliveira, A. L. (2023). "Tackling current production of HAp and HAp-driven biomaterials." *Mater. Adv.*

Vignesh Raj, S., Rajkumar, M., Meenakshi Sundaram, N., and Kandaswamy, A. (2018). "Synthesis and characterization of hydroxyapatite/alumina ceramic nanocomposites for biomedical applications." *Bull. Mater. Sci.*, 41(4).

Vijayalakshmi, V., Sadanandan, B., and Anjanapura, R. V. (2023). "In vitro comparative cytotoxic assessment of pristine and carboxylic functionalized multiwalled carbon nanotubes on LN18 cells." *J. Biochem. Mol. Toxicol.*, 37(3).

Vijayalakshmi, V., Sadanandan, B., and Venkataramanaiah Raghu, A. (2022). "Single walled carbon nanotubes in high concentrations is cytotoxic to the human neuronal cell LN18." *Results Chem.*, 4, 100484.

Vilardell, A. M., Cinca, N., Garcia-Giralt, N., Dosta, S., Cano, I. G., Nogués, X., and Guilemany, J. M. (2020). "In-vitro comparison of hydroxyapatite coatings obtained by cold spray and conventional thermal spray technologies." *Mater. Sci. Eng. C*, 107(June 2018), 110306.

Viswanath, B., and Ravishankar, N. (2006). "Interfacial reactions in hydroxyapatite/alumina nanocomposites." *Scr. Mater.*, 55(10), 863–866.

Volder, M. F. L. De, Tawfick, S. H., Baughman, R. H., and Hart, A. J. (2013). "Carbon nanotubes: Present and future commercial applications." *Science (80-.)*.

Vu, A. A., Robertson, S. F., Ke, D., Bandyopadhyay, A., and Bose, S. (2019). "Mechanical and biological properties of ZnO, SiO₂, and Ag₂O doped plasma sprayed hydroxyapatite coating for orthopaedic and dental applications." *Acta Biomater.*, 92, 325–335.

Vuoristo, P. (2014). *Thermal Spray Coating Processes. Compr. Mater. Process.*, Elsevier.

Wang, C., Tian, P., Cao, H., Sun, B., Yan, J., Xue, Y., Lin, H., Ren, T., Han, S., and Zhao, X. (2022). "Enhanced Biotribological and Anticorrosion Properties and Bioactivity of Ti6Al4V Alloys with Laser Texturing." *ACS Omega*.

Wang, K., Zhou, C., Hong, Y., and Zhang, X. (2012). "A review of protein adsorption

on bioceramics.” *Interface Focus*, Royal Society.

Wang, Y., Liu, X., Fan, T., Tan, Z., Zhou, Z., and He, D. (2017). “In vitro evaluation of hydroxyapatite coatings with (002) crystallographic texture deposited by micro-plasma spraying.” *Mater. Sci. Eng. C*, 75, 596–601.

Weber, M., Steinle, H., Golombek, S., Hann, L., Schlensak, C., Wendel, H. P., and Avci-Adali, M. (2018). “Blood-Contacting Biomaterials: In Vitro Evaluation of the Hemocompatibility.” *Front. Bioeng. Biotechnol.*, Frontiers Media S.A.

Widantha, K. W., Basuki, E. A., Martides, E., and Prawara, B. (2021). “Effect of hydroxyapatite/alumina composite coatings using HVOF on immersion behavior of NiTi alloys.” *J. Biomater. Appl.*, 36(3), 375–384.

Wiessner, J., Mandel, G., Halverson, P., and Mandel, N. (1988). “The effect of hydroxyapatite crystallinity on hemolysis.” *Calcif. Tissue Int.*, 42(4), 210–219.

Wu, Z., Chen, H., Huang, H., Zhao, T., Liu, X., Li, D., and Yu, Q. (2009). “A facile approach to modify polyurethane surfaces for biomaterial applications.” *Macromol. Biosci.*, 9(12), 1165–1168.

Xie, D., Howard, L., and Almousa, R. (2018). “Surface modification of polyurethane with a hydrophilic, antibacterial polymer for improved antifouling and antibacterial function.” *J. Biomater. Appl.*, 33(3), 340–351.

Xu, L. C., Bauer, J. W., and Siedlecki, C. A. (2014). “Proteins, platelets, and blood coagulation at biomaterial interfaces.” *Colloids Surfaces B Biointerfaces*, 124, 49–68.

Xue, W., Liu, X., Zheng, X., and Ding, C. (2005). “Effect of hydroxyapatite coating crystallinity on dissolution and osseointegration in vivo.” *J. Biomed. Mater. Res. - Part A*, 74(4), 553–561.

Yang, P., Wang, N., Zhang, J., Lei, Y., and Shu, B. (2022). “Investigation of the microstructure and tribological properties of CNTs/Ni composites prepared by electrodeposition.” *Mater. Res. Express*, 9(3), 036404.

Yang, Y. C. (2011). “Investigation of residual stress generation in plasma-sprayed hydroxyapatite coatings with various spraying programs.” *Surf. Coatings Technol.*, 205(21–22), 5165–5171.

Yang, Y. C., and Chang, E. (2003). “The bonding of plasma-sprayed hydroxyapatite coatings to titanium: Effect of processing, porosity and residual stress.” *Thin Solid Films*, 444(1–2), 260–275.

- Yu, M. F., Files, B. S., Arepalli, S., and Ruoff, R. S. (2000). “Tensile loading of ropes of single wall carbon nanotubes and their mechanical properties.” *Phys. Rev. Lett.*, 84(24), 5552–5555.
- Zadpoor, A. A. (2014). “Relationship between in vitro apatite-forming ability measured using simulated body fluid and in vivo bioactivity of biomaterials.” *Mater. Sci. Eng. C*, 35(1), 134–143.
- Zalnezhad, E., Musharavati, F., Chen, T., Jaber, F., Uzun, K., Chowdhury, M. E. H., Khandakar, A., Liu, J., and Bae, S. (2021). “Tribo-mechanical properties evaluation of HA/TiO₂/CNT nanocomposite.” *Sci. Rep.*, 11(1), 1–15.
- Zanello, L. P., Zhao, B., Hu, H., and Haddon, R. C. (2006). “Bone cell proliferation on carbon nanotubes.” *Nano Lett.*, 6(3), 562–567.
- Zhan, G. D., Kuntz, J. D., Wan, J., and Mukherjee, A. K. (2003). “Single-wall carbon nanotubes as attractive toughening agents in alumina-based nanocomposites.” *Nat. Mater.*, 2(1), 38–42.
- Zhou, H., Wu, T., Dong, X., Wang, Q., and Shen, J. (2007). “Adsorption mechanism of BMP-7 on hydroxyapatite (001) surfaces.” *Biochem. Biophys. Res. Commun.*, 361(1), 91–96.
- ZHOU, T., CHEN, H., YUE, Y. nan, FANG, X. yang, ZHANG, R. qian, GAO, X., and CAI, Z. bing. (2023). “Effect of coating thickness on interfacial adhesion and mechanical properties of Cr-coated zircaloy.” *Trans. Nonferrous Met. Soc. China (English Ed.)*, 33(9), 2672–2686.
- Zhu, X. D., Fan, H. S., Xiao, Y. M., Li, D. X., Zhang, H. J., Luxbacher, T., and Zhang, X. D. (2009). “Effect of surface structure on protein adsorption to biphasic calcium-phosphate ceramics in vitro and in vivo.” *Acta Biomater.*, 5(4), 1311–1318.
- Zhu, X. D., Fan, H. S., Zhao, C. Y., Lu, J., Ikoma, T., Tanaka, J., and Zhang, X. D. (2007). “Competitive adsorption of bovine serum albumin and lysozyme on characterized calcium phosphates by polyacrylamide gel electrophoresis method.” *J. Mater. Sci. Mater. Med.*, Springer, 2243–2249.

LIST OF PUBLICATIONS

Sl No.	Title of the paper	Authors (in the same order as in the paper. Underline the Research Scholar's name	Name of the Journal/ Conference, Vol., No., Pages	Month, Year of Publication	Category
1	Thermal spray processes influencing surface chemistry and in-vitro hemocompatibility of hydroxyapatite-based orthopedic implants	<u>Deep Shankar</u> , K. Jayaganesh, Niranjan Gowda, K.S. Lakshmi, K.J. Jayanthi, and Sudhakar C. Jambagi	Biomaterials Advances, 158-213791. https://doi.org/10.1016/j.bioadv.2024.213791	January, 2024	1
2	Effect of Surface Chemistry on Hemolysis, Thrombogenicity, and Toxicity of Carbon Nanotube Doped Thermally Sprayed Hydroxyapatite Implants	<u>Deep Shankar</u> , Sudhakar C. Jambagi, Niranjan Gowda, K.S. Lakshmi, K.J. Jayanthi, and Vikash Kumar Chaudhary	ACS Biomaterials Science & Engineering. 10, 3, 1403–1417 https://doi.org/10.1021/acsbiomaterials.3c00912	February, 2024	1
3	Improvements in bioactivity, blood compatibility, and wear resistance of thermally sprayed carbon nanotube reinforced hydroxyapatite-based orthopedic implants	<u>Deep Shankar</u> , Sudhakar C. Jambagi	Tribology International 197, 109809 https://doi.org/10.1016/j.triboint.2024.109809	May 2024	1

BIO-DATA

- 1 **Name** : Deep Shankar
- 2 **Fathers Name** : Ashok Kumar Prasad
- 3 **Date of Birth** : 30 October 1992
- 4 **Nationality** : Indian
- 5 **Marital status** : Married
- 6 **Address** : C/O Hari Shankar Gupta, Kishori Lal chowk
Bada Bazar, Madhubani, Bihar- 847211
- 7 **Mobile number** : +91 7204322434
- 8 **Email id** : deep.03nitk@gmail.com
- 9 **Educational qualifications**

Qualification	University/Board	Year of Passing
Ph.D. (Mechanical Engineering)	NITK, Surathkal	2024
M. Tech. (Manufacturing Engineering)	SLIET, Longowal	2017
B. E (Mechanical Engineering)	JSSATE, Bengaluru	2014